



HAL
open science

Soft interfaces : from elastocapillary snap-through to droplet dynamics on elastomers

Aurélie Hourlier-Fargette

► **To cite this version:**

Aurélie Hourlier-Fargette. Soft interfaces : from elastocapillary snap-through to droplet dynamics on elastomers. Mechanics [physics]. Université Pierre et Marie Curie - Paris VI, 2017. English. NNT : 2017PA066089 . tel-01618557

HAL Id: tel-01618557

<https://theses.hal.science/tel-01618557>

Submitted on 18 Oct 2017

HAL is a multi-disciplinary open access archive for the deposit and dissemination of scientific research documents, whether they are published or not. The documents may come from teaching and research institutions in France or abroad, or from public or private research centers.

L'archive ouverte pluridisciplinaire **HAL**, est destinée au dépôt et à la diffusion de documents scientifiques de niveau recherche, publiés ou non, émanant des établissements d'enseignement et de recherche français ou étrangers, des laboratoires publics ou privés.



Soft Interfaces:

from elastocapillary snap-through to droplet dynamics on elastomers

Thèse de doctorat de l'Université Pierre et Marie Curie

Spécialité : Mécanique

École Doctorale : « Sciences mécaniques, acoustique,
électronique et robotique de Paris »

Réalisée à l'Institut Jean le Rond d'Alembert

présentée par

Aurélie HOURLIER-FARGETTE

pour obtenir le grade de :
Docteur de l'Université Pierre et Marie Curie

soutenue le 12/06/2017

devant le jury composé de :

Mme Élise LORENCEAU
M. Frédéric RESTAGNO
Mme Marie LE MERRER
M. Benoît ROMAN
M. Robert STYLE
M. Régis WUNENBURGER
M. Arnaud ANTKOWIAK
M. Sébastien NEUKIRCH

Rapporteur
Rapporteur
Examineur
Examineur
Examineur
Président du jury
Directeur de thèse
Directeur de thèse

*À Adrien,
Merci d'être là, merci d'être toi.*

Acknowledgments

Ces années de thèse ont été une expérience particulièrement enrichissante pour moi, résultant d'interactions fructueuses avec de nombreuses personnes. Ce sont toutes ces personnes que je souhaite remercier aujourd'hui, non sans émotion, au moment où je m'appête à tourner la page de cette thèse pour m'envoler vers d'autres aventures en recherche, de l'autre coté de l'Atlantique.

Sébastien, Arnaud, sans vous cette thèse n'aurait pas été possible. Nos chemins se sont croisés il y a 7 ans (déjà!) lorsque, fraîchement arrivée à l'ENS, je vous contactais à la recherche d'un stage de L3. Vous m'avez ouvert les portes de la salle Savart avec un sujet expérimental qui m'a permis de goûter aux joies de l'élastocapillarité, et a orienté de nombreux choix que j'ai faits par la suite. A ce propos, je tiens à remercier Christophe (et les séminaires de la FIP), qui m'ont permis de connaître ∂^2 Alembert!

Sébastien, au début de ma thèse, tu m'as dit : "Sais tu pourquoi les zèbres ont des rayures? Parce que quand ils courent en troupeau, la lionne ne sait plus où donner de la tête : elle n'arrive pas à isoler visuellement un zèbre et se concentrer dessus. La première partie du métier de chercheur, c'est d'isoler un zèbre." Effectivement, tu avais raison : choisir son objet d'étude est une étape cruciale. Merci pour tes qualités scientifiques et pédagogiques bien sûr, mais aussi pour ta bienveillance, pour tes recommandations de lectures, et pour nos discussions sur le choix de mon futur postdoc ou encore sur la place des femmes en sciences.

Arnaud, merci pour ton enthousiasme, et pour ton incroyable capacité à faire des liens avec d'autres études, articles, documents qui datent d'il y a plus d'un siècle (n'oublions pas Miss Pockels), ou au contraire qui sont sortis la veille sur arXiv. Merci pour ton perfectionnisme et ton oeil artistique lorsqu'il s'agit par exemple de parler figures, ainsi que pour la façon passionnée dont tu abordes le travail expérimental : les manip ont toujours raison!

Je souhaite remercier l'ensemble des membres de mon jury pour l'attention qu'ils ont portée à mon travail de thèse. En particulier, je remercie vivement Élise Lorenceau et Frédéric Restagno d'avoir accepté la tâche de rapporteur malgré des emplois du temps bien chargés. I am grateful to Rob Style for his venue in Paris for my defense, and for the interest he took in my work. Je remercie Marie Le Merrer pour son enthousiasme concernant ma thèse, ainsi que pour la visite de l'ILM qu'elle m'a concoctée la semaine suivant ma soutenance. Merci à Benoit Roman pour les interactions scientifiques que nous avons eues (au PMMH ou, plus souvent, en conférences) et pour sa participation à mon jury de thèse. Merci beaucoup à Régis Wunenburger d'avoir présidé ce jury, ainsi que pour nos discussions au début de ma thèse.

Je suis également très reconnaissante au Département de Physique de l'ENS de m'avoir permis d'être agrégée préparatrice durant ma thèse, enrichissant ces quatre années d'une expérience d'enseignement particulièrement stimulante. Merci à Stephan Fauve, Jean-Michel Raimond et François Levrier, pour m'avoir confié des TD à la FIP mais aussi pour m'avoir permis de revenir à la prépa agreg, avec plaisir, transmettre à mon tour ce que j'avais eu la chance d'apprendre en préparant l'agrégation juste avant ma thèse. Merci à tous ceux qui contribuent à faire de la prépa agreg un lieu propice aux discussions scientifiques animées, aussi bien entre enseignants qu'avec les étudiants. J'ai une pensée toute particulière pour Benoît, Arnaud, Guillaume, Emmanuel et Kenneth, mais aussi pour Eric sans qui la prépa agreg (et en particulier sa collection) ne serait pas ce qu'elle est.

À ∂ 'Alembert, j'ai eu la chance d'effectuer ma thèse dans un environnement propice à l'interdisciplinarité. Outre mes directeurs de thèse et membres de jury, de nombreux chercheurs m'ont fait profiter de leurs compétences. Merci à tous. Christophe, tu m'as fait connaître ∂ 'Alembert et as su garder un oeil bienveillant sur mon travail : nos discussions, même peu fréquentes, m'ont permis de franchir certains obstacles, et je t'en remercie. Thomas, merci pour ta bonne humeur communicative, et pour le temps passé ensemble à construire des manips d'explosions de vésicules. Merci à toi et à Suzie pour vos conseils pour ma soutenance, merci également à vous deux pour notre sympathique séjour à Portland pour DFD. Stéphanie, un grand merci pour ton enthousiasme et ta gentillesse. Pierre-Yves, même si nos avis divergent concernant mon nom de famille, je te suis très reconnaissante pour tes conseils. Stéphane, merci d'avoir pris le temps de discuter de ma thèse malgré un emploi du temps chargé de directeur de ∂ 'Alembert. Djimédo, merci de prendre autant à coeur tes responsabilités à l'école doctorale. Guy-Jean, pardon d'avoir parfois réquisitionné la caméra rapide, merci pour ta patience et ta gentillesse. Joël, merci pour ta bonne humeur et ta bienveillance. Laurent, Jean-Camille, merci de m'avoir facilité l'accès à des conférences ou l'achat de matériel indispensable à ma thèse. Basile, merci beaucoup, grâce à toi j'ai beaucoup appris en mécanique des milieux continus. Arnaud L., merci pour les discussions variées qu'on a pu avoir, et aussi, merci pour ton investissement pour l'installation et la bonne utilisation de la découpeuse laser du labo, qui est un outil absolument génial!

Cet environnement propice à l'épanouissement est également le fruit d'une excellente ambiance entre thésards. Bab, Claude, un énorme merci pour les chocolats viennois partagés lorsque les manips ne marchaient pas. Merci pour votre aide au début de ma thèse. Paul, avec ton arrivée, un vent de créativité a soufflé en salle de manip! Merci pour tout, tu as été un allié précieux pour la deuxième partie de ma thèse. Etienne, merci pour tes conseils, en particulier avec LaTeX pour la rédaction. Je n'oublie pas les autres thésards et post-docs expérimentateurs : Nico, ses aventures de grimpe, et son aide pour le pot, Hervé (alias Peter Parker), Walid (spécialiste de multistabilité parfois bruyante), Virgile (chaleureux malgré des manips glaciales), Julien C. (co-utilisateur de PDMS), Emmanuel (et les explosions de ballons), Gounseti (spécialiste des ponts capillaires), Adrien B. (qui écoute les bulles). Merci à Claire, amenée aussi à manipuler avec les élastomères de dentiste, et à Estelle, je n'oublierai pas le ski et les manips de pailles. Plus généralement, merci à tous ceux avec qui j'ai pris plaisir à aller manger au RA, en vrac : Raph, Charles, Christian, Mehdi, Arthur, Antoine, Chia, Adi, Andres, Geoffroy, Hugo, Valentin, Aurélie, Barend, Jan, Thomas, David, Valentina, Luca, J-B, Omar, Jeff et bien d'autres. Et

merci Benjamin, même si on n'a pas réussi à te convaincre de venir au RA, tu as été un super co-bureau! Bon courage pour la fin de thèse. Merci à Julieng, à Quentin pour son enthousiasme débordant pour parler manips, mais également à Bertrand et Thomas, anciens co-bureaux, et à Marco et P-T, surtout pour le March Meeting 2012. Enfin, merci aux stagiaires qui contribuent à rendre la salle Savart si vivante à l'approche de l'été.

Je souhaite bien sûr remercier tous les gestionnaires de ∂ 'Alembert, et en particulier Olivier et Catherine qui se sont chargés le plus souvent de toutes les démarches liées aux commandes et aux missions me concernant.

Mais j'ai aussi eu la chance pendant ma thèse d'avoir de nombreuses interactions avec d'autres laboratoires. En ce qui concerne les manips, merci à Fabrice Monti pour son expertise en traitement plasma du PDMS, merci à Alexis Prévost et George Debrégeas pour l'utilisation du profilomètre du laboratoire Jean Perrin. Merci à Guylaine Ducouret pour l'utilisation du rhéomètre à l'ESPCI, à Natacha Krins et Cédric Boissière au LCMCP, à Emmanuelle Rio et Emilie Forel pour l'utilisation du tensiomètre Kibron et à Marion Grzelka pour l'ellipsométrie au LPS d'Orsay. Et enfin, merci beaucoup à Antoine Chateauminois au SIMM (ESPCI), pour cette fructueuse collaboration en ce qui concerne l'élimination des chaînes libres du PDMS.

Plus généralement, merci à toutes les personnes qui, de près ou de loin, ont influencé mon travail ou avec qui, plus simplement, j'ai pris plaisir à discuter, que ce soit à Paris, Grenoble, Peyresq, Biarritz, Agay, Leiden, Boston, Chicago, Portland, ou encore La Nouvelle Orléans. Merci à José Bico, Camille Duprat, Laurent Limat, Françoise Brochard, Etienne Barthel, Philippe Marmottant, François Boulogne, Denis Terwagne, Joel Marthelot, Etienne Reyssat, Evelyne Kolb, Stéphane Perrard, Cyprien Gay, et beaucoup d'autres. Many thanks to Dominic Vella for discussions, and to Randy Ewoldt, Vivek Sharma, and Monica Olvera de la Cruz for their invitations to give seminars in the Chicago area. And of course, I would like to thank Pedro Reis, who taught me during my internship in his group that there are no problems in research, only challenges!

Vient le tour des proches. Merci à mes parents qui m'ont fait baigner dans cet univers de curiosité scientifique depuis toute petite. C'est grâce à vous qu'est né mon intérêt pour la physique, mais aussi pour la créativité artistique. Benjamin, Caroline, merci pour vos talents de photographes, pour l'abonnement à votre canapé-lit que vous nous avez accordé, et pour votre précieuse amitié. Pauline, Marie, Estelle, Marie-Anne, Camille, merci pour ces belles amitiés nouées au fil des années. Marie, Bertrand, merci pour votre gentillesse et votre disponibilité, pour le pot de thèse bien sur, mais aussi dans la vie de tous les jours.

Adrien, tous les mots que je pourrais écrire ici pour te remercier ne seront jamais à la hauteur de ce dont je te suis redevable pour cette thèse. Merci de regarder le monde avec un oeil de physicien! Merci pour les nombreuses heures que tu as passées pour relire ce document ou encore pour discuter de dévalement de gouttes autour de notre tableau Velleda. On aurait envie de ne se souvenir que des bons moments de la thèse, mais quand les manips de marchaient pas, ou quand je n'avais pas encore isolé mon "zèbre", tu as été la personne en qui j'ai toujours pu trouver un soutien indéfectible. Merci. Je t'aime.

Introduction

Capillary forces are often too weak to deform a substrate, but are able to dominate elasticity at small scales, on soft materials. A water droplet can interact in a spectacular way with slender flexible structures such as thin elastic sheets or beams, inducing wrinkling, static or dynamic folding, aggregation of fibers, or buckling. Both Nature and industry present numerous examples of such phenomena, from the aggregation of wet hair to the unintended collapse of microstructures due to capillary forces. The role of surface tension in the mechanics of deformable solids is thus a question raising a growing interest in the soft matter community, in the case of both thin flexible structures and soft bulk elastomers. On a soft bulk elastic material, a droplet does not deform macroscopically the structure, but raises a wetting ridge at the triple line. The recent design of Slippery Lubricant Infused Porous Surfaces also leads to novel wetting dynamics studies to understand how droplets slide or roll on a micro- or nano-textured substrate infused with oil. This thesis takes place in this context, at the crossing between macroscopic observations and microscopic phenomena occurring at the scale of elastomer networks, focusing on mechanical instabilities and interfacial phenomena.

The manuscript is articulated around five chapters: chapter 1 introduces general concepts about elasticity and capillarity. Elastic structures and capillary interactions are also combined in a brief state of the art on elastocapillarity. In this introductory chapter, we lay foundation for the studies presented in the following chapters both from an elasticity point of view, by describing mechanical instabilities of slender beams, and from a capillary point of view, by analyzing static and dynamic wetting phenomena. In particular, the snap-through instability introduced here is investigated from an elastocapillary point of view in chapter 3, while the brief overview on droplet dynamics on inclined planes studies sets the background for our droplet dynamics experiments on elastomers, exposed in chapters 4 and 5.

The work presented in this thesis is mainly experimental: chapter 2 is a materials and methods section in which are summarized experimental techniques that are going to be used throughout the other chapters. In elastocapillarity, both the liquid properties and the elastic structures properties need to be carefully chosen and characterized. We describe the various elastomers employed in our work, the techniques used to tune their geometry, as well as the characterization tools to measure both elastic and geometrical parameters. We then focus on liquids, explaining how liquids are chosen and presenting viscosity and surface tension measurements methods, along with droplet deposition techniques. Force sensing and high speed imaging are also discussed in this chapter.

In chapter 3, we revisit the snap-through instability from an elastocapillary point of view, in the context of smart actuators. To do so, we deposit water droplets above or below elastic strips clamped at both ends and buckled in the upward or downward configurations. We show that capillary forces are strong enough at small scales to trigger a snap-through instability even against gravity, when a droplet is deposited below a downward buckled elastic strip. We investigate the statics and dynamics of this phenomenon, compare droplet-induced snap-through to dry point-force indentation on a buckled thin strip, and design several spin-off versions of our experiment including a condensation-induced setup that allows for a remote triggering of the instability and constitutes a humidity-controlled mechanical switch.

In the experiments performed in chapter 3, we notice that viscoelasticity in the elastomer strips might affect the snap-through dynamics. We design sliding droplet experiments on silicone elastomer samples to further investigate the dissipation processes both in the droplet and in the elastomer. However, we observe an unexpected droplet dynamics on silicone elastomers – a droplet deposited on a silicone elastomer presents two successive regimes characterized by two constant speeds – and decide to focus on the understanding of this phenomenon. Chapter 4 describes these investigations, collecting pieces of evidences to gain a better knowledge of the mechanisms underlying this two-regime behavior. We show that uncrosslinked oligomers, present in most commercial silicone elastomers, are responsible for the surprising droplet dynamics. We gain insight on the underlying phenomena by performing surface tension measurements, and investigate further the droplets speeds in the first and second regimes, comparing our results to the case of Slippery Lubricant Infused Porous Surfaces.

Chapter 5 is more exploratory than the previous ones, and supplements the results obtained in chapter 4 by focusing on the dynamics of contamination of water droplets by uncrosslinked chains present in silicone elastomers. We perform surface tension measurements at the scale of one single droplet, correlating the speed of a droplet to its actual surface tension. We show additionally that a sessile droplet also extracts uncrosslinked oligomers from a silicone elastomer sample, however, the timescales involved are completely different from the case of a moving droplet. Various configurations that exhibit a water - air - silicone elastomer triple line are investigated to determine whether extraction of uncrosslinked oligomers occurs at the triple line, and focus is finally given on potential applications of this phenomenon.

Articles published during this PhD work are presented in an appendix at the end of the manuscript, followed by the bibliography, a nomenclature guide, and an index.

Contents

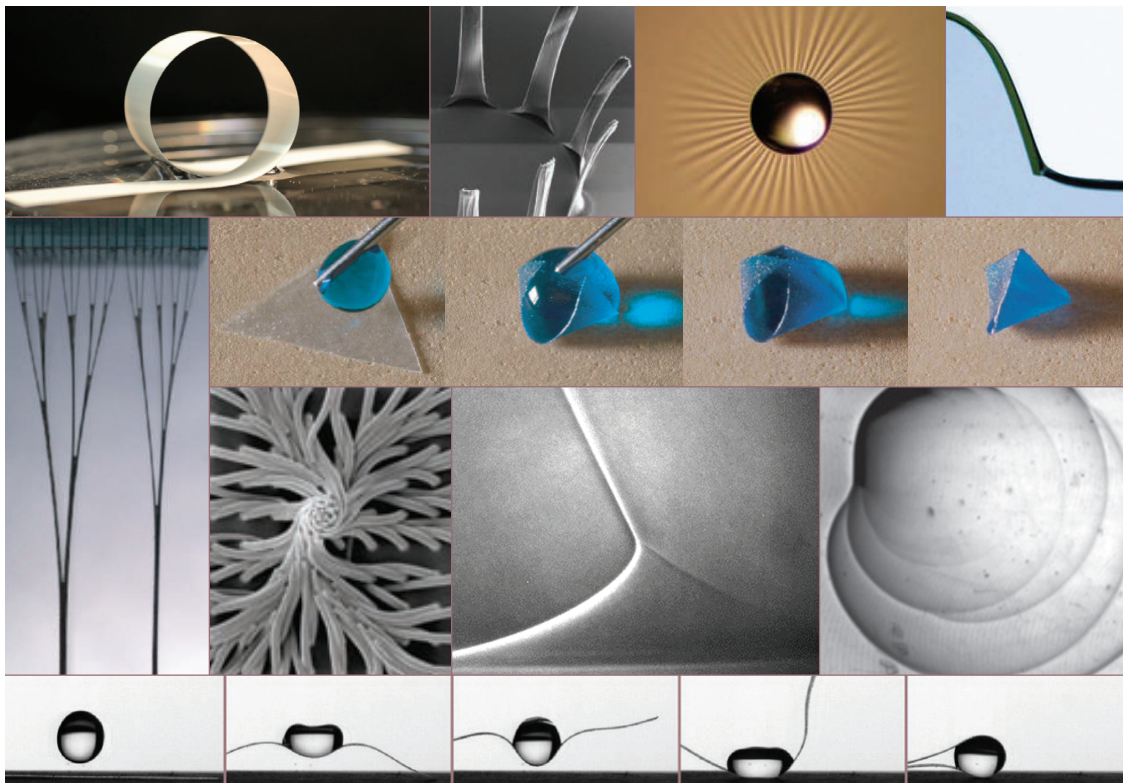
Acknowledgments	i
Introduction	v
1 Elasticity, capillarity, elastocapillarity: an introduction	1
1.1 Elasticity of slender beams: generalities on equilibrium, stability, and dynamics	2
1.1.1. Historical background	2
1.1.2. Mechanics of thin structures: beams, rods, sheets, shells	3
1.1.3. Bending and stretching	5
1.1.4. Buckling of a slender beam	6
1.1.5. Vibrations of a slender beam	9
1.1.6. Snap-through instability	10
1.2 Capillarity : from static to moving contact lines	11
1.2.1. Surface tension	11
1.2.2. Wetting : three-phase contact line	15
1.2.3. Triple line dynamics	17
1.2.4. Droplets on an inclined plane	19
1.3 Elastocapillarity with slender structures	24
1.3.1. Examples in Nature and in the industry	24
1.3.2. Elastocapillary length (slender structures)	30
1.3.3. State of the art: elastic sheets, strips, and fibers subjected to capillary forces	31
1.4 Elastocapillarity on soft polymer bulks	35
1.4.1. Statics: shape of the wetting ridge raised on a soft solid	36
1.4.2. Dynamics: moving contact lines on soft materials	38
2 Materials and Methods	41
2.1 Elastomer plates and strips	42
2.1.1. Materials selection and samples manufacture	42
2.1.2. Samples characterization: thickness and Young’s modulus	49
2.2 Microforce sensors	55
2.3 Liquids employed in our elastocapillary experiments	56
2.3.1. Basic requirements for liquids used in contact with silicone elastomers	57
2.3.2. Viscosity and surface tension measurements	58
2.3.3. Droplet deposition techniques	62
2.3.4. Ellipsometric characterization of an overlay of different liquids . .	63

2.4	High speed acquisition	65
2.4.1.	Fast cameras	65
2.4.2.	Lighting techniques	65
3	Elastocapillary snap-through	67
3.1	Context: smart actuators	68
3.1.1.	Various strategies used to engineer soft actuators	68
3.1.2.	Natural smart actuators: a source of inspiration	69
3.1.3.	Envisioning an elastocapillary snap-through actuator	71
3.2	Dry snapping experiments versus elastocapillary snapping	73
3.2.1.	Dry snapping: force-displacement curves	73
3.2.2.	Elastocapillary snapping: comparison with the dry case	75
3.2.3.	Snap-through against gravity	77
3.3	Spin-off versions of the experiment	78
3.3.1.	Droplets nucleated from water vapor	78
3.3.2.	Upscaled experiments using soap bubbles	79
3.4	Equilibrium: phase diagram	80
3.4.1.	Theoretical framework in the case of an elastocapillary snap-trough	80
3.4.2.	Phase diagram: varying the droplet size and position	82
3.5	Dynamics: snapping time	84
3.5.1.	Snapping time in the case of a dry setup	84
3.5.2.	Snapping time for elastocapillary snap-through events	87
3.6	Perspectives: viscous dissipation in the polymer	88
3.6.1.	Analysis of the snapping time for small polymer samples	88
3.6.2.	Design of sliding droplets experiments	89
4	An unexpected behavior for droplets dynamics on silicone elastomers	91
4.1	Two-regime dynamics of an aqueous droplet on a silicone elastomer	93
4.1.1.	Context	93
4.1.2.	From elastomer strips to elastomer plates	93
4.1.3.	Varying different parameters	96
4.2	Pieces of evidence to understand the two-regime behavior	98
4.2.1.	Tracking the motion inside a droplet: rolling rather than sliding	98
4.2.2.	Changing the temperature of the liquid used for droplet deposition	99
4.2.3.	Disturbing the triple line motion with an antistatic gun	100
4.2.4.	Using an obstacle to stop a droplet during its descent	101
4.2.5.	Turning the experimental setup upside down to re-use the same droplet on the same material	101
4.3	Role of uncrosslinked chains in the droplet dynamics	103
4.3.1.	Dow Corning Sylgard 184 PDMS uncrosslinked oligomers	103
4.3.2.	Washing procedure to remove uncrosslinked chains	104
4.3.3.	Droplet dynamics on washed elastomer plates	104
4.3.4.	Droplet dynamics on re-swelled elastomer plates	104
4.3.5.	Uncrosslinked chains collected by each droplet	106
4.3.6.	Composition of the uncrosslinked oligomers oil	106
4.3.7.	Link with adhesion-induced phase separation experiments	107
4.4	Surface tension measurements	108

4.4.1.	Useful insight from the literature	109
4.4.2.	Drawbacks of the hanging-drop method	110
4.4.3.	Surface tension of a liquid bath made of droplets collected in a Petri dish	110
4.4.4.	Results with Petri dishes of different sizes and made of different materials	111
4.4.5.	Generalization to water-glycerol mixture droplets	112
4.5	Quantitative speed measurements	113
4.5.1.	Experimental observations	113
4.5.2.	Discussion of the results obtained for the first regime	115
4.5.3.	Discussion of the results obtained for the second regime	116
4.6	Consequences and potential applications	120
4.6.1.	A simple test to evaluate the presence of uncrosslinked oligomers	120
4.6.2.	Similarities between our elastomer samples and SLIPS substrates: a <i>delayed slippery surface</i>	121
5	Extraction of uncrosslinked chains at triple lines: contamination dynamics	123
5.1	Link between surface tension evolution and duration of the first regime	124
5.1.1.	Measurement of the surface tension of one droplet during its descent	124
5.1.2.	Cloaking of a sessile droplet, lying on a horizontal PDMS surface	128
5.2	Localization of extraction at triple lines	131
5.2.1.	Cloaking of a flat liquid bath by oligomers extracted from a partially immersed PDMS plate	131
5.2.2.	Cloaking of a bubble deposited on a PDMS plate in a water bath	135
5.3	Sessile droplets contamination dynamics	136
5.3.1.	Contamination time as a function of the droplet radius	137
5.3.2.	Influence of other parameters: preliminary experiments	139
5.4	Moving droplets contamination dynamics	140
5.4.1.	Experimental results	140
5.4.2.	Discussion	141
5.5	Tuning the elastomer and droplet properties to achieve functionality	142
	Conclusion	145
	Appendix: published articles	149
	Bibliography	165
	Nomenclature	179
	Index	181

Chapter 1

Elasticity, capillarity, elastocapillarity: an introduction



We introduce here some general concepts that are discussed throughout the manuscript. Focus is first given on elasticity, in the context of slender structures and especially of slender beams, as a foundation for our elastocapillary snap-through experiment. We then introduce capillarity by defining surface tension and investigating static and moving contact lines, with an emphasis on droplet sliding dynamics. Capillarity and elasticity are eventually combined in a brief state of the art on elastocapillarity: capillary forces have the ability to shape elastic materials, causing large deformation of slender structures, or microscopic deformations localized at the triple line in the case of soft polymer bulks.

Contents

1.1	Elasticity of slender beams: generalities on equilibrium, stability, and dynamics	2
1.1.1.	Historical background	2
1.1.2.	Mechanics of thin structures: beams, rods, sheets, shells	3
1.1.3.	Bending and stretching	5
1.1.4.	Buckling of a slender beam	6
1.1.5.	Vibrations of a slender beam	9
1.1.6.	Snap-through instability	10
1.2	Capillarity : from static to moving contact lines	11
1.2.1.	Surface tension	11
1.2.2.	Wetting : three-phase contact line	15
1.2.3.	Triple line dynamics	17
1.2.4.	Droplets on an inclined plane	19
1.3	Elastocapillarity with slender structures	24
1.3.1.	Examples in Nature and in the industry	24
1.3.2.	Elastocapillary length (slender structures)	30
1.3.3.	State of the art: elastic sheets, strips, and fibers subjected to capillary forces	31
1.4	Elastocapillarity on soft polymer bulks	35
1.4.1.	Statics: shape of the wetting ridge raised on a soft solid	36
1.4.2.	Dynamics: moving contact lines on soft materials	38

1.1 Elasticity of slender beams: generalities on equilibrium, stability, and dynamics

In this section are discussed general concepts about elasticity, in the framework of linear elasticity of slender structures. Focus is given on slender beams undergoing buckling, snap-through, and vibrations, to introduce fundamental notions underlying the elastocapillary snap-through experiments described in chapter 3.

1.1.1. Historical background

A material subjected to traction, compression, or shear, is likely to undergo deformations. The question of quantifying the response of a material as a function of the applied loads was already raised by Galileo (1564-1642) as shown in the pictures in Fig. 1.1, reproduced from [1]. A simple tensile test (a), showing how a structure reacts to traction, is performed by hanging a dead load at the bottom of a sample and measuring its extension or recording its resistance to fracture. A bending test (b) consists in measuring the deflection of a beam clamped at one end, and subjected to a transverse force at the other end.

Indeed, a one-dimensional (beam) or two-dimensional (sheet) structure is likely to undergo two types of deformations: stretching (accommodating a load with an in-plane

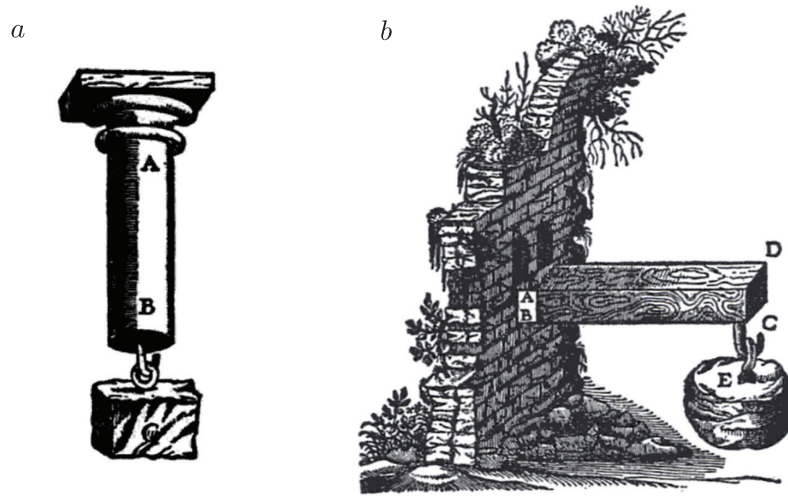


Figure 1.1 – (a) Galileo’s illustration of tensile test. (b) Galileo’s illustration of bending test. Reproduced from [1].

displacement) or bending (accommodating a load with an out-of-plane displacement). In the context of linear elasticity, these two types of deformations are related to the applied loads both by geometrical quantities and by a parameter depending only on the material, called Young’s modulus and denoted E in this manuscript. The so-called *Hooke’s law* corresponds to a linear relation between the force and the deformation in a tensile test, established first with springs and then with all *springy bodies* by Hooke (1635-1703). We consider a parallelepiped of length L_o and cross-section $S_o = hw$ where h is the thickness and w the width. If this sample is clamped at both ends and subjected to a tensile load F , Hooke’s law gives the relation between the actual length of the sample L and the tensile load, in the case of small deformations:

$$\frac{F}{S_o} = E \frac{L - L_o}{L_o}$$

The knowledge of the Young’s modulus E and of the geometrical parameters allows us to predict the deformation of a structure under a given loading. Euler (1707-1783) introduced variational calculations to obtain the shape of elastic curves undergoing bending, including contributions both on beams static configurations and on vibration modes. The out-of-plane deformation (buckling) of incompressible thin structures under compressive forces is nowadays often referred to as *Euler’s elastica* theory. The importance of geometry in the resistance to buckling-induced failure was already pointed out by Euler: *When the elasticity of the column and likewise its thickness remain the same, the weight P which it can carry without danger will be inversely proportional to the square of the height of the column; and a column twice as high will be able to bear only one-fourth of the load* [1].

1.1.2. Mechanics of thin structures: beams, rods, sheets, shells

A thin or slender structure, as the column described by Euler in the previous paragraph, is defined as a structure with a size in at least one dimension much smaller than the other. This type of object includes for instance rods, beams, strips, sheets, and shells. Slender

structures are likely to undergo large deformations as well as mechanical instabilities such as buckling or snap-through, which will be detailed later in this section. Although the mechanics of such structures has been studied in the past centuries, in particular to avoid failure in the case of construction materials, a recent focus is given on exploiting elasticity and elastic instabilities to achieve functionality [2], as well as on understanding daily life phenomena such as the breaking of spaghetti in multiple fragments [3] or the shape of curly hair in the gravity field [4, 5]. Indeed, the understanding of why spaghetti do not break in half relies on rods mechanics: once a first fracture occurs in the spaghetti, the sudden relaxation of the curvature at this new free end leads to a burst of flexural waves, likely to trigger new fracture events, as illustrated in Fig. 1.2(a). The shape of a curly hair in the presence of gravity is also determined by rods mechanics, more specifically by equilibrium configurations with a competition between elasticity and gravity, where natural curvature also plays a major role, as shown in Fig. 1.2(b).

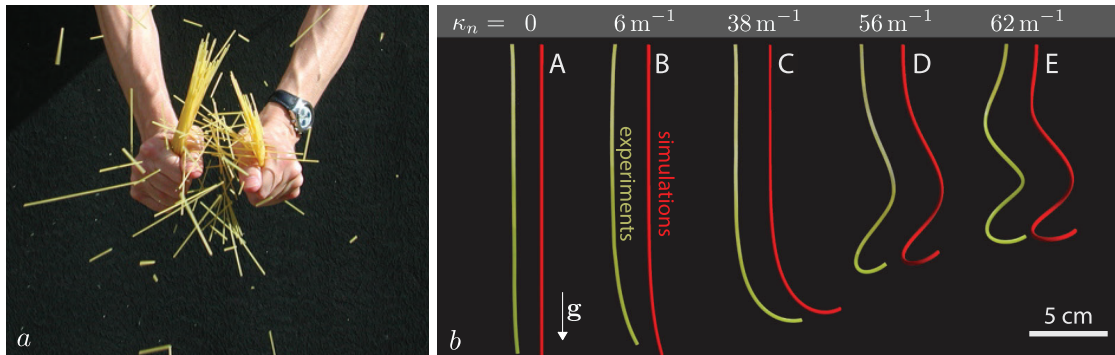


Figure 1.2 – (a) Spaghetti do not break in half: the first fracture event triggers flexural waves propagating along the rod, that lead to additional breakings [3]. Image: B. Audoly and S. Neukirch. (b) Equilibrium shapes of rods suspended under their own weight. The natural curvature κ_n is varied, while the length, radius, and material, are kept constant. Reproduced from [5].

The design of out-of-plane structures using bending of beams that pop up in a three-dimensional shape, as shown in Fig. 1.3(a), recently proved to be an innovative strategy to achieve three-dimensional micro- and nano-structures [6]. Such systems are promising in terms of electronic, optical and magnetic properties. Manufacturing conductive structures able to sustain large deformations is also a challenge for stretchable electronics. Beyond rods and beams, the mechanics of sheets and shells attracts a recent interest. Engineering structures that can undergo buckling-induced reversible folding under pneumatic actuation is a route towards soft robotics, as shown in the so-called *Buckliball* example [7] presented in Fig. 1.3(b). The geometry of the *Buckliball* consists of a spherical shell patterned with a regular array of circular voids. Below a critical pressure inside the ball, the thicker filaments between the voids buckle, leading to a decrease of the radius of the ball (negative Poisson's ratio effect). Taking advantage of this phenomenon could lead to new techniques for drug encapsulation, engineering of deployable structures, or actuation under various external stimuli including pH, temperature or ambient humidity. As described in [2], mechanical instabilities are now considered as a promising path to engineer innovative techniques and structures. Our study on capillarity-induced snap-through instability – described in chapter 3 – takes places in this context.

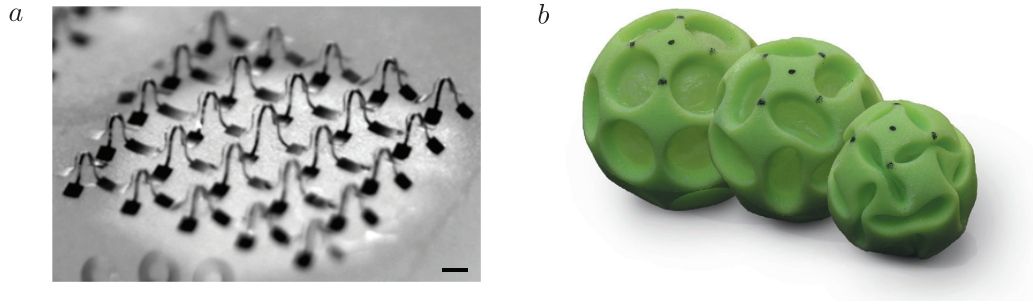


Figure 1.3 – (a) Buckling-induced three-dimensional mesostructure: a two-dimensional structure is bonded at selected points on a stretched elastomer. When tension inside the elastomer is released, the structure pops up out of plane. Scale bar is $200 \mu\text{m}$. Reproduced from [6]. (b) *Buckliball*: sequence of progressively deformed shapes as the pressure inside the structure is decreased. The structure consists of a spherical shell patterned with a regular array of circular voids. Reproduced from [8].

1.1.3. Bending and stretching

The Young’s modulus E of a material is often measured with a tensile test, directly linked to stretching properties of the sample. However, this parameter E also dictates the bending behavior of a sample, together with geometrical features. Two methods can be used to determine the equilibrium shape of a structure: minimizing the total potential energy, or using a force and moment balance. We first focus on energetic aspects, for an elastic beam as the one represented in Fig. 1.4. The situation illustrated in Fig. 1.4(b) is often referred to as *Euler elastica*: the shape of a slender and inextensible elastic beam subjected to compression was derived by Euler using calculus of variations.

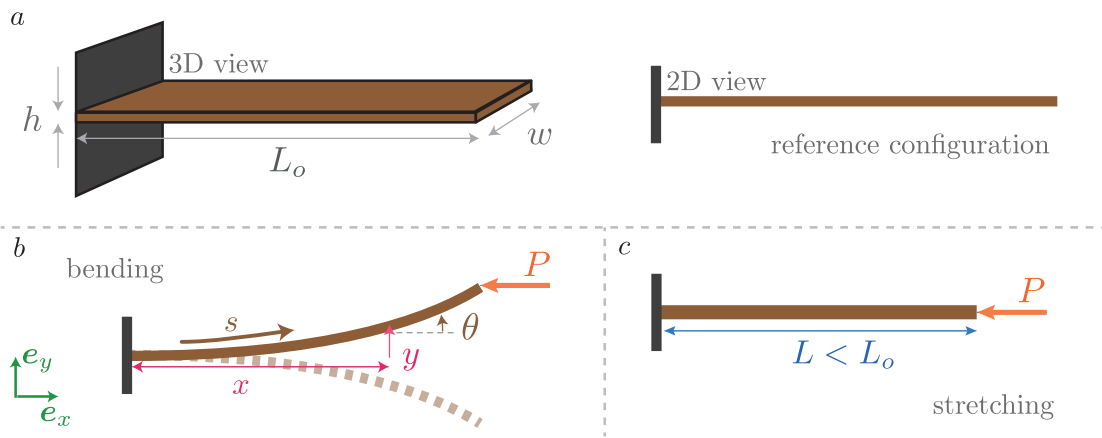


Figure 1.4 – (a) Reference configuration of a beam of length L_o , width w , and thickness h , clamped at one end. A compressive force is applied at the free end of the beam: the case of bending is depicted in (b), while the case of stretching is depicted in (c).

Denoting s the arclength, θ the local angle with the horizontal axis, and $I = h^3w/12$ the second moment of area of the cross-section of the beam, the energy associated to

bending is given by:

$$U_{\text{bend}} = \frac{EI}{2} \int_0^L (\theta')^2 ds$$

Now, denoting $A = hw$ the cross-section of the beam and ϵ the local strain (in the particular case of a homogeneous strain along the beam, $\epsilon = (L - L_o)/L_o$), the energy associated to stretching yields:

$$U_{\text{stretch}} = \frac{EA}{2} \int_0^L \epsilon^2 ds$$

The equilibrium configuration of a system is then determined by minimizing the total potential energy that can include bending energy, stretching energy, and additional terms, as for instance surface tension energies in the case of the elastocapillary snap-through experiments described in chapter 3.

The second method to determine equilibrium configurations is to perform a force and moment balance. In this case, the bending and stretching properties of a sample are taken into account through constitutive relations, that come in addition to the equations for the internal forces and for the internal moments. The bending constitutive relation for a linearly elastic material gives the relationship between the local internal moment M , the curvature θ' , and the elastic properties of the material: $M(s) = EI\theta'(s)$. As stretching only plays a minor role in the situations described in the following chapters, we only take bending deformations into consideration. We show below how to use the local force and moment balance to analyze the equilibrium shape of a beam clamped at both ends in the case of small deformations. The setup used in chapter 3 in the case of our elastocapillary snap-through experiments is indeed an elastic beam clamped at both ends and subjected to a compression that induces buckling of the beam.

1.1.4. Buckling of a slender beam

Several examples of buckling instabilities have already been shown in Fig. 1.3 and Fig. 1.4(b). A slender beam as the one described in Fig. 1.4(b) subjected to a compressive force takes one of the two bent equilibrium configurations, that are symmetrical: the configuration chosen by the beam often depends on imperfections in the system. Theoretical aspects of buckling are analyzed further in Timoshenko's *Theory of Elastic Stability* [9].

In the general two-dimensional situation of an inextensible beam subjected to forces per unit length P_x in the x direction and P_y in the y direction, the set of equations is the following:

$$\begin{aligned} x' &= \cos \theta & \text{and} & & y' &= \sin \theta \\ EI \theta' &= M(s) \\ M'(s) &= f_x(s) \sin \theta - f_y(s) \cos \theta \\ f'_x(s) &= -P_x(s) & \text{and} & & f'_y(s) &= -P_y(s) \end{aligned}$$

where $()'$ denotes the derivative with respect to s .

We analyze below two particular cases, illustrated in Fig. 1.5: buckling of a beam clamped at both ends and subjected to a compressive force (a), and buckling of a beam clamped at one end, due to the effect of its own weight (b).

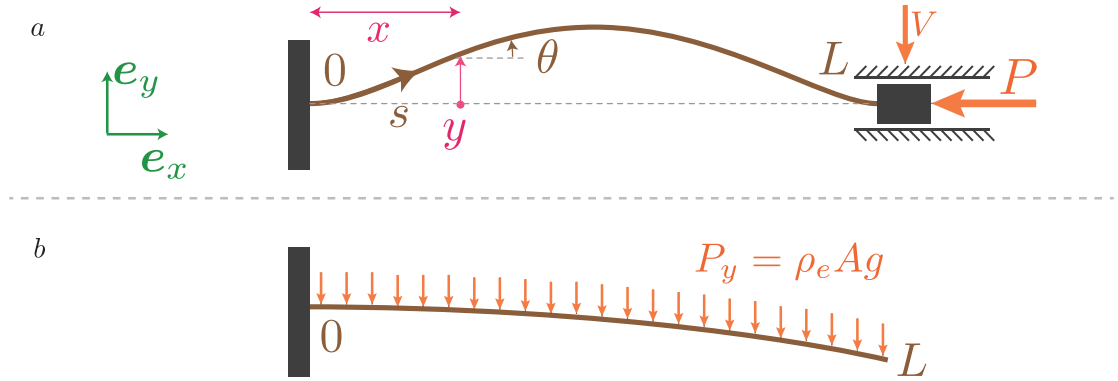


Figure 1.5 – (a) Buckling of a slender beam clamped at both ends and subjected to a compressive force P . (b) Buckling of a slender beam clamped at one end, free at the other end, and subjected to its own weight acting as a distributed force $P_y = \rho_e Ag$, denoting A the cross-section of the beam and ρ_e its density.

a) Buckling of a beam clamped at both ends

We focus on the particular case of a beam clamped at both ends, and subjected to a compressive force P in the x direction, applied locally at one end of the beam (Fig. 1.5(a)). This configuration is the starting point for the elastocapillary snap-through experiments presented in chapter 3. Denoting V the transverse force applied by the clamp on the beam, the equilibrium equation of the beam is:

$$EI \theta'' + P \sin \theta - V \cos \theta = 0$$

and needs to be solved with the boundary conditions $y = \theta = 0$ at $s = 0$ and $s = L$, corresponding to clamped ends. For the first buckling mode, it can be proved that V is equal to zero [10]. To determine the critical force that is required to induce buckling, a linearization gives the following equation for y :

$$EI y'''' + P y'' = 0$$

The general solution of this equation is:

$$y = C_1 \sin \left(\sqrt{\frac{P}{EI}} s \right) + C_2 \cos \left(\sqrt{\frac{P}{EI}} s \right) + C_3 s + C_4$$

The boundary conditions lead to a linear system in C_1 and C_2 (as $C_3 = C_4 = 0$), which has non trivial solutions only if its determinant is zero. The corresponding equation gives a critical value for the buckling load: in the case of a beam clamped at both ends, buckling occurs only if $P > P_c$, with

$$P_c = \frac{4\pi^2 EI}{L^2}$$

In the experiments described in chapter 3, the control parameter is the displacement of the right end of the beam and not the force applied by the clamp on the beam. However,

in the design of the experiment, we should keep in mind that there is a force exerted by the clamp on the beam, which is higher than this critical buckling force in the case of a buckled beam.

b) Equilibrium shape of a beam clamped horizontally at one end, subjected to its own weight

We now consider a beam clamped horizontally only at one end, and free at the other end (Fig. 1.5(b)). In the absence of gravity, the beam would be perfectly horizontal. However, in the gravity field, the own weight of the beam can induce bending deformations, as it acts as a distributed load on the beam. The corresponding distributed force is only in the vertical direction y and is given by $P_y = \rho_e Ag$, where ρ_e the density of the elastic material, and $g = 9.81 \text{ m.s}^{-2}$. The equation of the beam reads:

$$EI \theta'' + \rho_e Ag(s - L) \cos \theta = 0$$

In the case of small deformations, it can be linearized:

$$EI \theta'' + \rho_e Ag(s - L) = 0$$

The vertical displacement at the free end yields:

$$y(L) = \frac{\rho_e Ag L^4}{8EI}$$

Comparing this vertical displacement to the length of the beam sets an elastogravitational length L_{eg} :

$$\frac{y(L)}{L} = 8 \left(\frac{L}{L_{eg}} \right)^3 \quad \text{with} \quad L_{eg} = \left(\frac{EI}{\rho_e Ag} \right)^{1/3}$$

If the length of the beam is much smaller than L_{eg} , the effects of gravity are negligible and the vertical displacement is then much smaller than the length of the beam. The two limit cases $L \gg L_{eg}$ and $L \ll L_{eg}$ are illustrated in Fig. 1.6.

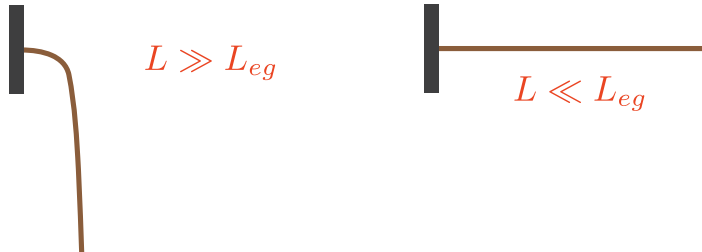


Figure 1.6 – Buckling of a slender beam clamped at one end, free at the other end, and subjected to its own weight. Two situations can occur: if $L \gg L_{eg}$, the deflection due to the beam's own weight is large, whereas if $L \ll L_{eg}$ the effects of gravity can be neglected.

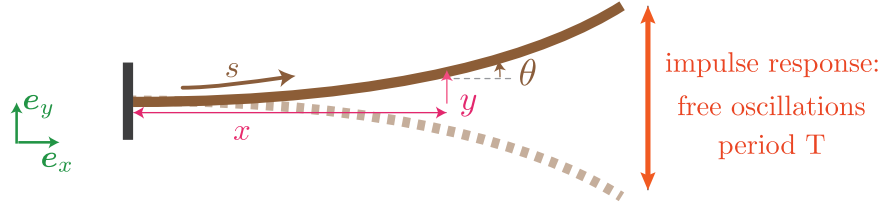


Figure 1.7 – Configuration used to study the impulse response of an elastic beam clamped at one end.

1.1.5. Vibrations of a slender beam

The dynamic response of an elastic beam clamped at one end is underlying a Young's modulus measurement method further described in chapter 2: we show here how to obtain the vibration frequency of the beam in the setup presented in Fig. 1.7.

To include dynamics in the previous beam equations, we add an inertial term in the force balance. As we study the free vibrations of the beam, we consider no external forces (the weight of the beam could be taken into account, but its effect is negligible provided that the length of the beam is smaller than the elastogravitational length L_{eg} defined in the previous paragraph). Dynamics of the beam is given by:

$$EI y(s, t)'''' + \rho_e A \ddot{y}(s, t) = 0$$

where $(\dot{})$ denotes the derivative with respect to time. The boundary conditions are now $y(s = 0, t) = y'(s = 0, t) = 0 \forall t$ at the clamped end, and $y''(s = L, t) = y'''(s = L, t) = 0 \forall t$ at the free end. We seek solutions of the form $y(s, t) = Y(s)e^{i\omega t}$. The general solution for $Y(s)$ is then:

$$Y = C_1 \cos(ks) + C_2 \cosh(ks) + C_3 \sin(ks) + C_4 \sinh(ks)$$

$$\text{with } k^4 = \frac{\rho_e A \omega^2}{EI}$$

Enforcing boundary conditions, we obtain a linear system which has non-trivial solutions only if its determinant is zero:

$$1 + \cos(kL) \cosh(kL) = 0$$

The first solution, corresponding to the first mode, is $kL = 1.88$. The frequency of the free vibrations is thus given by the relation:

$$\frac{1.88}{L} = \left(\frac{\rho_e A \omega^2}{EI} \right)^{1/4}$$

The period of the vibrations consequently yields [11]:

$$T = \frac{2\pi}{\omega} = 1.78 L^2 \sqrt{\frac{\rho_e A}{EI}}$$

In chapter 2, we use this expression to obtain the elastic properties of a beam by recording its vibrations. As the period of the vibrations strongly depends on the geometry of the beam, a precise measurement of L and $I \propto h^3 w$ is needed. This technique proves to be useful in the case of small samples, for which performing a tensile test is difficult.

1.1.6. Snap-through instability

A snap-through instability corresponds to a sudden transition from one buckled equilibrium position to another. In the case of a beam clamped at both ends, described in section 1.1.4., two symmetrical buckled shapes exist. When the beam is compressed, it takes one of the two arched symmetrical shapes (due to imperfections in the symmetry of the system). Under a transverse external load F , the structure can switch to the second arched shape: this dynamic event is called snap-through or snapping, and is illustrated in Fig. 1.8. Early contributions on snap-through of beams clamped at both ends include Timoshenko's work [12], and equilibrium positions as well as snap-through events have also been studied later as a function of the clamp angle at both ends, experimentally [13] and theoretically [14]. In the case of point-force indentation, the critical force needed to trigger a snap-through instability depends on the geometrical properties of the beam, on its Young's modulus, on the compression rate that was applied to induce buckling, and on the position of the indenter along the beam [15], as investigated further in chapter 3. More precisely, the critical force F_c is proportional to EI/L^2 , the prefactor being determined by the compression rate and the position of the indenter along the beam.

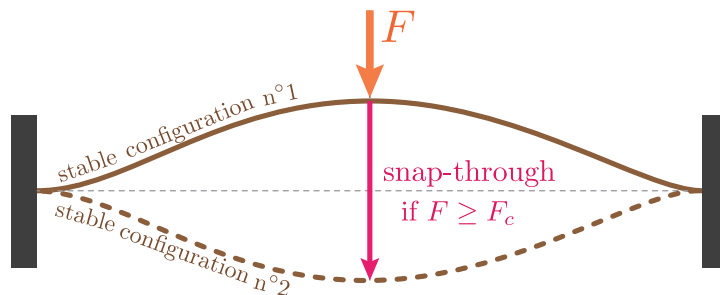


Figure 1.8 – Schematic representation of the snap-through instability of a beam clamped at both ends.

Such instabilities occur in bi-stable beams but also in bi-stable shells: a jumping popper toy is a simple example of system involving a fast eversion event, corresponding to a snap-through instability [16], as illustrated in Fig. 1.9(a). The understanding of the dynamics of the instability is a first step towards the creation of advanced materials involving snap-through events. Complex systems can be designed with structures able to undergo large and fast deformation, such as an array of microlenses [17], shown in Fig. 1.9(b). The snap-through transition allows for a fast mechanical switch from one stable shape to another: perspectives in terms of smart actuators taking advantage of fast movements induced by snap-through instabilities are further detailed in chapter 3.

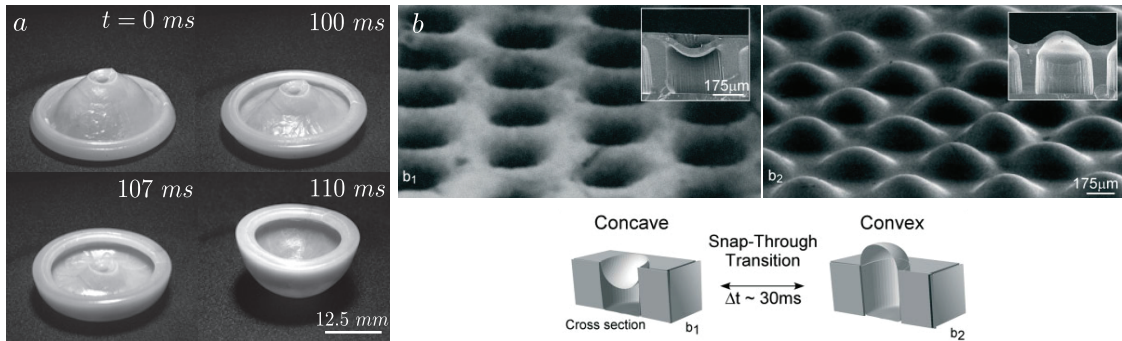


Figure 1.9 – (a) Snap-through of a jumping popper toy from a flat surface. Reproduced from [16]. (b) Silicone elastomer array of concave microlenses (b1) switchable to an array of convex microlenses (b2). The triggering mechanism is the development of osmotic stress, due to the swelling of the silicone elastomer with hexane. A snap-through instability allows for a fast transition from (b1) to (b2) configuration. Reproduced from [17].

1.2 Capillarity : from static to moving contact lines

In this section focused on capillarity, we first give a historical background and a definition of surface tension, before showing how it can shape interfaces. We then focus on wetting which corresponds to the situation where three phases are in contact: it is the case for instance when a liquid droplet is deposited on a solid substrate with surrounding air. The question of how a contact line is deformed when moving is addressed, and finally, focus is given on the literature on droplet dynamics on inclined planes.

1.2.1. Surface tension

a) Interfacial phenomena in everyday life

Interfaces between different phases are ubiquitous in Nature, and capillarity is responsible for numerous daily life phenomena. The shape of a dew droplet on a plant is determined by capillarity and gravity, as illustrated in Fig. 1.10(a) and (b). The free surface of a water bath seems to be elastic, allowing objects that would sink without this *interfacial tension* to stay at the surface of water. In Fig. 1.10(c), a drawing pin is shown to float upturned on water due to capillarity, despite its density being higher than the density of water. The interface is deformed near the pin, forming a meniscus. Two pins deposited on water would move toward one another due to the menisci: a daily life example of this phenomenon is the attractive interaction between breakfast cereals floating on milk [18]. Capillarity-induced floatation is also used by the water strider (Fig. 1.10(d)), which takes advantage of interfacial tension to stand and jump on water [19]. Let us now open a faucet: we might see the water column destabilizing into droplets. This phenomenon, called Rayleigh-Plateau instability, is controlled by surface tension. The formation of tears of wine is an additional example of surface-tension-induced daily life phenomenon, where evaporation also plays a role. As ethanol and water do not evaporate at the same speed, a surface tension gradient is created, giving birth to what is called a Marangoni flow (flow driven by surface tension gradients). As illustrated in Fig. 1.10(e), surface tension also plays a role in determining the shape of bubbles. More generally, the

study of foams and emulsions, of interest in detergency applications, is part of interfacial science.



Figure 1.10 – (a) and (b): Dew drops on plants. Images: B. Lorentz. (c) Drawing pin floating upturned on water. Capillary effects overcome the weight of the pin. Reproduced from [18]. (d) Water strider standing on water. Reproduced from [19]. (e) Soap bubbles in the wind. Image: B. Lorentz.

b) Historical background

Early observations on interfacial phenomena have been performed by Leonardo da Vinci and then by Newton in *Opticks*. However, quantitative studies on surface tension effects only began in the 18th century, mainly with Jurin's experiment [20], who recorded the rise of liquids in small diameter tubes. Indeed, the height of a liquid in a capillary tube is inversely proportional to the radius of the tube, known as *Jurin's law* nowadays. Pierre Simon de Laplace (1749-1827) and Thomas Young (1773-1829) then laid the foundations of interfacial science at the beginning of the 19th century [21, 22]. Among other decisive contributions, their names are now given to the *Laplace pressure* that quantifies the discontinuity of pressure across a non-planar interface, and to the *Young-Dupré's law* that determines the contact angle of a liquid droplet on a solid substrate, which are both detailed in the following paragraphs. With the advent of thermodynamics in the late 19th century, Lord Kelvin and Gibbs later achieved a better understanding of surface tension from a thermodynamics point of view.

c) Surface tension: definition

We consider a ring, with a loose thread connected to two points at the opposite ends of the ring. When dipping it into soap water and then taking it out, a soap film is formed on the ring. We now break the film on one side: the thread is immediately pulled by the film on the other side [23], as illustrated in Fig. 1.11(a, left). This simple experiment shows that the soap film exerts a force on the thread. After breaking one film, the shape

of the thread is a portion of circle: the surface of the soap film is as small as possible. A similar experiment can be performed by using a thread that is doubled for a short distance in the middle, and breaking the film between the two threads: a perfect circle is formed, as illustrated in Fig. 1.11(a, right). This observation highlights that creating an interface has an energetic cost.

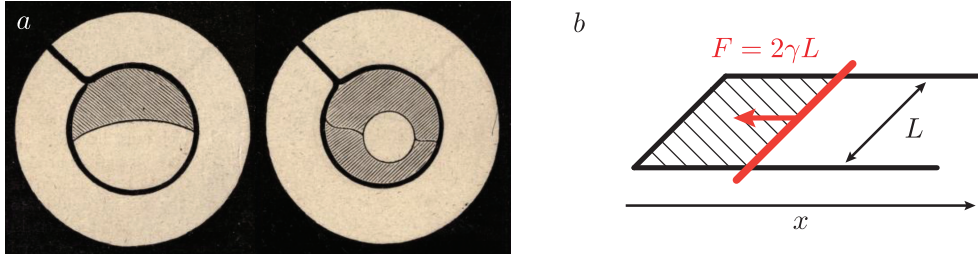


Figure 1.11 – (a) Left: A soap film is formed on a ring with a loose thread connected to two points at the opposite ends of the ring. When one of the two films is broken, the other pulls the thread, and the shape taken by the thread is a portion of circle. Right: Now the thread is doubled for a short distance in the middle; when the film between the two threads is broken, a perfect circle is formed. Reproduced from [23] (1890). (b) A soap film is formed between a U-shaped frame of width L and a slider. The force exerted by the soap film on the slider is $F = 2\gamma L$ and is independent of the distance x .

We now consider a U-shaped frame, with a soap film formed between this frame and a slider (Fig. 1.11(b)). The force F exerted by the soap film on the slider is independent of the distance x and is proportional to the width of the frame L . The surface tension, denoted γ , is thus defined such as $F = 2\gamma L$ (the factor 2 accounting for the two liquid-air interfaces in the case of a soap film). If the slider is moved by a distance dx to extend the size of the soap film, the work of the surface tension force reads $\delta W = Fdx = \gamma dA$, where $dA = 2Ldx$ is the increase in area of the total soap film-air interface. The notion of surface tension introduced here on the example of a soap film is more general: it can be extended to any interface between two phases (liquid-gas, solid-liquid, liquid-immiscible liquid for instance).

The existence of this interfacial force comes from microscale interactions between molecules: at an interface between two phases A and B, molecules of type A are only partially surrounded by other type A molecules. As molecules attract each other by interactions such as Van der Waals forces, having molecules at an interface is energetically unfavorable [24]: in the bulk of a liquid, cohesive forces between molecules are balanced, while molecules at the edge are pulled together towards the liquid. The surface tension can thus be seen as the price to pay for bringing molecules at an interface.

d) Discontinuity in pressure across a non-planar interface

Surface tension is at the origin of an overpressure in the interior of drops and bubbles. This phenomenon was first analyzed by Laplace at the beginning of the 19th century [22]. We consider an interface of surface tension γ that has the shape of a portion of cylinder of radius of curvature R (Fig. 1.12). We focus on a rectangular section of length L and width w .

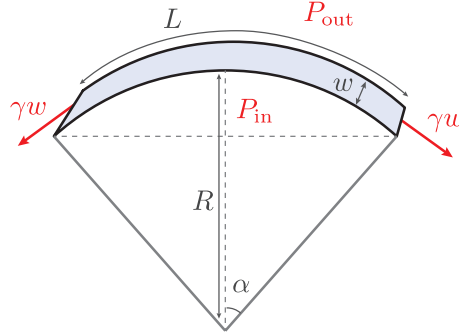


Figure 1.12 – Notations used to quantify the discontinuity in pressure $P_{\text{in}} - P_{\text{out}}$ across a non-planar interface. The system on which the force balance is applied is a rectangular portion (of length L and width w) of a cylindrical interface (of radius of curvature R).

Denoting P_{out} the outside pressure and P_{in} the inside pressure, a vertical force balance on this small portion of the interface yields:

$$(-P_{\text{out}} + P_{\text{in}})w2R \sin \alpha - 2\gamma w \sin \alpha = 0$$

The discontinuity in pressure across the interface is then given by:

$$P_{\text{in}} - P_{\text{out}} = \frac{\gamma}{R}$$

In the case of a non cylindrical interface, of principal curvatures R_1 and R_2 , the force balance on a small portion of the interface can be performed taking into account the contributions in the two directions, leading to the following expression:

$$P_{\text{in}} - P_{\text{out}} = \frac{\gamma}{R_1} + \frac{\gamma}{R_2}$$

The discontinuity in pressure across a non planar interface thus corresponds to an overpressure inside a bubble or a droplet, usually called *Laplace pressure*.

e) Minimal surfaces : predicting the shape of an interface

A soap bubble blown from any wire shape is finally spherical: in this section, we show how surface tension determines the shape of an interface. When a wire frame that has the shape of triangular prism is plunged in soapy water, the soap film that forms is an assembly of flat surfaces, as illustrated in Fig. 1.13(a). The angles where three surfaces meet are all equal in this case [23]. A helix shape with a wire in the center also gives an interesting soap bubble shape (Fig. 1.13(b)).

The shape that is chosen by the structure is minimizing its interfacial energy. As this energy is proportional to the surface of the interface, it corresponds to minimizing the surface of the structure. Variational calculation can be used to perform energy minimization, by writing the Lagrangian of the system and using Euler-Lagrange equations. Such a variational approach will be used in chapter 3 to minimize the total energy of a drop-strip system, including interfacial energies, but also elastic energies. Constraints will be taken into account using Lagrange multipliers.

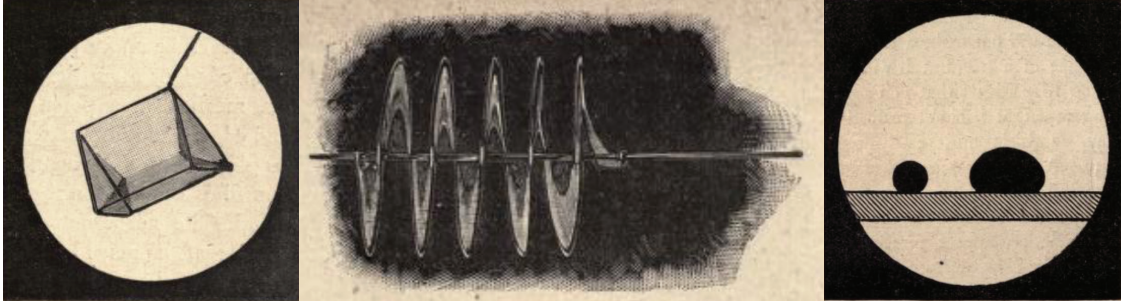


Figure 1.13 – (a) Soap bubbles formed on a triangular prism wire frame. (b) Soap bubble formed on a wire frame that has the shape of a helix with a wire in the center. (c) Illustration of the influence of gravity on the shape of a liquid droplet. Pictures reproduced from [23].

In the previous examples, gravity has been neglected. In the case of a water droplet, the competition between gravity and capillarity sets a gravitocapillary length L_{gc} . If droplets are much smaller than this typical size, gravity does not affect their shape, while droplets bigger than L_{gc} are flattened by gravity (Fig. 1.13(c)). The relative strength of gravity and capillarity is determined by comparing the hydrostatic pressure in a droplet of radius R and density ρ_l , which is equal to $2\rho_l Rg$, to the Laplace pressure, which is equal to $2\gamma/R$ [24]. This leads to the following expression for L_{gc} , below which the effects of gravity are negligible:

$$L_{gc} = \sqrt{\frac{\gamma}{\rho_l g}}$$

1.2.2. Wetting : three-phase contact line

Wetting is defined as the study of interfacial phenomena between three different phases. These three phases can be air, liquid, and solid (or a second liquid in which the first one is immiscible) for instance. Many examples in Nature involve such a three-phase contact, from capillary imbibition of a porous soil to droplets sitting on a car windshield.

a) Spreading parameter

When a liquid droplet is deposited on a solid substrate, it can either stay as a droplet (partial wetting) or spread completely on the substrate (total wetting). The parameter that quantifies this phenomenon is called the spreading parameter, and is defined as [24]:

$$S = \gamma_{sa} - (\gamma_{sl} + \gamma_{la})$$

where γ_{sa} is the surface tension of the solid-air interface, γ_{sl} the surface tension of the solid-liquid interface, and γ_{la} the surface tension of the liquid-air interface. When $S > 0$, the liquid completely wets the solid, and forms a thin film above it. When $S < 0$, the situation corresponds to partial wetting: in this case, a droplet deposited on a solid substrate does not form a film but a spherical cap with a finite contact angle value (Fig. 1.14).



Figure 1.14 – A liquid droplet is deposited on a solid surface. Depending on the value of the spreading parameter S , total wetting ($S > 0$) or partial wetting ($S < 0$) occurs.

The spreading parameter can also be used to determine if a liquid spreads or not on a bath of another liquid in which it is immiscible. The liquid bath takes the place of the solid in the situation described above. In this case,

$$S = \gamma_{l_1a} - (\gamma_{l_1l_2} + \gamma_{l_2a})$$

where γ_{l_1a} is the surface tension of the liquid bath - air interface, $\gamma_{l_1l_2}$ the surface tension of the liquid bath - liquid droplet interface, and γ_{l_2a} the surface tension of the liquid droplet - air interface [25].

b) Contact angles: Young-Dupré's law and Neumann's construction

We consider a droplet deposited on a solid surface. In the case of a negative spreading parameter, the droplet sits on the solid, with an equilibrium contact angle θ_E (Fig. 1.15(a)) that is determined by Young-Dupré's law [21, 24]:

$$\gamma_{la} \cos \theta_E = \gamma_{sa} - \gamma_{sl}$$

This expression can be derived by balancing the capillary forces acting on the triple line along the horizontal axis, or by an energetic approach by calculating the amount of work done when the contact line is displaced [24]. In the case of a liquid droplet sitting on a bath of another liquid in which it is immiscible, the angles must satisfy the so-called *Neumann's triangle* or *Neumann's construction* [26, 27], corresponding to the force balance at the triple line (Fig. 1.15(b)).

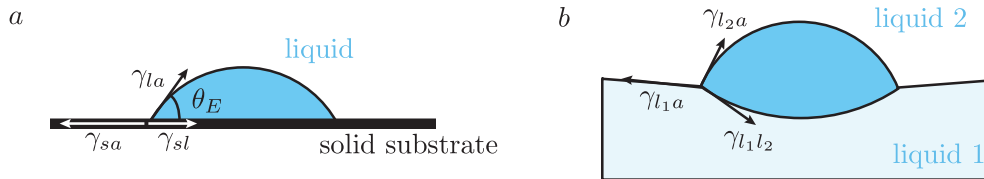


Figure 1.15 – (a) Droplet sitting on a solid substrate: the equilibrium contact angle θ_E is determined by Young-Dupré's law. (b) Droplet on a liquid bath in which it is immiscible: a liquid lens is formed, the geometry being determined by a balance of surface tension forces.

c) Contact angle hysteresis

We consider here the case of a sessile droplet on a *real* solid substrate. Young-Dupré's law assumes the existence of a unique contact angle. However, in many practical situations,

the contact angle has a value $\theta \neq \theta_E$. More precisely, the contact angle θ of a sessile droplet on a solid substrate takes different values in a certain range [28]:

$$\theta_{sr} < \theta < \theta_{sa}$$

where the angle θ_{sa} , or static advancing contact angle, is reached when the solid/liquid contact area increases (quasi-statically), and the angle θ_{sr} , or static receding contact angle, is reached when the solid/liquid contact area decreases (quasi-statically). Surface roughness is underlying this hysteresis phenomenon [29], as the contact line is likely to be pinned on defects on the solid substrate. Indeed, surfaces used for droplet dynamics experiments presented in chapter 4 present a high contact angle hysteresis, as shown in Fig. 1.16. A water droplet inflated on a silicone elastomer substrate (PDMS Dow Corning Sylgard 184) exhibits large contact angles (around 120°), while the same droplet exhibits smaller contact angles when deflated (around 65°).

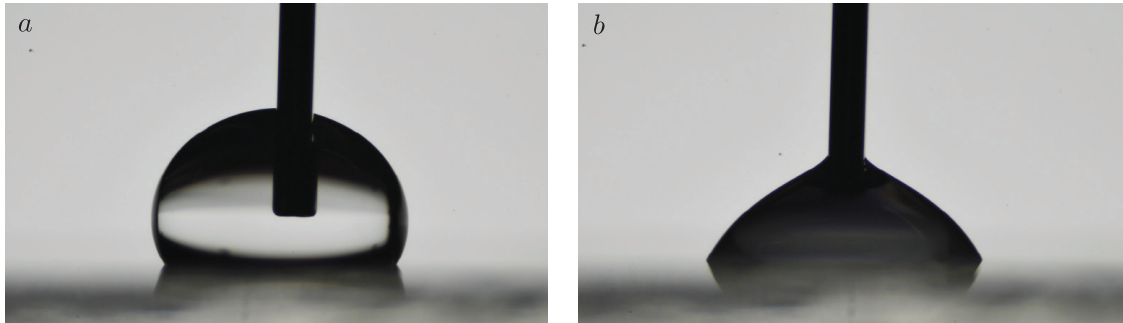


Figure 1.16 – (a) Water droplet inflated on a silicone elastomer surface (Dow Corning Sylgard 184 PDMS). (b) Water droplet deflated on the same silicone elastomer surface. The contact angle exhibits a huge variation between case (a) and case (b), evidencing a high contact angle hysteresis. Typical droplet radius is a few millimeters.

1.2.3. Triple line dynamics

In the following paragraphs, we recall historical results about triple line dynamics, introducing a dependence of the contact angles on the speed at which the triple line is moving. However, the study of moving contact lines is still a very active and controversial research area, with numerous recent articles in the literature.

a) Huh and Scriven's paradox

Huh and Scriven first pointed out in 1971 a paradox about hydrodynamics in the vicinity of a triple line: applying the no-slip condition to a flow in the region of a contact line leads to a diverging energy dissipation [30]. Tentatives to solve this paradox are numerous in the literature: various mechanisms have been proposed to relieve the singularity near a contact line [31]. A summary of the paradox is given below, while regularizations of the singularity are discussed in the following paragraphs.

We consider a liquid wedge moving at a constant velocity U on a solid plate, and assume that the contact angle at the triple line is finite and denoted θ . All notations are

specified in Fig. 1.17(a). The problem is analyzed in the creeping flow approximation [31]. At a distance x from the liquid wedge, the vertical velocity gradient $\partial U_x/\partial z$ is of the order $U/h(x)$. For small and slowly varying θ , $h(x) \simeq x\theta(x)$.

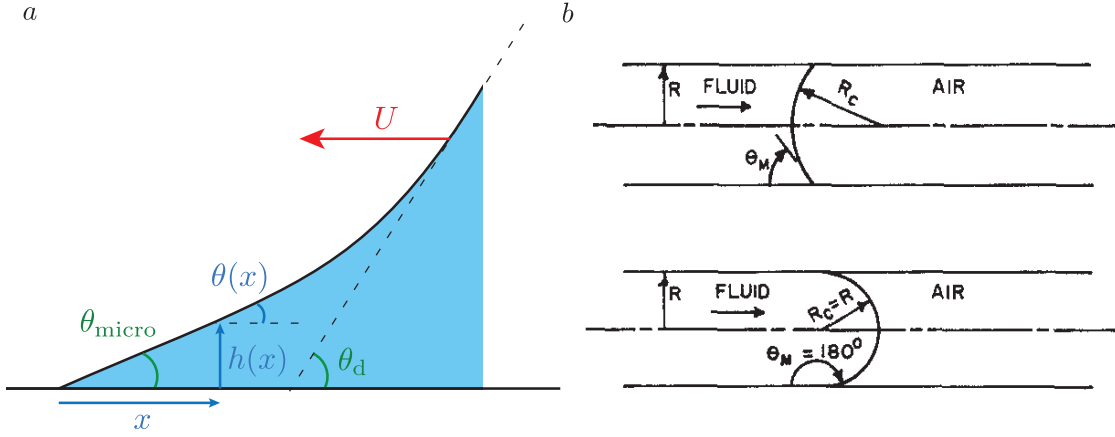


Figure 1.17 – (a) Advancing contact line. At a distance x from the wedge, the liquid height is denoted $h(x)$ and the angle with the horizontal axis is denoted $\theta(x)$. The macroscopic dynamic contact angle θ_d differs from the microscopic contact angle θ_{micro} . (b) Experiment used to measure advancing contact angles in a capillary tube by Hoffman. Reproduced from [32].

Denoting μ the liquid viscosity, the energy dissipated in the wedge, per unit time and unit length of the contact line, is given by:

$$D_{\text{viscous}} \simeq \mu \int_{L_{\text{micro}}}^{L_{\text{macro}}} \frac{U^2}{h} dx \simeq \frac{\mu U^2}{\theta} \ln \frac{L_{\text{macro}}}{L_{\text{micro}}}$$

In this expression, the bounds of the integral are L_{macro} , which is an outer length scale (that is typically the radius of a droplet if the moving contact line is part of a sliding droplet), and L_{micro} , which should be equal to zero in the case of a no-slip condition at the triple line. A zero value for L_{micro} results in a logarithmically diverging expression for D_{viscous} . This result, called *Huh and Scriven paradox*, is illustrated in Huh and Scriven's article [30] by the following example: *not even Herakles could sink a solid if the physical model were entirely valid*.

b) Reliefs of the singularity and Cox-Voinov relation

Various propositions to solve the Huh and Scriven's paradox can be found in the literature and are summed up in a review on wetting and spreading by D. Bonn et al [31] and in a review on moving wetting lines by T. Blake [33]. Among those regularizations, we can mention the use of Navier slip boundary condition at the triple line (introducing a slip length), suggested by Huh and Scriven [30] by introducing a cut-off length at small scales L_{micro} , and used by Voinov [34]. Another category of regularization covers evaporation/condensation mechanisms: the molecular kinetics approach consists in zooming on the contact line and considering the statistical dynamics at the molecular scale [33].

We focus on one of the main hydrodynamic approaches, often referred to as Cox-Voinov relation. This result was first formulated by Voinov in 1976 [34], and further extension to

two fluids of different viscosities was then derived by Cox ten years later [35]. Several assumptions are used: viscous dissipation is assumed to be dominant, inertial effects are neglected, as well as contact angle hysteresis. The wedge is considered under the lubrication approximation, meaning that the shape of the angle of the wedge is varying slowly. The balance of viscous and capillary forces gives the following relationship between the height of the wedge at one distance x_1 from the singularity and the height of the wedge at another distance $x_2 > x_1$ from the singularity:

$$(h'(x_2))^3 - (h'(x_1))^3 = \pm 9 Ca \ln\left(\frac{x_2}{x_1}\right)$$

where $Ca = \mu U/\gamma$ is the capillary number, comparing relative strength of viscous effects and capillary effects: μ is the viscosity of the liquid, γ its surface tension, and U the speed of the wedge. The \pm sign accounts for an advancing contact line (+) or a receding contact line (-). Considering one microscopic length and one macroscopic cut-off lengths, the dynamic macroscopic contact angle θ_d is linked to the microscopic contact angle θ_{micro} (which is determined by local interactions between the different phases) by the relationship [33]:

$$\theta_d^3 = \theta_{micro}^3 \pm 9 Ca \ln\left(\frac{L_{macro}}{L_{micro}}\right)$$

where L_{macro} is a typical macroscopic length (size of the droplet for instance) and L_{micro} is a typical microscopic length, required for a non-diverging expression, as already mentioned when describing the Huh and Scriven paradox. This approach corresponds to introducing a slip length instead of the no-slip boundary condition.

Early experimental observations by Hoffman [32] in the setup described in Fig. 1.17(b) show an evolution of the dynamic contact angle proportional to $Ca^{1/3}$ in the case of total wetting, in agreement with the Cox-Voinov relation but also with similar approaches, as the one derived by De Gennes [24] which yields, for small contact angles, the relationship:

$$\theta_d(\theta_d^2 - \theta_{micro}^2) = \pm 6 Ca \ln\left(\frac{L_{macro}}{L_{micro}}\right)$$

More recent results obtained with silicone oil droplets sliding down on glass treated with a fluoro-polymer [36] exhibit a better agreement with Cox-Voinov relationship than with De Gennes's one. The question of the dynamic contact angles is not yet completely solved, and is still an active research domain attracting interest [37].

1.2.4. Droplets on an inclined plane

In this section, we describe both theoretical and experimental results in the literature on droplets sliding down (or rolling down) inclined planes. We outline here the general framework that will be used to analyze our experiments featuring droplets on inclined elastomer plates (chapter 4).

a) Onset of motion

Early references on the behavior of liquids drops on inclined surfaces include Macdougall and Ockrent's, Frenkel's, and Bikerman's contributions in the mid-twentieth century [38, 39, 40]. In Frenkel's article, the problem of a drop deposited on an inclined surface is

considered in a two-dimensional approximation, assimilating the shape of the drop to an infinite cylinder. On a horizontal surface, the two contact angles are equal. If the surface is gradually tilted, the contact angle varies and takes a value $\theta_2 > \theta_0$ for the front angle and $\theta_1 < \theta_0$ for the rear angle. This corresponds to the picture reproduced in Fig. 1.18(a). As the tilting angle α is further increased, θ_2 increases and θ_1 decreases, until reaching a critical value $\alpha = \alpha^*$ at which the drop begins to move [39]. At the onset of motion, the weight of the droplet overcomes capillary pinning forces, and the angles θ_1 and θ_2 correspond respectively to the static receding and advancing contact angles.

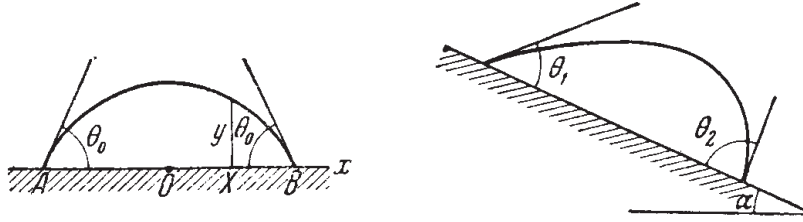


Figure 1.18 – Droplet lying on a horizontal surface, with two equal contact angles (left), and on an inclined plane, where contact angles are no longer symmetric (right). Reproduced from [39].

Measurements of θ_1 and θ_2 for steady droplets as the angle of the inclined plane α is varied (below α^*) were performed experimentally by Macdougall and Ockrent [38]. They found experimentally for various droplet-plane systems that:

$$\cos \theta_1 - \cos \theta_2 \propto \sin \alpha$$

and linked the prefactor to the geometry of the droplet, its density and surface tension, and gravity, suggesting that this setup could be a method for determining the surface tension of liquids.

Understanding what determines the onset of motion of a droplet is of interest in many situations, as in the case of raindrops sticking or sliding on a vehicle windshield, to cite a daily life example. In the 1960s, Furmidge analyzed further the onset of motion of droplets on an inclined plane in the context of spray retention, to predict the degree of retention of a liquid on a solid and facilitate the formulation of spray fluids [41]. We consider a droplet with static advancing contact angle θ_{sa} , static receding contact angle θ_{sr} , density ρ_l , volume V , and surface tension γ . The onset of motion corresponds to the angle α^* for which:

$$\rho_l V g \sin \alpha^* = \gamma w (\cos \theta_{sr} - \cos \theta_{sa})$$

where $g = 9.81 \text{ m}\cdot\text{s}^{-2}$ and w is the maximal lateral extension (width) of the droplet [41]. This equation is not predictive since the width of the droplet is unknown *a priori*. An extension to a three dimensional model predicting the onset of motion without requiring to know the lateral extension of the droplets was performed later by E. B. Dussan [42, 43].

b) Sliding or rolling?

Once the droplet is moving, the question of the velocity field inside the liquid is raised. The case of a moving contact line has already been mentioned, underlining that dynamic

contact angles are modified compared to static angles, and that a slip length might exist to regularize the Huh and Scriven paradox occurring in the case of a no-slip boundary condition [30]. Yarnold reported in 1938 that *if a pool of mercury moving on a gently sloping plane surface is observed it appears to roll. The velocity of the top surface, as is shown by the movement of dust particles, is considerably greater than the velocity of the pool as a whole, while there is little doubt that the bottom surface of the mercury in contact with the solid is very nearly at rest* [44], suggesting a possible rolling motion inside the droplet. On the other hand, Bikerman [40] pointed out a sliding motion for the droplets used in his experiments, verifying (by tinting the rear part of droplets) that no movement similar to what was described by Yarnold occurred.

In fact, the motion inside the droplet is complex, and depends on the viscosity, weight and shape of the droplet, as well as on the frictional forces at the supporting surface: rolling and sliding motions are indeed both reported in the literature. Thin-sheet-like drops seem to rather slide, while more spherical drops rather roll [45]. In Fig. 1.19 are presented early visualizations of rolling motions in droplets. Fig. 1.19(a) shows vortices, evidencing a rolling motion at the front end of a droplet that exhibits a long rear (not shown on the picture) in which sliding occurs [46]. Various visualization methods are used in [47]: coalescence of two droplets of glycerol, one dyed, the other transparent, shows that the rolling motion tends to mix the two droplets. The dyed liquid that was initially at the rear of the droplet comes to the front when the plane is tilted, as shown in Fig. 1.19(b). Another experiment in the same article, shown in Fig. 1.19(c), consists in placing a small amount of food dye in a honey drop on a tilted Plexiglas plane, highlighting a rolling motion.

The question of a rolling or sliding motion in our study on droplets dynamics on elastomers is addressed in chapter 4 by using cocoa particles as tracers.

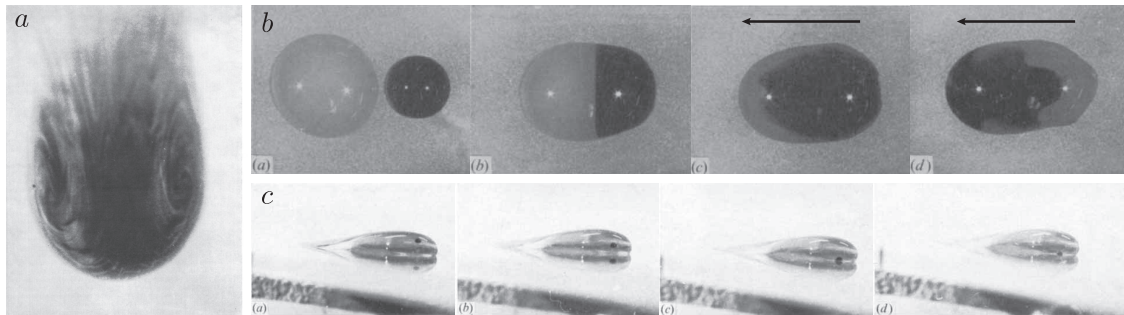


Figure 1.19 – (a) Vortex motion in a moving drop head. Reproduced from [46]. (b) Coalescence of two drops of glycerine on a bee’s wax surface. The plane is then tilted (left side lowered) and the dark dye goes from the right to the left of the droplet, corresponding to a rolling motion in the drop. Reproduced from [47]. (c) Drop of honey moving down a Plexiglas tilted surface. A small amount of food dye highlights a rolling motion inside the drop. Reproduced from [47].

c) Final speed reached by a droplet

The question of the speed of a droplet of volume V and density ρ_l moving on an inclined plane is raised in numerous articles in the literature, see for example [36, 48, 49, 50]. We summarize here a simplified approach, that will be used to analyze the results for droplet

dynamics on vertical elastomer planes in chapter 4. In the case of a vertical plane, the gravitational force acting on the droplet is given by:

$$F_g = \rho_l V g .$$

The descent of the drop begins only if $F_g > F_{cl}$, F_{cl} being the contact-line pinning force:

$$F_{cl} \propto \gamma w (\cos \theta_{sr} - \cos \theta_{sa}),$$

where γ is the surface tension of the liquid-air interface, w the maximal width of the droplet, θ_{sr} the static receding angle and θ_{sa} the static advancing angle. Once steady motion is reached, the value of the droplet speed is obtained by balancing the weight F_g with the sum of the contact line pinning force F_{cl} and the viscous dissipation force in the droplet F_μ . Quantifying the exact viscous dissipation inside a droplet is difficult, as it would require to compute the whole velocity field inside the liquid. In particular, the dissipation might be located in the bulk, or localized in the receding corner of the droplet. The shape of the droplet depends on its speed, as described in the Cox-Voinov relation and in Hoffman's experiments mentioned in the previous section, but the droplet speed also depends on its shape because the viscous dissipation depends on the velocity field inside the drop. However, a simple scaling approach in the case of bulk dissipation yields:

$$F_\mu \propto \frac{\mu U \mathcal{S}}{h},$$

where U is the droplet speed, μ the viscosity of the liquid, \mathcal{S} the contact area of the droplet with the substrate, and h the droplet height. Three dimensionless numbers are useful to analyze the motion of a droplet: the Reynolds number Re compares relative strengths of viscosity and inertia, the capillary number Ca (already mentioned in the previous section) compares the relative effects of viscous forces and surface tension, and the Bond number Bo compares gravity and surface tension forces. The expressions of these three dimensionless numbers are thus:

$$Re = \frac{UV^{1/3}\rho_l}{\mu}$$

$$Ca = \frac{\mu U}{\gamma}$$

$$Bo = \frac{\rho_l V^{2/3} g}{\gamma}$$

The present approach is only valid for viscous drops with low Re . We balance the gravity force with viscous dissipation and capillary pinning forces, and use $\mathcal{S} = V^{2/3}$ and $h = w = V^{1/3}$ in our scaling approach. This leads to a linear relationship between Ca and Bo , above a threshold value corresponding to the overcoming of pinning forces by gravity:

$$Ca \propto Bo - (\cos \theta_{sr} - \cos \theta_{sa})$$

Although not valid at high Re , this relationship has been found to capture the dynamics of droplets even when Re is of order one [36], as shown in Fig. 1.20. In the inertial limit (high Re), boundary layer models are required to capture the droplet speed, as shown in [50] in the case of Re varying from a few hundreds to almost ten thousands.

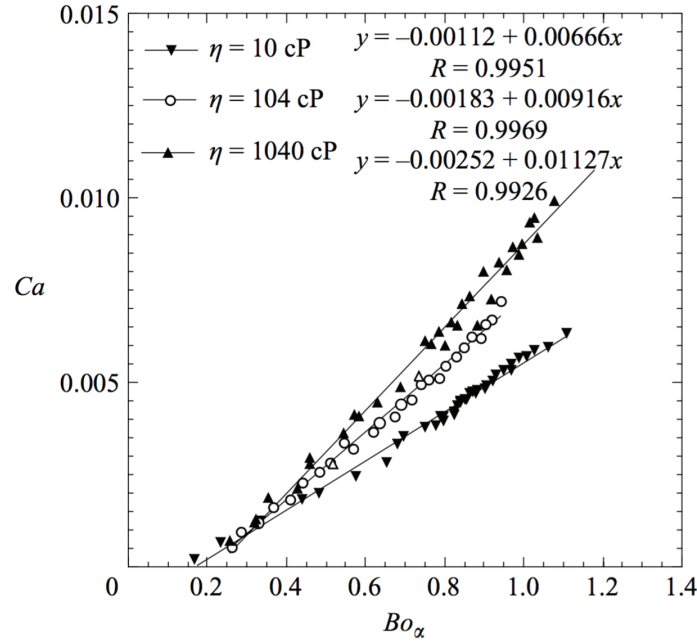


Figure 1.20 – Non-dimensional velocity Ca of silicone drops on an inclined plane made of glass coated with a fluoro-polymer, as a function of $(Bo \sin \alpha)$ where α is the angle of the inclined plane: a linear relationship is found between Ca and $(Bo \sin \alpha)$. The volume of the drops is fixed to $V = (6.0 \pm 0.2) \text{ mm}^3$. Small variations in wetting properties are suggested to be responsible for the different slopes. Reproduced from [36].

d) Shape transition at the rear of a droplet

When the capillary number Ca exceeds a critical value, a shape transition at the rear of the droplet has been observed [48]. As shown in Fig. 1.21, a silicone oil droplet running down an inclined plane made of glass coated with a fluoro-polymer may exhibit a cusped tail that emits smaller drops (*pearls*). When increasing the speed of the droplet by increasing the tilting angle, a transition from a rounded shape to a cusped tail occurs. The singular interface at the rear adopts the shape of a cone, derived theoretically using a lubrication model [51], and observed experimentally [36, 48]. These observations highlight that the way a droplet moves down an inclined plane is not straightforward and still constitutes an active research area.

In our experiments on droplets dynamics on elastomers described in chapter 4, pearling can be observed for large droplet volumes and thus large speeds. However, in all our quantitative measurements, the speed of the droplets is kept below the pearling threshold.

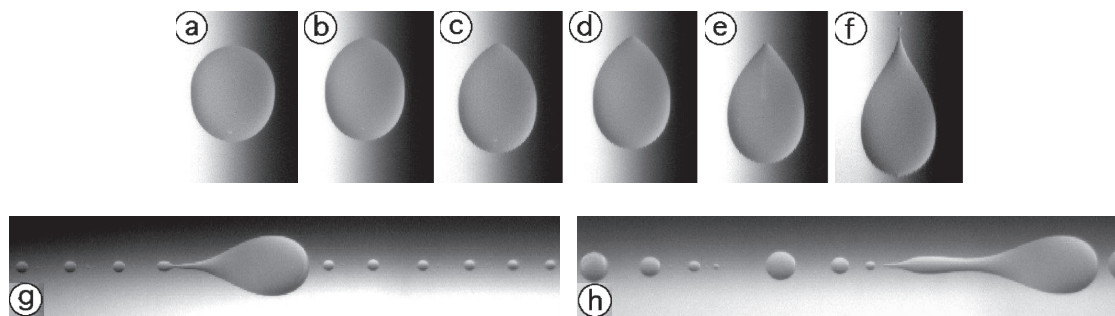


Figure 1.21 – Different shapes of silicone oil droplets running on a tilted plane made of glass coated with a fluoro-polymer. From (a) to (h), the velocity is increased by increasing inclination. (a)-(b): rounded drops at low speed. (c)-(e): corner angled drops, the cusp becoming sharper as velocity increases. (f)-(h): pearling transition (small droplets are released at the rear). Reproduced from [48].

1.3 Elastocapillarity with slender structures

In the previous sections, we have described separately capillary forces and elastic structures; here we combine these two ingredients. A slender elastic structure – such as a thin sheet, a thin strip or a thin fiber – is a flexible object that can be deformed by capillary forces at small scales. We briefly summarize the state of the art in elastocapillarity with slender structures, and highlight the crucial role of geometry in systems involving both capillary forces and elastic bending or stretching.

1.3.1. Examples in Nature and in the industry

Competition between elasticity and capillarity occurs both in Nature and in the industry, leading to desired phenomena such as achievement of vital functions or design of micro-electro-mechanical systems (MEMS), or to unintended events such as folding of insect wings or aggregation of micropillars. We describe below several examples of natural elastocapillary phenomena, before focusing on the drawbacks and advantages of elastocapillary events in the design of micro- and nano-structures in the industry.

a) Natural phenomena involving elasticity and capillarity

Nature offers numerous examples of elastocapillary interactions: flexible structures are ubiquitous as they often confer benefits such as aerodynamic efficiency or enhanced resistance to fracture, and water in various forms – water baths or vapor that can condensate into droplets – is likely to interact with these elastic structures. Some animals even use the competition between elasticity and capillarity to achieve vital functions by improving the way they move or catch preys.

Water striders, for instance, take advantage of the elastocapillary interaction to strengthen their jumping abilities on water [19]. This situation is similar to the piercing of an interface by an elastic rod [52]: the long and compliant legs of the water strider do not pierce the surface of water and thus do not sink. Another interesting strategy is adopted by some pond insects to move onto land [53]: as they must ascend a meniscus,

they exploit the attractive force between two similar menisci by bending their back to generate lateral forces and climb a meniscus, as shown in Fig. 1.22(a). This is not directly an elastocapillary phenomenon, but shows how forces exerted on a structure by capillarity depend on its geometry. An interesting mechanism is also used by spiders to keep their web under tension and catch preys [54]: capture threads remain taut even when contracted, as illustrated in Fig. 1.22(b). The underlying mechanism is the spooling of the thread inside droplets due to capillary forces. Coils inside each droplet appear, allowing the thread (and thus the whole web) to remain taut. But the simplest elastocapillary example is encountered in our everyday life, and shown in Fig. 1.22(c): wet hair forms bundles due to a competition between elasticity and capillarity [55]. Even though this phenomenon does not confer enhanced abilities, it illustrates well the way capillarity and elasticity compete in our daily life.

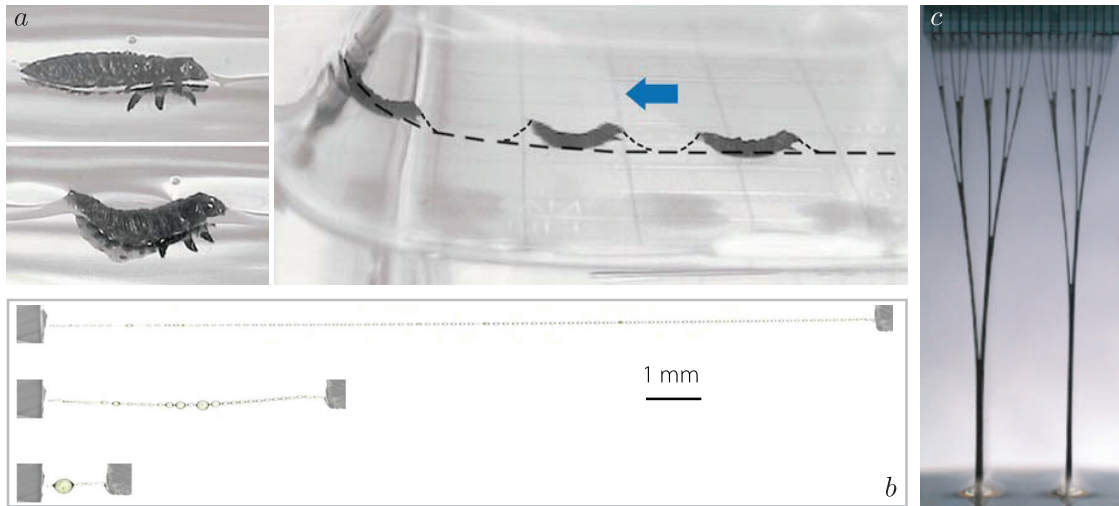


Figure 1.22 – (a) Meniscus climbing insect: by deforming its back, *Pyrrhalta nymphaeae* generate lateral forces by deflecting the free surface. Reproduced from [53]. (b) In-drop spooling of spider capture thread: each of the droplets can spool and pack the core filament, keeping the thread and thus the whole web under tension. Whether stretched or relaxed, the silk thread remains taut. Reproduced from [54]. (c) Elastocapillary coalescence in wet hair: a hierarchical bundling pattern is observed, due to a competition between capillarity and elasticity in the wet flexible lamellae forming the brush. Reproduced from [55].

In most examples presented above, Nature takes advantage of the interaction between liquids and elastic structures. However, in some cases, flexibility is a drawback, causing harmful elastocapillary interactions to occur. It is the case for mosquito wings, that are likely to undergo capillarity-induced folding [56], as shown in Fig. 1.23. Fog causes an accumulation of droplets on the mosquito wings, bending them into taco shapes and rendering them useless for flight. The pulmonary airway closure due to surface-tension-driven instabilities is another striking example of catastrophic elastocapillary event [57]. The compliant airways of babies may be deformed by an excess of liquid, ultimately leading to a collapse and thus a blockage of the respiratory system.



Figure 1.23 – Folding of a mosquito wing due to elastocapillary deformations. Reproduced from [56]. Note that between the last two pictures of the sequence, the bigger drops on the right wing fall, leaving behind a folded wing unsuitable for flight.

b) Drawbacks of elastocapillary phenomena in the industry

Harmful elastocapillary phenomena do not only occur in Nature: nano- and micro-fabrication requires manufacturing structures at a scale where capillarity often overcomes elasticity. Wet lithography is a popular technique to manufacture micro-electro-mechanical systems (MEMS). However, it requires rinsing of the substrate after etching a given pattern with a photosensitive resin. This rinsing step is likely to cause elastocapillary interactions. Capillary bridges form between the different parts of the structure when the liquid evaporates, and induce attractive forces, ultimately leading to the failure of the structure. Thin walls of photoresist have been shown to collapse after being rinsed [58], while a forest of nanotubes forms teepees [59] or cellular geometric patterns [60] when rinsed with a wetting liquid, as illustrated in Fig. 1.24(a) and (b). The final geometry depends both on the elastic properties of the structure and on the wetting properties of the liquid used for rinsing. Failure of elastic structures also occurs when a capillary bridge is created between a suspended plate and a rigid mounting [61], as shown in Fig. 1.24(c). In all these examples, the cleaning step, necessary in the manufacturing process, induces a harmful elastocapillary deformation of the structure. Different strategies to tackle this problem are found in the literature: a possible solution is to use superhydrophobicity to reduce the effect of the elastocapillary interaction on the nanopillars [59]. Another strategy is to take advantage of the deformations induced during evaporation of the liquid [62, 63, 64]: this approach proves to be a successful way to manufacture complex structures, as described in the following paragraph.

c) Using elastocapillarity to engineer complex structures

A better understanding of elastocapillary interactions has led to the design of systems combining elasticity and capillarity to build complex structures, overcoming the harmful effects caused by capillarity in MEMS manufacturing. We describe below how carbon nanotube forests subjected to elastocapillary interactions can be turned into complex hierarchical structures, before focusing on folding-induced three dimensional structures built using two-dimensional patterns. Indeed, numerous examples in the literature show that capillary forces acting on small elastic structures provide an innovative and cost-effective process to manufacture complex and robust micro- and nano-scale structures.

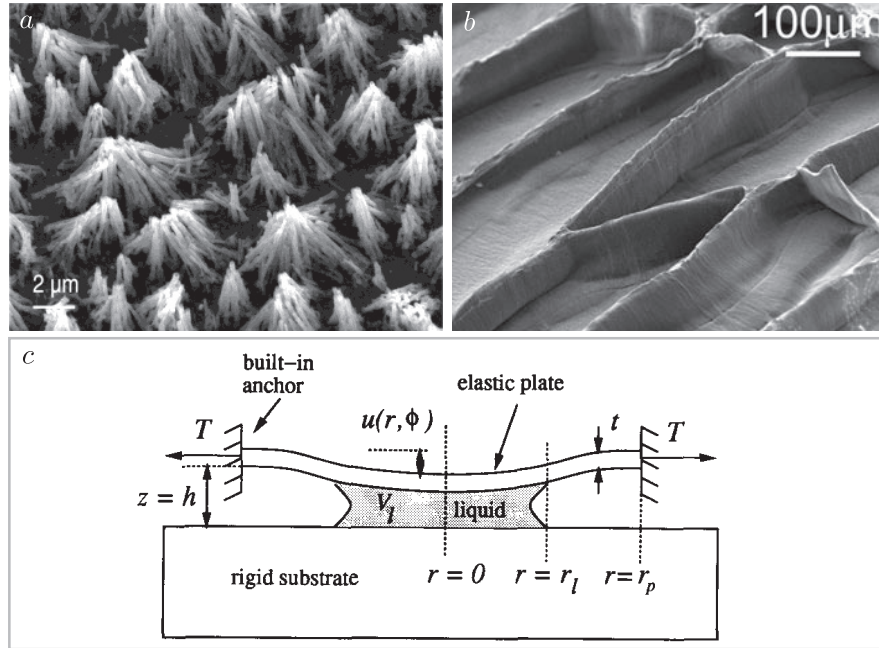


Figure 1.24 – (a) Formation of teepees after rinsing a carbon nanotube forest. Reproduced from [59]. (b) When rinsing a carbon nanotube forest, the final pattern is determined by the elasticity of the pillars and the wetting properties of the liquid: instead of teepee shapes, cellular patterns can be formed during the rinsing step. Reproduced from [60]. (c) Failure of a micro-electro-mechanical system that includes a suspended plate and a rigid mounting. Reproduced from [61].

Hierarchical nanostructures engineered by pillars self assembly The observation of the formation of teepees [59] or cellular patterns [60] due to the evaporation of liquid in a carbon nanotube forest is a first step in the process of engineering more complex structures using elastocapillary self-assembly. Ordered hierarchical helical assemblies have been obtained using a periodic array of nanopillars [62]: spontaneous helicity is induced in a polymeric nanobristle when liquid is evaporated. The final size of the ordered helical clusters depends on the competition between elasticity and capillarity, as shown in Fig. 1.25(a). The two-dimensional pattern on which the carbon nanotube forest is grown can also be tuned to create various complex structures [63]: a catalyst is patterned on a surface so that carbon nanotubes only grow at desired places. Liquid is then condensed on the substrate, and evaporation generates three-dimensional shapes that depend not only on elasticity and capillarity but also on the chosen two-dimensional pattern. Examples of such structures are shown in Fig. 1.25(b). Elastocapillary deformation of a hydrogel micropillar array have also been shown to trigger color changes of the structure due to light scattering [64]. Bragg diffraction of ordered micropillar arrays is responsible for giving a color to the sample when the structure is periodic. The refracted wavelength depends on the periodicity of the array. When pillars form random clusters, no wavelength is selected, which causes the sample to appear white, as shown in Fig. 1.25(c). Elastocapillary aggregation of micropillar arrays is thus a successful way of tuning the shape of microstructures, with promising perspectives for manufacturing surface textures with controllable wetting, adhesion, optical, or electrical properties, as well as for energy

applications through supercapacitors design [65].

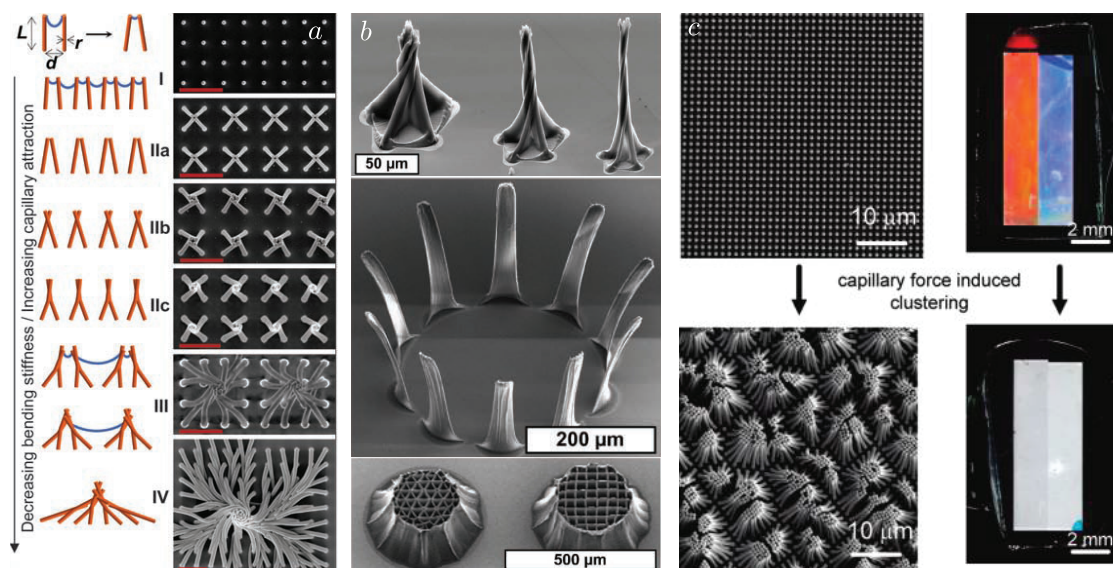


Figure 1.25 – (a) Schematic diagram (left) and scanning electron microscopy images (right) showing the capillarity-driven formation of hierarchical helical patterns in a polymeric nanobristle. The red scale bars are 4 μm . Reproduced from [62]. (b) Diverse three-dimensional microarchitectures obtained by capillarity in patterned forests of carbon nanotubes. The final shape results from both the elastocapillary interactions and the shape of the two-dimensional pattern used to grow the carbon nanotube forest. Reproduced from [63]. (c) Scanning electron microscopy (left) and optical images (right) of micropillar arrays before and after clustering. Two different colors in the top right picture result from Bragg diffraction of micropillar arrays with different periodicities. Random clustering causes whiteness of the sample for both periodicities in the bottom right picture. Reproduced from [64].

Formation of 3D structures from 2D patterns A two-dimensional flat surface can be turned into a three-dimensional structure using pattern design and elastocapillary interactions. This strategy is used to build MEMS since the 1990s, by depositing solder droplets on micromachined two-dimensional shapes [66]. As described in Fig. 1.26(a), the solder is liquid when deposited and exerts capillary forces on the two-dimensional pattern, which results in an out-of-plane deformation. The solder eventually solidifies, leading to a robust three-dimensional shape, the equilibrium angle of a given structure depending on the volume of solder deposited. The micro-fan described in [67] and shown in Fig. 1.26(b) is an interesting example of micro-structure built with this technique: solder is used to achieve a specific angle-of-attack for the fan blades. Micrometer-scale polyhedra can also be shaped with elastocapillary forces [68], as shown in Fig. 1.26(c). These three-dimensional structures are promising in terms of perspectives, including applications ranging from photovoltaic solar panels [69] to drug delivery [70].

Desktop-scale experiments have also been performed in the literature to further understand the competition between elasticity and capillarity, using millimetric or centimetric elastic structures and water. The underlying mechanism is the same as in micrometer scale assemblies: capillary forces are exerted on elastic structures, leading to large deformations. The folding of a structure results from a minimization of the sum of the bending and

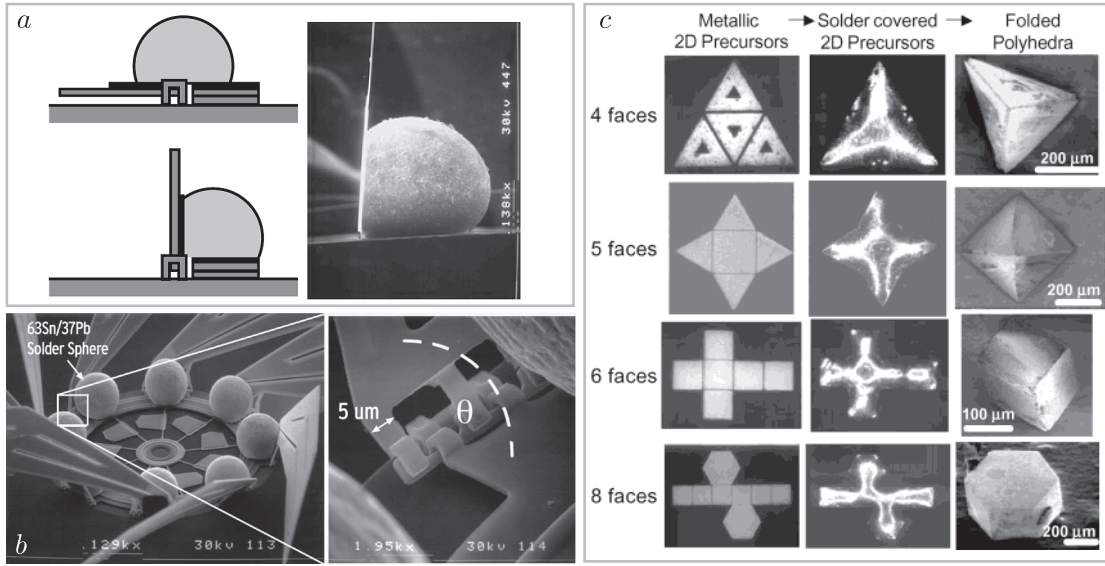


Figure 1.26 – (a) Schematic and picture of a simple solder-assembled structure. The typical volume of the solder droplet is 10^{-5} mL, and can be changed to tune the final angle of the fold. Reproduced from [66]. (b) Solder self-assembled micro-fan, using this technique to achieve a desired angle-of-attack for the blades. Reproduced from [67]. (c) Micrometer-scale polyhedra, assembled using metallic two-dimensional patterns and liquid solder: metallic two-dimensional structures prior to folding (left), two-dimensional precursors after dip-coating with solder (middle) and scanning electron microscopy images of polyhedra with bare metallic faces, ranging in size from 100 to 300 μm on a side (right). Reproduced from [68].

surface tension energies of the system: folding a two-dimensional shape into a three-dimensional structure has a cost in terms of bending energy but reduces the surface of liquid in contact with air. Taking advantage of this phenomenon, water droplets deposited on two-dimensional thin polymer patterns are shown to promote folding of the structure, enhanced by water evaporation [71]. A wide variety of final shapes is achieved through careful tuning of the initial flat shape, chosen to be for instance a triangle (Fig. 1.27(a)), a flower-shape pattern, or a layout designed to achieve a cubic three-dimensional structure, to cite only a few. It is possible to add a dynamic component to this experiment by having a droplet impact on the same kind of two-dimensional polymer pattern [72]. This results in a faster manufacturing process, and in the existence of an additional parameter to tune the final shape of the structure, namely the speed of the droplet. An example of two different shapes obtained by changing the speed of a droplet impacting on a given pattern is shown in Fig. 1.27(b). Recent extensions in this field include elastocapillary origamis with extremely thin polymer films: in the particular case of an ultra-thin film, bending occurs at no energetic cost, the final shape of a droplet wrapped in a thin polymer film being then completely determined by geometric considerations to minimize the area of the water-air interface [73]. Eventually, Fig. 1.27(c) illustrates a technique for grabbing water inspired by floating flowers: a passive pipetting mechanism occurs when the petal-shaped object is lifted from the water bath [74]. This unusual pipetting technique inspired a culinary device designed with renowned chef José Andrés to deliver small volumes of palate cleanser liquor between courses.

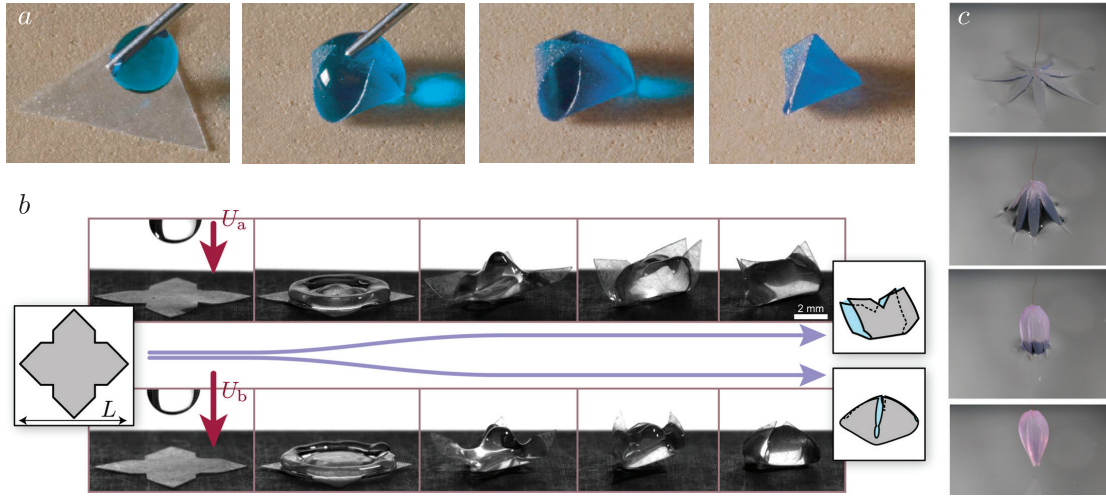


Figure 1.27 – (a) Elastocapillary origami: a water droplet deposited on a two-dimensional polymer thin sheet results in an encapsulation of the droplet, forming a three-dimensional shape. Reproduced from [75]. (b) Dynamic elastocapillary origami: the final three-dimensional shape adopted by the elastic sheet can be tuned by changing the speed at which the droplet impacts the polymer substrate. Reproduced from [72]. (c) Elastopipette: a flower-shape elastic sheet is used to grab a well-defined quantity of liquid. Reproduced from [76].

Beyond harmful effects, elastocapillary interactions turn out to be a promising tool to engineer self-assembled microstructures. In the following paragraph, we go further in the description of the competition between elasticity and capillarity, introducing an elastocapillary length for slender structures that quantifies the relative importance of surface tension forces compared to the flexibility of an elastic structure.

1.3.2. Elastocapillary length (slender structures)

A simple system is used in [76] to illustrate how bending and surface tension energies set a critical length, called the elastocapillary length. An elastic sheet of length L , width w , thickness h , and Young's modulus E is coated with a thin layer of liquid, of liquid-air surface tension γ . This sheet is put in contact with a rigid cylinder of radius R , coated with the same liquid. Two configurations can arise, depending on the relative strength of bending energies and surface energies, as illustrated in Fig. 1.28(a). Wrapping the sheet around the cylinder implies a cost in terms of bending energy: the bending energy is increased by $EIL/2R^2$, where $I = h^3w/12$. However, wrapping the sheet induces a gain in terms of surface energies of $2\gamma wL$. A minimization of the total energy shows that the sheet is expected to spontaneously wrap the cylinder if $R > \sqrt{EI/\gamma w}/2$. The characteristic length for which bending and capillary effects are of the same order of magnitude is thus defined as:

$$L_{ec} = \sqrt{\frac{EI}{\gamma w}}$$

This critical lengthscale depends on the wetting properties of the liquid (γ), on the elastic properties of the material (E) and on the geometry of the system (h , w , and consequently $I = h^3w/12$). Tuning the geometry of a sample is thus an efficient way of promoting or hindering elastocapillary interactions.

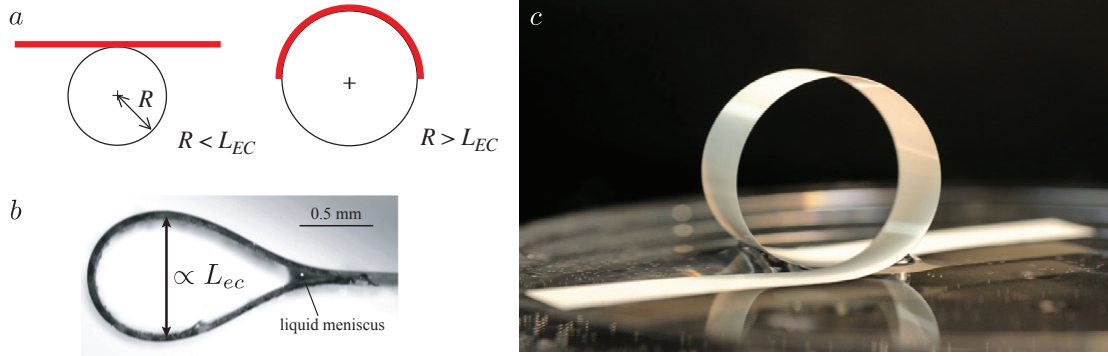


Figure 1.28 – (a) Wrapping a wet sheet on a wet cylinder is energetically favorable if the bending energy cost is smaller than the surface energy gain; it is the case when the cylinder radius is larger than a critical length of order of magnitude L_{ec} . Reproduced from [52]. (b) Racket shape formed with an elastomer strip. The liquid ethanol meniscus tends to keep the loop tight while bending rigidity tends to open the loop. The equilibrium shape is fitted to extract the value of L_{ec} . Reproduced from [71]. (c) Lamella forming a loop at a liquid interface (scale bar: 3cm). The radius of the loop is proportional to L_{ec} . Reproduced from [76].

Different examples are considered in the literature to quantify the elastocapillary length: an elastic rod growing inside a droplet of fixed size remains straight if the system size is smaller than a critical value, ultimately piercing the droplet-air interface. On the contrary, a rod (with the same elastic properties and same radius) turns out to buckle inside the droplet if the system size is bigger than a critical size, this critical size being proportional to L_{ec} [77]. Measuring the elastocapillary length can also be performed by forming a racket shape with a polymer strip, held by a meniscus of a wetting liquid such as ethanol [71], as shown in Fig. 1.28(b). Surface tension effects would tend to close the loop, whereas the energetic cost required to bend the structure would tend to open the loop. The two-dimensional equilibrium shape of the loop, computed by solving Euler Elastica's equations, highlights that the width of the loop is proportional to L_{ec} . A last example, illustrated in Fig. 1.28(c), consists in forming a loop with a strip above the surface of water. The competition between bending rigidity (that tends to increase the radius of the loop) and surface tension forces acting at the menisci (that tend to decrease the radius of the loop) sets an equilibrium configuration. The radius R of the circular loop is given by $R = L_{ec}/\sqrt{2(1 + \cos\theta)}$, where θ is the liquid contact angle on the strip [76].

1.3.3. State of the art: elastic sheets, strips, and fibers subjected to capillary forces

Beyond the examples in Nature and in the industry presented in section 1.3.1., numerous fundamental studies involving a competition between elasticity and capillarity

are found in the literature. In the following paragraphs, we describe early elastocapillarity considerations as well as more recent elastocapillarity experiments using various elastic structures, such as sheets, strips, and fibers. We thus supplement the state the art description begun in section 1.3.1. and highlight the importance of geometry in these examples.

a) Elastocapillarity with thin sheets

The elastocapillary origami shown in section 1.3.1. is an example of interaction between a droplet and an elastic sheet. Beyond this specific case, various situations involving elastocapillary interactions between a thin sheet and a liquid are described in the literature. Early theoretical considerations were performed in the 1980s by Fortes [78] and Shanahan [79, 80], focusing on a droplet standing on an elastic sheet, considering both two-dimensional and three-dimensional models, and suggesting the existence of both axisymmetric and non-axisymmetric shapes for the droplet and the underlying substrate in the three dimensional case. From an experimental point of view, pioneering observations reporting elastocapillary deformation of a thin sheet include early experiments performed by A. I. Bailey in the 1950s [81] on mica sheets, as well as observations of the deformation of a thin graphite layer by a liquid droplet or a non-epitaxed Pb crystallite in the early 1990s [82].

In Fig. 1.29, we show examples of interactions between thin sheets and liquids reported more recently in the literature. The example of a compressed elastic sheet floating at the surface of water, shown in Fig. 1.29(a), illustrates a wrinkle to fold transition to minimize the sum of the bending energy and the hydrostatic pressure term, as the sheet has to lift water to create wrinkles [83]. In this problem, density effects matter rather than capillarity, but the sheet sticks to the water surface due to capillarity. A second example consists in depositing a water droplet at the surface of a freely floating polystyrene film of tens of nanometers in thickness [84]. The resulting wrinkling pattern, shown in Fig. 1.29(b), is reported to be primarily due not to the weight of the drop, but to the capillary force exerted on the film at the air-water-polystyrene contact line. In [84] are derived scalings showing the dependence of the number of wrinkles and of their length as a function of the surface tension and diameter of the drop, and of the thickness and Young's modulus of the film. Another interesting example consists in wrapping a sphere, coated with ethanol, with an elastic sheet with no initial curvature, coated with the same liquid. This leads to contact zones with wavy patterns and unstuck parts of the sheet that do not touch the sphere [85]: in Fig. 1.29(c), a fluorescent dye allows for a visualization of the liquid meniscus that delimits both regions. A balance between stretching and surface tension energies provides the typical width of the contact zone, while a balance between bending and surface tension energies explains the complexity of the pattern (branches for instance, as it is the case in Fig. 1.29(c)).

b) Elastocapillarity with strips

Experiments with elastic strips rather than sheets often lead to a two-dimensional setup or modeling. In the case of the experiment called *elastic meniscus* shown in Fig. 1.30(a), a flexible strip is clamped at one end in a narrow box filled with liquid. As the liquid is withdrawn from the box, the strip adopts an equilibrium shape that depends on its elastic properties and on the liquid density and surface tension [86]. This experiment

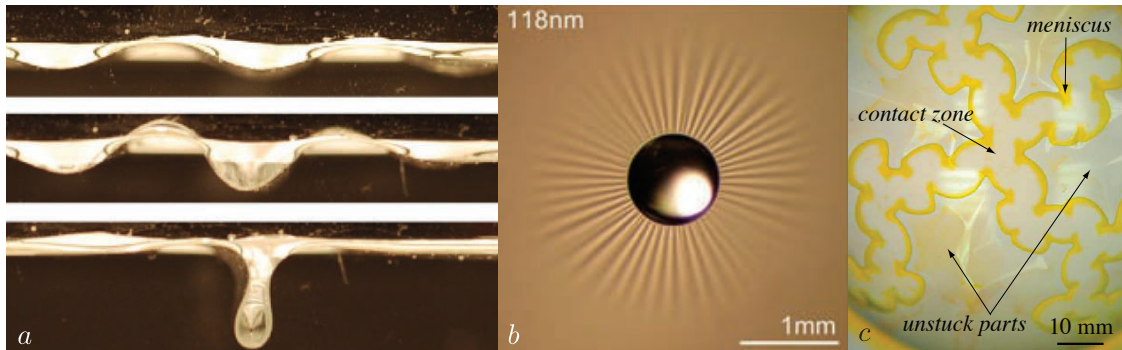


Figure 1.29 – (a) Wrinkle to fold transition of a compressed elastic sheet lying at a water-air interface. Reproduced from [83]. (b) Water droplet of radius 0.5 mm deposited on a freely floating polystyrene film of thickness 118 nm. Capillary forces exerted by the droplet on the film result in a wrinkling pattern. Reproduced from [84]. (c) An elastic sheet with zero natural curvature is placed onto a rigid sphere coated with ethanol, which totally wets both the sheet and the sphere. The region in contact with the sphere forms branched wavy patterns, and the unstuck parts of the sheet do not touch the sphere. The limit between contact regions and unstuck parts of the sheet is visualized with a fluorescent dye. Reproduced from [85].

is purely two-dimensional, which is no longer the case when working with elastic strips and water droplets. Indeed, the footprint of a droplet deposited on an elastic strip is delimited by the borders of the strip, as shown in the left picture in Fig. 1.30(b), but the overall shape of the droplet results from the minimization of the surface energies. A two-dimensional modeling, shown in the right picture in Fig. 1.30(b), is a simplified model that nevertheless captures properly the combined effects of elasticity and capillarity in drop-strip systems [87]. A comparison between experimental data and two-dimensional simulations in the case of a droplet impacting an elastic strip is shown in Fig. 1.30(c): the two-dimensional model captures not only the final shape of the strip but also the time evolution of the drop-strip system. In chapter 3, we will thus use a two-dimensional modeling when focusing on the snap-through instability of an elastic strip triggered by a water droplet.

c) Elastocapillarity with fibers

Elastocapillarity experiments with fibers are common in the everyday life. We already mentioned the aggregation of wet hair [55], but a similar phenomenon occurs when a paint brush is plunged into water and withdrawn from the water bath: this situation was already pointed out as a scientific question by Charles Vernon Boys in 1890 [23], constituting a first simple elastocapillarity experiment. In an assembly of fibers, capillary forces are likely to create bundles, both in macroscopic systems such as wet hair and in microscopic carbon nanotube forests, as shown in section 1.3.1..

However, there is no need of an assembly of fibers to observe interesting elastocapillary phenomena: the aggregation of wet hair can be analyzed by starting with a two-fiber setup. In fact, the experiments performed in [55] featured lamellae to model hair instead of circular cross-section rods, but the physical ingredients are similar: a simple system of two lamellae clamped at one end is withdrawn from a liquid bath. If the clamps are separated by a distance d , the distance from the clamp L_{dry} at which the two lamellae

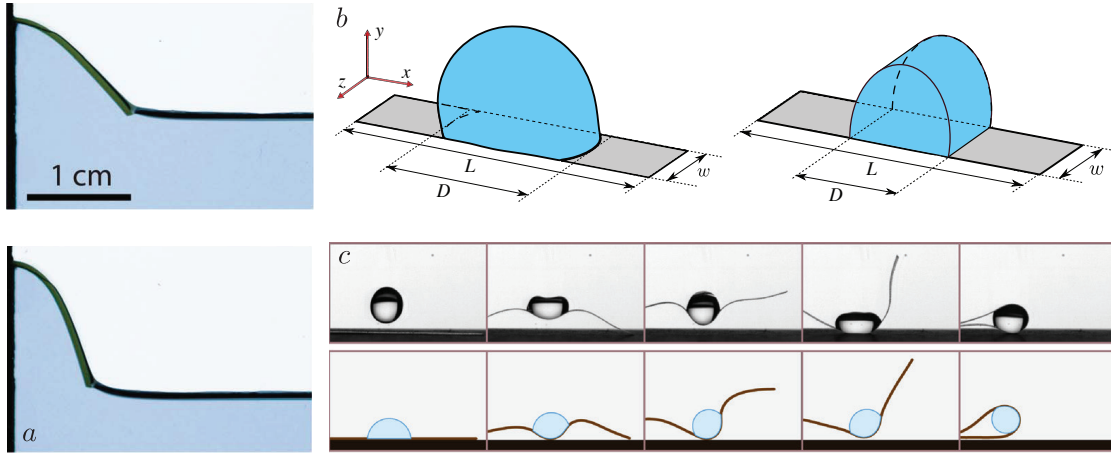


Figure 1.30 – (a) *Elastocapillary meniscus*: shape adopted by a polyvinylsiloxane strip on water in a narrow box filled with liquid, when the liquid is gradually withdrawn from the box. Reproduced from [86]. (b) Shape of a liquid drop standing on a strip, computed with *Surface evolver* (left) and with a two-dimensional modeling in which the liquid-air interface is cylindrical (right). Reproduced from [87]. (c) Drop impact on a long and thin polymer strip lying on a substrate: comparison between experimental results (top) and two-dimensional simulations (bottom). Strip dimensions are $L = 5$ cm and $w = 2$ mm, and drop radius is $R = 1.55$ mm. Reproduced from [72].

aggregate is given by $L_{\text{dry}}^2 \propto L_{\text{ec}} d$ [55]. This experiment constitutes an additional example showing the importance of the elastocapillary length in the resolution of elasticity versus capillarity competition problems. Experiments with droplets deposited on two fibers with a circular cross-section have also been performed [88], as shown in Fig. 1.31(a): depending on the volume of a droplet deposited between two flexible fibers and on the length of the fibers, no spreading, partial spreading, or total spreading occurs. The geometry is more complex, as the liquid can adopt different shapes (surrounding the fibers, or being completely included in the volume between the two fibers). An array of such flexible fibers recently proved to be an efficient elastocapillary mist collector [89].

Elastocapillarity experiments with one single fiber also exhibit promising perspectives: a thin fiber is easily bent by a liquid droplet, as shown in Fig. 1.31(b). Taking advantage of this phenomenon, a capillary windlass effect inspired by spider-silk supercontraction abilities (described in 1.3.1.) has led to the design of a biomimetic ultra-stretchable fiber [54, 90, 91]. During compression, the excess fiber is spooled inside a droplet and capillary forces keep the system taut, while during elongation, the fiber is gradually released: if a large number of spools is uncoiled, a high stretchability is achieved. Fig. 1.31(c) presents a phase diagram in terms of fiber radius a and droplet radius R : the compressive capillary force $2\pi a\gamma$ (where γ is the surface tension of the droplet) is required to overcome the elastic bending force $\pi E a^4 / 8R^2$ (where E is the Young's modulus of the fiber) for the fiber to coil inside the droplet [91]. If coiling occurs, the fiber exhibits unique mechanical properties, e.g. a ultra-stretchability with no fatigue for the material. This phenomenon, illustrated in Fig. 1.31(d), is an additional example in which buckling induces functionality rather than failure. In the context of stretchable electronics, such fiber-droplet systems are promising to build buckling-activated microstructures using in-drop coiling.

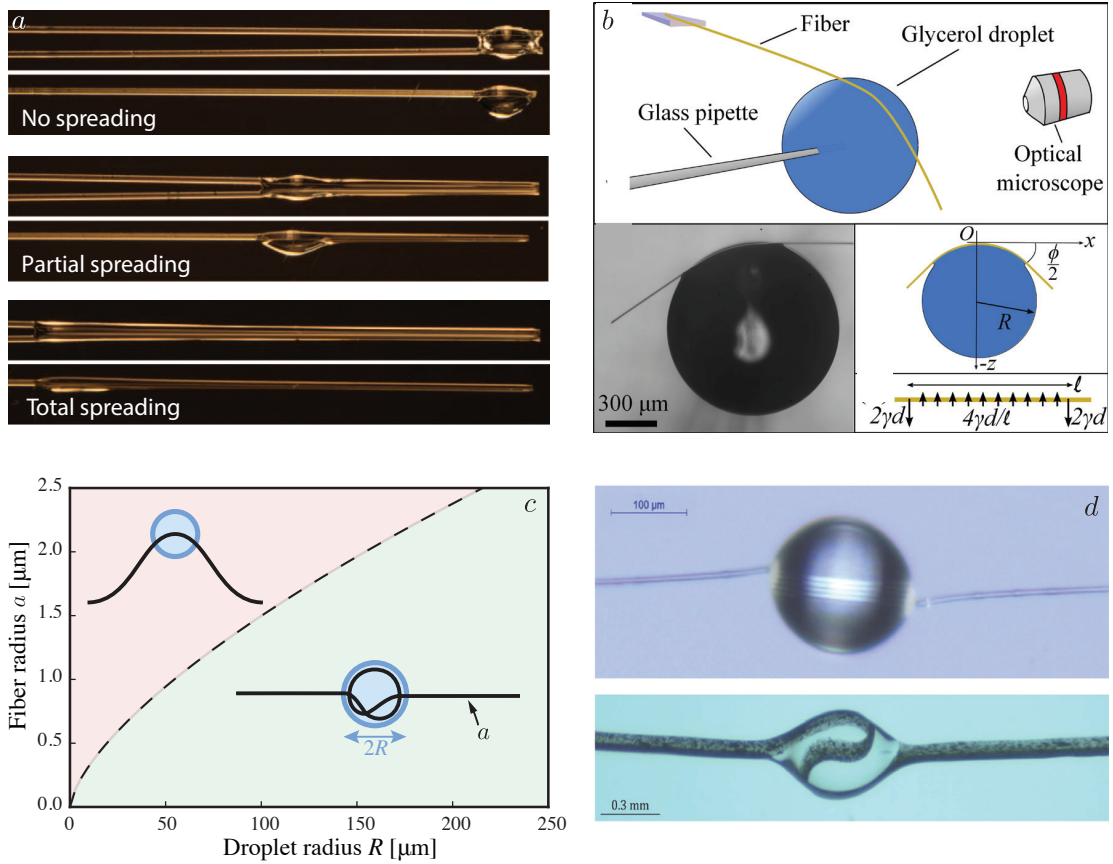


Figure 1.31 – (a) Three different final states of a drop between two flexible fibers. From top to bottom, the volume of the droplet remains the same, and the length of the fibers is increased. Fibers are clamped at the left end. Reproduced from [88]. (b) Shape of a polystyrene fiber (clamped at one end, free at the other end) put in contact with a glycerol droplet. Reproduced from [92]. (c) Regions in the fiber radius a versus droplet radius R phase diagram where a silicone oil droplet ($\gamma = 21$ mN/m) triggers coiling (in green) or not (in red) of a fiber ($E = 1$ Gpa). For a given fiber radius a , in-drop coiling will be energetically favorable for a large enough droplet. Reproduced from [91]. (d) Top: polyurethane fiber with circular cross-section spooled in a silicone oil drop. Bottom: polyvinylsiloxane beam with rectangular cross-section bent in a silicone oil drop. Reproduced from [90].

1.4 Elastocapillarity on soft polymer bulks

In the previous section, focus has been given on macroscopic deformations caused by capillarity on a slender object. In the case of an extremely soft solid, microscopic deformations have also been shown to occur at the triple line. We focus here on wetting on bulk soft solids, investigating the shape of a static wetting ridge, before giving a brief outline of the literature on moving contact lines on soft substrates.

1.4.1. Statics: shape of the wetting ridge raised on a soft solid

a) From Young's angle to Neumann's construction: wetting ridge on a soft solid

Two classical results have been presented in section 1.2.2.: wetting on solid surfaces is usually studied in the framework of Young-Dupré's relation, while the case of a droplet lying on a liquid substrate in which it is immiscible is described in the framework of Neumann's construction. The situation where a droplet is lying on an extremely soft gel can be thought as being an intermediate case (Fig. 1.32(a) and (b)). However, the description of the deformation of the gel by capillary effects is complex [93, 94].

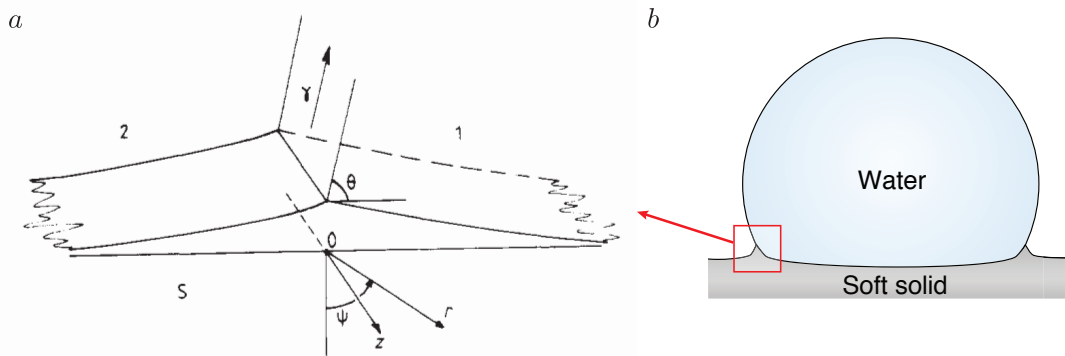


Figure 1.32 – (a) Local shape of a wetting ridge at a three-phase contact line. Reproduced from [95]. (b) Schematic illustrating the existence of a wetting ridge in the case of a droplet on a soft substrate. Reproduced from [96].

The existence of a wetting ridge raised by a droplet lying on a soft substrate was already foreseen in the 1950s in a discussion between J. J. Bikerman and R. E. Johnson [81], pointing out that *real solids are not unchangeable* (based on observations by A. I. Bailey of capillarity-induced deformations of mica sheets) and hoping to detect a wetting ridge on gels. Lester [27] then performed the earliest modeling that includes effects of solid strain in contact angle equilibrium. The theoretical description of the shape of the ridge was refined in the 1980s by Rusanov [97] and Shanahan [95, 98], introducing a logarithmically diverging shape for the ridge, and a characteristic lengthscale for the height of the ridge, equal to γ/E , where γ is the surface tension of the liquid and E the Young's modulus of the soft solid. This elastocapillary length for the wetting ridge may not be confused with the elastocapillary length for a slender structure described in the previous section. Here the competition between the bulk elasticity and the capillary force at the triple line determines the height of the ridge. Examples of the typical height of the ridge raised by a water droplet on different materials are given in Table 1.1.

In addition to the formation of a wetting ridge localized at the triple line, a soft solid is likely to be deformed by the pressure exerted by the droplet on the whole footprint, which is equal to the sum of the Laplace and hydrostatic pressures. In the case of droplets deposited on a thin soft gel layer prepared above a stiffer substrate, the effect of finite thickness of the gel layer results in a change in the shape of the ridge, that includes the apparition of a dimple in the elastic material [99].

The solid's own surface tension also strongly couples to its deformation, especially in

Material	Young's modulus	Typical ridge height (water droplet)
Steel	200 GPa	$\ll 1 \text{ \AA}$ (model not relevant at this scale)
PDMS Sylgard 184	1.8 MPa	40 nm
Nusil ultrasoft gel	250 Pa	0.3 mm

Table 1.1 – Typical ridge height for various materials. PDMS Sylgard 184 and Nusil ultrasoft silicone gel are described further in chapter 2. Note that in the case of PDMS Sylgard 184 used in chapters 3, 4 and 5, the height of the wetting ridge is only a few tens of nanometers: its effect on wetting dynamics will thus be neglected.

the vicinity of the cusp (in a scale much smaller than γ/E). As illustrated in Fig. 1.33, soft solids have been recently shown to undergo capillarity-driven instabilities [100], highlighting the role of the solid's own surface tension. However, one needs to be careful of what is called surface tension in the case of a soft solid. Two different quantities can be defined: the surface energy, denoted γ , defined such as the energy gained from stretching the interface is equal to γ multiplied by the gain of interfacial area, and the surface stress, denoted Γ [101]. For a simple liquid, the surface stress is equal to the surface energy, and both are referred to as the surface tension. However, for a soft solid, the surface energy might be strain dependent, with the following relationship between Γ and γ : $\Gamma = \gamma + d\gamma/d\epsilon$, where ϵ is the strain. This phenomenon, called Shuttleworth effect [102], has been recently observed in soft solids in the case of a ridge raised by a liquid droplet [103].



Figure 1.33 – Rayleigh-Plateau instability occurring in an agar-agar cylinder, due to the solid's own surface tension. The initial radius of the cylinder is $240 \mu\text{m}$. Reproduced from [100].

Beyond the theoretical description of the ridge, we present in the following paragraphs various experimental techniques used in the literature to visualize a wetting ridge, ranging from white light interferometry to confocal fluorescence and X-ray microscopies.

b) Experimental visualizations of the wetting ridge

The visualization of a wetting ridge is made easier when the chosen substrate is extremely soft (see Table 1.1), and when the surface tension of the droplet is high. In this context, early observations of a wetting ridge were performed by Bikerman, showing that mercury drops produced a $40 \mu\text{m}$ ridge on a hydrogel with a Young's modulus $E = 6 \text{ kPa}$, as reported in [104]. Further experiments were performed in the late 1970s in the case of different types of methacrylate gels: visualizations of a frozen water droplet lying on the substrate were performed by scanning electron microscopy (SEM), the ice disappearing rapidly after insertion in the SEM [105]. Evidencing the existence of a wetting ridge was an achievement, however, these measurements did not capture the precise geometry of the ridge. In their pioneering work to gain insight on the local geometry of the wetting ridge, Carré and Shanahan [106] used white light interferometry,

as shown in Fig. 1.34(a). Confocal microscopy was then used to record the shape of the interface between a poly-(dimethylsiloxane) substrate and a drop of ionic liquid [107]. More recent experiments include confocal microscopy visualizations with fluorescent particles embedded on the surface [108]. However, the most striking recent experiment is probably the X-ray visualization of a water droplet on a silicone gel reproduced from [96] in Fig. 1.34(b). The determination of the ridge geometry in various cases is still a very active research field, including for instance ongoing Schlieren imaging experiments [109].

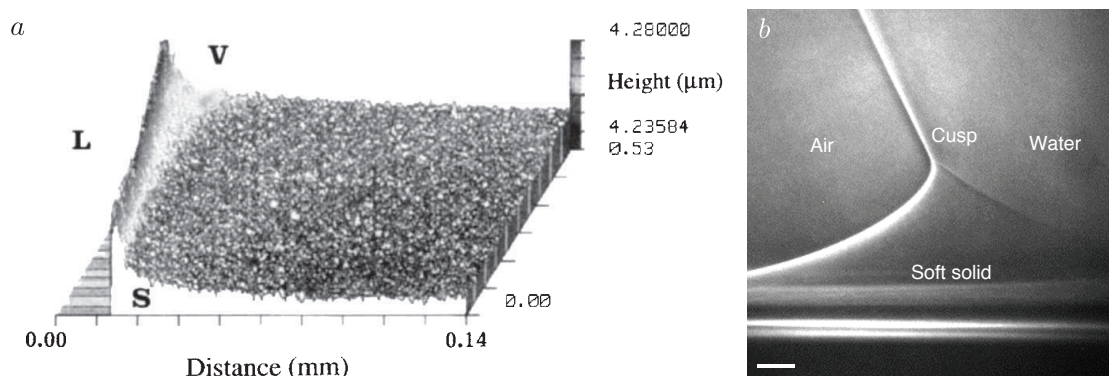


Figure 1.34 – (a) White light interferometry measurements of the ridge raised by a tricresylphosphate droplet on a silicone elastomer. Reproduced from [106]. (b) X-ray imaging of the wetting ridge raised by a water droplet on a silicone gel. Scale bar is 2 μm . Reproduced from [96].

c) Wetting ridge growth dynamics

X-ray microscopy visualizations of wetting ridges were also performed as a function of time to record the ridge formation [96]: a non-volatile ethylene-glycol 40% aqueous solution (EG 40%) is used instead of evaporating water drops. The ridge growth is shown in Fig. 1.35, until depinning caused by injection of an additional volume of EG 40% occurs. The angle of the ridge, denoted here θ_s , interestingly remains constant during the ridge growth.

1.4.2. Dynamics: moving contact lines on soft materials

When a triple line is moving on a soft substrate, the wetting ridge described in the previous paragraphs accompanies the motion (in cases where the growth dynamics of the ridge is fast compared to the speed of the droplet). The displacement of a deformation leads to an energy dissipation in a viscoelastic soft substrate. Pioneering work by Shanahan and Carré [110] demonstrates experimentally the existence of a viscoelastic braking for a droplet sliding down a soft rubber inclined plane (Fig. 1.36(a)). More recently, a stick-slip motion was observed on soft substrates, both in the case of an inflated droplet [111], as illustrated in Fig. 1.36(b), and in a dip-coating geometry [112]. The pinning/depinning mechanism leading to the droplet motion was further analyzed in [113], highlighting that droplets move over viscoelastic substrates by surfing a ridge, see Fig. 1.36(c): the contact line depins and slides down the wetting ridge, forming a new one after a transient.

Droplets were also shown to undergo durotaxis [114], moving towards softer regions of a patterned substrate. The driving force allowing the droplets to move results from

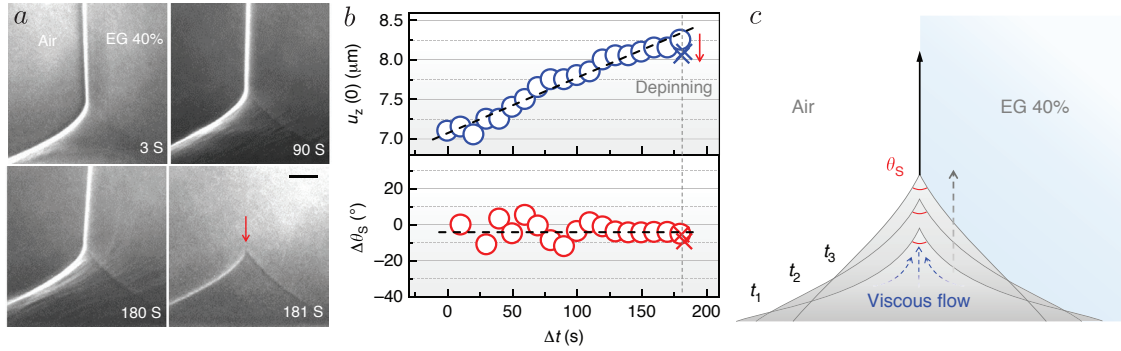


Figure 1.35 – Ridge growth dynamics. (a) Sequential snapshots of a cusp during ridge growth for an ethylene-glycol (EG) 40% aqueous solution drop on a silicone gel. The scale bar is $2 \mu\text{m}$. (b) Ridge height $u_z(0)$, and change of the ridge angle $\Delta\theta_s$ as a function of time. (c) Schematic illustration of the ridge growth. Reproduced from [96].

a difference in contact angles across the droplet, due to a difference in stiffness of the underlying material. Different situations have been analyzed in the literature, including drop impact on soft solids [115], or interaction between several droplets. Interestingly, the interaction between two droplets lying on a soft material (or so-called *inverted Cheerios effect*) depends on the thickness of the soft layer [116]: droplets on a thick and soft substrate attract each other, as it is the case for two menisci of same sign on a liquid bath, while droplets on a thin layer of elastomer have a repulsive interaction due to the existence of dimples around the droplets.

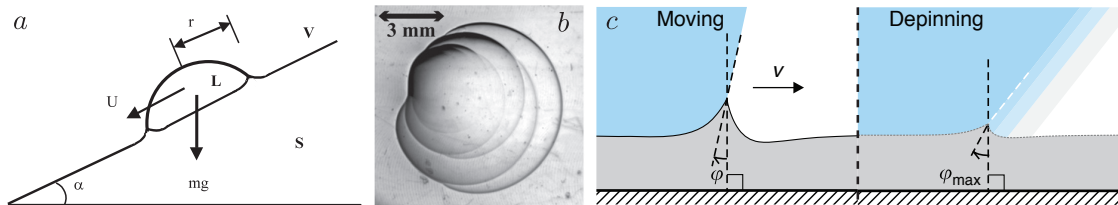


Figure 1.36 – (a) Setup used in the pioneering experiments of Shanahan and Carré: a droplet is sliding down an inclined plane made of rubber. Reproduced from [110]. (b) Stick-slip motion observed on a styrene-butadiene-styrene-paraffin gel when gradually inflating a water droplet: the picture of the gel was taken after the inflation process was finished and the droplet was removed. The droplet leaves multiple circular patterns. Reproduced from [111]. (c) Pinning/depinning mechanism of a contact line moving on a soft solid. Reproduced from [113].

Conclusion

In this introductory chapter, we have discussed general concepts about elasticity and capillarity, before describing the state of the art in elastocapillarity both on slender structures and on soft bulk materials. In terms of elasticity, focus has been given on statics and dynamics of flexible beams. We have included a description of two instabilities, namely buckling and snap-through, that are of interest in the context of the elastocapillary

snap-trough experiments presented in chapter 3. We have also underlined the recent interest for using such instabilities to promote functionality rather than studying them to avoid failure, as it was the case in the past century. In terms of capillarity, we have recalled classical results such as the definition of surface tension and its ability to shape interfaces. Focus has then been given on wetting, which corresponds to a three-phase interaction, and on moving contact lines. Finally, a brief overview of the literature on droplets sliding (or rolling) on inclined planes has been given, in order to lay foundation for the understanding of our experiments on droplet dynamics on elastomers, presented in chapter 4. Combining elasticity and capillarity constitutes a research domain attracting growing interest, called elastocapillarity. A few decades ago, focus was mainly given in avoiding harmful elastocapillary interactions in microfabrication. However, elastocapillary interactions recently proved to be useful to manufacture both hierarchical fiber assemblies and three-dimensional origamis. In this context, we have recalled the definition of the elastocapillary lengthscale, which corresponds to the length for which elastic and surface energies are of the same order of magnitude. The state of the art on elastocapillarity with sheets, strips, and fibers has then been described, highlighting macroscopic deformations caused by capillarity on elastic structures. At the microscale, deformations can occur at the triple line, however, the elastic material has to be extremely soft for the deformation to be visualized. In this framework, we have summarized the recent interest for both static and dynamic wetting on extremely soft bulk substrates.

Chapter 2

Materials and Methods

droplets deposition

spin-coating

drawdown bar

liquids

backlighting

silicone elastomers

tensile test viscosimeter

vibrations

ellipsometry

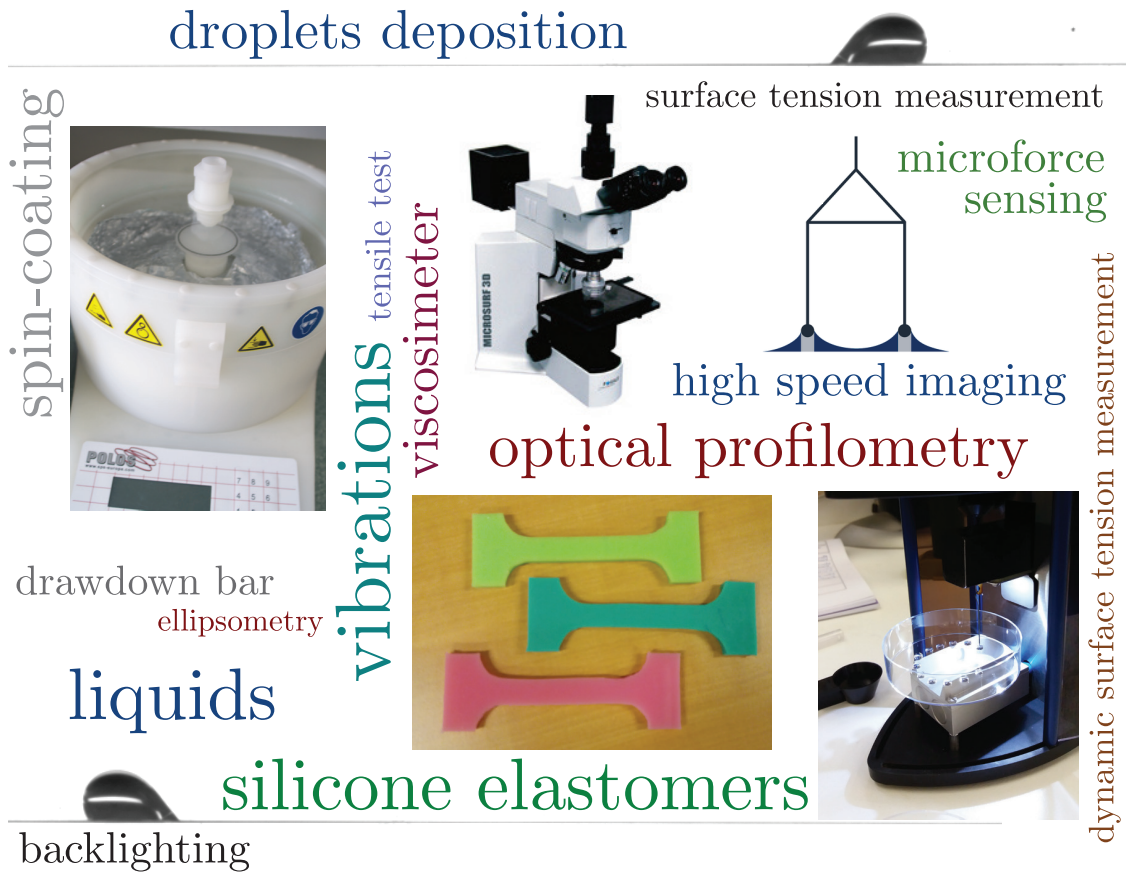
surface tension measurement

microforce sensing

high speed imaging

optical profilometry

dynamic surface tension measurement



Some experimental techniques are crucial to the obtention of the results presented in the following chapters. Here is a Materials and Methods chapter summarizing the employed techniques that range from elastic samples manufacture and characterization to liquids selection and liquids properties measurements: studying elastocapillarity implies to choose both the appropriate elastic and liquid materials. This chapter also includes details about microforce sensing, as well as a presentation of dynamic measurement techniques such as high speed acquisition or dynamic surface tension measurement.

Contents

2.1 Elastomer plates and strips	42
2.1.1. Materials selection and samples manufacture	42
2.1.2. Samples characterization: thickness and Young's modulus	49
2.2 Microforce sensors	55
2.3 Liquids employed in our elastocapillary experiments	56
2.3.1. Basic requirements for liquids used in contact with silicone elastomers	57
2.3.2. Viscosity and surface tension measurements	58
2.3.3. Droplet deposition techniques	62
2.3.4. Ellipsometric characterization of an overlay of different liquids	63
2.4 High speed acquisition	65
2.4.1. Fast cameras	65
2.4.2. Lighting techniques	65

2.1 Elastomer plates and strips

2.1.1. Materials selection and samples manufacture

Studying the competition between elasticity and capillarity requires to use compliant elastic solids likely to be deformed by capillary forces. Two different paths lead to highlight capillarity effects on an elastic object: choosing a very soft elastic material, or tuning the geometry of a stiffer material to obtain a slender and thus flexible object.

The following paragraphs describe a panel of elastomers that can be used for elastocapillarity experiments, as well as techniques to design the geometry of elastomer samples by cutting strips out of thin polymer films.

a) Silicone elastomers

Elastomers are rubbery materials composed of long polymer chains, crosslinked to form an elastic matrix. Such materials exhibit a high resistance to fracture and samples can be stretched up to several times their initial length. The Young's modulus is the parameter quantifying the rigidity of a material in the linear regime, as explained in chapter 1.

We first need to refine what is called "soft" or "flexible" in the context of our study, by comparing the Young's modulus of a substrate to the appropriate quantities in our experiments. In the case of a bulk substrate used for elastocapillarity experiments, the softness is quantified by comparing the height of the deformation due to surface tension at the triple line with a microscopic characteristic length, for instance the size of the monomers constituting the polymer network. As shown in chapter 1, a material for which capillary effects induce a non-negligible deformation at the triple line typically has a Young's modulus lower than 100 kPa. Elsewhere, in the case of slender – and thus flexible – objects, the length of the samples has to be compared with the elastocapillary length, defined in chapter 1. Since we are working with samples of dimensions h , w , and L with

1. Part 1 and part 2 are thoroughly stirred by hand for 4 minutes, in proportions 10:1.
2. The mixture is then degassed for 10 minutes in a vacuum chamber (the vacuum is shut down several times during this step to make bubbles at the free surface burst).
3. The samples are prepared with the liquid mixture by casting or thin film manufacturing.
4. Samples are placed in the oven for 2 hours at 60 °C, and stay at room temperature for at least 48 hours before being used in experiments.

Changing the curing temperature changes the elastomer properties [119], as shown in a graph of the Young's modulus as a function of the curing temperature reproduced in Fig. 2.2. The point corresponding to the Young's modulus measurement of our PDMS samples cured at 60 °C is added in red on this graph, and a good agreement is found with the experimental data from [119]. All experiments shown in Fig. 2.2 are performed with a 10:1 usual base-to-curing-agent ratio.

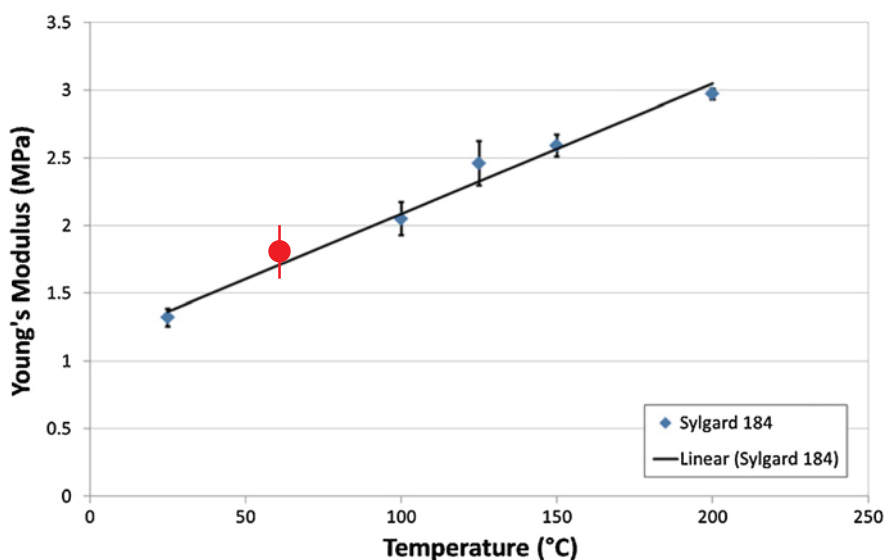


Figure 2.2 – Evolution of the Young's modulus of Dow Corning Sylgard 184 PDMS as a function of the curing temperature, adapted from [119]. The red point added on the graph is the Young's modulus measured for our samples cured at 60°C.

The elastic and viscoelastic properties of the crosslinked polymer can also be tuned in a more wider range by changing the base-to-curing-agent ratio, as shown in Fig. 2.3.

Zhermack Elite Double polyvinylsiloxanes The Elite Double polyvinylsiloxane range from Zhermack company, designed for dental model duplication purposes, is used in droplets dynamics experiments detailed in chapter 4. As for PDMS, the polymer kit comes into two bottles, a base and a catalyst, to be mixed with a 1:1 ratio in order to obtain a crosslinked elastomer. The quick curing time of these dental polymers at room temperature make them a good choice for rapid prototyping.

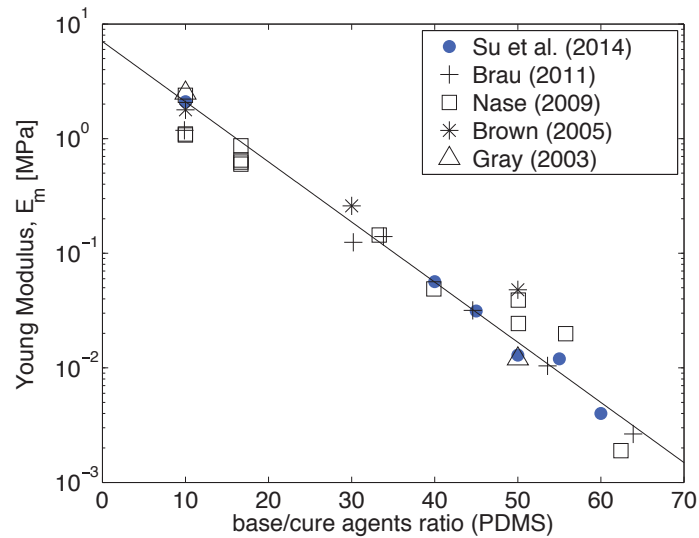


Figure 2.3 – Evolution of the Young’s modulus of Dow Corning Sylgard 184 PDMS as a function of the base-to-curing-agent ratio, reproduced from the Supplementary Information of [120].

The Elite Double range is composed of several Shore A hardnesses that correspond to several Young’s moduli, ranging from 250 kPa to 1.2 MPa (Table 2.1). The color of the polymer is different for each Shore A value, to easily link the color of an object to its elastic properties.

Esprit Composite elastomers Besides dental applications, polymers are also used in the entertainment industry to manufacture masks, costumes and fake wounds. The Esprit Composite elastomers that we use in droplets dynamics experiments detailed in chapter 4 are designed for such applications. RTV 001, EC00, EC13 and EC33 polymers are transparent poly-addition silicone elastomers that can be dyed for disguise purposes. RTV EC13 and EC33 have respectively Shore A hardnesses of 13 and 33, which correspond to a range similar to the Elite Double range. However, RTV 001 and EC00 are much softer (of the order of 5 and 50 kPa respectively). The manufacturing process is quite similar to the one of the Elite Double polymers, with a 1:1 mixing ratio and a fast crosslinking step at room temperature (RTV standing for Room Temperature Vulcanization).

Summary of elastomers properties Table 2.1 is an overview showing the properties of different elastomers used or considered to be used in our experiments.

b) Tuning the geometry: thin films manufacture

Two geometries are employed for the elastic samples in our experiments: bulk samples (used in experiments described in chapters 4 and 5), and slender objects, namely flexible strips (used in experiments described in chapter 3). Bulk samples of several millimeters thicknesses can be easily built by casting elastomers in 12 cm square Petri dishes. Yet, manufacturing slender objects like thin strips requires a more refined process which consists in cutting small pieces from thin elastic films. A first step in this direction is

Elastomer	Young's modulus	Working time	Crosslinking time	Color
Dow Corning				
Sylgard 184 PDMS	~ 1.8 MPa	1 h 30	2 h at 60°C	transparent
CY 52-276	~ 3 kPa	30 minutes	2 h	transparent
Zhermack				
Elite Double 8	~ 250 kPa	10 minutes	20 minutes	pink
Elite Double 22	~ 900 kPa	10 minutes	20 minutes	dark green
Elite Double 32	~ 1.2 MPa	10 minutes	20 minutes	light green
Esprit Composite				
RTV 001	~ 5 kPa	10 minutes	1 h	transparent
RTV EC00	~ 50 kPa	15 minutes	1 h 30	transparent
RTV EC13	~ 400 kPa	45 minutes	3 h	transparent
RTV EC33	~ 1.2 MPa	20 minutes	3 h	transparent
Nusil Gel 8100	~ 250 Pa	unknown	1 h at 100°C	transparent
Smooth-on Ecoflex	~ 10 to 100 kPa	30 minutes	4 h	translucent

Table 2.1 – Young's modulus order of magnitude (the Young's modulus highly depends on the manufacturing protocol), working and crosslinking time at room temperature (otherwise specified), and color for various elastomers. The elastomer brands are shown in bold characters.

to obtain thin elastomer films of uniform thickness, using the liquid base and catalyst mixture to spread a thin liquid film that is then crosslinked (in the oven or at room temperature, depending on the employed elastomer).

Various techniques are used in research and industry to manufacture thin liquid films, all based on fluid dynamics principles. In the following paragraphs, we describe two techniques effectively used to build our samples: spin-coating, and film application with a drawdown bar. However, we also mention another widely spread technique called dip-coating: a thin film is formed by withdrawing a plate from a liquid bath at a controlled speed. The film thickness is set by the competition between viscous effects, capillary forces, and gravity. The faster the substrate is withdrawn, the thicker the film deposited [121].

Spin-coating Spin-coating is a common method to obtain a liquid film of uniform thickness by depositing a liquid droplet on a rotating plate. Preparation of thin uniform films with this technique have first been reported in the context of paint coatings at the beginning of the 20th century [122], while the earliest modeling of the flow of a viscous liquid on a rotating disk was performed in the 1950s by Emslie, Bonner and Peck [123].

We consider a disk, rotating at angular speed Ω , on which an amount of liquid is deposited. The liquid is assumed to be newtonian and incompressible, its density is denoted ρ_l and its dynamic viscosity μ . Capillary forces, gravity and Coriolis forces are neglected. The liquid layer is also assumed to be radially symmetric, and the problem is studied in the scope of the lubrication approximation. We use cylindrical coordinates (r, θ, z) , denote $h(r, t)$ the thickness of the thin film, and assume the slope $\partial h / \partial r$ to be small or zero (Fig. 2.4(c)). In the lubrication approximation the flow can be described by

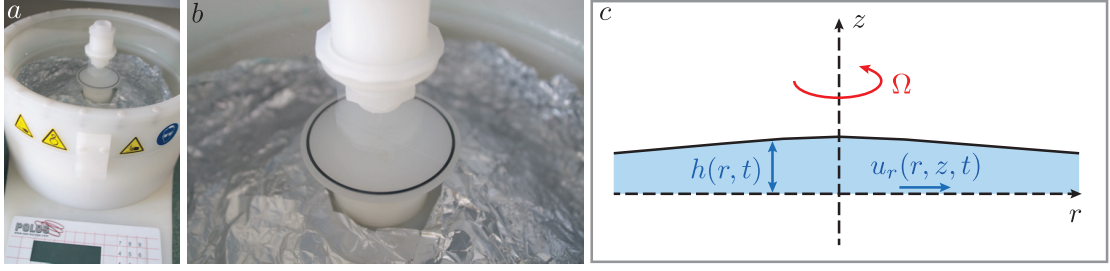


Figure 2.4 – (a) POLOS 300HD spin-coater used in our experiments. (b) Zoom on the chuck; vacuum is used to maintain the glass plate on the chuck when the apparatus is rotating. (c) Schematic diagram showing the notations used in the model.

a radial speed component $u_r(r, z, t)$ and an orthoradial component $u_\theta(r)$ that is equal to the local speed at the surface of the rotating disk $u_\theta(r) = r\Omega$.

Balancing the viscous forces and centrifugal forces per unit volume yields:

$$-\mu \frac{\partial^2 u_r}{\partial z^2} = \rho_l \Omega^2 r$$

This equation is integrated using the following boundary conditions: the radial speed u_r vanishes at the solid interface $z = 0$, and $\partial u_r / \partial z$ vanishes at the free surface $z = h(r, t)$. The radial speed u_r is thus found to be:

$$u_r = r\Omega^2 \frac{\rho_l}{\mu} \left(zh - \frac{z^2}{2} \right)$$

The radial flow per unit circumference is given by:

$$q = \int_0^h v dz = \frac{\rho_l \Omega^2 r h^3}{3\mu}$$

We use the equation of continuity:

$$r \frac{\partial h}{\partial t} = \frac{\partial(rq)}{\partial r},$$

to write the time-evolution of the thickness:

$$\frac{\partial h}{\partial t} = -K \frac{1}{r} \frac{\partial}{\partial r} (r^2 h^3), \text{ with } K = \frac{\rho_l \Omega^2}{3\mu}$$

Without seeking a general solution to this equation, a particular case can be analyzed. By assuming an initially uniform height h_o , and a uniform height $h(t)$ (instead of $h(r, t)$) during the liquid film flattening down, the previous equation yields [123]:

$$\frac{dh}{dt} = -2Kh^3,$$

which means that:

$$h = h_o \left(1 + \frac{t}{\tau} \right)^{-1/2}, \text{ where } \tau = \frac{1}{4Kh_o^2}$$

Two main results are highlighted in this expression: a thick layer thins out more rapidly than a thin one, and with a given initial thickness h_0 the time necessary to reach a thickness h_1 is proportional to $1/\Omega^2$. In a real experimental setup, some assumptions of the above model are not valid, which means that this result should only be considered as an estimate: the liquid layer is not initially flat nor infinite. Depending on the liquid used, some evaporation effects might also have to be taken into account [124].

To make our PDMS thin films, we use a POLOS 300HD spin-coater (Fig. 2.4(a)). A thin liquid PDMS film is spread on a glass plate by spin-coating, before being cured in the oven. The glass plate is fixed on the spin-coater chuck and remains in place with a vacuum pump system that counteracts the centrifugal force applied on the plate (Fig. 2.4(b)). A liquid PDMS mixture droplet is deposited on the middle of the plate, and spreads when the spin-coater rotates.

The initial condition is not exactly a flat layer, but our procedure with the spin-coater comprises two steps: the first step is a speed ramp going from 0 to 500 rotations per minute in 5 seconds followed by a 10 seconds speed plateau at 500 rotations per minute. It allows the liquid to spread on the glass and form a thick layer of nearly uniform thickness. The second step varies depending on the desired thickness, and comprises a speed ramp going from 500 rotations per minute to a final speed Ω_f , and a 40 seconds speed plateau at Ω_f (the higher Ω_f the smaller the resulting thickness). Ω_f is chosen between 1000 and 2000 rotations per minute, to form samples of thicknesses between 33 and 68 micrometers (more details are given in the thickness measurements paragraph), used for our snap-through experiments described in chapter 3.

Automatic film applicator Another possible way of manufacturing thin films of uniform thickness is to use a drawdown bar. A metal bar containing a gap of known clearance is moved at a constant speed and spreads an amount of liquid deposited beforehand in front of the applicator (Fig. 2.5(a)). Provided that the quantity of liquid is sufficient enough, the uniform thickness of the resulting film is determined by three parameters: the height of the gap of the applicator, its speed, and the fluid viscosity.

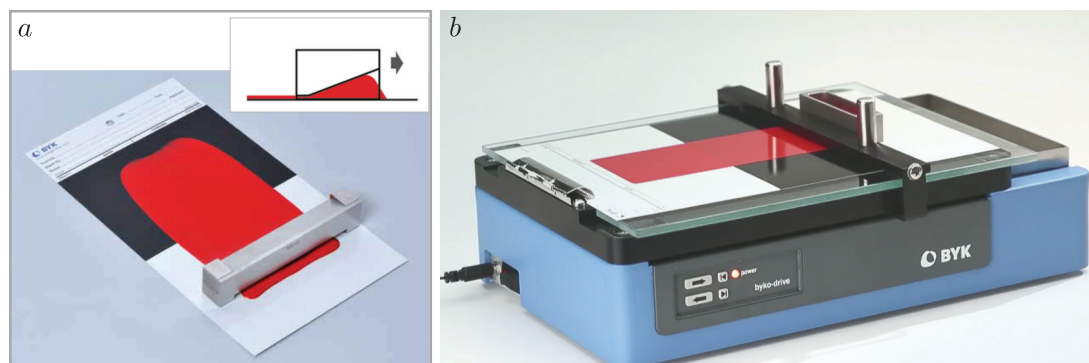


Figure 2.5 – (a) Drawdown bar. (b) Automatic film applicator using a drawdown bar. Both pictures are reproduced from www.byk.com.

This technique allows us to manufacture large polymer sheets on various samples such as glass but also glassy paper cards or flexible plastic sheets, which is not the case for spin-coating. Spin-coating requires to work with a rigid but low weight substrate,

typically a small glass plate, to allow the vacuum pump to counterbalance centrifuge effects so that the samples remain in place. In the drawdown bar method, the size limit is set by the width of the applicator and the length of the substrate on which liquid is spread.

We use a BYK-Gardner Byko-drive applicator to spread liquid elastomer mixtures, before the crosslinking process. In this setup, a vacuum plate is used to securely flatten the drawdown chart, in order to avoid slippage during the application. The automatic applicator moves a drawdown bar at a constant speed, with a better reproducibility of the process than with a bar moved by hand (Fig. 2.5(b)). At a given speed and with a given gap size, the thickness of the films depends on the viscosity of the polymer mixture. The resulting thickness is therefore measured afterwards in our experiments, as for spin-coating manufactured samples. Samples manufactured with this technique are mainly used in the context of preliminary experiments not detailed in this manuscript.

Gravity-driven films Depositing some liquid polymer on top of a vertical plate is a quick method to manufacture a thin plate of nearly homogeneous thickness on the direction perpendicular to gravity, and of varying thickness in the other direction. We use a 15 cm by 10 cm glass plate, and choose to put the longer side perpendicular to gravity to get long strips of nearly constant thicknesses: a 2 mm strip (cut in the direction perpendicular to gravity) has an almost homogeneous thickness, with a thickness difference between the 2 sides of less than a few percents. These samples allow us to cover a wide range of thicknesses with only one plate manufacturing step, and are used only to make preliminary experiments, the thickness of each strip being checked with an optical profilometer.

Cutting samples out of polymer thin films The next step after obtaining a thin elastic film of constant thickness is to cut strips out of it. Two different techniques are used depending on the substrate on which the thin film is manufactured. On a glass substrate (mainly for spin-coated samples), strips are carefully cut out of the polymer plate by hand with a cutter, as it is the case for our snap-through experiments in chapter 3. However, when using a plastic sheet as a substrate (with a drawdown bar), a more sophisticated and more precise cutting technique is used: the substrate and the sample are cut together with a Fiskars rotary paper trimmer. In the latter case, the elastomer sample is took off the substrate after cutting.

2.1.2. Samples characterization: thickness and Young's modulus

a) Thin film thickness measurement

The order of magnitude of a film thickness is known by choosing the spin-coating or drawdown bar parameters, namely the rotation speed for spin-coating and the gap thickness for the drawdown bar technique (when all the other parameters are kept constant). However, the precise thickness needs to be determined for each sample because the viscosity of the liquid mixtures used to manufacture the elastomers changes as function of the temperature and of the time lapse between the preparation of the mixture and its spreading. Different techniques are available for thickness measurements: in the following paragraphs, we describe both optical profilometry and an induction-based technique used in a device sold with our automatic film applicator by BYK.

Optical profilometry An optical profilometer is an apparatus using white light interferometry to measure variations of height within a sample. A light beam is split, and half of the beam is reflected on the sample (Fig. 2.6(a)). When this reflected beam and the split beam (reflected on a reference mirror) are combined again, they form interference fringes provided the optical path in the two beams is almost the same. The idea is to perform a vertical scan to measure a variation of height between one zone of a sample (chosen as a reference) and the other parts of the sample. An optical path difference between the reference zone and the analyzed zone is measured by looking for interference fringes on the first zone and then on the second zone of the sample when moving the sample along the beam axis.

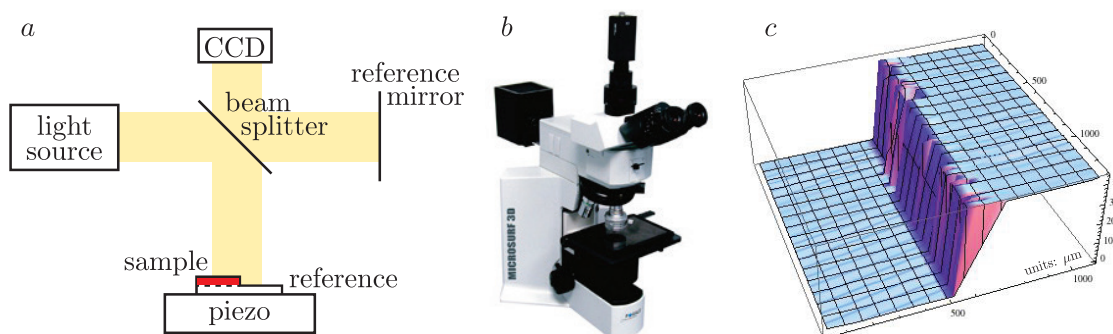


Figure 2.6 – (a) Schematic illustrating the basic principles of an optical profilometer. (b) M3D Fogale Nanotech profilometer (picture from www.fogale-semicon.com). (c) 3D representation of thickness measurements performed for a spin-coated PDMS sample ($\Omega_f=1500$ rpm). The left part is the glass slide (used as a height reference) while the right part is the PDMS sample.

The optical profilometer used to measure the thickness of our samples is a M3D Fogale Nanotech model (Fig. 2.6(b)), with a spatial resolution in the Oxy plane of about $1 \mu\text{m}$ and a vertical resolution of about 10 nm , linked to the specifications of the piezoelectric plate used to move the sample along the vertical axis. Experiments were performed at Laboratoire Jean Perrin, UPMC, and we are grateful to Alexis Prevost and Georges Debréguas for their help with this apparatus. To measure the thickness of a PDMS film spin-coated on a glass plate, the film is left on the glass substrate, and a small part of the PDMS film is cut. We thus obtain a sample where one part is made of a PDMS layer above a glass layer, and the other part comprises only the glass layer. This latter part is used as a reference to measure the thickness difference between this point on the glass surface and points on the PDMS film (Fig. 2.6(a)). An example of the thickness profile obtained for one of our PDMS samples is shown in Fig. 2.6(c). The left part is the glass slide on which the PDMS was spin-coated, and the right part is the PDMS film above the glass slide. The irregularities of the ridge are due to the fact that the sample was cut by hand with a cutter. A summary of the experimental results for spin-coated samples used in chapter 3 is shown in Table 2.2. For each individual sample the thickness needs to be checked as it depends on the experimental conditions (temperature, time between the preparation of the mixture and the spin-coating step).

Induction-based device The thickness of a thin film can also be measured by using a device sold by drawdown bar manufacturers. With an elastomer, this technique has a

Ω_f (rotations per minute)	Measured thickness (μm)
2000	33.7 ± 0.5
1500	43.0 ± 0.5
1000	68.3 ± 0.5

Table 2.2 – Thickness of the elastomer samples manufactured by spin-coating for various final rotation speeds Ω_f , measured with a M3D Fogale Nanotech optical profilometer. These samples are the one used in the elastocapillary snap-through study presented in chapter 3. The error bars quantify the deviation from a flat substrate: precision is not limited by the profilometer vertical resolution.

much lower precision than optical profilometry, but is useful for quick estimates.

The idea is to work with a device capable of measuring its own distance to a metallic plate. The Byko-test 8500 Fe/NFe model sold by BYK (Fig. 2.7) exploits induction phenomena to measure the distance between the sensor and a ferromagnetic (Fe) or non-ferromagnetic (NFe) plate. The thickness measurement of a polymer thin film is performed by placing this sample between the sensor and the metallic plate. In fact, the polymer samples consist of two layers: the thin polymer film and the card or plastic sheet on which the film was deposited. The measurement of the total thickness and of the thickness of the card or plastic sheet alone yields the value of the polymer film thickness. However, the main issue when measuring the thickness of an elastomer sample is to use the sensor tip without indenting the elastomer, at the risk of underestimating the film thickness: the typical precision for a $100 \mu\text{m}$ PDMS or Zhermack Elite Double film is around $\pm 2 \mu\text{m}$, determined by performing several measurements during which we tried to exert no indenting force while staying in contact with the sample.

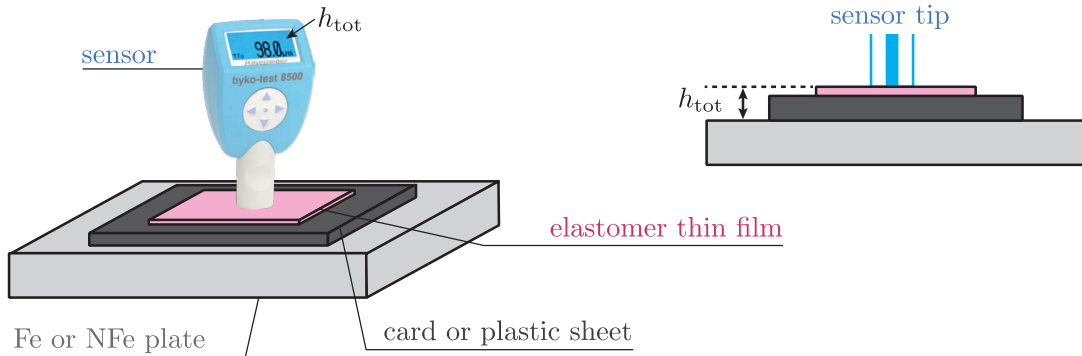


Figure 2.7 – Configuration used for measurements with a BYK Byko-test sensor. Sensor picture reproduced from the user manual, available on www.byk.com.

The plate choice (Fe or NFe) depends on the thin film properties: a Fe plate is used only for non-magnetic thin films, while a NFe plate is used only with insulating films. In the case of a ferromagnetic mount, the measurement is done by evaluating the change in magnetic field emitted by a coil due to the presence of a ferromagnetic plate. The modification of the field is related to the distance between the probe and the plate: an appropriate calibration allows us to measure the sample thickness. For a

non-ferromagnetic plate, the method is quite similar and is based on the modification of a magnetic field by Eddy-current induced in the plate, which are created by the applied magnetic field but also affect it in return. This feedback depends on the distance between the probe and the plate. In our experiments, we use an aluminium (NFe) plate, but both Fe and NFe techniques could be used for silicone elastomers. However, this device is only used in the context of preliminary experiments.

b) Young's modulus measurement techniques

Testing machine A usual technique to measure the Young's modulus of a material is to perform a tensile test; the Young's modulus is determined as the slope of the stress-strain curve in the linear regime. For our experiments, we measure the Young's moduli of dogbone-shape samples (Fig. 2.8(b) and (c)) with a Shimadzu testing machine (Fig. 2.8(a)).

The Young's modulus is deduced from the stress-strain curve by using Hooke's law (see chapter 1), valid only for small $(L - L_o)/L_o$:

$$\frac{F}{S_o} = E \frac{L - L_o}{L_o}$$

where F is the measured force, S_o the initial cross-section of the sample, L the length of the sample, and L_o the initial length of the sample. $(L - L_o)/L_o$ is kept under 10% in our experiments. We show a stress-strain curve for a Dow Corning Sylgard 184 PDMS sample in Fig. 2.8(d), and the results of our measurements for different materials are brought together in Table 2.3.

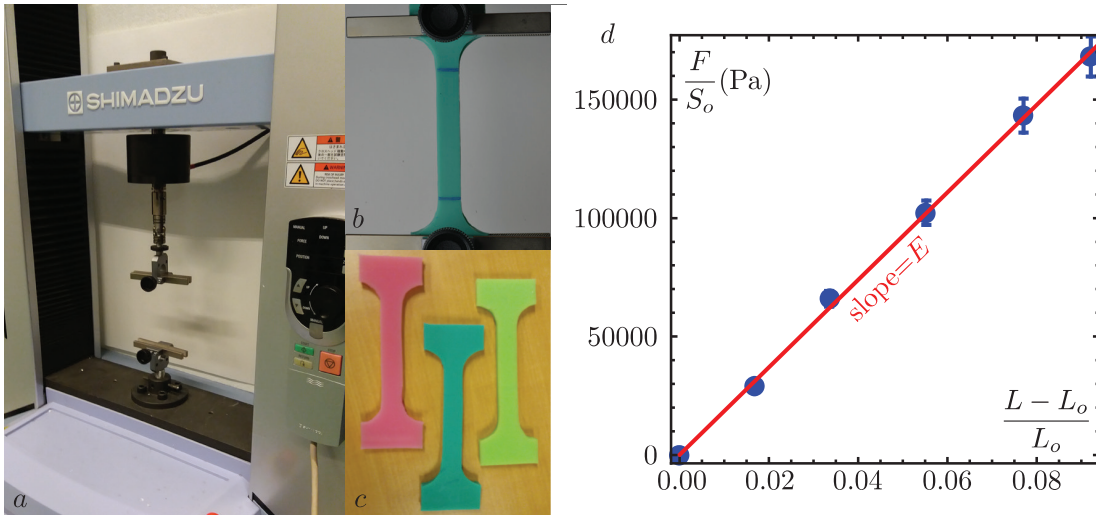


Figure 2.8 – (a) Shimadzu tensile test machine. (b) Dogbone sample clamped at both ends. (c) Dogbones made of Zhermack Elite Double 8, Elite Double 22 and Elite Double 32 dental polymers. Different hardnesses correspond to different colors to easily link the color of an object to its elastic properties. (d) Stress-strain curve for a PDMS Dow Corning Sylgard 184 sample of thickness 5.05 mm and width 1.15 cm (dimensions of the middle part of the dogbone).

Elastomer	Measured Young's modulus
Dow Corning Sylgard 184 PDMS	1.84 ± 0.10 MPa
Elite Double 8 Zhermack	240 ± 15 kPa
Elite Double 22 Zhermack	900 ± 50 kPa
Elite Double 32 Zhermack	1.23 ± 0.10 MPa
RTV EC13 Esprit Composite*	330 ± 20 kPa
RTV EC33 Esprit Composite*	1.05 ± 0.10 MPa

Table 2.3 – Young's moduli of different elastomers measured with a tensile test on dogbone shape samples. *Despite degassing in a vacuum chamber, some bubbles are clearly visible in our EC13 and EC33 dogbones. This implies a possible modification of the Young's modulus.

Vibration-based technique for slender strips When using slender elastic objects such as elastomer strips, a convenient technique to measure directly the product EI is to record vibrations of the strip clamped at one end (Fig. 2.9). This technique is also a good way to check if the Young's modulus varies as a function of the thickness of the material (as suggested in [125] and discussed in the following paragraphs), by performing measurements for very thin samples. Indeed, a tensile test proves to be difficult when the samples are too thin.

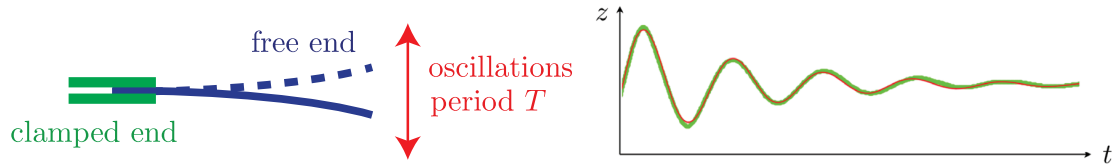


Figure 2.9 – Vibration-based Young's modulus measurement: the response of a strip clamped at one end to an impulse excitation is recorded and analyzed.

For a strip of rectangular cross-section $A = hw$, where h is the thickness of the sample (dimension perpendicular to the clamp) and w its width, the second moment of area of the cross-section I is given by $I = h^3w/12$. Considering a strip of length L and density ρ_e , the movement period, as derived in chapter 1, yields [11]:

$$T = 1.78L^2\sqrt{\frac{\rho_e A}{EI}} = 1.78L^2\sqrt{\frac{12\rho_e}{Eh^2}}$$

The motion of the strip after an impulse excitation at the tip is recorded with a fast camera and analyzed with ImageJ; results for samples of thicknesses ranging from $37 \mu\text{m}$ to $380 \mu\text{m}$ are shown in Fig. 2.10. The uncertainties taken into account in the error bars are dominated by the uncertainties on h for the vertical axis, and on L for the horizontal axis.

The linearity of the graph in Fig. 2.10 proves that the Young's modulus in our samples does not vary significantly as a function of the thickness h . In addition, we verified that

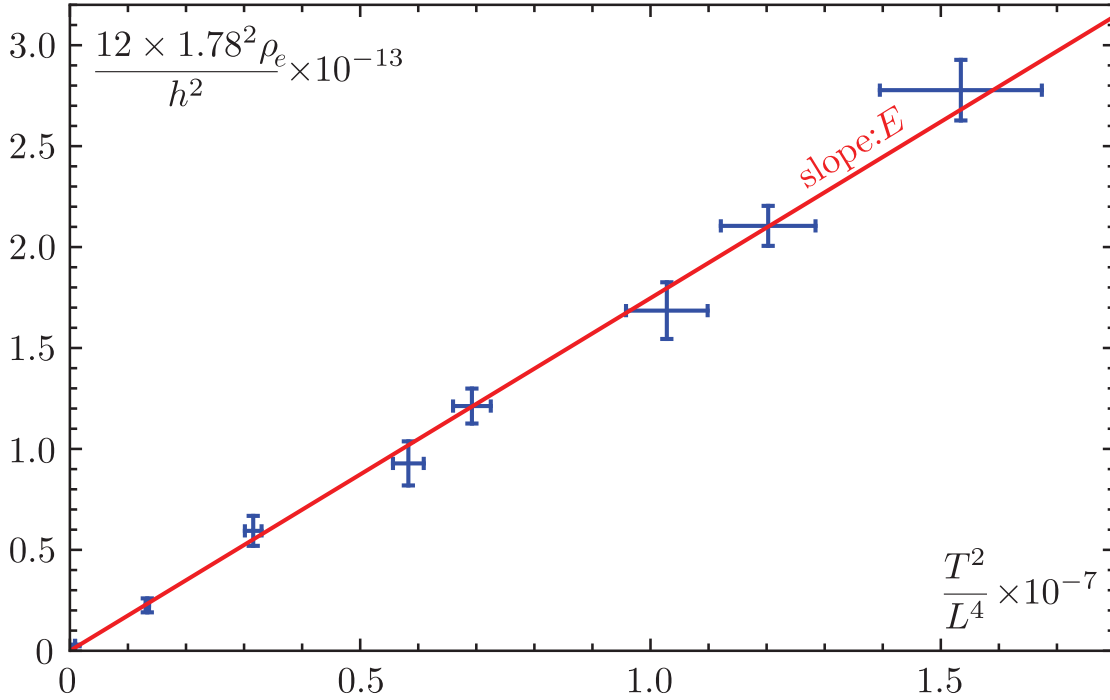


Figure 2.10 – Results of our vibration-based Young’s modulus measurement for Dow Corning Sylgard 184 PDMS samples. The Young’s modulus is given by the slope of the red fit, and is found to be 1.75 ± 0.10 MPa.

changing the length of a strip of fixed thickness (and thus the frequency of the vibrations) does not affect significantly the result in terms of Young’s modulus over the range of vibrations frequencies reached in the set of experiments presented in Fig. 2.10.

The independence of the Young’s modulus as a function of the thickness of thin PDMS plates observed here is in contradiction with what was found for the same range of thicknesses in [125], reproduced in Fig. 2.11. However, the difference between our results and the measurements performed in [125] might be explained by small differences in the protocol used to prepare the samples. Especially, the exact reference of the Dow Corning PDMS used is not specified in [125] and is certainly different from the Sylgard 184 PDMS used to carry out our experiments.

The Young’s modulus of our PDMS, constant as a function of the samples thickness, corresponds to the slope of the graph in Fig. 2.10 and is found to be 1.75 ± 0.10 MPa. This value is in good agreement with tensile tests measurements ($E_{\text{tensile test}} = 1.84 \pm 0.10$ MPa). However, a silicone elastomer is not purely elastic: experiments with such elastomers usually involve a loss of energy by viscous dissipation inside the material. This is suggested by the damping of the oscillations in Fig. 2.9, and will be discussed in chapter 3.

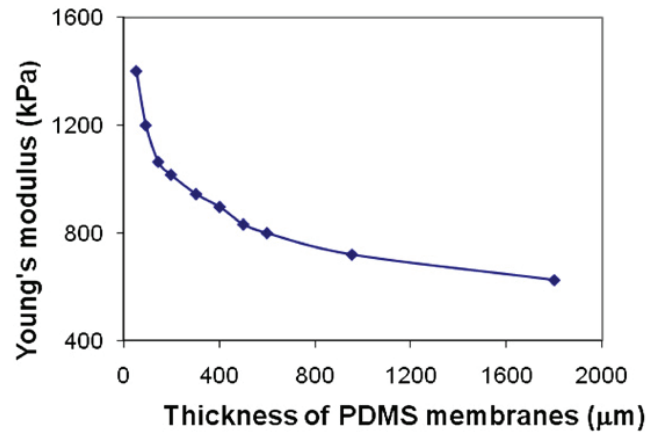


Figure 2.11 – Dependence of the Young’s modulus in the thickness of PDMS membranes, reproduced from [125]. The results for our PDMS strips are not in good agreement with this graph, as we record no significant dependence of Young’s modulus in the thickness of our samples ($E = 1.75 \pm 0.10$ MPa). The thickness of our samples range from $37 \mu\text{m}$ to $380 \mu\text{m}$, where this graph highlights a huge Young’s modulus variation. However, the PDMS used in these experiments is certainly a different reference from Dow Corning from the one we are using, as shown by the discrepancy between the Young’s moduli found there and our constant result, $E = 1.75 \pm 0.10$ MPa.

2.2 Microforce sensors

Snap-through experiments with polymer samples typically involve forces of a few micronewtons. To be able to measure such forces, we use capacitive deflection measurement force sensors from Femtotools Swiss high-tech company. These devices are capable of measuring forces from millinewtons down to several nanonewtons: the sensor comb-like configuration is described in [126], where it is used to characterize fruit-fly flight behavior (Fig. 2.12(b)).

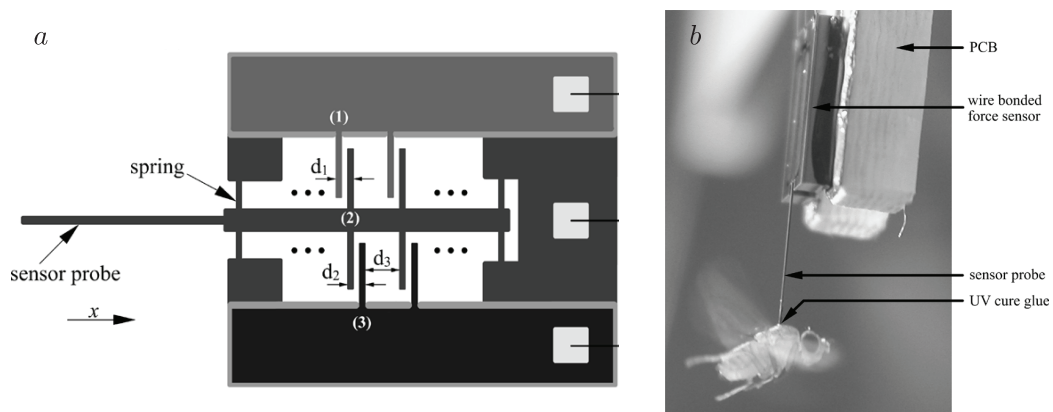


Figure 2.12 – (a) Femtotools capacitive measurement sensor: the distance between two comb sets is changed when stretching or compressing the sensor probe, resulting in a capacitance change. (b) Flight force sensing of a fruit-fly. Both pictures are reproduced from [126].

The basic idea behind this uniquely sensitive device is to measure the force applied on the sensor tip by measuring the displacement of a movable comb set in comparison to a stationary comb set. The tip and the movable comb system are interdependent, and held with springs (Fig. 2.12(a)). When the tip is stretched or compressed, the movable comb system is displaced and this change in distance between the two comb sets results in a capacitance change. A calibration of the capacitance as a function of the applied force is performed by Femtotools for each sensor individually. The outside geometry of a FT-S100 sensor is shown in Fig. 2.13: the part of the tip that is effectively in contact with a substrate for indentation experiments is a square with $50\ \mu\text{m}$ sides, allowing for local force measurements.

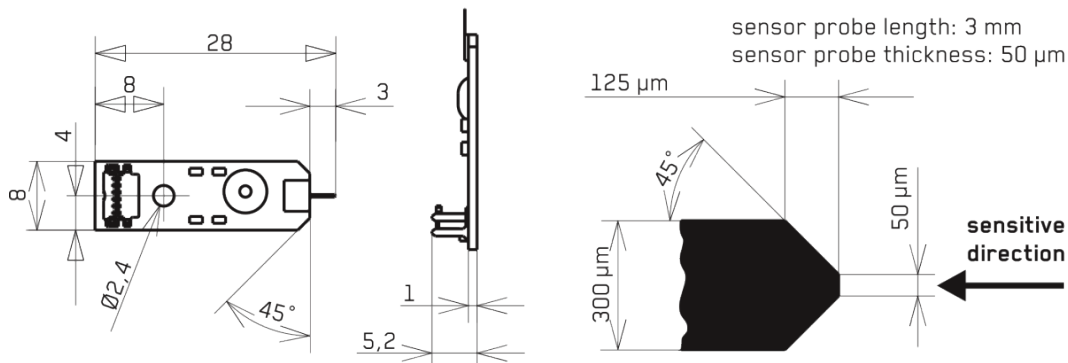


Figure 2.13 – Sensor geometry, reproduced from FT-S100 Microforce Sensing Probe manual, from www.femtotools.com.

Different sensing probes with different sensitivities are available to comply with the force ranges and resolutions required for various experiments:

- A FT-S270 sensor (discontinued by Femtotools) is used in our snap-through experiments (chapter 3): the FT-S270 force range is $\pm 2000\ \mu\text{N}$ and its sensitivity at 10 Hz is $0.4\ \mu\text{N}$.
- A FT-S100 sensor is used to perform surface tension measurements (chapter 5): the FT-S100 force range is $\pm 100\ \mu\text{N}$ and its sensitivity at 10 Hz is $0.005\ \mu\text{N}$. The sensor tip can be used in contact with a liquid but is very fragile and requires cautious manipulation.

Measurements can be carried out with a frequency range going from 10 Hz to 1000 Hz, which is faster than the required specifications both for our indentation measurements (performed in static configurations) and for our surface tension measurements (performed at a speed controlled by the user to be slow enough for the sensor to be used in proper conditions).

2.3 Liquids employed in our elastocapillary experiments

We describe here the selection and characterization of the liquids used in our experiments. The first step is to choose a liquid that does not swell the employed elastomer: this choice is made by using swelling parameters tables found in the literature. We then

give details on surface tension and viscosity measurement techniques, with an emphasis on a surface tension measurement technique used to determine the liquid-air surface tension of a single millimetric droplet. We also investigate the different ways to easily and reproducibly deposit a droplet on a substrate, and finally describe ellipsometry techniques to characterize an overlay of different liquids.

2.3.1. Basic requirements for liquids used in contact with silicone elastomers

Some experiments involve swelling of an elastomer by a solvent, see [127] and Fig. 2.14: a PDMS elastomer sample is deformed when a droplet of silicone oil is deposited on the sample. However, in our elastocapillarity experiments such as elastocapillary snap-through or droplets dynamics on elastomers, swelling needs to be avoided: we look at the interaction between a droplet and an elastomer induced by capillary forces, not by swelling phenomena.



Figure 2.14 – Bending and twisting of a soft material (PDMS) due to non-homogenous swelling with silicone oil, adapted from [127]. Swelling is to be avoided in the context of our studies.

Avoiding swelling begins by choosing a good liquid-elastomer couple for our experiments. This choice is guided by tables in the literature giving the swelling ratio for PDMS in different solvents [128], reproduced in Table 2.4 for the liquids of interest in our study. The swelling ratio is defined as $S = D/D_o$, where D is the length of an elastomer sample when it is completely immersed in the solvent (at a swelling equilibrium) and D_o is the length of the dry elastomer sample.

Solvent	Swelling ratio S
water	1.00
glycerol	1.00
ethylene glycol	1.00
ethanol	1.04
acetone	1.06
toluene	1.31
chloroform	1.39
PDMS oil	∞^*

Table 2.4 – Swelling parameter S for various solvents, reported from [128]. The swelling ratio is defined as $S = D/D_o$, where D is the length of a Dow Corning Sylgard 184 PDMS sample in the solvent and D_o is the length of the dry PDMS. * Swelling of PDMS oil in PDMS crosslinked samples is in fact not infinite due to the existence of a maximal extension for the crosslinked network.

Water and glycerol are two liquids for which the PDMS swelling parameter is 1.00, which means that they do not swell PDMS at all. Moreover, a wide viscosity range

can be reached by using water-glycerol mixtures. The surface tension of water-glycerol mixtures is ranging from 64 mN.m^{-1} to 72 mN.m^{-1} at room temperature, which makes such liquids good candidates for our elastocapillary experiments. We choose to work with water-glycerol mixtures ranging from 0% to 85% of glycerol: we avoid glycerol fractions larger than 85% because pure glycerol is highly hygroscopic and its viscosity is likely to decrease due to small amounts of absorbed water.

2.3.2. Viscosity and surface tension measurements

a) Viscosity measurements

Viscosity measurements for our water-glycerol mixtures are performed with a KF10 Brookfield falling-ball viscosimeter. The dynamic viscosity of the liquid is determined by measuring the falling time of a ball between the upper and lower ring marks displayed on the falling tube; several balls of different diameters and densities are available to carry out experiments within a wide range of viscosities. The setup also includes a thermostatically controlled water bath around the falling ball tube, to perform viscosity measurements at various temperatures. The viscosity of our water-glycerol mixtures is measured at several temperatures in the range of temperatures reached in the room during the experiments (varying between 19° and 27°). For each experiment, the temperature in the room is measured and the mixture viscosity is extrapolated from the values measured at different temperatures with the viscosimeter. Densities are measured with an oscillating U-tube densimeter, and results for the viscosities and densities of our water-glycerol mixtures are shown in Table 2.5.

Glycerol	Water	$T(^{\circ}\text{C})$	$\rho_l \text{ (kg.m}^{-3}\text{)}$	$\mu \text{ (mPa.s)}$
50%	50%	19.3 ± 1.0	1124 ± 1	6.2 ± 0.2
60%	40%	25.3 ± 1.0	1150 ± 1	8.7 ± 0.2
65%	35%	27.0 ± 1.0	1164 ± 1	11.1 ± 0.2
75%	25%	20.7 ± 1.0	1192 ± 1	34.1 ± 0.5
85%	15%	27.5 ± 1.0	1219 ± 1	68.1 ± 1.0

Table 2.5 – Mixing ratios, temperature T during the experiments, density ρ_l measured with an oscillating U-tube densimeter, and viscosity μ deduced from measurements with a KF10 Brookfield falling ball viscosimeter, for the different mixtures used. The uncertainty on the viscosity values mainly comes from the uncertainty on the temperature: during one set of experiments, the temperature evolves within a 1 or 2 Celsius degrees range.

b) Surface tension measurements

Surface tension of a large liquid bath The surface tension of our water-glycerol mixtures is measured in our experiments with a Krüss K6 manual tensiometer (Fig. 2.15(a)). In this tensiometer, a torsion wire is connected to a measuring ring. To perform a measurement, the ring is first immersed and then quasi-statically withdrawn from the bath: the liquid is lowered and the force applied by the torsion wire is raised at the same time, in order for the apparatus arm to be always horizontal. The surface tension is read on a calibrated scale when the ring detaches from the liquid bath (some calibration weights are used to adjust the torsion of the wire).

This method is called Du Nouy ring: a schematic diagram of the forces involved on the ring is shown in Fig. 2.15(b), reproduced from www.kruss.de. The results of the surface tension measurements for our water-glycerol mixtures are shown in Table 2.6.

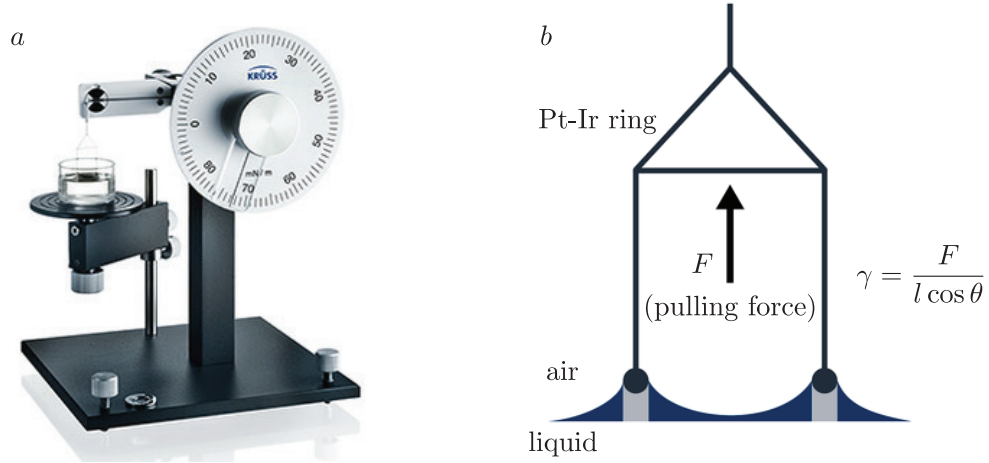


Figure 2.15 – (a) Krüss K6 tensiometer. (b) Schematic diagram of the Du Nouy ring method. Both pictures are reproduced from www.kruss.de.

Glycerol	Water	γ (mN.m ⁻¹)
50%	50%	69.0 ± 0.5
60%	40%	68.4 ± 0.5
65%	35%	67.9 ± 0.5
75%	25%	67.1 ± 0.5
85%	15%	66.5 ± 0.5

Table 2.6 – Surface tension γ of the liquid-air interface measured with a Krüss K6 manual tensiometer for the different mixtures used.

The material used to build the ring is platinum-iridium. This alloy generally forms a contact angle $\theta = 0^\circ$ with liquids, and is easy to clean. However, this apparatus requires to work with a liquid bath of at least 4 cm diameter so that the centimeter-sized ring can be immersed in the bath without being disturbed by the meniscus developing at the wall of the container. This measurement requires that a sufficient quantity of liquid is available. Techniques to measure the surface tension of one single millimetric droplet are described in the following paragraph.

Surface tension of a single millimetric droplet A smaller probe than the Krüss K6 ring is needed to measure the surface tension inside a single millimetric droplet lying on a substrate, as it is the case in the experiments described in chapter 5. The forces involved in the system are proportional to the perimeter of the probe: working with a smaller probe also means working with a more sensitive device.

The Kibron EZ-Pi⁺ tensiometer (Fig. 2.16(a)) allows us to work with small probes (0.5 mm diameter cylinders) that can easily be immersed in a millimetric droplet. The

measurement is performed using an ultrasensitive microbalance embedded inside the tensiometer, and the inert metal probe is cleaned before each measurement with a butane torch. With liquid baths, this technique gives the same kind of results as a manual tensiometer, with a better resolution. In the scope of our experiments, the main advantage of this apparatus is to enable us to work with tiny samples including millimetric droplets.

However, in the case of small droplets, a correction is needed because of the Laplace pressure inside the drop: the difference between the surface tension measured in a droplet and the surface tension of an infinite bath of the same liquid evolves as a function of the radius of curvature at the top of the drop, as shown in Fig. 2.16. The total force exerted on the probe is the sum of the surface tension force and of a Laplace pressure term acting on the lower surface of the probe. Denoting R_{curv} the radius of curvature of the droplet at the top, a the radius of the section of the cylindrical probe, γ_{real} the real surface tension of the liquid, the total force acting on the probe reads:

$$F = 2\pi a\gamma_{\text{real}} - \pi a^2 \frac{2\gamma_{\text{real}}}{R_{\text{curv}}}$$

Thus the measured surface tension γ_{measured} is given by the following relation:

$$2\pi a\gamma_{\text{measured}} = 2\pi a\gamma_{\text{real}} - \pi a^2 \frac{2\gamma_{\text{real}}}{R_{\text{curv}}}$$

The normalized difference between the surface tension measured for a droplet and the surface tension of an infinite liquid bath reads:

$$\frac{\gamma_{\text{measured}} - \gamma_{\text{real}}}{\gamma_{\text{real}}} = \frac{a}{R_{\text{curv}}}$$

We deposit a water droplet of given volume on a polystyrene Petri dish (on which contact angles of a water droplet are similar to that on PDMS), and first measure the curvature at the top of the droplet. We then measure the surface tension of this droplet with a Kibron EZ-Pi+ tensiometer, and calculate the normalized difference between the surface tension measured for the droplet and the surface tension of an infinite water bath. The experiment is repeated for various droplet sizes, and results are displayed in Fig. 2.16(b).

The results shown in Fig. 2.16(b) are in good agreement with the expression calculated for the normalized difference between the surface tension measured for a droplet and the surface tension of an infinite liquid bath. The red line is a linear fit estimating the value of a to be $198 \mu\text{m}$, to be compared to $250 \mu\text{m}$ which is the value given by the supplier for the radius of the probe (checked by measuring the probe with a Leica microscope: its radius is found to be $248 \pm 5 \mu\text{m}$). The uncertainties on the surface tension measurements shown on the error bars of Fig. 2.16(b) can explain the discrepancy between the result of the fit and the real probe diameter. A calibration of the sensor is needed every 5 to 10 measurements, which leads to an additional source of uncertainty for our measurements, taken into account in the error bars. The calibration performed here is used in chapter 5 to calculate the Laplace pressure corrective term in the case of droplets with a small radius of curvature. The real surface tension of these droplets is then deduced from the measured surface tension.

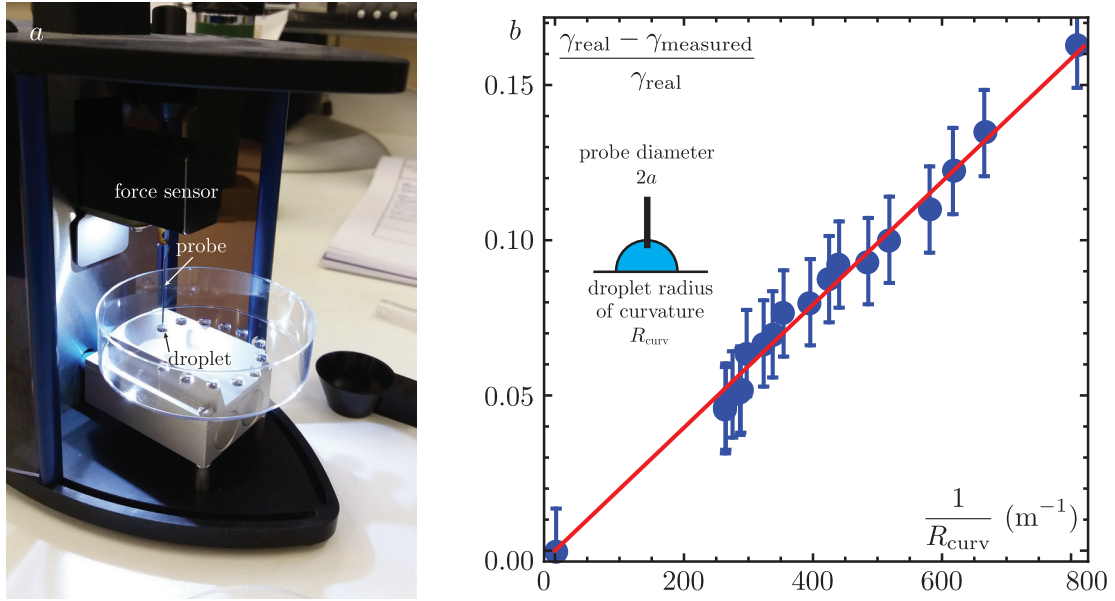


Figure 2.16 – (a) Kibron EZ-Pi⁺ tensiometer. (b) Normalized difference between the measured surface tension for a droplet and the surface tension of an infinite liquid bath, plotted as a function of the inverse of the radius of curvature at the top of the drop (measured with ImageJ).

Surface tension measurements as a function of time The Kibron EZ-Pi+ tensiometer also enables us to perform surface tension measurements as a function of time. In the temporal acquisition mode, the probe is positioned precisely at the liquid-air interface and the force exerted on it by the liquid is monitored with time while the rod remains static; surface tension measurements are automatically performed by the tensiometer software. This surface tension acquisition mode is used for experiments presented in chapter 5 on cloaking dynamics of a water droplet by PDMS oil.

Hanging droplet measurements Another way of measuring the surface tension of a droplet is to hang it from a capillary tube. This method is inappropriate for experiments in which a droplet needs to be in contact with a substrate, or for experiments in which a thin film at the water-air interface can be broken by manipulating the droplet, as it is the case in experiments described in chapters 4 and 5. However, in usual cases, it proves to be an interesting technique to measure the surface tension of liquids available only in small quantities: the shape of a droplet hanging from a capillary tube only depends on the Bond number $Bo = \rho_l g V^{2/3} / \gamma$, where ρ_l is the density of the liquid, V the volume of the droplet, and γ the liquid-air surface tension. The shape of the hanging droplet is fitted to extract the value of the Bond number and thus the value of the surface tension.

A simpler way of estimating the surface tension of a liquid is just to make a droplet fall from a capillary tube and weight this droplet (or make one hundred droplets fall from the capillary tube and weight the obtained liquid bath). This technique was first introduced by Tate in 1864 [129]: at the detachment, the gravitational force pulling the droplet down is equal to the surface tension force holding the drop pendant. For a capillary tube of radius R , an approximate force balance is thus given by what is known as Tate's law:

$$\rho_l V g = 2\pi R \gamma$$

However, in this expression, V is only an estimate, because the volume of the detached droplet is always smaller than the total volume that was held pendant by capillary forces. The normalized difference between the detached volume and the total volume changes as a function of the capillary diameter, as described in details in [130] and [131].

2.3.3. Droplet deposition techniques

a) Droplet falling from a capillary tube

The falling drop technique mentioned in the above paragraph also constitutes a good way of producing droplets of given volume (provided that they are delivered quasi-statically). Volumes of water droplets falling from metal capillary tubes of various diameters are summarized in Table 2.7. A syringe pump is easily connected to a capillary tube in order to produce thousands of droplets all of the same size: such an automated experimental setup is used in chapter 4 to collect thousands droplets after their descent on an elastomer inclined plane.

Tip color	Inner diameter (μm)	Outer diameter (μm)	Water droplet size (μL)
olive	1600	1830	32.9
amber	1370	1650	30.3
green	840	1270	20.1
pink	610	910	15.8
blue	410	710	12.9
orange	330	640	11.2
red	250	510	9.7
clear	200	410	7.9
lavender	152	300	5.6
yellow	102	230	5.0
green	80	210	4.0

Table 2.7 – Size of a water droplet falling from a Techcon dispensing tip (metal capillary tube) for different dispensing tip sizes, at room temperature. The measurement is performed by using a scale to weight 100 droplets, and the droplets are delivered quasi-statically.

Although it is a convenient way to produce droplets of controlled size, this technique does not allow to gently deposit a droplet on a substrate with zero initial speed.

b) Hamilton syringe

For snap-through experiments described in chapter 3, a Hamilton syringe is used to deposit droplets on a buckled elastic strip. With this technique, we can gently deposit small droplets, but the accuracy on the deposited volume is limited. In cases where the volume is a crucial parameter, the projected area on a side picture is measured and this parameter (that is linked to the droplet volume) is used instead of the volume read on the syringe.

c) Electronic micropipette

A much easier way to gently deposit droplets of controlled size is to use an electronic micropipette. For the experiments described in chapters 4 and 5, we use a Sartorius eLINE Electronic Pipette able to deliver volumes from 5 to 120 μL , with a systematic error of 2.5% and a random error of 1% for a 12 μL droplet. This micropipette can be used to perform multiple deliveries (for instance, up to 10 droplets of 12 μL volume with only one aspiration step of 120 μL), which turns out to be convenient for our droplets dynamics experiments. The hydrophobicity of the dispensing cones and the choice of the lower dispensing speed are two parameters that help the delivery of a droplet on a substrate with a zero initial speed.

2.3.4. Ellipsometric characterization of an overlay of different liquids

Ellipsometry is a technique based on light polarization used to characterize a thin layer of liquid on another (immiscible) liquid. We use this characterization method in chapter 5 in the context of preliminary experiments, and present here only the basis of this experimental technique.

a) Polarization

The electric and magnetic fields \vec{E} and \vec{B} in electromagnetic plane waves are transverse to the direction of propagation: these vectors are contained in the plane (Oxy) perpendicular to the direction of propagation z . Polarization refers to the time-evolution of the electric field: in the case of an elliptical polarization, the electric field is written as:

$$\vec{E} = a_x \cos(\omega t + \phi_1) \vec{u}_x + a_y \cos(\omega t + \phi_2) \vec{u}_y$$

When electromagnetic waves interact with matter, the two components of the polarization a_x and a_y on the two axes x and y are not necessarily modified the same way [132]. In the following paragraph, we illustrate this phenomenon on the classical example of the Brewster angle.

b) Brewster angle

We consider the case of a wave propagating in a medium of refractive index n_1 , reflecting on a planar interface with a medium of refractive index n_2 . Instead of denoting x and y the two axes necessary to describe the polarization state, the two components are often referred to as p polarization (parallel to the plane of incidence) and s polarization (perpendicular to the plane of incidence), \vec{E} is thus written as $\vec{E} = \vec{E}_s + \vec{E}_p$.

These two polarization components are modified in a different way by the reflection on the plane. There exist one angle of incidence, called Brewster's angle, for which the reflected light is completely polarized in the direction perpendicular to the plane of incidence: after the reflection, $\vec{E} = \vec{E}_s$, and $\vec{E}_p = 0$ (Fig. 2.17).

At this particular angle, the direction of propagation of the refracted light in the medium of refractive index n_2 is perpendicular to the direction of propagation of the reflected light in the medium of refractive index n_1 . When excited by the refracted p -polarization, the electric dipoles in the medium of refractive index n_2 do not emit any wave in the direction of excitation. As a result, there is no reflected light parallel to the

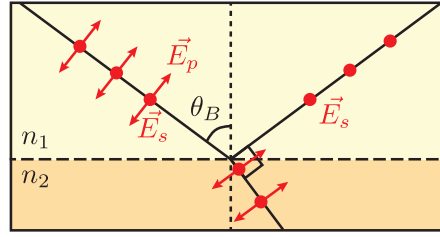


Figure 2.17 – Polarization of light in the case of a reflection at the interface between two materials of different refractive index, at the Brewster angle.

plane of incidence for an angle of incidence θ_1 such as $\theta_1 + \theta_2 = 90^\circ$, where θ_2 is the refraction angle. According to Snell-Descartes law, $n_1 \sin \theta_1 = n_2 \sin \theta_2$. At Brewster's angle, $n_1 \sin \theta_B = n_2 \sin (90^\circ - \theta_B) = n_2 \cos \theta_B$. Brewster's angle is thus defined by:

$$\theta_B = \arctan \frac{n_2}{n_1}$$

This configuration is an example illustrating that the p -polarization and s -polarization are not modified the same way by a reflection at an interface. Therefore, the analysis of the reflected light gives information on the surface on which the light is reflected: the corresponding measurement technique is called reflection ellipsometry.

c) Ellipsometry

Generally speaking, ellipsometry is the measurement of the polarized state of an electromagnetic wave. We focus here on reflection ellipsometry which consists in analyzing the change in polarization of light after reflection of a sample. The sample can consist in one single medium, but more interestingly, it can be formed by different layers of different refractive index.

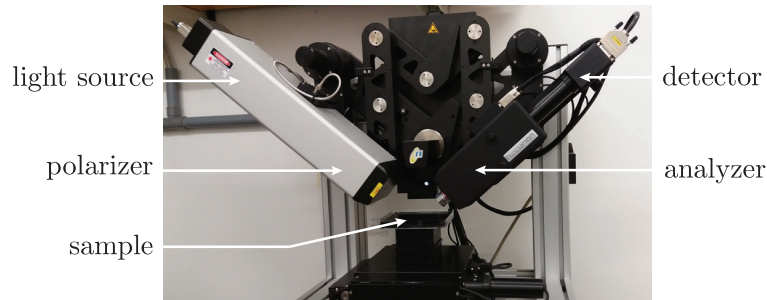


Figure 2.18 – Ellipsometer: the polarization of the reflected light is studied as a function of the polarization of the incident light, for different wavelengths and angles of incidence.

The modification of the polarization is described by two parameters [133]:

- one amplitude ratio Ψ , defined as $\tan \Psi = |R^p| / |R^s|$, where R^p and R^s are the reflection coefficients in amplitude, for the p -polarization and s -polarization respectively.

- one phase difference Δ between the incident and reflected light.

The values of these two parameters depend on the material on which light is reflected, on the wavelength of the incident light, and of the angle of incidence (AOI). A commercial ellipsometer (Fig. 2.18) is an apparatus measuring the two parameters Δ and Ψ for various wavelengths and angles of incidence. A fit of the unknown parameters (for instance the thickness of a layer, or the refractive index of this layer) is then performed by the ellipsometer software, following a model.

2.4 High speed acquisition

2.4.1. Fast cameras

Studying the dynamics of elastocapillary phenomena implies to be able to capture fast events. In terms of imaging, the elastocapillary snap-through experiment (chapter 3) and the study of droplets dynamics on elastomers (chapters 4 and 5) are performed with video acquisition at speeds from ten to several thousands frames per second.

Video acquisitions above one thousand frames per second (for the study of the snap-through dynamics presented in chapter 3) are performed with a Photron SA5 high speed camera. The resolution of this camera is 1024×1024 pixels up to 7000 frames per second. Videos are usually recorded at 2000 frames per second.

Droplets dynamics on elastomers experiments, presented in chapters 4 and 5, do not require to be recorded at such fast speeds. A better resolution is achieved by using a Hamamatsu Orca Flash camera, with a 2048×2048 pixels sensor. In this case, videos are recorded with frame rates ranging from 10 to 1000 frames per second.

2.4.2. Lighting techniques

High speed acquisition implies to use an appropriate lighting; it is even the case for medium speed acquisition as soon as the flickering frequency of usual lamps is reached. In addition, working with droplets (which are transparent, but act as lenses for the incoming light) requires to finely tune the experimental setup. Performing acquisitions with a good contrast allows us to keep the post-processing step as simple as possible.



Figure 2.19 – Droplet moving down on a vertical strip (gravity is pointing towards the right in the two pictures). (a) Side view with a white and localized background, so that the droplet appears black. (b) Front view with a black and localized background with light coming sideways, so that the droplet appears white.

For the droplets dynamics experiments described in chapters 4 and 5, we work with a white LED backlight placed behind our setup, with some masks around the useful zone, so that the droplet appears black and the background white. The position of the masks on the backlight are fine-tuned so that a maximum area of the droplet appears

black and the white zone inside the droplet is reduced to the image of the backlight by the droplet acting as a lens (Fig. 2.19(a)). Another technique, shown in Fig. 2.19(b), consists in having a small dark background behind the droplet with light coming from a large backlight positioned behind this localized dark background. Thus, the image of the background by the droplet acting as a lens is almost everywhere white, with a tiny black strip in the middle of the droplet. The background appears black and the droplet white. A good lighting allows an easier detection of the droplet for experimental data post-processing.

Conclusion

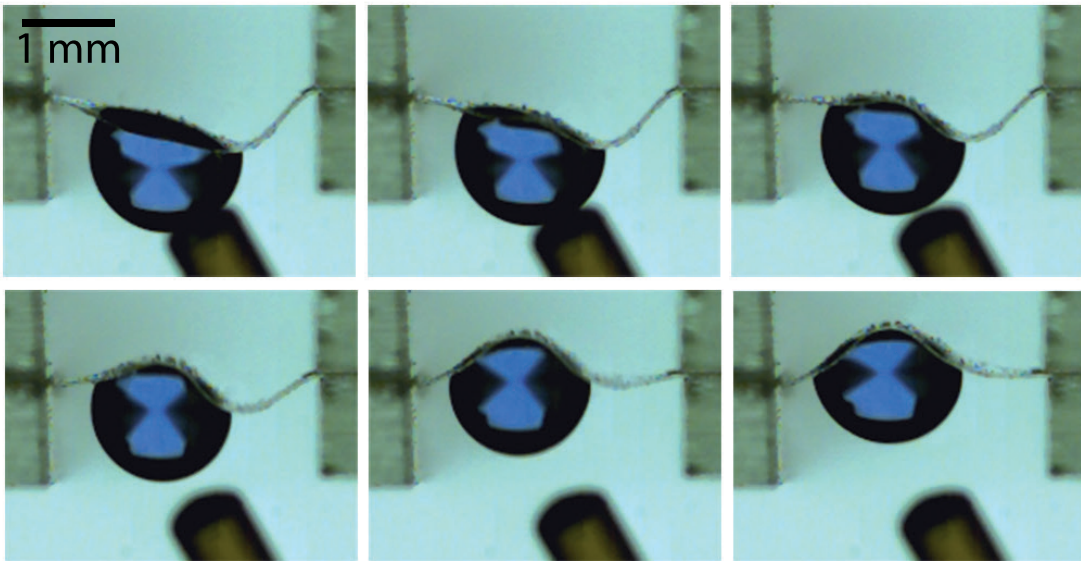
The goal of this Materials and Methods chapter was to give an overview of the main experimental techniques necessary for the experiments described in the following chapters: the use of each technique in the different chapters is summarized in Table 2.8. From elastic materials to liquids, we have detailed here the choice and characterization methods of the materials we are working with in our experiments. We have also described more specific techniques such as force sensing, droplet deposition, and surface tension measurements in the case of small droplets.

	chapter 3	chapter 4	chapter 5
Elastomers	PDMS	PDMS, EC33, EC13, ED22	PDMS
Sample geometry	strips	bulk	bulk
Liquids	water	water-glycerol	water
Surface tension measurements	manual tensiometer	manual tensiometer	Kibron EZ-Pi+
Droplet deposition	Hamilton syringe	micropipette and falling droplet	micropipette
High speed acquisition	Photron SA5	Hamamatsu Orca Flash	Hamamatsu Orca Flash
Microforce sensing	Yes	No	Yes
Ellipsometry	No	No	Yes

Table 2.8 – Use of the different techniques detailed here in the following chapters.

Chapter 3

Elastocapillary snap-through



In this chapter, we show that capillary forces are strong enough to trigger a snap-through instability at small scales, and even counterbalance gravity for a droplet deposited below a downward buckled elastic strip. We compare droplet-induced snap-through to point-force indentation on a buckled thin strip, and investigate both the statics and dynamics of this phenomenon. We build an equilibrium and stability phase diagram, varying the droplet size and its position on the strip, and show that the water droplet only *triggers* the instability, the snapping time being determined by classical beam bending dynamics. Several spin-off versions of the experiment are also designed, including a humidity-controlled mechanical switch and upscaled experiments using soap bubbles instead of water droplets.

Contents

3.1	Context: smart actuators	68
3.1.1.	Various strategies used to engineer soft actuators	68
3.1.2.	Natural smart actuators: a source of inspiration	69
3.1.3.	Envisioning an elastocapillary snap-through actuator	71
3.2	Dry snapping experiments versus elastocapillary snapping	73
3.2.1.	Dry snapping: force-displacement curves	73
3.2.2.	Elastocapillary snapping: comparison with the dry case	75
3.2.3.	Snap-through against gravity	77
3.3	Spin-off versions of the experiment	78
3.3.1.	Droplets nucleated from water vapor	78
3.3.2.	Upscaled experiments using soap bubbles	79
3.4	Equilibrium: phase diagram	80
3.4.1.	Theoretical framework in the case of an elastocapillary snap-through	80
3.4.2.	Phase diagram: varying the droplet size and position	82
3.5	Dynamics: snapping time	84
3.5.1.	Snapping time in the case of a dry setup	84
3.5.2.	Snapping time for elastocapillary snap-through events	87
3.6	Perspectives: viscous dissipation in the polymer	88
3.6.1.	Analysis of the snapping time for small polymer samples	88
3.6.2.	Design of sliding droplets experiments	89

3.1 Context: smart actuators

Research into smart actuators and stimuli-responsive materials is attracting growing interest, as described in a recent review about soft actuators for small-scale robotics [134]. Different strategies are implemented both in Nature and in the industry: among them, taking advantage of mechanical instabilities is one successful way of inducing rapid movements [135].

3.1.1. Various strategies used to engineer soft actuators

Numerous means of actuation are used to build smart actuators. Stimuli-responsive materials can be triggered by electric or electrostatic actuation, which induces electrochemical transfer of charged dopants [136], electrowetting phenomena [137] or evaporation through heating [138] as shown in Fig. 3.1(a). In the latter case, the actuation mechanism relies on a bilayer composite structure, and the two buckling steps are triggered by different actuation signals: a high humidity level implies an expansion of one layer resulting in buckling of the composite bilayer material in one direction, while buckling in the other direction is performed with an electric actuation that rapidly evaporates water in the wet layer. A direct thermally-induced actuation is also possible, as described in [139] in the case of semi-flexible bimetal-based thermal energy harvesters. In addition, an example of solvent-induced actuation is reported in [140]. The development of soft actuators and

artificial muscles also includes research on the conversion of light into shape changes. The intensity and polarization of light irradiation can be quickly and easily changed and is thus a convenient triggering signal. Photomechanical effects in polymeric materials are reported in [141] in the case of photo-initiated snap-through of buckled arches. As shown in Fig. 3.1(b), molecular switches sensitive to UV light and embedded in liquid-crystalline polymer springs also achieve reversible winding/unwinding steps under UV-light actuation [142].

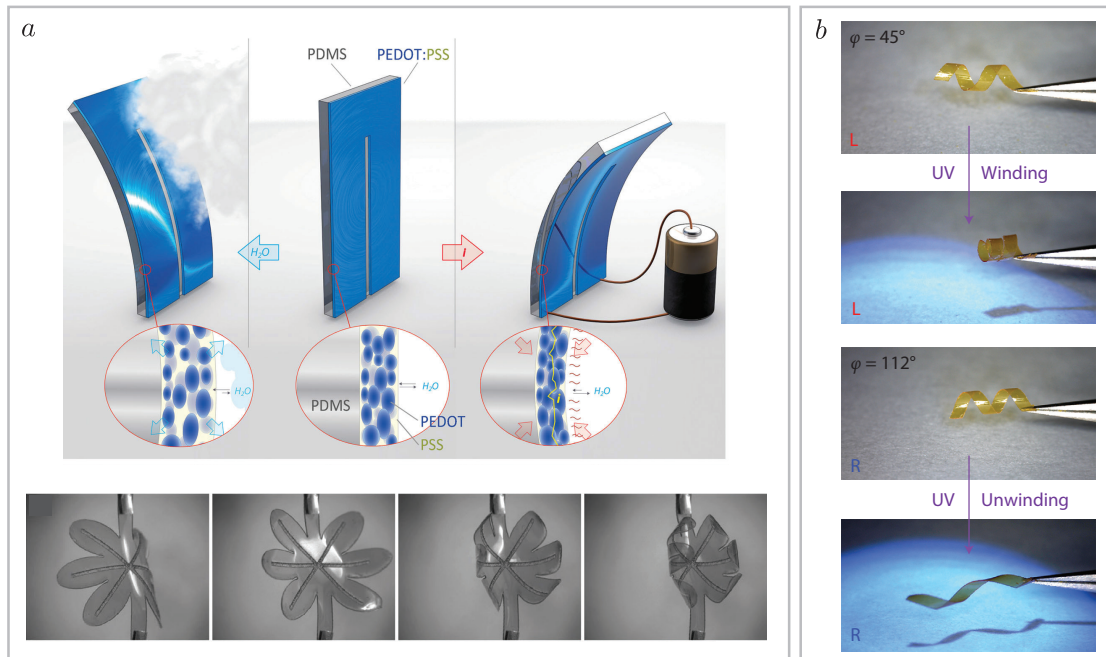


Figure 3.1 – (a) Buckling of a bilayer composite structure: buckling in one direction is triggered by increasing the humidity, while buckling in the other direction is electrically-induced through heating and evaporation of water in the PEDOT-PSS layer. Reproduced from [138]. (b) Reversible winding and unwinding induced by UV lighting. The material is made of molecular switches responsive to UV light, embedded in liquid-crystalline polymer springs. Reproduced from [142].

Taking advantage of magnetic forces is also a strategy used to build soft actuators: an investigation of buckling shapes of beams clamped at both ends under magnetic actuation is performed in [143], and an inchworm motion is reproduced by a polymeric micro-robot actuated by a magnetic field in [144]. The current interest for exploring new strategies to manufacture smart actuators is driven by potential applications such as soft robotics or micro-electro-mechanical systems (MEMS), and recent research also includes biomimetic approaches. The following paragraph exhibits natural stratagems used by plants to promote fast motion without muscles.

3.1.2. Natural smart actuators: a source of inspiration

Various vital functions in plants rely on fast movements, to spread spores or seeds, defend against predators, or catch preys for carnivorous plants. In some cases, the triggering mechanism depends on a change in ambient humidity, using different processes:

Fig. 3.2(a) illustrates how a bilayer composite made of one hygroscopic and one non-hygroscopic material results in an unfolding of ice-plant seeds capsules [145]. Equisetum spores also use a hygroscopic process to move with four elaters that deploy upon drying and fold back in humid air, as shown in Fig. 3.2(b): jumps occur when the spores suddenly thrust themselves after being tightly folded [146], and jumping spores are carried away by the wind again to be spread farther. The sensitive leaves of Mimosa Pudica undergo an osmotically-induced folding when they are touched, to defend against predators [147], while the fern sporangium uses a unique mechanism to send spores: a catapult is triggered by cavitation bubbles formed when water evaporates [148], as shown in Fig. 3.2(c).

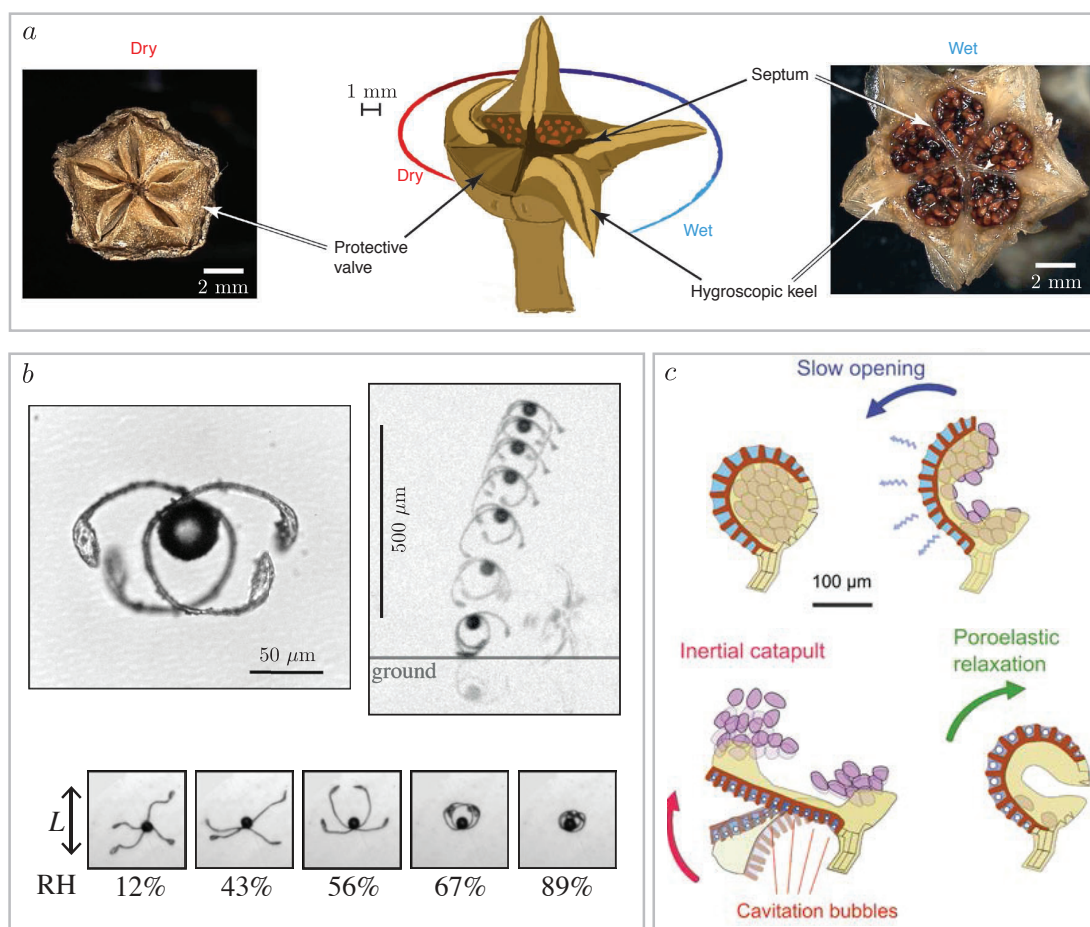


Figure 3.2 – (a) Ice-plant seed capsule in a dry (left) and in a wet (right) environment. A bilayer composite made of a non-hygroscopic wall and of a hygroscopic keel results in an unfolding of the ice-plant seed capsule in a humid environment. Reproduced from [145]. (b) The shape of the Equisetum spores changes when varying the relative humidity (RH): four elaters deploy at low humidity levels, and curl around the spherical body at high humidity levels. When drying, spores can suddenly leave the ground and be carried away by the wind. Reproduced from [146]. (c) The opening and closing of fern sporangium use two different mechanisms: the opening is slow, and followed by the apparition of cavitation bubbles which trigger an inertial catapult. Reproduced from [147].

The energy release mechanisms used by plants sometimes rely on mechanical instabili-

ties, as for the carnivorous Venus flytrap [149]: its rapid closure takes only 100ms and is one of the fastest movements existing in plants. The trap closure is triggered by the mechanical stimulation of hairs located on the leaf, which results in a two steps mechanism: an active biochemical step, followed by a passive elastic snapping of the trap. The elastic energy stored in the plant is suddenly released, which results in a ultra-fast motion. The open and closed states of the Venus flytrap are shown in Fig. 3.3(a). Another example of the use of a snap-through instability in plants is shown in Fig. 3.3(b): Utricularia are small underwater plants that use an elastic instability to promote fast suction to catch preys [150]. Malaria infected cells also exhibit snapping events (fast shell eversion) that result in a rapid ejection of parasites [151].



Figure 3.3 – (a) Venus flytrap in its open (left) and closed (right) states: the ultra-fast closing of the trap corresponds to a snap-through mechanical instability. Reproduced from [149]. (b) Utricularia underwater suction trap: a snap-through step is used to produce a fast motion and induce suction in the trap. Reproduced from [150].

3.1.3. Envisioning an elastocapillary snap-through actuator

The examples presented in the previous paragraph involve a snapping instability including fast movements and curvature reversals that are a consequence of the sudden release of stored elastic energy and its transfer into kinetic energy. As the importance of capillary interactions at small scale have been demonstrated in several situations such as capillary origami or aggregation of wet fibers (see section 1.3), we here investigate the possibility of triggering a snap-through event by capillary forces. We revisit the classical snap-through instability described in section 1.1 by adding a new ingredient: capillarity.

Experiments are performed with thin flexible strips to build a system where a competition between elasticity and capillarity occurs, as described in chapter 1: the dimensions and bending rigidity of the samples are key parameters that should be carefully chosen to aim for a capillarity-induced snap-through. The elastomer samples employed in this chapter are elastic strips cut from Dow Corning Sylgard 184 PDMS spin-coated thin films (the manufacturing and characterization processes of such samples have been detailed in chapter 2). Elastic strips of length L , width w , and thickness h are clamped at both ends with cut edge microscope slides, and the end-to-end distance, denoted Δ , is set to a value smaller than L to induce buckling (Fig. 3.5). We denote $I = h^3w/12$ the second moment of area of the cross-section of the strips, and ρ_e the density of the elastomer. For Dow Corning Sylgard 184 PDMS, the specific gravity announced in the datasheet is 1.03; we approximate ρ_e to 10^3 kg/m^3 in our study. Two experimental setups, referred to as

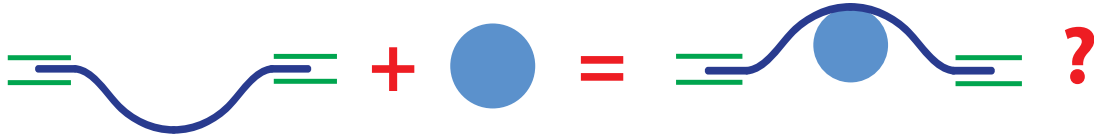


Figure 3.4 – The challenge posed in this chapter is the following: is it possible to trigger an elastic snap-through instability with capillary forces, by depositing a water droplet on or under a buckled elastic strip?

S1 and S2, are used for the experiments presented in this chapter: their properties are listed in Table 3.1, and the Young’s modulus of these samples is found to be $E = 1.5$ MPa. Talc powder is used to avoid the strip to stick to itself and to the glass clamps, and the contact angle of water droplets deposited on such strips is $110 \pm 10^\circ$.

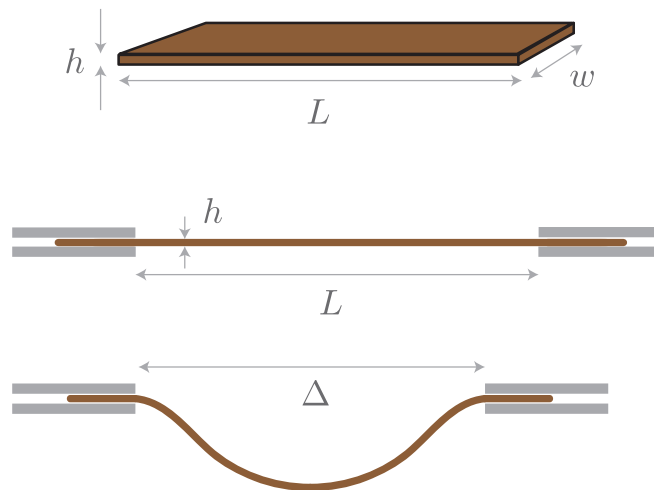


Figure 3.5 – A strip of length L , width w , and thickness h is clamped at both ends with microscope cut edge slides. When the end-to-end length is reduced to a value $\Delta < L$, the initially straight strip buckles and adopts an arched shape.

#	L (mm)	w (mm)	h (μm)	Δ/L	L_{ec}/L
S1	5.0	1.07	68.3	0.95	6.7
S2	3.5	0.98	33.7	0.90	13.6

Table 3.1 – Length L , width w , thickness h , confinement parameter Δ (defined in Fig. 3.5), and elastocapillary length L_{ec} (defined in chapter 1) for the two experimental setups, referred to as S1 and S2.

3.2 Dry snapping experiments versus elastocapillary snapping

In order to reveal the role of capillarity in droplet-induced snap-through instabilities, we start with considering a ‘dry’ setup, and carry out force-displacement measurements.

3.2.1. Dry snapping: force-displacement curves

a) Experimental measurements

To perform force-displacement measurements on a buckled polymer strip, a Femto-tools FT-S270 microforce sensor (described in section 2.2) is mounted on a SmarAct nanopositioner SLC-1730. A picture and a schematic diagram of the experimental setup are shown in Fig. 3.6: our control parameter is the vertical displacement of the sensor, and the force F applied by the strip on the sensor is recorded as a function of the height H of the sensor. All the measurements are performed on the experimental setup S1 (Table 3.1). We place the sensor at a given position x along the strip, and move the sensor down in the vertical direction to carry out point-load indentation of the strip. It should be noted that the confinement is small enough for the precise way with which the vertical loading is applied to be disregarded [15], but large enough for extension effects to be negligible [16]. The strip shape is considered to be invariant in the direction perpendicular to the schematic shown in Fig. 3.6(b).

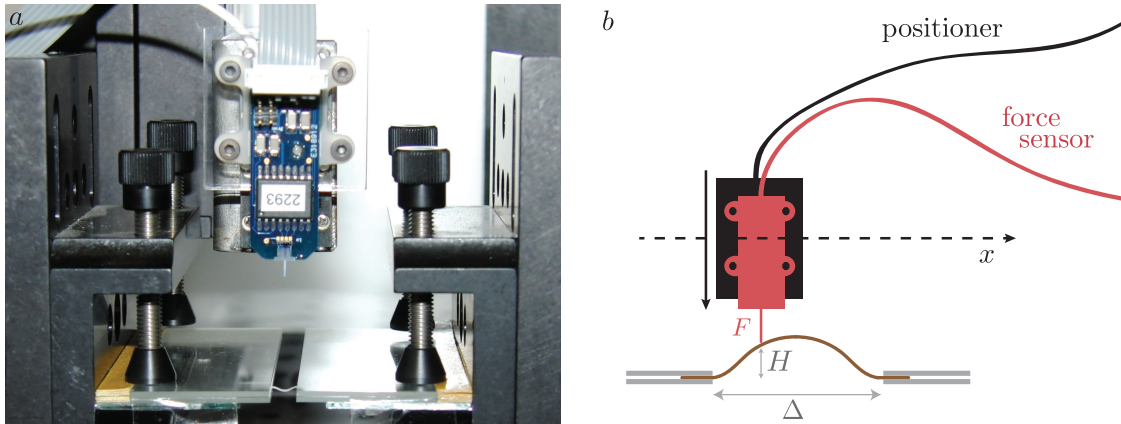


Figure 3.6 – (a) Photograph of the experimental setup to perform force-displacement measurements, showing the microforce sensor as well as the mounting used to clamp elastic strips at both ends. (b) Schematic diagram of the experiment: for a given x position of the sensor, the force F exerted by the strip on the sensor is recorded as a function of the vertical position H of the sensor.

In Fig. 3.7, we show force-displacement measurements for different sensor positions x . Results obtained by indenting the strip at the middle ($x = \Delta/2$) are shown in Fig. 3.7(b): the experimental points, in green, are obtained by following the curve from right to left, as H is decreased during the experiment. We observe that, as the sensor is moved down, the exerted force increases up to F_{\max} . The strip shape remains symmetric until F_{\max} is reached. When moving the sensor further, the force reduces and the shape is no longer symmetric. The force exerted on the sensor vanishes when H is equal to zero: at this point, the strip shape is that of the second mode of buckling (anti-symmetric mode). When H is decreased further, the strip detaches from the indenter, as the unstable anti-symmetric

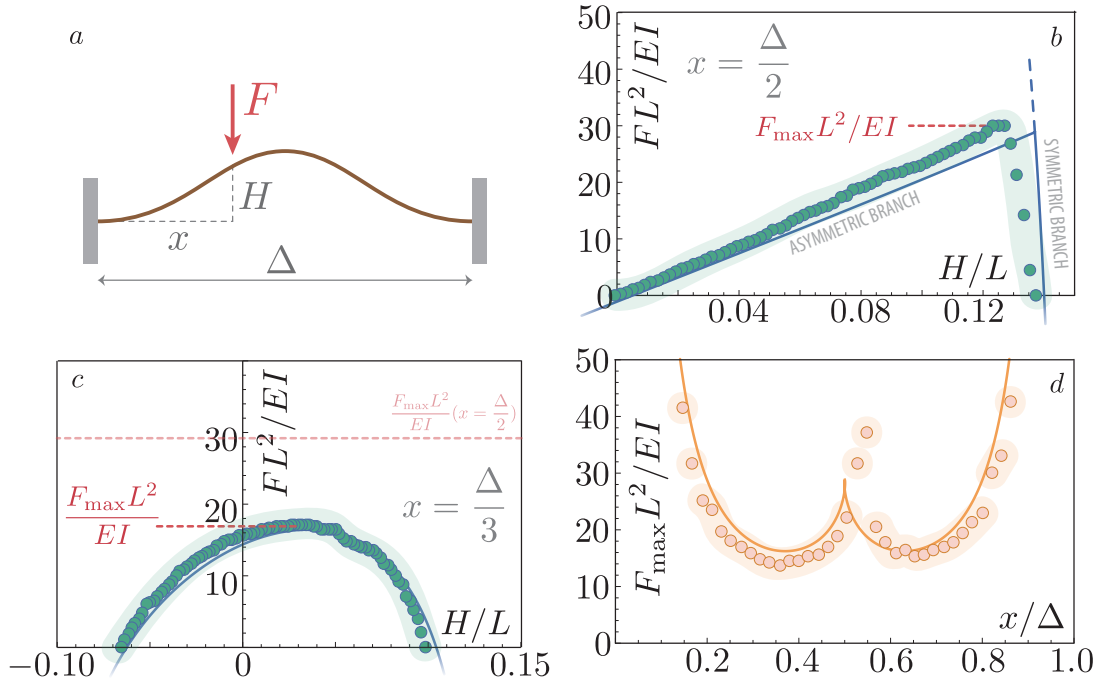


Figure 3.7 – (a) Schematic showing the notations used in the experiments. (b) Force-displacement curve obtained for a sensor position along the strip $x = \Delta/2$. The dimensionless force FL^2/EI is plotted as a function of the dimensionless height of the sensor H/L . (c) Same experiment in the case where $x = \Delta/3$. (d) F_{\max} (defined in (b) and (c)) is recorded as a function of the sensor position along the strip x . The dimensionless threshold force to induce snap-through $F_{\max}L^2/EI$ is plotted as a function of the dimensionless position along the strip x/L , evidencing two preferential positions where the threshold force is minimal: $x/\Delta \simeq 0.37$ and 0.63 . In all the graphs, points correspond to experimental data and continuous lines to computational results. The order of magnitude of the error bars on experimental points is given by the light green and light orange zones.

mode is switched to the downwards symmetric buckling mode. In the case of a force-controlled measurement (instead of a displacement-controlled measurement as performed here), snap-through would occur as soon as F_{\max} is reached, and the anti-symmetric branch of the graph would not be recorded experimentally.

Interestingly, the force F_{\max} – which corresponds to the threshold force needed to induce snap-through – exhibits a sharp dependence on the x position of the sensor. Results obtained by indenting the strip at a position $x = \Delta/3$ are shown in Fig. 3.7(c). Beyond the change in shape of the force-displacement curve, the value of F_{\max} is significantly lowered compared to the $x = \Delta/2$ case. Imperfection sensitivity in indentation at the middle of buckled strips have already been reported in [152], but we illustrate here the dependence of F_{\max} as a function of the lateral position used for indentation x along the whole x accessible range (Fig. 3.7(d)). These results highlight that an optimal position to induce snap-through (with a force as small as possible) is located around $x = \Delta/3$ (and $x = 2\Delta/3$ as the problem is symmetric).

In all the graphs shown in Fig. 3.7, a good agreement is found between experimental points and computation results, shown as continuous lines, obtained in the framework

presented in the following paragraph.

b) Theoretical framework

The shape of an elastic strip subjected to point-load indentation is determined by solving the Kirchhoff equations, in the case of an inextensible strip. Notations are defined in Fig. 3.8. We recall here the equations, already mentioned in chapter 1:

$$\begin{aligned}x' &= \cos \theta & \text{and} & & y' &= \sin \theta \\EI \theta' &= M(s) \\M'(s) &= f_x(s) \sin \theta - f_y(s) \cos \theta \\f'_x(s) &= -P_x(s) & \text{and} & & f'_y(s) &= -P_y(s),\end{aligned}$$

where $()'$ denotes the derivative with respect to s , and P_x and P_y are forces exerted on the strip per unit length. In the case of point-force indentation, P_y is a Dirac function located at the indentation point.

These equations are solved with the boundary conditions $y = \theta = 0$ at the two ends of the strip, corresponding to clamped-clamped boundary conditions. As this set of equations is a two-point boundary value problem, a shooting method is used, and bifurcation curves are extracted from a numerical path following approach. Resulting curves are shown in Fig. 3.7 and compare well with experimental data points.

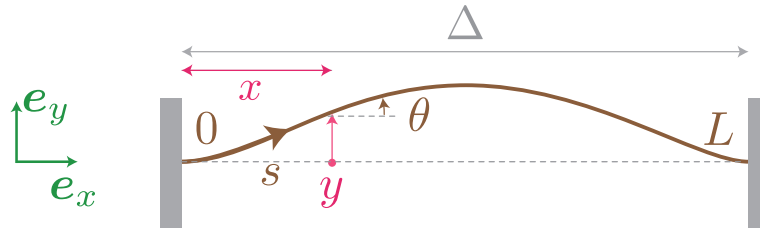


Figure 3.8 – Notations used to write the Kirchhoff equations: a strip of length L is clamped at both ends and confined with an end-to-end distance Δ . The curvilinear abscissa is denoted s , and for each value of s , the position is defined by a couple of coordinates x and y . We denote θ the angle between the tangent to the curve and the horizontal axis.

3.2.2. Elastocapillary snapping: comparison with the dry case

a) Experimental observations

We now replace the point-load indentation by a water droplet, and perform similar force-displacement measurements to compare results obtained with a droplet to results obtained previously with a dry setup. To do so, we deposit a droplet on or under a buckled elastic strip in the upward configuration, and we plot the dimensionless weight of the droplet FL^2/EI (where $F = \rho_l V g$ is the weight of a droplet of volume V and density ρ_l), as a function of the dimensionless height of the middle of the strip H/L . As the volume of the drop is increased, the height of the arch decreases until a limit is reached where snap-through occurs (Fig. 3.9). Droplets hung below the buckled strip are shown

as yellow triangles (*hanging-drop* setup), while droplets deposited above the buckled strip are shown as purple squares (*sitting-drop* setup). The present dead loading makes the anti-symmetric branch unstable, as opposed to the rigid loading setup of Fig. 3.7. We overlay the dry loading points in Fig. 3.9 as green circles for comparison purpose.

Much heavier drops are required to trigger a snap-through instability in the hanging-drop setup as compared to the sitting-drop setup, the dry setup being intermediate: in the experimental configuration S1 (Table 3.1), snap-through occurs above a critical volume of $9 \mu\text{L}$ in the hanging-drop setup, while the critical volume is only $2 \mu\text{L}$ in the sitting-drop setup. We conclude that only considering the weight of the drop is not enough: capillary forces have a strong influence on snap-through.

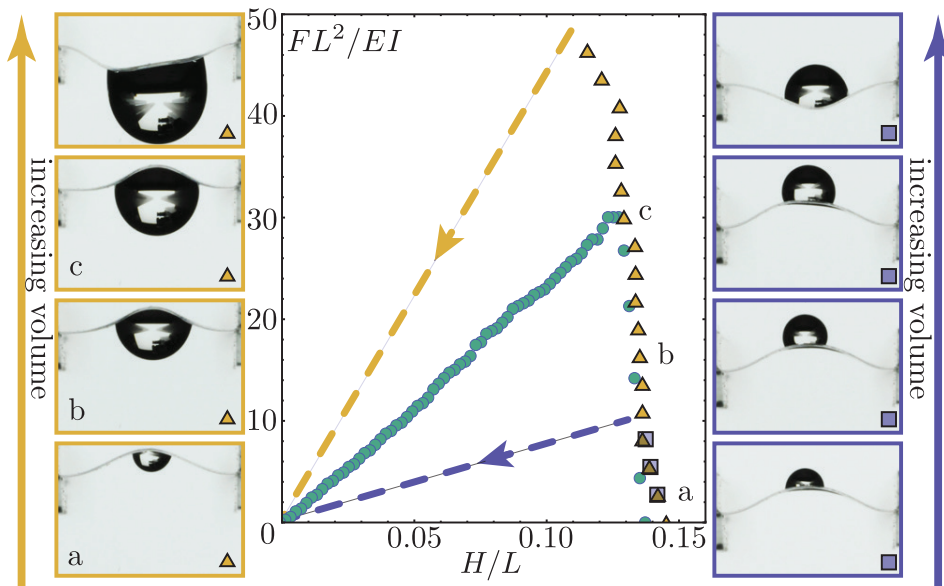


Figure 3.9 – Influence of capillarity on the bifurcation diagram of Fig. 3.7. Drops of increasing volume are hung below (yellow triangles) or deposited above (purple squares) the elastic strip S1 (Table 3.1), buckled upwards with $\Delta = 0.95L$. As the non-dimensional drop weight FL^2/EI increases, the deflection H/L of the strip midpoint decreases, up to a point where snapping occurs (indicated by the dashed lines on the diagram). For comparison we plot the data of Fig. 3.7, filled circles, performed on the same S1 strip. For both square and triangle sets, the volume increase between each measure is $0.5 \mu\text{L}$, corresponding to a non-dimensional force increase of 2.73. The left (yellow) panel shows hanging configurations with, from bottom to top, $V = F/\rho_l g = 0.5 \mu\text{L}$, $3 \mu\text{L}$, $5.5 \mu\text{L}$, $9 \mu\text{L}$, with $\rho_l = 1000 \text{ kg/m}^3$. The right (purple) panel shows sitting configurations with, from bottom to top, $V = 0.5 \mu\text{L}$, $1 \mu\text{L}$, $1.5 \mu\text{L}$, $2 \mu\text{L}$.

b) Capillary effects seen as two effective bending moments

Capillary forces acting on the elastic strip combine meniscus forces and Laplace pressure. A schematic in Fig. 3.10(a) shows that these capillary forces can be described as two effective bending moments applied at the triple line. Depending on the configuration, these bending moments do not have the same consequences: they promote the eversion of

the strip when the drop is located above and hinder it when it is located below. A simple illustration of these bending moments is shown in Fig. 3.10(b): a droplet deposited on a strip lying on a table is able to lift the two sides of the strip, due to these effective bending moments. This phenomenon is close to the eversion mechanism of inelastic shells, and can be easily understood by taking the example of an orange peel: to reverse the curvature of a naturally curved orange peel, we usually exert two effective bending moments that result from the forces applied with our fingers. The same action is performed when playing with a jumping popper to reverse its natural curvature.

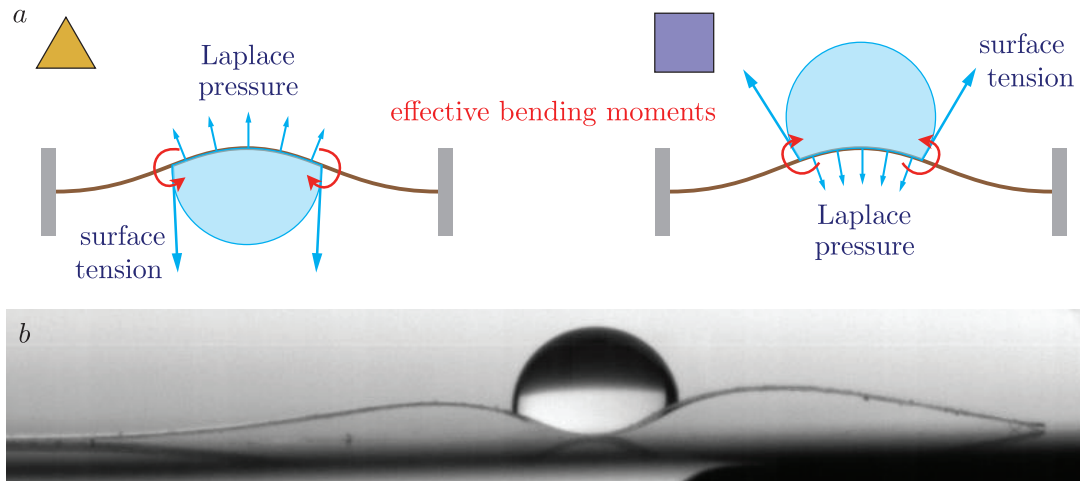


Figure 3.10 – (a) Interpretation of the results obtained in Fig. 3.9: the combined effects of Laplace pressure and surface tension act as two effective bending moments located at the triple line. These bending moments prevent the strip from snapping through in the hanging-drop case, but act towards a snap-through instability in the sitting-drop configuration. (b) Simple experiment to show the effect of these two bending moments: a droplet is deposited on an elastic strip lying on a hydrophobic table. Capillary bending moments are able to lift the strip on the left and right sides of the droplet. Image: M. Rivetti.

3.2.3. Snap-through against gravity

In the previous paragraph, we have shown that in the case of a droplet deposited above a buckled elastic strip in the upward configuration, capillary forces act towards triggering the snap-through instability. Another configuration of interest is the case of a droplet deposited below a buckled elastic strip in the downward configuration. In this situation, the effective bending moments act towards snapping, whereas the weight of the droplet is preventing the strip from snapping. We thus investigate the possibility of reverse elastocapillary snap-through, against gravity.

In Fig. 3.11, a water droplet (dyed with blue ink for visualization purposes) is released from a hydrophobic needle onto the lower side of a PDMS strip buckled in the downward configuration: the droplet weight tends to hinder the instability. A snap-through instability is nevertheless triggered by the droplet, evidencing that capillary forces are strong enough to counterbalance gravity at small scales. For a given elastic strip, the droplet size and position are two parameters of interest: dependence upon these parameters is investigated

further in a phase diagram presented in section 3.4. In the usual snap-through instability, the elastic energy, stored in the system before the instability and suddenly released in the form of kinetic energy when the system switches from one equilibrium position to another, is mainly lost. However, in this setup, part of the energy is used to make the liquid drop climb in the gravity field.

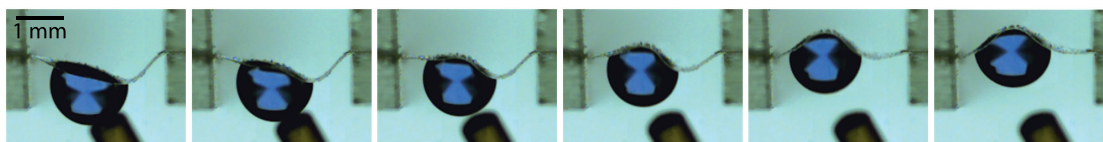


Figure 3.11 – Snap-through against gravity. Using a PTFE coated needle, a drop is gently deposited under a downward buckled PDMS strip (experimental setup S2 (Table 3.1)). Within a few milliseconds, capillary forces induce a snap-through elastic instability of the strip which jumps to the upward buckled state. In this setup surface tension overcomes both elastic forces and gravity. The liquid is tap water dyed with blue ink for visualization purposes, and the time interval between each snapshot is 5 ms.

3.3 Spin-off versions of the experiment

3.3.1. Droplets nucleated from water vapor

Instead of depositing a water droplet with a needle, nucleating droplets from water vapor allows for a remote triggering of the instability. In the setup shown in Fig. 3.12, droplets are nucleated on a PDMS strip, treated to be hydrophilic on its lower side, by using a kettle and a pipe system.

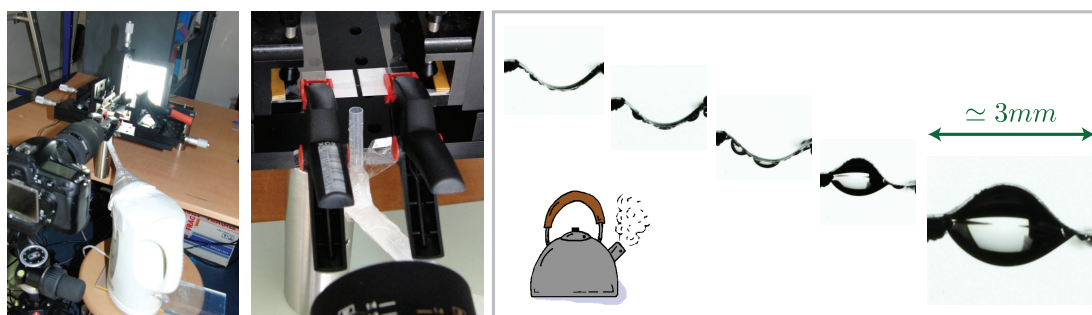


Figure 3.12 – Experimental setup used to nucleate droplets under a buckled elastic strip treated to be hydrophilic on its lower side. Droplets nucleate under the strip and coalesce to trigger a snap-through instability after a few minutes of exposure to water vapor.

Hydrophilisation of one side of the PDMS strip is achieved with an oxygen plasma treatment (we are grateful to Fabrice Monti, ESPCI, for his help with this technique). A PTFE coating is also used to manufacture hydrophobic clamps, so that water only condenses on the lower side of the buckled strip. As the steam flow is switched on, small droplets nucleate on the lower side of the PDMS strip. Coalescence events then

occur, eventually leading to the formation of a large droplet that successfully triggers a snap-through instability. Beyond demonstrating that capillary snap-through can be induced remotely, this experiment opens interesting perspectives for our elastocapillary snap-through system acting as a humidity-controlled mechanical switch. This device could be used as a moisture sensor, triggering a mechanical signal once ambient humidity is sufficiently high for droplets to nucleate and grow on the polymer strip.

3.3.2. Upscaled experiments using soap bubbles

Elastocapillary snap-through induced with water droplets implies to work at millimetric scales. This constraint is released when working with soap bubbles: we thus design upscaled snap-through experiments. A soap bubble has a negligible weight compared to a water droplet of same size, is much less deformed by gravity [153], and does not flow when upscaling the experiment up to ten-centimeter soap bubbles. The surface tension of the liquid used to build soap bubbles is smaller than the surface tension of pure water ($\gamma \simeq 30$ mN/m for the soapy solution and $\gamma \simeq 72$ mN/m for pure water). However, the effective action of the bubble on the strip is linked to the value of 2γ as the soap film presents two liquid-air interfaces (instead of γ in the case of a droplet, with a single liquid-air interface). A first setup, presented in Fig. 3.13, consists in depositing a soap bubble under a buckled PDMS strip of centimetric scale. The bubble deposition is followed by a snap-through event. To gently deposit a bubble, an assembly of at least two bubbles is built and only one bubble is deposited: the detachment of the bubble from the companion bubble results in negligible perturbation of the system, which is not the case when a bubble has to detach from a solid surface (the deposition step is visible on the first picture in Fig. 3.13).

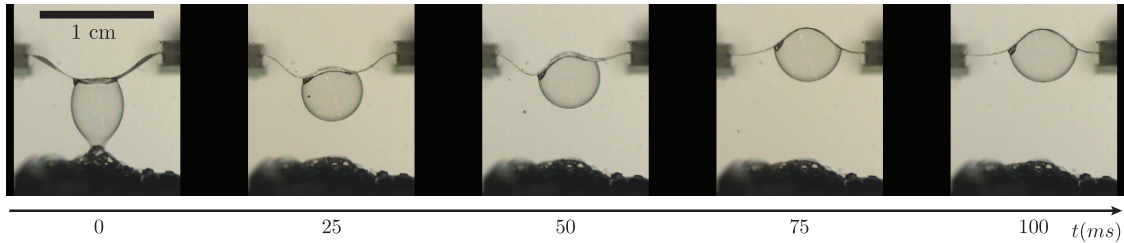


Figure 3.13 – A soap bubble is deposited under a PDMS strip buckled in the downward configuration, and snap-through is successfully observed against gravity. The sample dimensions are $L = 1.2$ cm, $w = 2.8$ mm, $h = 68.3$ μm , and the confinement parameter Δ is approximately $0.9L$.

Experiments can be upscaled further using a metallic foil instead of PDMS samples. The experiment presented in Fig. 3.14 is performed with a ten-centimeter diameter soap bubble deposited on a buckled metal foil in the upward configuration. Elastocapillary snap-through is successfully observed in this configuration. However, due to gravity-induced drainage, a soap bubble is thinner at the top than at the bottom: depositing a soap bubble under a metal foil is thus more difficult than depositing it above. This explains why snap-through against gravity has not been successful in our experiments due to bursting of the bubble at the instant of deposition.

These spin-off versions of our snap-through experiment open the perspective of an elastocapillary snap-through humidity-controlled smart actuator, and provide additional evidences of the importance of capillary forces in liquid-driven snap-through instabilities.

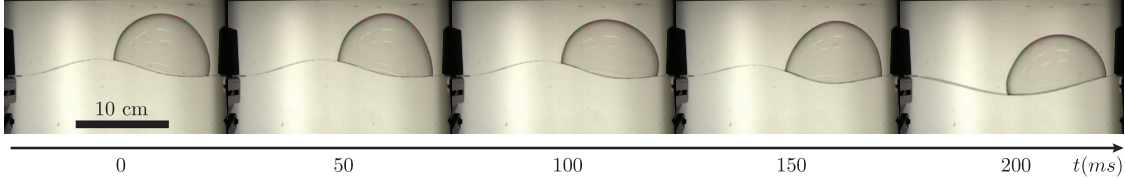


Figure 3.14 – A snap-through event is triggered on a metallic foil of dimensions $L = 24$ cm and $w = 7.8$ cm with a 10 cm diameter soap bubble. The confinement parameter Δ is approximately $0.98L$.

3.4 Equilibrium: phase diagram

In this section, we investigate the equilibrium shapes of drop-strip systems and their stability. We build a phase diagram giving the equilibrium state (buckled downward or upward) of an initially buckled strip below which a water droplet is deposited, as a function of the droplet weight and of the position at which it is deposited along the strip.

3.4.1. Theoretical framework in the case of an elastocapillary snap-trough

A two-dimensional model is used to numerically compute the equilibrium and stability of drop-strip systems (Fig. 3.15(a)). Assuming that the droplet is a portion of cylinder is of course an approximation: Fig. 3.15(b) shows the shape of a bubble on a metallic foil: the footprint of the bubble on the strip is not exactly a rectangle (as assumed in the 2D model) and the shape of the bubble is chosen by the system to minimize its potential energy, the bubble thus does not exhibit sharp edges. However, we will see that this model provides results in good agreement with experiments, using one adjustable parameter to counterbalance the fact that in the model the effective surface of the drop is not minimal because of its cylindrical shape. In the literature, such approximations have already been reported to successfully capture elastocapillary phenomena involving drop-strip systems [87], as mentioned in chapter 1 (Fig. 1.30(b) and (c)).

The schematic diagram in Fig. 3.15(a) shows the parameters used in the modeling. The notations used for the strip are the same as for the dry setup, adding an index s to differentiate notations corresponding to the strip from notations corresponding to the droplet: we use the arclength s along the strip to parametrize its position $\mathbf{r}_s(s) = (x_s(s), y_s(s))$. The unit tangent, $\mathbf{t}_s(s) = d\mathbf{r}_s/ds$, makes an angle $\theta_s(s)$ with the horizontal: $\mathbf{t}_s = (\cos\theta_s, \sin\theta_s)$. The strip is clamped at both ends which are separated by a fixed distance Δ .

We now need additional parameters to characterize the droplet position and shape. The drop lies between positions $s = s_A$ and $s = s_B$ on the strip, and the liquid-air interface is parametrized with its own arclength σ . The contact angles are denoted α_A and α_B . The shape of the liquid-air interface is denoted $\mathbf{r}_i(\sigma) = (x_i(\sigma), y_i(\sigma))$, has total contour length ℓ , and the unit tangent makes an angle $\theta_i(\sigma)$ with the horizontal (Fig. 3.15(a)).

Modification of the Kirchhoff equations used in the case of dry snap-through (section 3.2) occur via the expressions of the forces per unit length P_x and P_y . The droplet exerts a pressure on the strip equal to the sum of the Laplace and hydrostatic pressures, as well as surface tension forces localized at the triple line and oriented along the water-air

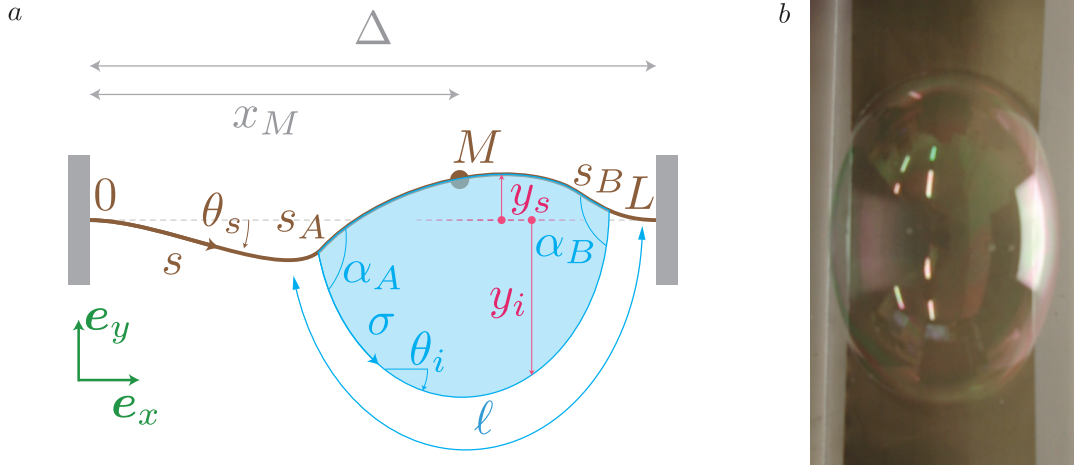


Figure 3.15 – (a) Schematic diagram of the two-dimensional model used for our drop-strip system: the system is assumed to be invariant in the direction perpendicular to the Oxy plane. (b) Top view of a bubble lying on a metallic strip. In the model, the bubble is assumed to be a portion of cylinder, having a rectangular footprint on the strip: the deviation from this two-dimensional model can be easily seen on the picture.

interface. κ_i is the curvature of the water-air interface, which is unknown yet. Denoting w the width of the strip and h its thickness, the distributed forces due to pressure forces are then equal to:

$$P_x = \sin \theta_s [\gamma \kappa_i - \rho_l g (y_s - y_i)] w$$

$$P_y = -\cos \theta_s [\gamma \kappa_i - \rho_l g (y_s - y_i)] w - \rho_e g h w$$

where ρ_e is the density of the strip. The gravity potential energy of the strip $\rho_e g h w$ is in fact negligible compared to that of the droplet. In addition, localized surface tension forces are included as Dirac functions: they have an amplitude γw and are oriented along the water-air interface. The Kirchhoff equations including the new forces due to the water droplet are solved with the boundary conditions $y_s = \theta_s = 0$ at the two ends of the strip. Continuation techniques are used to track equilibrium states along branches in bifurcation diagrams, and sliding of the drop is prevented by constraining the mean position $s_M = (s_A + s_B)/2$ and the mean contact angle $(\alpha_A + \alpha_B)/2 = 110^\circ$ in the computations. Examples of equilibrium configurations computed with this technique compare well with shapes observed experimentally, as shown in the qualitative comparison presented in Fig. 3.16.

Another way of writing the equations is to use the energy of the system and to perform minimization under constraints. The bending energy of the strip and gravity potential energy of the water are:

$$E_{\text{bend}} + E_{\text{hydro}} = \frac{Eh^3}{24} \int_0^L [\theta'_s(s)]^2 ds + \rho_l g \iint_{\mathcal{A}} y d\mathcal{A}$$

where $\mathcal{A} = \int_0^\ell y_i(\sigma) x'_i(\sigma) d\sigma - \int_{s_A}^{s_B} y_s(s) x'_s(s) ds$ is the area between the strip and the liquid-air interface. The energy per unit area of solid-liquid (respectively solid-air, and

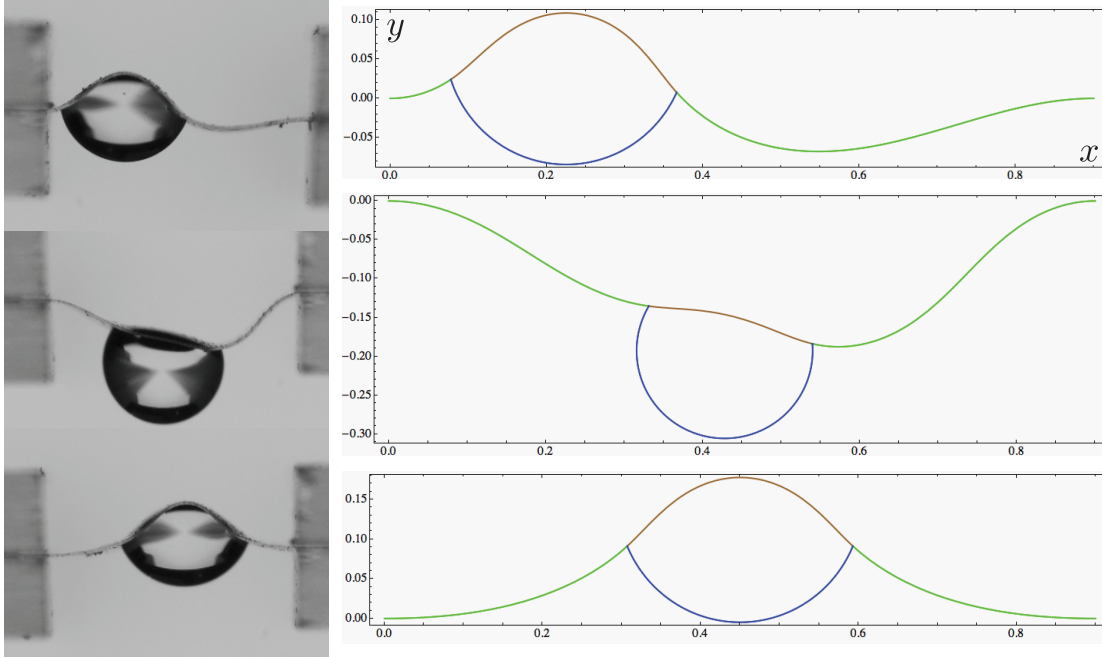


Figure 3.16 – Qualitative comparison between shapes observed experimentally and drop-strip systems obtained numerically. In the numerical profiles, distances are rescaled by the length L of the strip. Experiments are performed with the setup S2 (Table 3.1).

liquid-air) interface is noted $\gamma_{\ell s}$ (resp. γ_{sv} and γ). The total interface energy is then:

$$E_{\text{surf}} = (s_B - s_A)\gamma_{\ell s} + [L - (s_B - s_A)]\gamma_{sv} + \gamma \ell$$

The total potential energy $U = E_{\text{bend}} + E_{\text{hydro}} + E_{\text{surf}}$ has to be minimized under the constraints of inextensibility $\mathbf{r}'_s(s) = \mathbf{t}_s$, constant area \mathcal{A} , and matching conditions $\mathbf{r}_s(s_A) = \mathbf{r}_i(0)$ and $\mathbf{r}_s(s_B) = \mathbf{r}_i(\ell)$.

The two approaches (balance of forces and moments, or minimization of the total potential energy) are equivalent, and the numerical results presented here are obtained by solving the Kirchhoff equations and using numerical path following methods.

3.4.2. Phase diagram: varying the droplet size and position

As shown in Fig. 3.16, the equilibrium shape of a drop-strip system depends on the droplet size and position along the strip. To further inquire relative strengths of capillarity, weight, and elastic forces, we study the following setup: the elastic strip S2 (Table 3.1) is buckled downward and a drop is hung at a given location under the strip. We build a phase diagram using two parameters: the total weight F of the drop and the abscissa x_M of the middle point of the wet region of the beam. In Fig. 3.17(a), we record if a snapping event occurs when a droplet of given values of F and x_M is hung below a strip buckled downward: snapping events are shown as blue triangles, while systems which are stable in the downward position are shown as red triangles.

For small drops (*i.e.* small F), capillary forces exceed self-weight (a drop deposited under a rigid surface does not fall if small enough) but are not powerful enough to

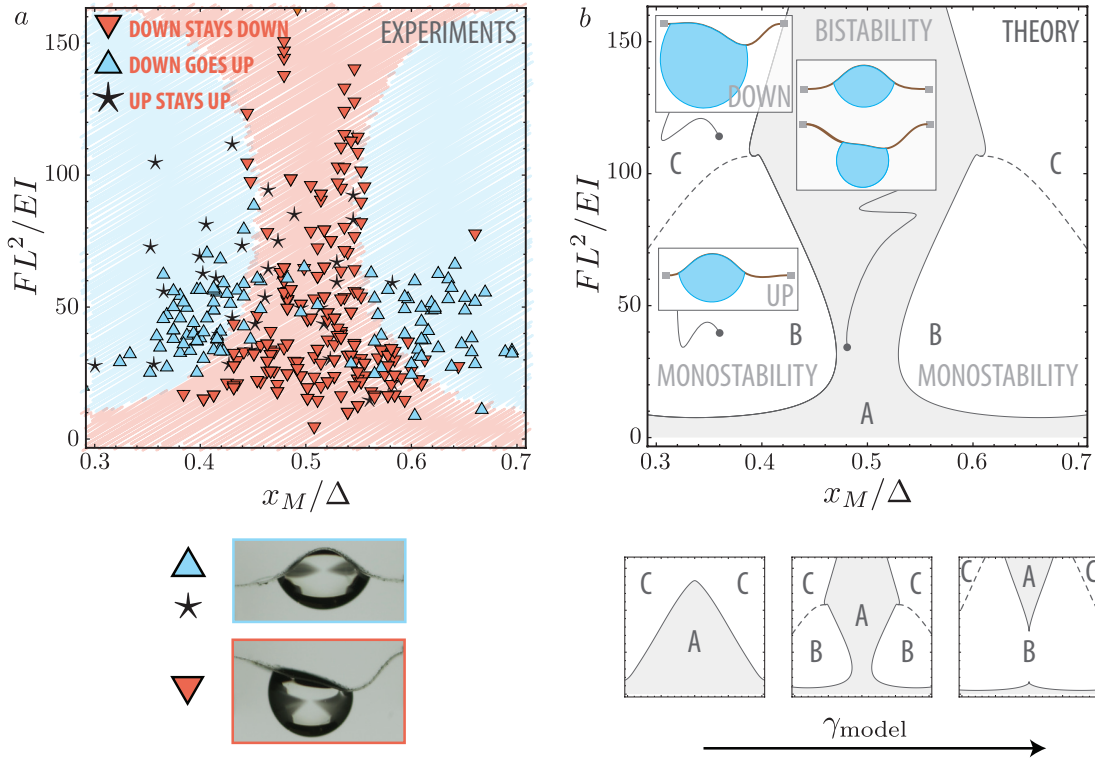


Figure 3.17 – Phase diagram for elastocapillary snapping: a drop is hung under a strip and the conditions for snapping to occur are investigated in terms of droplet size and position. (a) Experimental phase diagram in the (x_M, F) plane: a droplet is deposited below a strip buckled in the downward configuration, resulting in a snap-through event (blue triangles), or in an equilibrium configuration in a downward position (red triangles). Black star markers \star correspond to experiments where a droplet is deposited under a buckled strip in the upward position, resulting in an upward configuration. Colored zones are a guide to the eye. (b) Theoretical phase diagram showing bistable A and monostable B and C regions: a reduced effective surface tension $\gamma_{\text{model}} = 0.67\gamma$ was used to take into account differences between the three-dimensional experiments and the two-dimensional modeling. The evolution of the phase diagram as a function of the value of γ_{model} is shown at the bottom, with from left to right, $\gamma_{\text{model}} = 0.38\gamma$, 0.67γ , and 0.96γ .

overcome elastic forces and the system stays in the downward configuration. In this case, the lever arm of the effective bending moments discussed earlier is not large enough: the wet length is indeed a key factor determining the behavior of elastocapillary systems [72]. For moderate drops (with larger wet lengths) we see in Fig. 3.17(a) that, provided the location of the drop is carefully chosen, snapping occurs, resulting in a final state where the strip is bent upward: in this case capillary forces overcome both weight and elastic forces. For large drops capillarity still defeats elasticity but self-weight is too large and the system stays in the downward configuration.

These experimental results are compared to the theoretical phase diagram shown in Fig. 3.17(b), plotted with a modified value for the surface tension $\gamma_{\text{model}} = 0.67\gamma$, which is required to take into account differences between a two-dimensional model and a three-dimensional experiment. Stability of the system is assessed by computing the

linearized dynamics around the equilibrium solution, and the continuous curve corresponds to loss of the stability of an equilibrium configuration. The dashed curve corresponds to the smooth transition from downward buckled states ($y_M < 0$) to upward buckled states ($y_M > 0$). These two curves divide the (x_M, F) plane in three regions. In region A, which lies below the instability curve, downward and upward buckled configurations are both found to be stable. As the crossing of the instability curve is associated with the loss of stability of one of the configurations, in the two regions above the instability curve there is only one stable configuration: upward for region B, below the dashed curve, and downward for region C, above the dashed curve.

The experimental results presented in Fig. 3.17(a) show that in the bistable region A, a drop deposited under a downward buckled strip leads to a downward final state unless the perturbation created during the deposition is too large and the system jumps to an upward final state, whereas in the monostable region B the final state is always an upward configuration. As a cross-check we have experimentally hung drops under upward buckled strips and found that in regions A and B the system stays in the upward configuration (markers \star in Fig. 3.17(b)): this confirms the bi-stability of region A. We observe good agreement between experiments (Fig. 3.17(a)) and theory (Fig. 3.17(b)), provided that the surface tension is chosen to be $\gamma_{\text{model}} = 0.67\gamma$. Indeed, the topology of the phase diagram is altered by changes in the value of γ_{model} : we show at the bottom of Fig. 3.17(b) three phase diagrams corresponding to three values of γ_{model} .

The knowledge of the equilibrium and stability positions of drop-strip systems is essential to envision perspectives such as manufacturing elastocapillary snap-through smart actuators. The results presented here provide useful information to choose both the size of a droplet and the position at which it should be deposited to achieve a release of energy through a snapping event.

3.5 Dynamics: snapping time

After investigating equilibrium and stability of drop-strips systems, the question of the snap-through dynamics is raised. In this section, we aim for understanding the time needed to switch from one buckled configuration to another, both in dry and elastocapillary setups.

3.5.1. Snapping time in the case of a dry setup

We consider a beam or a strip clamped at both ends and buckled in the upward configuration. In the case of a point-load indentation at the middle of the strip, we have observed in Fig. 3.7(b) that the indenter touches the elastic strip only until the height H is zero, corresponding to the second mode of the elastica. The dynamics in the first part of the experiment (until $H = 0$) depends only on the speed at which the indenter is displaced, as we control the displacement. After reaching this position, a snap-through instability occurs and the strip suddenly switches to the downward configuration. We investigate here the dynamics of this fast phenomenon, illustrated in Fig. 3.18.

The position of the middle point of the strip is recorded as a function of time: once the indenter is no longer in contact with the strip, the displacement of the middle of the strip as a function of time follows an exponential evolution, as shown in Fig. 3.19. The orange curve corresponds to the displacement versus time recorded experimentally, while

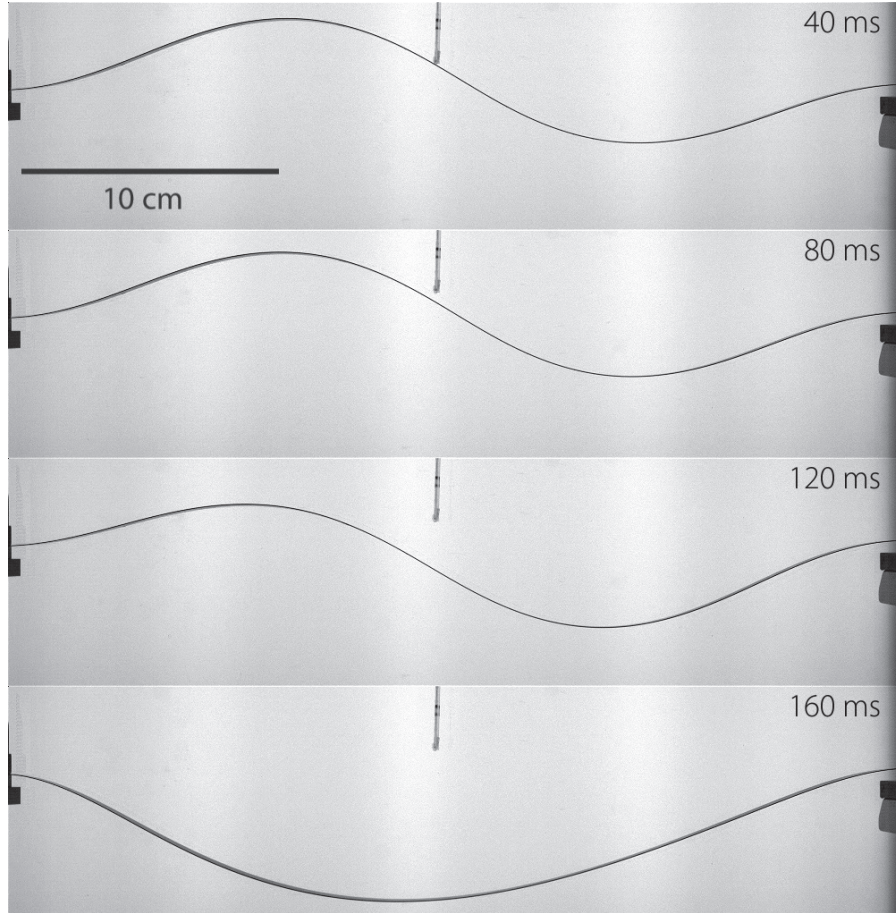


Figure 3.18 – Indentation-induced snap-through of a metal ruler clamped at both ends. The length of the ruler is $L = 36.8$ cm and the confinement parameter is $\Delta = 0.95L$.

the black dashed curve is an exponential fit. In inset is shown a log-linear representation of the same data, highlighting the exponential evolution for the displacement as a function of time. More precisely, the position of the middle of the strip as a function of time is modeled by the following function:

$$y(s, t) = y_i(s) + Y(s) e^{t/\tau_{\text{snap}}}$$

where τ_{snap} is the characteristic timescale for the exponential growth, and $y_i(s)$ corresponds to the initial shape of the strip (here a second mode of buckling, corresponding to the schematic on the left in Fig. 3.19). From a theoretical point of view, this timescale is linked to the growth rate of the snap-through instability. Let us consider a beam in the second mode of buckling. As this mode is unstable, when computing the vibrations around this configuration

$$y(s, t) = y_i(s) + Y(s) e^{i\omega t},$$

purely imaginary values for the vibration pulsation ω are found. The vibration mode with ω purely imaginary for which $|\omega|^2$ is maximum is the dominant one, and grows

exponentially. We can define a dimensionless growth rate μ using the scaling time $T = L^2 \sqrt{\rho_e A / EI}$, the equation for $y(s, t)$ being then:

$$y(s, t) = y_i(s) + Y(s) e^{\mu t / T}$$

The growth rate μ is both extracted from our experimental data, and computed numerically: in the case presented in Fig. 3.19, the experimental value is $\mu = 23 \pm 2$ and the computed value is $\mu = 24.26$. Our model thus captures well the experimental data. Note that the confinement parameter is $\Delta = 0.95L$ both for experiments and numerics. A change in Δ leads to a change in μ : numerically, the growth rate is found to be $\mu = 24.42$ for $\Delta = 0.9L$. As we used a scaling time T that includes all the dependence in the elastic and geometrical properties of the samples, the numerically computed value $\mu = 24.26$ is valid for samples with various elastic and geometrical features, provided that the strip can be considered as slender and purely elastic, and that the confinement parameter is $\Delta = 0.95L$.

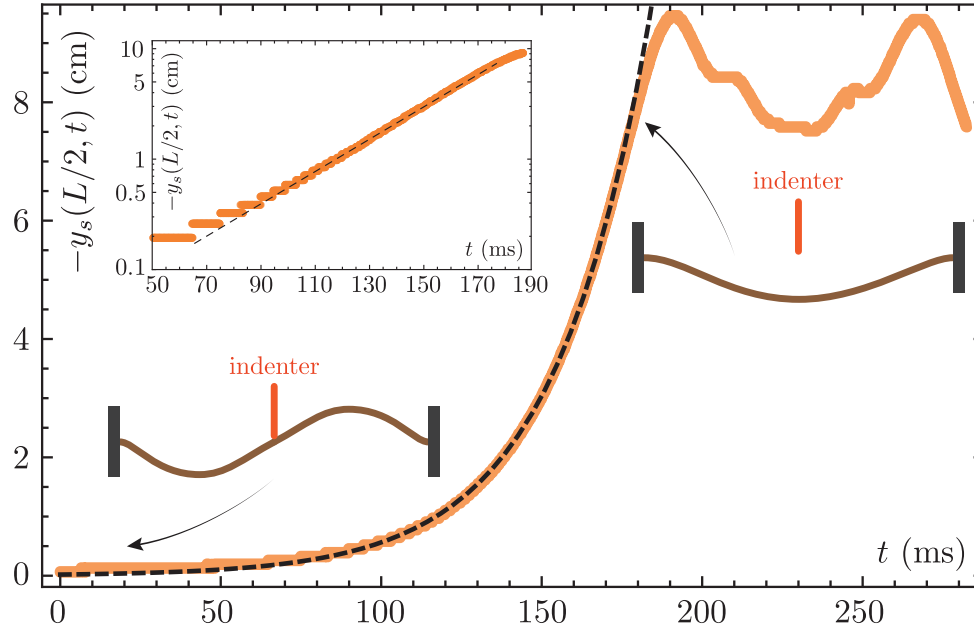


Figure 3.19 – Displacement of the middle point of a metal ruler as a function of time in the case of an indentation-induced snap-through: the experimental setup is similar to the one used in Fig. 3.18, with here $L = 67.9$ cm and $\Delta = 0.95L$. The orange line corresponds to the experimental measurements and the dashed black line is an exponential fit of the data. Inset: same data in a log-linear representation.

Once the strip has switched to the downward position, many oscillations occur to dissipate its kinetic energy (top right corner in Fig. 3.19).

Position of points located at different places on the strip – and not only the point located at the middle of the strip – exhibit a similar displacement versus time behavior, with the same growth rate for the exponential fit.

The same analysis is performed for various elastic strips and beams, ranging from millimetric polymer samples to one-meter metal rulers. For each sample, the growth rate

μ is extracted from the experimental data, and compared to the value extracted from the numerics $\mu = 24.26$. In Fig. 3.20, we plot $L^2/\mu = \tau_{\text{snap}}\sqrt{EI/\lambda}$ (where $\lambda = \rho_e A$ is the lineic mass of the beam) as a function of the length of the beam. The theoretical prediction, shown as a red dashed line, corresponds to $\tau_{\text{snap}} = (L^2/24.26)\sqrt{\lambda/EI}$. We observe a good agreement between the theoretical prediction and the experimental data, except a deviation for small polymer samples: this deviation could be attributed to viscoelastic dissipation inside the samples. In most cases, snap-through is induced by point-load indentation. However, we observe that using a dead load instead of controlling the displacement induces similar snapping times (recorded by fitting the displacement of the middle of the strip as a function of time by an exponential curve), even though the initial configuration of the strip is not a second buckling mode.

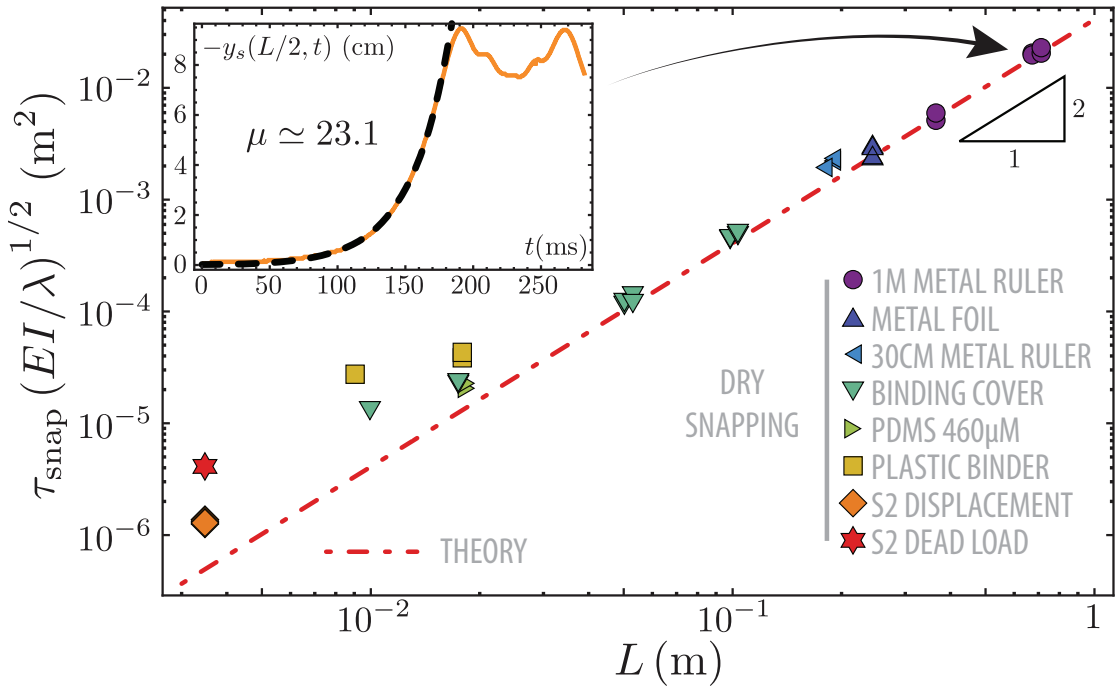


Figure 3.20 – Snap-through dynamics in the case of dry snap-through: $L^2/\mu = \tau_{\text{snap}}\sqrt{EI/\lambda}$ is plotted as a function of the length of the beam. The theoretical prediction (red dashed line) has a slope 1/2 in this log-log diagram. The experimental points correspond to displacement-induced and dead-load-induced snap-through experiments, with samples ranging from a one meter metal ruler to a millimetric PDMS strip (sample S2 (Table 3.1)). Inset corresponds to data shown in Fig. 3.19.

3.5.2. Snapping time for elastocapillary snap-through events

In the case of snap-through induced by a droplet, new phenomena could affect the dynamics, as the inertia of the drop or viscous dissipation inside the droplet. In Fig. 3.21, we compare snapping time recorded in the case of dry snap-through to elastocapillary snapping times, recorded by fitting the displacement of the middle of the strip as a function of time by an exponential curve. Experiments have been performed with samples of different sizes and different materials, with water droplets and with soap bubbles.

We observe no significant difference between colored points corresponding to dry snap-through, and white points corresponding to elastocapillary snap-through: the elastocapillary snapping time is thus determined mainly by beam bending dynamics. The droplet only triggers the instability, the dynamics being then ruled by elastic properties of the strip.

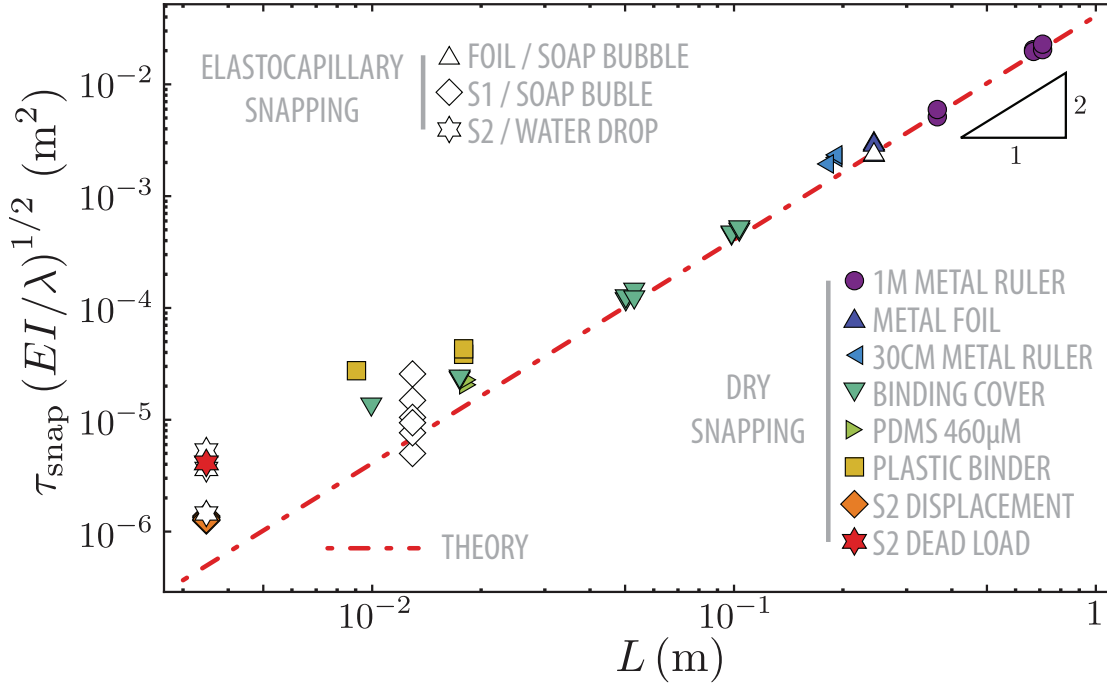


Figure 3.21 – Comparison between dry and elastocapillary snapping times. $\tau_{\text{snap}} \sqrt{EI/\lambda}$ is plotted as a function of the length of the beam. The theoretical prediction (red dashed line) has a slope 1/2 in this log-log diagram and corresponds to beam bending dynamics. Colored points correspond to dry snap-through experiments, while white points correspond to snap-through experiments with a droplet or a soap bubble (samples S1 and S2: see Table 3.1). No significant difference is observed between dry and elastocapillary snapping times.

3.6 Perspectives: viscous dissipation in the polymer

3.6.1. Analysis of the snapping time for small polymer samples

A deviation from the theoretical dry snapping time is observed for small PDMS samples, as shown in Fig. 3.21: for strips smaller than a few centimeters, the snapping time is longer than expected, both for dry and elastocapillary snap-through. This phenomenon might be explained by viscoelasticity properties of polymer samples: if some energy is dissipated in the polymer strip, the snap-through dynamics is likely to be slowed down.

In elastocapillary phenomena, energy dissipation processes can happen both in the polymer strip and in the liquid droplet. A droplet sliding down on a PDMS strip clamped at one end constitutes a simple configuration where these two processes are in competition. In the case of a viscous droplet on a non-viscoelastic polymer, dissipation might occur mainly in the droplet, while in the case of a less viscous droplet on a viscoelastic polymer,

dissipation might occur mainly in the polymer strip. Consequently, we design sliding droplet experiments to identify dissipation processes at play in this kind of elastocapillary phenomena.

3.6.2. Design of sliding droplets experiments

When a droplet is deposited on a sufficiently flexible strip, it deforms the strip macroscopically. We consider such a droplet sliding down on an elastic strip clamped at one end (Fig. 3.22(a)). The macroscopic deformation is moving together with the droplet, and dissipation processes are likely to happen in the whole region of the strip that is deformed by the droplet. A parallel can be made between this experiment – where a water droplet sliding down on an elastic strip generates the propagation of a deformation along the strip – and *ruck in a rug* experiments performed in [154, 155, 156] – where a fold in an elastic strip lying on an inclined plane propagates, driven by gravity (Fig. 3.22(b)). These studies show that the ruck reaches a constant speed, but the dissipation mechanisms at play are unclear: in [154], air drag and viscous dissipation within the ruck are briefly mentioned, while the role of air drag is shown to be negligible in [155]. Finally, peeling events at the two ends of the ruck are shown to be a good candidate for the dissipation process in [156].

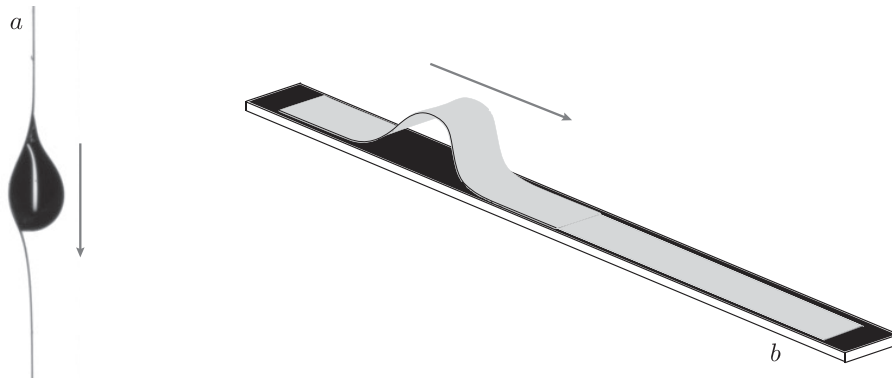


Figure 3.22 – Similarities between experiments featuring a droplet sliding on a strip clamped at one end (a) and ruck in a rug experiments where a fold in an elastic strip propagates due to gravity (b), reproduced from [154].

Experiments with a droplet sliding on a polymer strip involve no peeling events as there is no underlying substrate, but dissipation processes are likely to occur both in the droplet and in the strip. However, the viscous properties of the droplet and viscoelasticity of the elastomer can be changed independently.

Beyond the dissipation processes caused by macroscopic deformations, a water droplet lying on a sufficiently soft elastomer is likely to raise a microscopic ridge at the triple line (as shown in section 1.4) which is likely to dissipate energy as well [110]. The dissipation processes at play might then change when going from a flexible strip to a soft bulk polymer, from macroscopic deformations to localized deformations at the triple line. However, when designing sliding droplet experiments both on flexible strips and on bulk substrates, we observed an unexpected sliding behavior: a droplet sliding down on a silicone elastomer strip or plate seems to exhibit two successive regimes with two different constant speeds.

We focus on the understanding of this surprising phenomenon in the following chapter.

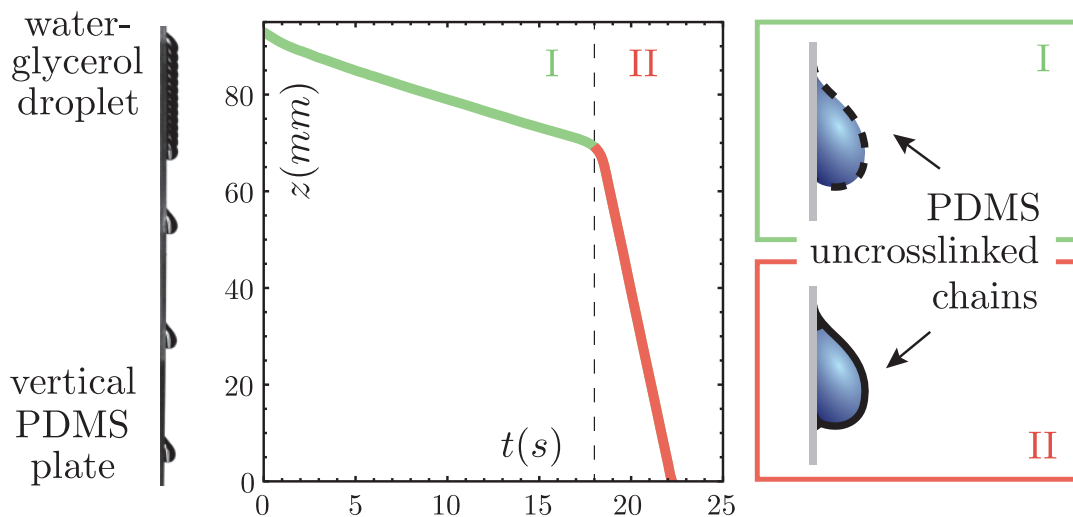
The study that has been presented in this chapter 3 is the subject of our article on elastocapillary snap-through [157], published in Physical Review Letters and reproduced in the appendix of this manuscript.

Conclusion

We have shown that capillary forces play a major role in the triggering of a snap-through instability with a water droplet: when a droplet is deposited above or under a strip in the upward configuration, considering only the weight of the droplet leads to an incorrect prediction of the snap-through threshold. Laplace pressure and surface tension forces act as two effective bending moments that promote the instability when a droplet is deposited above a strip buckled in the upward configuration and hinder it when deposited below. These bending moments are the key point that explains why we manage to successfully trigger an elastocapillary snap-through instability even against gravity. In the case of dry snap-through, the elastic energy stored in the system before the instability is suddenly released in the form of kinetic energy and is essentially lost. However, in our elastocapillary setup, part of the energy is used to lift the liquid drop. Spin-off versions of our elastocapillary-induced snap-through setup include both upscaled experiments using soap bubbles and a remotely induced snap-through device taking advantage of condensation of water vapor. These experiments demonstrate that elastocapillary snapping is a good candidate to engineer microactuators or moisture sensors, constructively using capillarity at small scales. We have then built experimental as well as theoretical phase diagrams showing the equilibrium and stability of drop-strip systems as a function of the position and the weight of the deposited droplet. The snap-trough dynamics has eventually been investigated to gain a better knowledge of the time required to switch from one equilibrium position to the other. In the case of elastocapillary snap-through, the droplet only triggers the instability, and the subsequent dynamics is ruled by elasticity. The existence of a small deviation from the theoretical snapping time for small polymer samples lead us to design sliding droplet experiments, analyzed in the following chapter.

Chapter 4

An unexpected behavior for droplets dynamics on silicone elastomers



In this chapter, we observe and investigate an unexpected behavior in the dynamics of aqueous droplets on vertical plates of silicone elastomers. During its descent, a droplet moving on a silicone elastomer plate surprisingly exhibits two regimes with two constant speeds and a sharp transition between them. We demonstrate that this two-regime behavior is due to the presence of uncrosslinked oligomers in the silicone plate. Silicone uncrosslinked chains are gradually collected by the droplet during its descent, and affect the surface tension of the droplet: we show that the sharp transition in speed coincides with a sudden surface tension variation. During the first regime, the dynamics is set by the competition between gravity, capillary pinning forces, and viscous dissipation in the droplet, whereas in the second regime, the dynamics of the droplet is also affected by the presence of the oil cover.

Contents

4.1	Two-regime dynamics of an aqueous droplet on a silicone elastomer	93
4.1.1.	Context	93
4.1.2.	From elastomer strips to elastomer plates	93
4.1.3.	Varying different parameters	96
4.2	Pieces of evidence to understand the two-regime behavior	98
4.2.1.	Tracking the motion inside a droplet: rolling rather than sliding	98
4.2.2.	Changing the temperature of the liquid used for droplet deposition	99
4.2.3.	Disturbing the triple line motion with an antistatic gun	100
4.2.4.	Using an obstacle to stop a droplet during its descent	101
4.2.5.	Turning the experimental setup upside down to re-use the same droplet on the same material	101
4.3	Role of uncrosslinked chains in the droplet dynamics	103
4.3.1.	Dow Corning Sylgard 184 PDMS uncrosslinked oligomers	103
4.3.2.	Washing procedure to remove uncrosslinked chains	104
4.3.3.	Droplet dynamics on washed elastomer plates	104
4.3.4.	Droplet dynamics on re-swelled elastomer plates	104
4.3.5.	Uncrosslinked chains collected by each droplet	106
4.3.6.	Composition of the uncrosslinked oligomers oil	106
4.3.7.	Link with adhesion-induced phase separation experiments	107
4.4	Surface tension measurements	108
4.4.1.	Useful insight from the literature	109
4.4.2.	Drawbacks of the hanging-drop method	110
4.4.3.	Surface tension of a liquid bath made of droplets collected in a Petri dish	110
4.4.4.	Results with Petri dishes of different sizes and made of different materials	111
4.4.5.	Generalization to water-glycerol mixture droplets	112
4.5	Quantitative speed measurements	113
4.5.1.	Experimental observations	113
4.5.2.	Discussion of the results obtained for the first regime	115
4.5.3.	Discussion of the results obtained for the second regime	116
4.6	Consequences and potential applications	120
4.6.1.	A simple test to evaluate the presence of uncrosslinked oligomers	120
4.6.2.	Similarities between our elastomer samples and SLIPS substrates: a <i>delayed slippery surface</i>	121

4.1 Two-regime dynamics of an aqueous droplet on a silicone elastomer

4.1.1. Context

As described in the last paragraph of chapter 3, investigating the sources of energy dissipation in elastocapillary experiments lead us to deposit droplets on vertical elastomer strips and plates. The initial goal was to link the final speed reached by a droplet to the different dissipation sources: viscoelasticity in the elastomer sample and viscous dissipation inside the drop. However, we observed that a droplet deposited on a Dow Corning Sylgard 184 PDMS strip exhibited not only one but two speeds. As shown in Fig. 4.1, the droplet begins moving at a first regime with constant speed U_1 , followed by a transition to a second regime with a faster constant speed U_2 . These findings contrast with experimental results found in the literature on droplet dynamics on various substrates [36, 50]: usually, a droplet rapidly reaches one constant final speed, as described in chapter 1. Our primary goal thus became to understand why this astonishing two-regime behavior occurs in our experimental setup.



Figure 4.1 – A 10% water - 90% glycerol droplet of volume $7 \mu\text{L}$ is deposited on a Dow Corning Sylgard 184 PDMS strip of thickness $56 \mu\text{m}$ and width 1.3 mm . The strip is clamped at the top and left free at the bottom. Two regimes with two different speeds can be identified: snapshots are taken every 2.25 seconds, and the 14 pictures presented here begin 60s after the deposition of the droplet, to focus on the transition from the first to the second regime.

4.1.2. From elastomer strips to elastomer plates

a) Strips and plates: our definition

We first need to refine what is called *strip* and *plate* in this chapter. As shown in Fig. 4.2, an object classified as a *strip* in this work is a slender elastomer object of dimensions h , w , and L chosen so that $h \ll w \ll L$ and $w \leq R_{\text{drop}}$, where R_{drop} is the droplet radius. A water droplet deposited on such a strip is constrained in width, as the footprint of the droplet on the strip is bounded by two parallel lines, the borders of the strip. A macroscopic deformation of the strip occurs provided that $R_{\text{drop}} \geq L_{ec}$, where

L_{ec} is the elastocapillary length. This condition is satisfied for the drop-strip system shown in Fig. 4.1.

In contrast, a thick *plate* is a material of thickness h of a few millimeters: it satisfies not only the condition $h \gg h_{\text{ridge}}$ (where h_{ridge} is the dimension of the wetting ridge raised at the triple line), but also $R_{\text{drop}} \ll L_{ec}$, meaning that there is no macroscopic deformation of the plate. The deformation of the substrate is microscopic and located at the triple line. The height of the wetting ridge is of order of magnitude $h_{\text{ridge}} = \gamma/E = 40$ nm for a PDMS sample of Young's modulus $E = 1.8$ MPa and a water droplet of surface tension $\gamma = 72$ mN/m: its influence might thus be neglected. In particular, the PDMS we use is considered as *rigid* compared to the elastomers used in the literature on wetting ridges described in section 1.4. The width w and length L of the plate are both much bigger than the diameter of a droplet in order to prevent geometrical constraints due to the borders of the sample. For convenience, PDMS plates are used lying on a rigid PMMA plate. As no macroscopic deformation of the PDMS plates is observed under capillary effects, using a rigid mounting under them should not modify anything in our experiments.

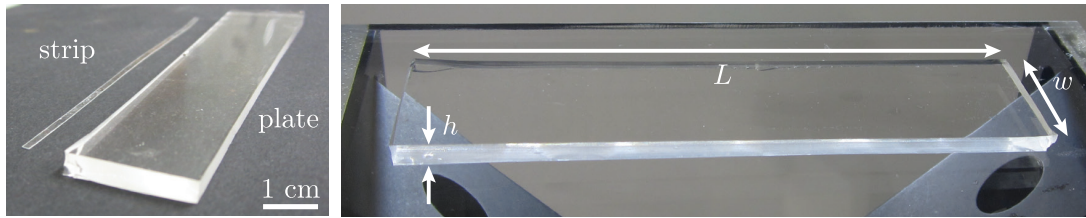


Figure 4.2 – Illustration of the difference between what is called *strip* and what is called *plate* in this chapter. A PDMS strip is a slender elastomer object of dimensions h , w , and L chosen so that $h \ll w \ll L$ and $w \leq R_{\text{drop}}$, where R_{drop} is the droplet radius. A PDMS plate is a thick and large PDMS sample, with $R_{\text{drop}} \ll L_{ec}$, where R_{drop} is the droplet radius and L_{ec} the elastocapillary length. The width w and length L of the plate are several times larger than the droplet diameter.

b) First experiments on PDMS strips

Our first observation of a two-regime behavior occurred when performing experiments on Dow Corning Sylgard 184 PDMS strips clamped at one end and free at the other end. In Fig. 4.1, the pictures on the right show that the deformation of the strip becomes larger when the weight of the part of the strip located below the droplet becomes smaller. However, this is not enough to explain the existence of a two-regime behavior, which remains when working with a strip under tension. Experiments are carried out both with strips clamped at both ends, and with strips hanging a weight at the bottom end. These two techniques put the strip under tension, and thus reduce the macroscopic elastocapillary deformations. There is however a small difference between these two setups: in the first case, the end of the strip is not allowed to move at all, whereas in the second case, the strip is under tension but the position of the end of the strip is still free to move (we impose a force and not a displacement). In all these experiments, the same qualitative two-regime behavior is observed.

Another observation is that the two sides of a PDMS strip are not equivalent. When

a droplet moves on the side of the strip that cured in contact with air, the speeds in the first and in the second regimes are larger than when the experiment is performed on the side of the strip that cured in contact with the glass substrate (see chapter 2 for manufacturing protocols). For experiments presented in the following sections, we work with the sides of the samples cured in contact with air.

c) Generalization to PDMS plates

Using a thick plate instead of a thin strip modifies two ingredients that could affect the droplet dynamics: on a large and thick plate, there is no geometrical constraint on the width of the droplet, and no macroscopic elastocapillary deformation. However, the influence of macroscopic elastocapillary deformations has already been tested with experiments featuring strips under tension. Our results demonstrate that the geometry of the substrate – strip or plate – does not affect the existence of a two-regime behavior. Fig. 4.3 shows the two-regime dynamics of a 40% water - 60% glycerol mixture droplet of volume $21.5 \mu\text{L}$ deposited on a Dow Corning Sylgard 184 PDMS of thickness 3 mm. All height-versus-time graphs presented in this chapter are obtained by using the ImageJ Analyze Particles function on a binary video: the height of the droplet is in fact the height of the center of mass of the 2D projection of the droplet on the video frame.

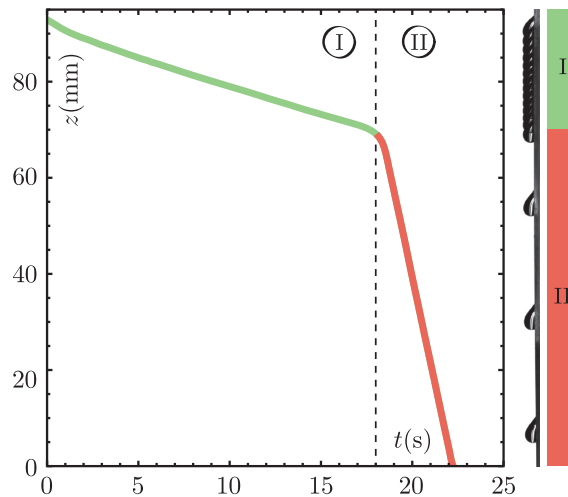


Figure 4.3 – A 40% water - 60% glycerol mixture droplet of volume $21.5 \mu\text{L}$ is deposited with no initial speed on a vertical PDMS plate. Two regimes with two different constant speeds are identified (I and II). The picture on the right consists of snapshots taken every 1.28 s and superimposed together.

In Fig. 4.3, we clearly identify two regimes with two constant speeds and a sharp transition between them. As the plate width is more than five times larger than the drop diameter, we conclude that the two-regime behavior is not due to geometrical constraints on the width of the droplet. In most experiments presented in this chapter, we choose to work with plates rather than with strips, to keep our system as simple as possible. Indeed, the literature about droplets dynamics is by far more abundant on plates than on strips, which allows us to compare our results to both experimental and theoretical results in the literature on droplet motion on various substrates.

4.1.3. Varying different parameters

a) Droplet dynamics on PDMS plates: influence of the droplet size and of the water-glycerol mixing ratio

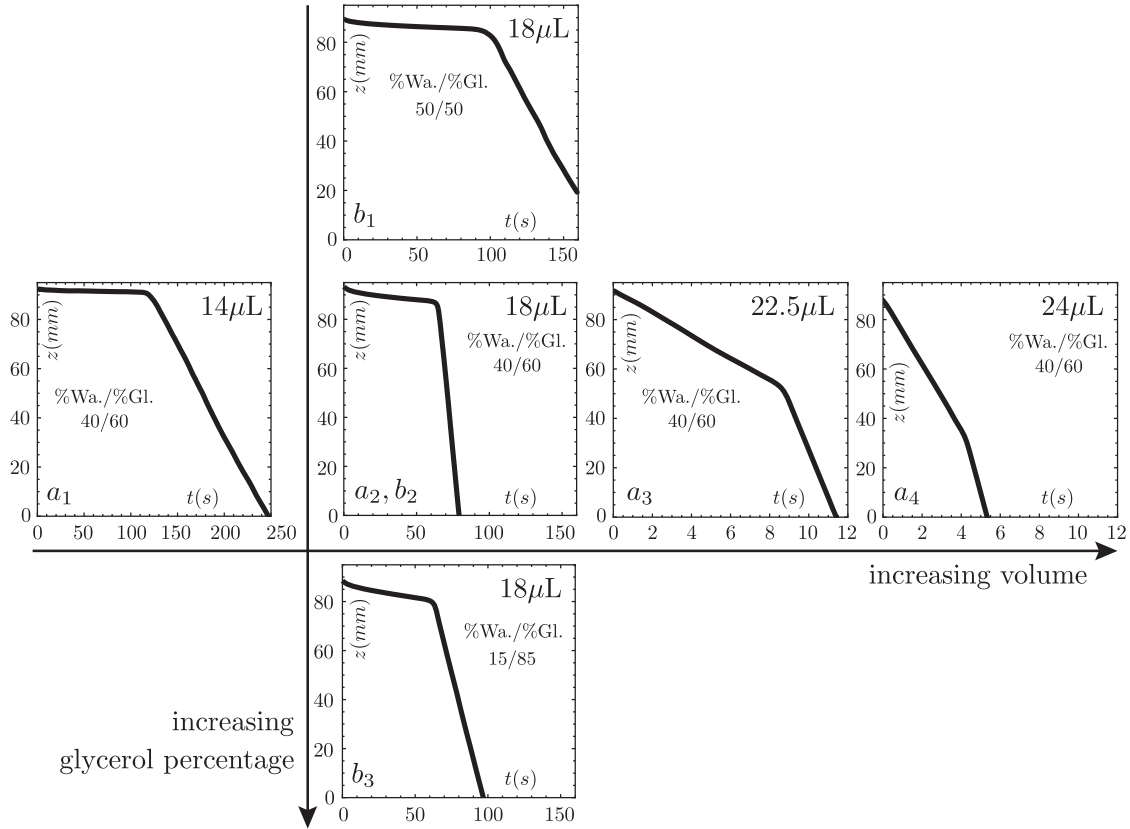


Figure 4.4 – Horizontal line: 40% water - 60% glycerol mixture droplets of volumes 14 μL (a_1), 18 μL (a_2), 22.5 μL (a_3), and 24 μL (a_4) are deposited with no initial speed on a vertical PDMS plate. The same qualitative two-regime behavior is observed when varying the droplet size, although the ratio between the first speed and the second speed varies. Vertical line: 18 μL droplets of 50% water - 50% glycerol (b_1), 40% water - 60% glycerol (b_2), and 15% water - 85% glycerol (b_3) mixtures are deposited with no initial speed on a vertical PDMS plate. The same qualitative two-regime behavior is observed when varying the water-glycerol mixing ratio.

Fig. 4.4(a) shows height-versus-time diagrams for various droplet sizes deposited on a vertical Dow Corning Sylgard 184 PDMS thick plate. The two-regime behavior remains for both small and large droplets. Apart from changing the droplet size, the liquid used for the droplet can be modified. As explained in chapter 2, we choose to work with water-glycerol mixtures because of their non-swelling properties when used in contact with PDMS: as the water-glycerol mixing ratio is varied (so that the viscosity of the liquid is varied over almost two decades, see chapter 2), the two-regime behavior also remains (Fig. 4.4(b)). Quantitative speed measurements obtained when varying both the droplet size and the water-glycerol mixing ratio are presented and discussed in section 4.5.

b) Droplet dynamics on other silicone elastomers

Although we choose to focus on experiments on Dow Corning Sylgard 184 PDMS in the following sections, the same qualitative two-regime behavior is observed on several other silicone elastomers (see chapter 2 for elastomer samples characterization). In Fig. 4.5(a),(b),(c) and (d), we show examples of droplet dynamics on Esprit Composite RTV EC13 and EC33, Elite Double 22, and PDMS cured during 24h at 120°C, all exhibiting 2 regimes.

On the contrary, droplets deposited on a glass plate (treated so that the contact angle of water on this plate is roughly the same as on a PDMS plate), on a latex plate, and on a polyester plate only exhibit one regime with one constant speed (Fig. 4.5(e),(f),(g)) These results are consistent with droplet dynamics on various substrates described in the literature [36, 50] (see chapter 1). In this case, the single final speed is determined by the competition between the weight of the droplet, capillary pinning forces, and viscous dissipation inside the droplet.

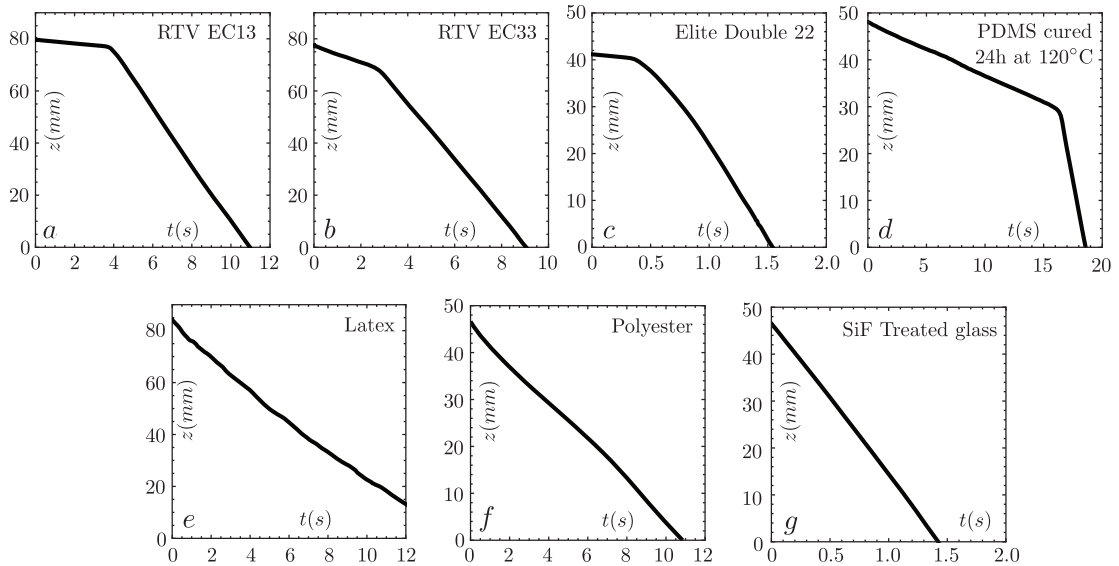


Figure 4.5 – (a) 40% water - 60% glycerol mixture droplet of volume $18\mu\text{L}$ deposited on a RTV EC13 plate. (b) 40% water - 60% glycerol mixture droplet of volume $18\mu\text{L}$ deposited on a RTV EC33 plate. (c) 50% water - 50% glycerol mixture droplet of volume $15\mu\text{L}$ deposited on an Elite Double 22 elastomer sheet of $147\mu\text{m}$ thickness manufactured on top of a plastic cover. (d) 40% water - 60% glycerol mixture droplet of volume $14\mu\text{L}$ deposited on a Dow Corning Sylgard 184 elastomer sheet of around $100\mu\text{m}$ thickness on top of a glass slide, cured during 24h at 120°C. (e) 40% water - 60% glycerol mixture droplet of volume $22\mu\text{L}$ deposited on a rigid plate covered with a latex membrane. (f) 40% water - 60% glycerol mixture droplet of volume $18\mu\text{L}$ deposited on a polyester plate. (g) 40% water - 60% glycerol mixture droplet of volume $18\mu\text{L}$ deposited on a glass plate (SiF treated, to have droplets contact angles comparable to those on PDMS). On (a),(b),(c),(d), two regimes are clearly identified, whereas on (e),(f),(g), only one regime is present.

Rapid tests were also performed on Ecoflex 50 and Ecoflex gel. On these materials, we do not clearly identify two regimes, but the behavior of the droplet just after withdrawing the micropipette can be analyzed either as a single regime-behavior or a two-regime

behavior with a fast first regime. Further analysis would be required on these samples.

4.2 Pieces of evidence to understand the two-regime behavior

This section describes a series of experiments performed towards the understanding of the mechanism underlying the two-regime behavior. Some experiments in this section are carried out with PDMS strips, but similar results are expected on PDMS plates (the sample type is specified in each section).

4.2.1. Tracking the motion inside a droplet: rolling rather than sliding

The two-regime behavior could come from a sliding-to-rolling (or rolling-to-sliding) transition. A change in the motion inside the droplet could affect the rate of viscous dissipation inside the liquid and thus result in a change in speed for the droplet. To test this hypothesis, our strategy consists in incorporating tracer particles inside the droplet. We perform experiments both with glitter and with cocoa particles as tracers, and both show a rolling motion in the first and in the second regime. We preferred cocoa particles as the glitter particles are too big to act as passive tracer particles (they are only ten times smaller than the radius of the droplet) and are deposited on the PDMS substrate when they are close to the receding triple line. Results shown in Fig. 4.6 are obtained with cocoa particles incorporated to a $17 \mu\text{L}$ droplet of a 40% water - 60% glycerol mixture, deposited on a PDMS plate.

These particle-tracking experiments give evidence that the two-regime behavior is not explained by a sliding-to-rolling transition, or rolling-to-sliding transition.

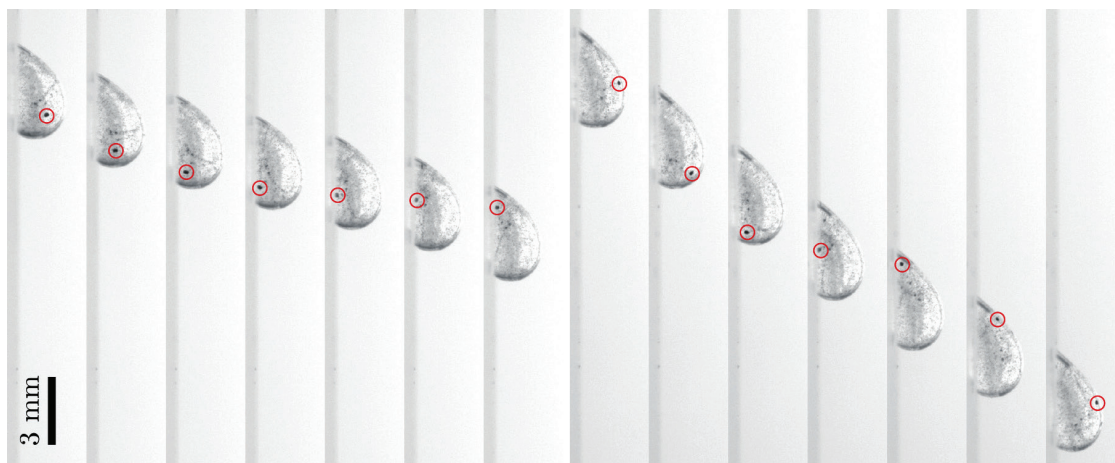


Figure 4.6 – Cocoa particles are incorporated into a 40% water - 60% glycerol mixture droplet to track liquid motion inside the droplet, when deposited on a PDMS plate. The motion of one aggregate of cocoa particles (more visible on the video than smaller cocoa particles) is isolated using red circles. (a) Motion during the first regime. Snapshots are taken every second. (b) Motion during the second regime. Snapshots are taken every 0.2 second. In both regimes we observe a rolling motion: the speed transition is not explained by a sliding-to-rolling transition.

4.2.2. Changing the temperature of the liquid used for droplet deposition

As the experimental setup includes heat sources such as the lighting and the camera, a change in the droplet temperature during the experiment could affect the droplet dynamics and be a candidate for the mechanism underlying the two-regime behavior. If the droplet is initially cold, and is heated during its descent, its viscosity and surface tension are decreased, which could result in a increase of its speed. To test this hypothesis, we perform experiments with different initial temperatures for the liquid bath used for pipetting the droplets: we deposit 50% water - 50% glycerol mixture droplets of volume $9 \mu\text{L}$ on a PDMS strip with an electronic micropipette. The room temperature is 16°C , and pipetting is performed in liquid baths of different temperatures: 16°C , 22°C , 28°C , 34°C , 44°C , and 55°C . As the micropipette tip is not insulated, the temperature of the droplet when it is deposited (a few seconds after pipetting) might differ from the temperature of the liquid bath, which explains why we choose to explore such a large range of liquid bath temperatures. A droplet warmer than the PDMS sample temperature should cool down during the experiment, and thus be subjected to a temperature change during its descent.

In all the experiments, we observe a two-regime behavior, with a second speed higher than the first speed (Fig. 4.7), as in the experiments performed with a liquid at room temperature. This result excludes the hypothesis of a two-regime behavior due to a temperature change of the droplet during the experiment: if this hypothesis was true, using a droplet warmer than the sample should lead either to a two-regime behavior with a final speed slower than the initial speed, or to a one regime behavior.

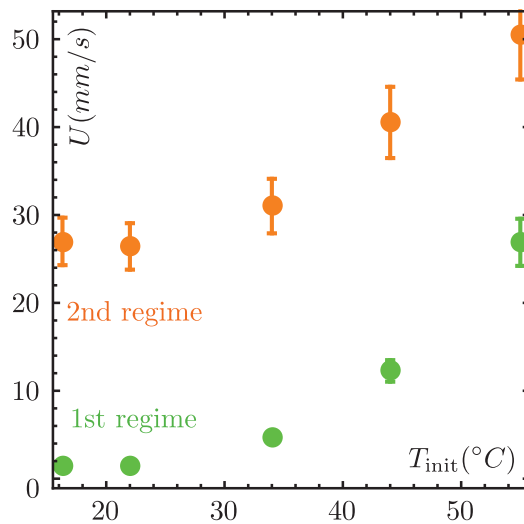


Figure 4.7 – Speed measured in the first (green) and second (red) regime as a function of the temperature of the liquid bath used for pipetting. Speeds are measured on the videos with the following protocol: the trajectory of the droplet is plotted (with the reslice tool of ImageJ) to extract the two zones in which the speed is constant. The two constant speeds are then evaluated by measuring the distance traveled by the droplet between the first and last frame of each zone. Each point shown here is an average of two measurements, and the error bars evaluate the reproducibility of the results.

4.2.3. Disturbing the triple line motion with an antistatic gun

One of the envisioned hypothesis was that the droplet could accumulate static charge by friction on the polymer. To disrupt this phenomenon, we use an antistatic gun (Zerostat MILTY, Fig. 4.8), which is a device useful to keep films, glass, or plasticware dust and lint free, working with two powerful piezoelectric crystals. When the trigger of this device is squeezed, a positive ions flow is generated, and when it is relaxed, a negative ions flow is generated. Each squeeze of the trigger corresponds to a 1.5 Coulomb charge. Using this device on a water-glycerol mixture droplet moving on a PDMS plate results in a small motion of the triple line. The experiment shown in Fig. 4.8 consists in using several times this antistatic gun during the descent of a water-glycerol mixture droplet on a PDMS plate. We plot a spatiotemporal diagram: the pixel line in red is recorded as a function of time. When the antistatic gun is used, it is put between the camera and the droplet, which results in a black vertical line in the spatiotemporal diagram. Between these vertical lines, we see a large black line, which corresponds to the trajectory of the droplet, and is bounded by the receding line and front edge of the droplet (as the advancing contact angle is larger than 90° , we do not see the advancing line but the front edge of the droplet on a front side video).

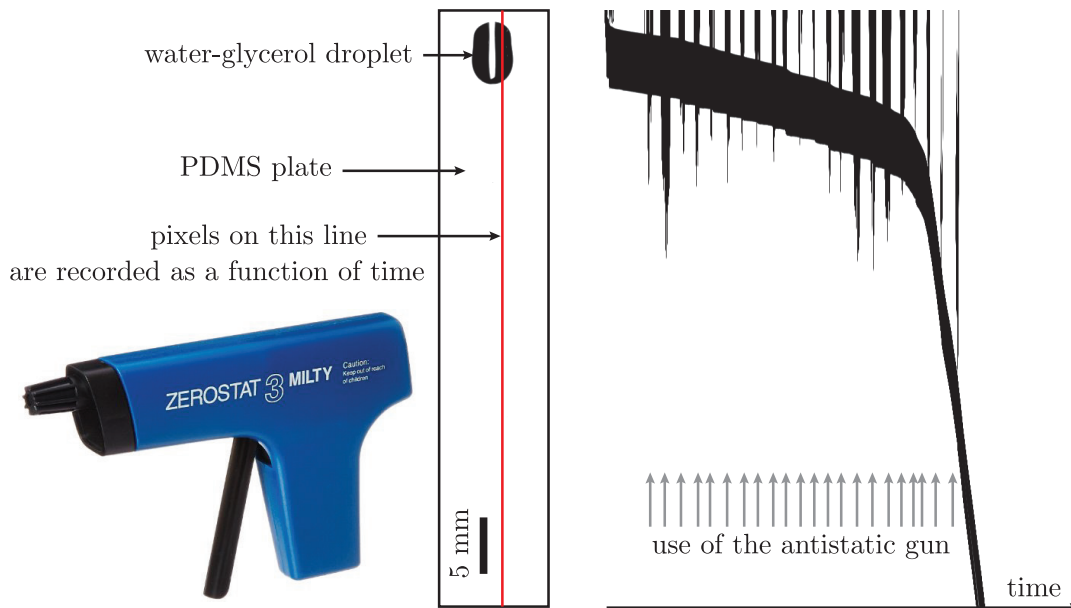


Figure 4.8 – Zerostat MILTY antistatic gun, and its use in our experiments: a 50% water - 50% glycerol mixture droplet of volume $25 \mu\text{L}$ is deposited on a vertical PDMS plate. During its descent, we record the pixel line shown in red, and we plot this line as a function of time (spatiotemporal diagram). The large black line shows the droplet trajectory (delimited by the receding line and the front edge of the droplet), and the vertical black lines are present only when the antistatic gun is used. The droplet contact lines move when the antistatic gun is used but the global trajectory is not significantly changed compared to a dynamics without antistatic gun shoots.

Using the antistatic gun affects the droplet dynamics by inducing small displacements of the triple line, but does not affect the global dynamics with two regimes; the time necessary to reach the second regime is of the same order of magnitude as in experiments

without using the antistatic gun. Although this experiment does not bring quantitative results, it shows the robustness of the two-regime behavior, which is reproducible even when we try to disrupt the droplet trajectory.

4.2.4. Using an obstacle to stop a droplet during its descent

Another method to disrupt a droplet trajectory is to put an obstacle on its way. We use a micropipette tip covered with Parafilm to stop the droplet during its descent: this obstacle can be easily removed without pulling liquid off the droplet, taking advantage of the hydrophobic properties of Parafilm. We show in Fig. 4.9 the spatiotemporal diagram of a water-glycerol mixture droplet deposited on a vertical PDMS strip, stopped by an obstacle just after reaching the second regime.

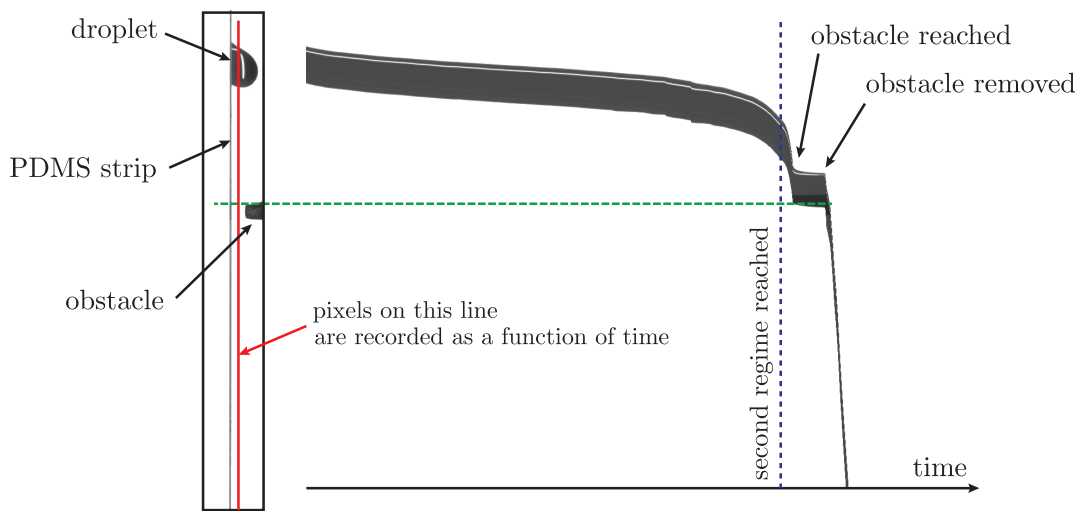


Figure 4.9 – A water - glycerol mixture droplet is deposited on a PDMS strip, and a micropipette tip covered with Parafilm is used as an obstacle that stops the droplet once it has reached the second regime. The tip is then removed, allowing the droplet to continue its descent. The droplet rapidly reaches the speed corresponding to the second regime.

Although the droplet was stopped, it rapidly reaches a second regime dynamics as soon as the obstacle is removed. This result highlights that the droplet speed regime depends on its history and not only on its initial speed, and leads us to design another simple experiment. A setup that can be turned upside down allows for re-using the same droplet on the same sample for several successive descents without requiring any obstacle to stop the droplet.

4.2.5. Turning the experimental setup upside down to re-use the same droplet on the same material

We design the following setup: a PDMS strip or plate is attached to an adjustable angle mounting plate, free to rotate over 180° , with two mechanical stops for the two vertical positions of the sample (Inset of Fig. 4.10). This setup allows us to rapidly but smoothly turn the setup upside down, in order to re-use the same droplet on the same sample for several descents. Experiments are carried out both on strips and on plates.

Results presented in Fig. 4.10 correspond to experiments on a PDMS plate, the droplet behavior is qualitatively the same on a PDMS strip. During the first descent, a droplet exhibits two successive regimes, while during the second descent, only one regime is observed. The speed of this single regime corresponds to the speed in the second regime of the first descent. The setup can be turned upside down several times, and the same result is found for all the following descents. In Fig. 4.10, we record the odd descents (n° 1 (black), 3 (light blue), 5 (medium blue), 7 (dark blue)) for one single droplet. However, due to video acquisition constraints, the even descents (n° 2 (light rose), 4 (medium/light rose), 6 (medium rose), 8 (dark rose)) are recorded for another droplet, all parameters being kept constant between the two experiments. The small variability on the droplet volumes delivered by the micropipette explains the slight variation in speeds between the odd and even descents experiments: the droplet used for the even descents was certainly a few percent larger in volume than the droplet used for the odd descents. Inside each set of descents (3,5,7) and (2,4,6,8), the droplet constant speed decreases slightly as a function of the number of the descent: this can be explained by a small decrease of the droplet volume by evaporation.

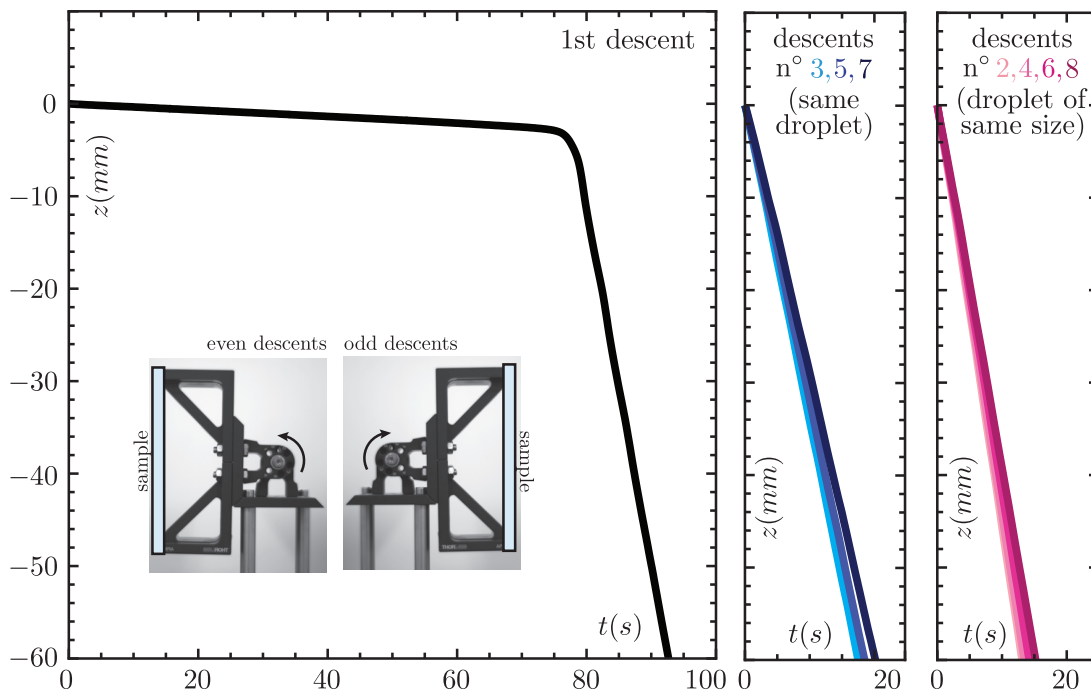


Figure 4.10 – A 40% water - 60% glycerol mixture droplet of volume $15 \mu\text{L}$ is deposited on a Dow Corning Sylgard 184 PDMS plate, attached to an adjustable angle mounting (Inset). The deposition is performed on a plate in the horizontal position, and the adjustable mounting angle is alternatively set to 0° and 180° to re-use the same droplet for several descents. $z = 0$ corresponds for each trajectory to the height of the droplet at the beginning of each descent. The first descent comprises 2 regimes, while the following descents only exhibit one single regime, at the speed corresponding to the second regime of the first descent.

Two possible phenomena could cause the difference observed between the first descent and the following descents:

- the droplet is modified during its first descent
- the substrate surface is modified by the droplet during its descent.

We can easily get rid of the second hypothesis by looking at a droplet moving just behind another droplet: both the leading and following droplets exhibit two regimes. These observations advocate for a modification of the droplet during the first descent: when reaching the second regime, the droplet properties probably differ from those of a droplet of the initial water-glycerol mixture used.

4.3 Role of uncrosslinked chains in the droplet dynamics

4.3.1. Dow Corning Sylgard 184 PDMS uncrosslinked oligomers

The manufacturing protocol of our Dow Corning Sylgard 184 PDMS samples has been described in chapter 2: the resulting elastomer is a crosslinked network of poly-(dimethylsiloxane) polymer chains. However, when PDMS oligomers are crosslinked to form the polymer network, a few oligomer chains are not incorporated into the polymer matrix. A PDMS sample thus contains uncrosslinked low-molecular-weight oligomers, which can be removed from the bulk PDMS by using a swelling solvent. An extraction procedure using chloroform as a solvent is reported in [158], but several solvents can be used to extract uncrosslinked chains. Fig. 4.11, reproduced from [128], shows the relationship between the percentage of extracted chains and the swelling ratio D/D_o of a solvent, where D is the length of an elastomer sample when it is completely immersed in the solvent (at a swelling equilibrium) and D_o is the length of the dry PDMS.

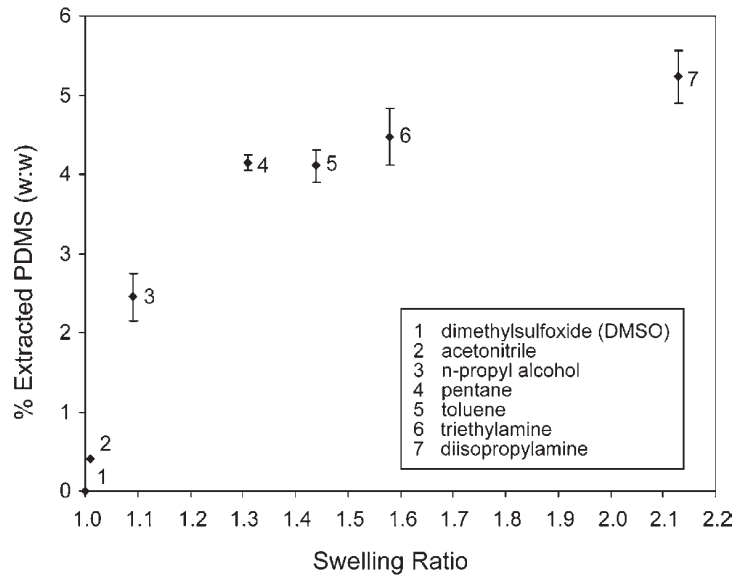


Figure 4.11 – Relation between the percentage of extracted chains with a solvent and the swelling ratio of PDMS in this solvent, reproduced from [128].

In order to understand if the uncrosslinked chains play a role in the two-regime behavior that we observe on silicone elastomers, we worked with Antoine Chateauminois

(SIMM, ESPCI) to perform washing experiments to remove as much uncrosslinked chains as possible from our PDMS samples.

4.3.2. Washing procedure to remove uncrosslinked chains

We extract uncrosslinked chains from our PDMS samples by using toluene as a swelling solvent. The washing procedure is the following:

1. PDMS samples are placed for one week in a toluene bath, which is renewed every day in order to keep the concentration in extracted PDMS oligomers low.
2. During a second week, PDMS substrates are de-swollen by progressively replacing toluene by a poor solvent of PDMS, namely ethanol. Indeed, ethanol has a PDMS swelling ratio smaller than that of toluene (Table 2.4).
3. The samples are finally placed in a vacuum oven to evaporate all the solvents.

Each sample is weighted before and after the washing procedure: results are shown in Table 4.1. The removed uncrosslinked chains constitute around 5% of the total weight of our PDMS samples.

Initial mass (g)	Final mass (g)	Variation (%)
2.41	2.27	5.8%
10.16	9.67	4.8%
8.71	8.21	5.7%

Table 4.1 – Mass variation of the Dow Corning Sylgard 184 PDMS samples treated with our washing procedure.

4.3.3. Droplet dynamics on washed elastomer plates

When depositing a droplet on a washed elastomer sample, we observe that the droplet dynamics comprises only one single regime. This one-regime behavior on washed samples is observed for various droplet volumes and various water-glycerol mixing ratios, from pure water to 90% glycerol mixture. As an example, we show in Fig. 4.12 the dynamics of a 21.5 μL droplet of 40% water - 60% glycerol mixture on a washed PDMS plate. **This experiment is a clear evidence of the crucial role played by the free oligomers of the substrate**, as removing the uncrosslinked chains allows us to get rid of the unusual two-regime behavior.

4.3.4. Droplet dynamics on re-swelled elastomer plates

The key role of uncrosslinked chains is investigated further by re-swelling a washed sample from the previous paragraph (on which one single regime is identified) with a commercial PDMS v50 oil (Sigma Aldrich). We gently deposit a small amount of v50 oil at the PDMS sample surface and absorb the excess with a paper towel. Although we do not control the exact amount of oil absorbed by PDMS, this experiment gives interesting qualitative results. We show in Fig. 4.13 the dynamics of a 50% water - 50% glycerol mixture droplet of volume 18 μL on a PDMS sample washed with toluene and

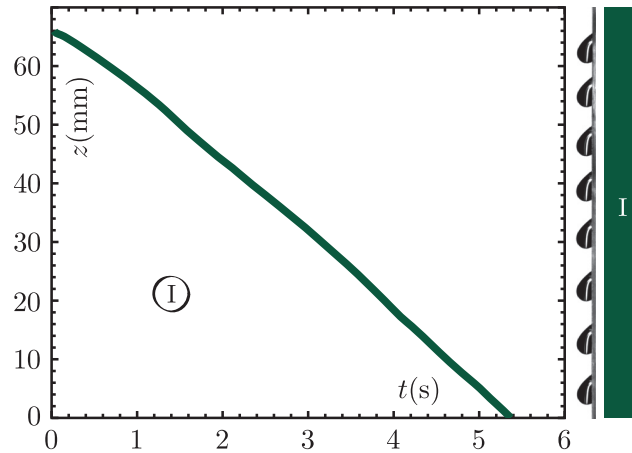


Figure 4.12 – A 40% water - 60% glycerol mixture droplet of volume $21.5 \mu\text{L}$ is deposited on a vertical PDMS plate treated using our washing procedure (with toluene as a swelling solvent). A single regime is identified. The picture on the right consists of snapshots taken every 0.64s and superimposed together.

re-swelled with v50 silicone oil. This experiment enables us to recover the two-regime behavior, and highlights once again the role of uncrosslinked oligomer chains. Indeed, the absorbed silicone oil plays the role of the uncrosslinked chains in the case of an untreated sample. A better control of the quantity of oil absorbed in the PDMS sample could lead to interesting quantitative studies, and is part of the perspectives of this work.

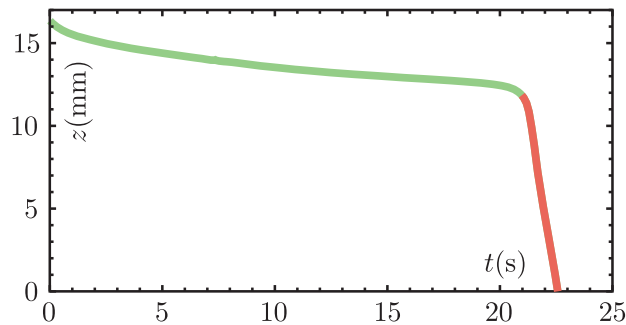


Figure 4.13 – A 50% water - 50% glycerol mixture droplet of volume $18 \mu\text{L}$ is deposited on a vertical PDMS plate that has been washed with toluene and re-swelled with v50 silicone oil. Two speed regimes are identified.

These experiments show that the uncrosslinked chains are responsible for the two-regime behavior, but do not give details on how these chains cause a sudden speed change for the droplet: the macroscopic observation of the dynamics of an aqueous droplet is the consequence of a microscopic mechanism at the scale of the polymer network. The following step is to clarify the role of these uncrosslinked chains in the droplet dynamics.

4.3.5. Uncrosslinked chains collected by each droplet

Uncrosslinked chains responsible for the two-regime behavior might migrate onto the droplet surface, as PDMS oil has a positive spreading parameter on water. Unfortunately, an hypothetical oil film on a single droplet is invisible to the naked eye. However, collecting 1500 such droplets in a beaker after their two-regime descent on an untreated PDMS sample results in a direct visualization of oil at the surface of the beaker, as shown in Fig. 4.14. The control experiment on a toluene-treated PDMS sample leads to no visible oil at the surface of the beaker.

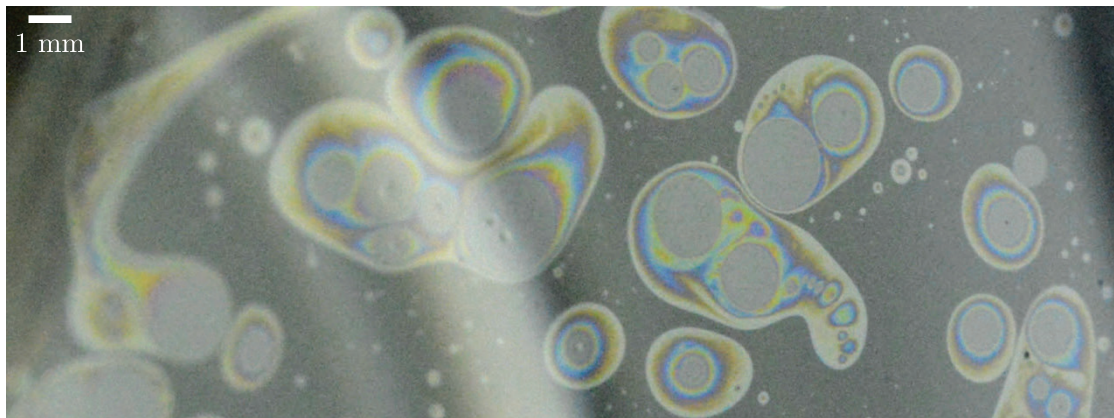


Figure 4.14 – Oil collected by 1500 droplets ($33 \mu\text{L}$ each) after their two-regime descent on untreated PDMS, at the surface of a 50 mL beaker of diameter 4.2 cm. The colored zones correspond to thicknesses of the order of light wavelengths, and transparent lenses correspond to thicker oil zones.

This result means that each droplet is collecting a small amount of PDMS oil, extracted from the PDMS network. We observe colored zones corresponding to thicknesses of the order of light wavelengths, and transparent lenses corresponding to thicker oil zones. It is difficult to estimate the exact amount of oil collected in the beaker, as the oil lenses contain more liquid than the colored parts of the film corresponding to thicknesses of the order of light wavelengths, and zones around the colored part of the film are thinner than light wavelengths. However, a rough estimate of the amount of oil collected by each droplet can be given by multiplying the surface of the beaker by an optical thickness ($0.5 \mu\text{m}$) and dividing by the number of droplets: around $4 \times 10^{-4} \mu\text{L}$ of oil is collected by each droplet (which is about 10^5 times smaller than the droplet volume). However, this value should be considered only as a rough estimate, since the oil film at the free surface of the beaker is far from being of homogeneous thickness of $0.5 \mu\text{m}$. Assuming that each droplet is covered by a thin oil film, this estimates implies that this film would be nanometric (tens of nanometers).

4.3.6. Composition of the uncrosslinked oligomers oil

A better knowledge of the composition of the oil observed at the surface of the beaker would require further chemical analysis. However, experimental data in the literature already provide useful insight to determine the uncrosslinked chains length distribution. PDMS is a widely used material for microfluidic devices in various research

fields, including bioengineering and especially cell cultures in PDMS microchannels: in this context, uncrosslinked PDMS oligomers have already been observed in microchannel media, but also identified in membranes of cells cultured in PDMS microchannels [159]. This article, by K.J. Regehr and collaborators, focuses on biological implications of the use of PDMS as a culture medium, and shows mass spectroscopy analysis of water aspirated from Dow Corning Sylgard 184 PDMS microchannels after a 24-hour incubation. The results, reproduced in Fig. 4.15, give the distribution in length of the extracted uncrosslinked oligomers, which are present in a continuous range from fewer than 20 to more than 90 monomers. The oligomers extracted from our PDMS samples probably have the same range of length distribution. To go further, a direct measurement (by mass spectroscopy for instance) could confirm the length distribution of uncrosslinked PDMS chains in our experiments.

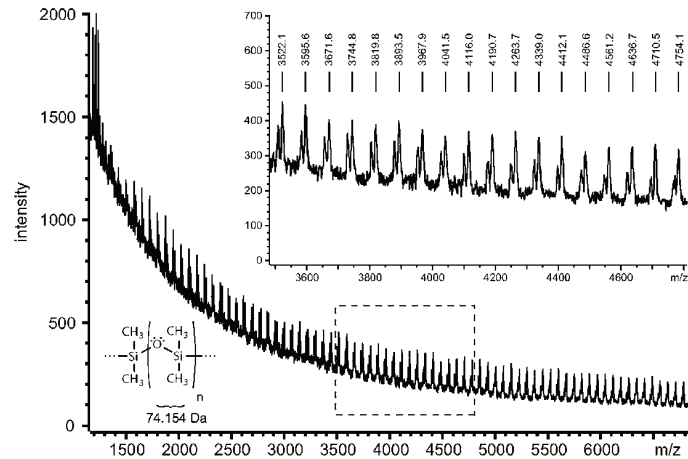


Figure 4.15 – Mass spectroscopy analysis of water aspirated from microchannels after a 24-hour incubation. Uncrosslinked oligomers are visible as a regularly repeating signal extending from under 1500 m/z (mass divided by charge number) to over 7000 m/z . Given the mass of a dimethylsiloxane monomer and assuming single charges on oligomers, these results evidence that PDMS oligomers are present in a continuous range from fewer than 20 to more than 90 monomers. Reproduced from [159].

4.3.7. Link with adhesion-induced phase separation experiments

The presence of oil at the surface of a liquid bath comprising many droplets (Fig. 4.14) shows that each droplet, during its descent, collects a small amount of uncrosslinked chains: a capillarity-induced phase separation certainly occurs at the triple line. Such a phase separation was reported in the case of adhesion in a recent paper by Jensen et al. [160]: a rigid silica sphere is deposited on a soft elastomer of Young's modulus $E = 5.6$ kPa, containing 62% of uncrosslinked oligomers. Uncrosslinked chains are shown to phase-separate from the core of the gel by adhesion at the contact line with the rigid object. Some liquid polymer is extracted from the gel and forms a wedge: instead of having a three-phase contact line, a four-phase contact zone is created, as shown in Fig. 4.16. In the case of a water droplet on a PDMS sample, the spreading parameter

of PDMS oil on water is positive: the extracted uncrosslinked chains certainly form a wetting ridge, but also spread to form a thin layer on the whole water-air interface.

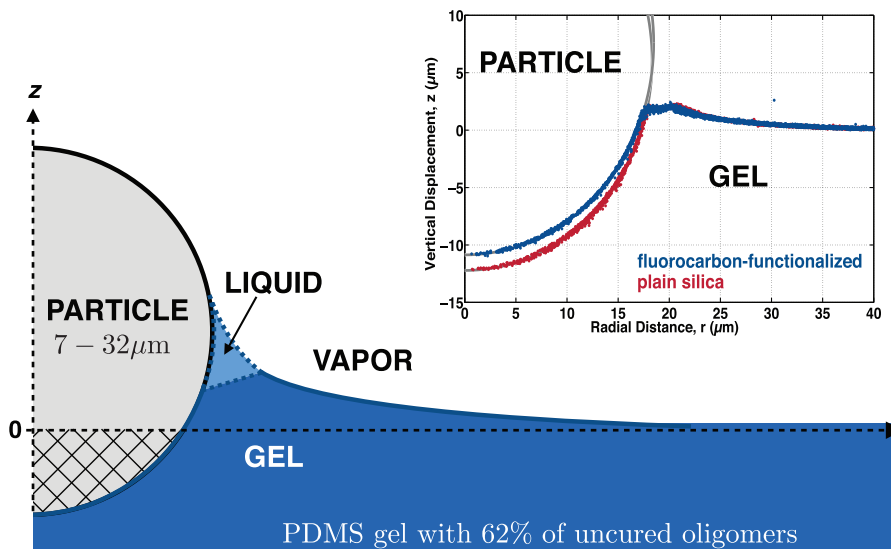


Figure 4.16 – Adhesion-induced phase separation: as some liquid PDMS is extracted from the core of the PDMS gel, a four-phase contact zone is created instead of a usual three-phase contact line. The graph shows the position of the top gel interface for two types of beads: fluorocarbon-functionalized, and plain silica. These results are obtained by recording the position of fluorescent beads adsorbed at the surface of the gel. Adapted from [160].

The technique used in [160] to show the existence of a liquid PDMS wedge consists in comparing the direct image of the sphere on the gel to a fluorescence microscopy image showing only fluorescent 48-nm beads adsorbed at the surface of the gel. The geometry of the liquid PDMS wedge is completely determined from these two measurements. Using the same technique to visualize a four-phase contact zone between a water droplet, a PDMS substrate, extracted PDMS oligomers, and vapor, might be tried. However, a similar technique has already been used in [108] to visualize the elastomer ridge raised by a contact line, and no noticeable oil wedge has been observed. A visualization of the contact line at the microscale would lead to a better understanding of the oligomers extraction process, and is part of the perspectives of this work.

4.4 Surface tension measurements

We have shown that uncrosslinked chains are extracted from the PDMS matrix during the droplet descent: as these chains have a positive spreading parameter on water, they are likely to form a thin film at the water-air interface. In this section, we use surface tension measurements to analyze further the evolution of the thin oil film during the droplet descent.

4.4.1. Useful insight from the literature

PDMS oil has a positive spreading parameter on water, which means that a PDMS oil droplet deposited on a liquid bath rapidly spreads to form a thin oil layer [161]. The polymer is insoluble in water but it is amphiphilic due to the oxygen of the siloxane groups, which causes its spreading at a water-air interface. In our case, PDMS oil extracted from the PDMS substrate should form a thin film that completely covers the droplet.

Experimental studies of monolayer PDMS oil films at the surface of a water bath were performed in the 1990s: a result presented in [162] gives some clues about the mechanism underlying the sharp transition between the first and the second regime observed in our experiments. When a commercial silicone oil (V100 or V1000) is spread on water, under a critical surface concentration c_1 , the surface tension of the liquid bath is the surface tension of water (Fig. 4.17(a)). The surface concentration c_1 corresponds to a sharp transition in surface tension. The surface tension then reaches a plateau when increasing the surface concentration further. Similar surface tension observations performed with natural oils such as olive or castor oil were already reported more than one century ago by A. Pockels [163], Lord Rayleigh [164], and I. Langmuir [165].

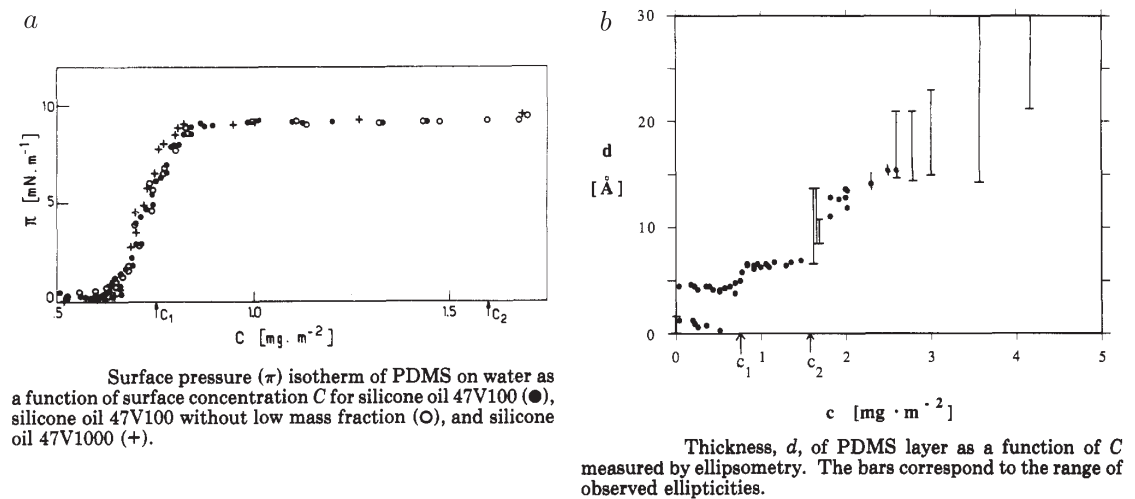


Figure 4.17 – (a) Surface tension modification as a function of the surface concentration in PDMS oil, for 3 different PDMS oils. The surface tension γ for a given surface concentration in PDMS reads $\gamma = \gamma_o - \Pi$, where γ_o is the surface tension of a water bath without PDMS film, and Π is the surface pressure of the PDMS layer. (b) Ellipsometric measurements showing the thickness of the PDMS film as a function of the surface concentration. The surface concentration c_1 and c_2 mentioned on this graph are the same as on (a): for surface concentrations below c_1 , the surface tension is close to the pure water surface tension, and the observed ellipticities alternatively correspond to pure water and to a PDMS layer of non-zero thickness: the authors suggest that the surface is partially covered with polymers domains of size greater than the illuminated area. Both graphs are reproduced from [162].

Ellipsometric measurements (Fig. 4.17(b)) highlight a correlation between the value of the surface tension and the thickness of the oil film: below a surface concentration c_1 , ellipsometric measurements alternatively correspond to a pure liquid bath and to an oil cover of non-zero thickness: the authors suggest that below c_1 , the polymers are not covering completely the surface of water but form domains of thickness around

0.5 nm at the surface of water. Below the surface concentration c_1 , the proportion of the surface covered by oil domains increases when increasing the surface concentration, but the surface tension remains close to the surface tension of water. Between the surface concentrations c_1 and c_2 , the oil film does not form domains any more, but completely covers the water-air interface. The thickness of one monomer is of the order of 0.7 nm [166], which means that in this surface concentration range, a monolayer oil film is spread over the entire the water-air interface. In this situation, the surface tension of the liquid bath is significantly different from the surface tension of pure water, but is not the surface tension of pure PDMS oil. For surface concentrations larger then c_2 , the oil film becomes thicker but non homogeneous, as shown by the error bars in Fig. 4.17(b). This result is consistent with the non-homogeneous oil film observed at the surface of the beaker in which 1500 droplets were collected after their two-regime descent on PDMS (section 4.3.5.).

These results contrast with what is usually found for the spreading of surfactants at a water-air interface: the decrease of the surface tension is generally linear with the surface concentration in surfactants. This unusual evolution as a function of the surface concentration, with a sharp transition both in terms of surface tension and of thickness of the oil layer, could be associated to our sharp speed transition and explain the two-regime behavior. As surface tension variation and creation of a homogeneous oil film seem to be closely linked, we perform surface tension measurements to obtain information about the thin film covering droplets in our experiments.

4.4.2. Drawbacks of the hanging-drop method

To measure the surface tension of a water droplet before and after sliding down on an elastomer plate, we first choose to perform hanging-drop experiments (technique described in chapter 2). A water droplet is collected in a capillary tube after reaching the second regime, and its surface tension, deduced from its shape, is compared to the surface tension of pure water. We find that the surface tension of a water droplet measured with this technique after reaching the second regime is equal to the surface tension of pure water. We also make an interesting observation: if a water droplet collected in a capillary tube after reaching the second regime is put back on the PDMS sample, it exhibits two regimes, as if it was a new and clean droplet. When a droplet is put back on the sample, it should exhibit only one single regime (the second one), as this experiment should be similar to that consisting in turning the setup upside down several times, described in section 4.2.5.. We conclude that the oil film wrapping the droplet is probably broken when collected in the capillary tube, and design another experiment to perform surface tension measurements.

4.4.3. Surface tension of a liquid bath made of droplets collected in a Petri dish

To measure the surface tension without breaking the oil film wrapping the droplet, we use the following setup: water-glycerol droplets of radius $r = 2.0$ mm are deposited with a syringe pump onto an inclined PDMS plane. Droplets are rolling down the plane and are collected in a 55mm diameter Petri dish after reaching the second regime (Fig. 4.18(a)). Surface tension of the liquid in the Petri dish is measured, using the ring method with a Krüss K6 manual tensiometer (described in chapter 2), as function of the collected

volume. Experiments are performed both for droplets deposited on untreated Sylgard 184 PDMS and on toluene-treated PDMS, and results are shown in Fig. 4.18(b). For the untreated sample, we observe a dramatic decrease of the surface tension around a collected volume of 3 mL (the beginning of the transition is around 2 mL).

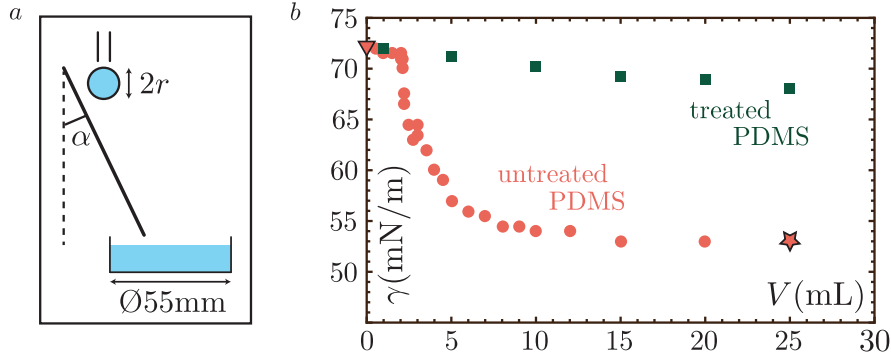


Figure 4.18 – (a) Experimental setup, with $\alpha = 29.2^\circ$ and $r = 2$ mm. (b) Surface tension of different volumes of water droplets collected in a Petri dish after reaching the second regime during their descent on untreated PDMS (red dots). The same experiment is performed on toluene-treated PDMS for comparison, with droplets collected after their descent on a 10 cm sample (dark green squares). Each point on this graph is obtained independently from the others (a 25 mL volume is not reached by reusing a 20 mL volume and adding 5 mL, as the surface tension measurement with a ring could result in a loss of oil chains stuck on the ring when it is withdrawn).

We assume that each droplet is covered by a homogeneous oil film after reaching the second regime: as the ratio of the surface of one droplet to the surface of the Petri dish is approximately 100, around 100 droplets (corresponding to a 3 mL volume) need to be collected to get in the Petri dish an oil film of the same thickness as the one around the droplets. The sharp decrease of the surface tension for a volume around 2 mL in Fig. 4.18(b) means that each droplet, during its descent, is subjected to a sharp surface tension variation. We therefore conjecture that as the droplet is moving down on PDMS it is gradually covered with oil and eventually subjected to a change in surface tension. Using the results given in [162] (Fig. 4.17), the change in surface tension is linked to the formation of a homogeneous oil film that completely covers the droplet. We thus explain the sharp transition in speed between the two regimes by a sudden change between two states for the droplet: we conjecture that before the transition, the droplet is only partially covered by uncrosslinked chains, while after the transition, a homogeneous oil film is completely wrapping the droplet, certainly together with oil wetting ridges. The droplet dynamics in the second regime is likely to be affected by this oil cover.

4.4.4. Results with Petri dishes of different sizes and made of different materials

We perform the same experiments with Petri dishes of different sizes and made of different materials to test the reproducibility of these results. Fig. 4.19 shows the evolution of the surface tension measured in different kinds of Petri dishes as a function of the volume of droplets collected rescaled by the surface of the Petri dish.

In the first experiments, presented in red, we use a 55 mm polystyrene Petri dish, and,

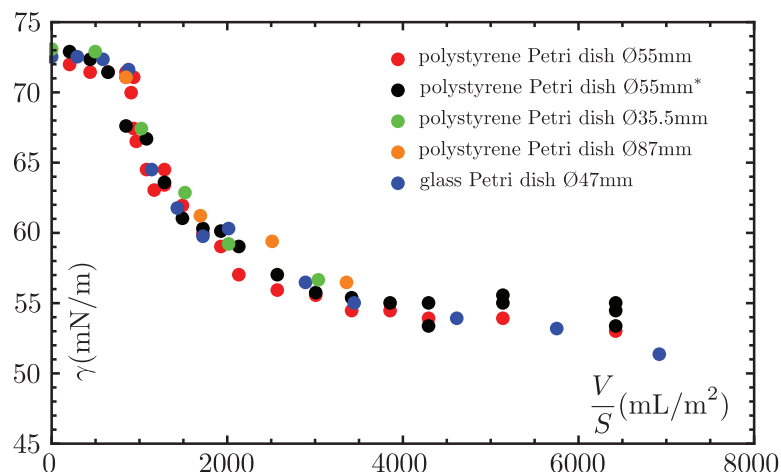


Figure 4.19 – Surface tension of given volumes of water droplets collected in Petri dishes of different sizes and made of different materials after reaching the second regime during their descent on untreated PDMS. The volumes are rescaled by the surface of the Petri dish, and a collapse of all the data is obtained.

only for volumes that are too small to form a flat interface, we pre-fill the Petri dish with water. Indeed, it is necessary to have a flat interface for the surface tension measurements with our Krüss K6 tensiometer. The second set of experiments, shown in black, is the same experiment, but with pre-filling the Petri dish with water for all volumes. The third and fourth sets of experiments, in green and orange, are performed with Petri dishes made of the same material but of different sizes, and the last set of experiments, in blue, is carried out with a glass Petri dish. The collapse of all the data rescaled by the surface of the Petri dish shows that there is no influence of the Petri dish material on the measured surface tension, and that the ratio of the droplet surface to the surface of the Petri dish is the good parameter for a rescaling. This collapse excludes the hypothesis of having some PDMS chains stuck on the material constituting the Petri dish during the experiment (oil has a very different wetting behavior on polystyrene and on glass: if some chains were stuck on one of the Petri dish materials, the surface concentration in PDMS would be lower, and the surface tension transition would occur for a larger volume).

4.4.5. Generalization to water-glycerol mixture droplets

Experiments presented in Fig. 4.18 and Fig. 4.19 are all performed with water. The same setup is then used to measure the surface tension in the case of water-glycerol mixtures. Fig. 4.20 shows the initial and final surface tension for various water-glycerol mixing ratios. The initial surface tension is defined as the surface tension of the liquid before sliding down on PDMS, and the final surface tension is defined as the surface tension measured for 25 mL collected after reaching the second regime. We observe that the difference between these two surface tensions does not vary with the water-glycerol mixing ratio.

These first surface tension measurements, obtained not by measuring directly the surface tension of a droplet but by measuring the surface tension of liquid bath composed

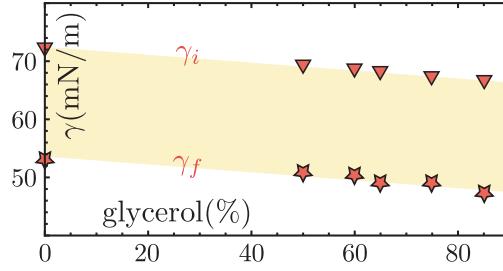


Figure 4.20 – Surface tensions measured before the experiment (γ_i) and in a Petri dish containing 25 mL of droplets collected after reaching the second regime (γ_f), for different water-glycerol mixing ratios.

of collected droplets, already show that a sharp transition in surface tension certainly coincides with the transition in speed. Measurements of surface tension on single droplets, performed in chapter 5, confirm this conclusion. We anticipate on these results, as they are of interest for a better understanding of quantitative speed measurements presented in the following section. In chapter 5, we demonstrate experimentally that during the first regime, the speed of the droplet has a constant value U_1 and its surface tension has a constant value γ_1 , and during the second regime, the speed of the droplet has a constant value U_2 and its surface tension has a constant value γ_2 . We thus conjecture that the transition from a partial oil film (patches on the droplet) to an oil film completely wrapping the droplet occurs exactly at the same time as the speed transition, and is thus responsible for this sharp speed transition.

4.5 Quantitative speed measurements

The mechanism underlying the two-regime behavior has been identified in the previous section: the droplet is progressively covered by uncrosslinked polymer chains, which results in a sudden surface tension modification when a critical surface concentration in PDMS uncrosslinked chains is reached. However, the droplet dynamics can be affected not only by the surface tension change, but also by the presence of an oil film (and possibly oil wetting ridges) around the droplet. In the following paragraph, we analyze further speed measurements in both the first and second regime in the case of an untreated PDMS sample, and compare these results to the single speed measured on toluene-treated PDMS. In the experiments presented here, we keep the angle of the inclined plane constant (vertical plate), and we change the size of the droplets and the water-glycerol mixing ratio. The properties (viscosity, surface tension, and density) of the different water-glycerol mixtures are given in chapter 2, and droplet volumes are kept under the threshold at which pearling occurs [36, 48].

4.5.1. Experimental observations

We here present experimental results of water-glycerol mixture droplets deposited on a vertical untreated Dow Corning Sylgard 184 PDMS plate. Each experimental data point is an average of five to ten measurements for most experimental points (except for experiments at very low speeds, which are longer to carry out) and the error bars

(not drawn on the graphs) are of the order of magnitude of the markers size, and are dominated by the error on the delivered droplet volume. In Fig. 4.21(a), we show the speeds measured in the first and second regimes, for a 35% water and 65% glycerol mixture. We also present results for a less viscous mixture (50% water - 50% glycerol) in Fig. 4.21(b), and for a more viscous mixture (25% water - 75% glycerol) in Fig. 4.21(c). Light green markers correspond to the speed measured in the first regime, and red markers to the speed measured in the second regime.

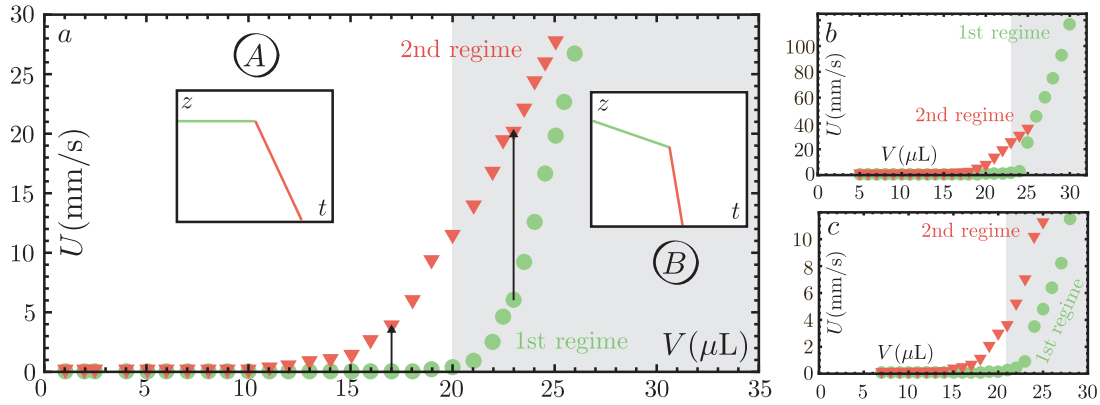


Figure 4.21 – (a) 65% glycerol - 35% water droplet speeds U on untreated PDMS as a function of its volume V , in first (light green circles) and second regime (red triangles). (b) Same experiment for a 50% glycerol - 50% water mixture. (c) Same experiment for a 75% glycerol - 25% water mixture.

These experimental results lead to interesting observations that will be discussed in the following paragraphs:

- For a given volume, the speed in the second regime is higher than in the first regime.
- By comparing Fig. 4.21(a), (b), and (c), we observe that the difference in behavior between the first and second regime (that can be quantified by looking at the shape of the experimental curves at large volumes) depends on the fluid viscosity.
- A threshold volume can be defined for the first regime curve: this threshold divides the graph in two zones A and B (Fig. 4.21(a)). In zone A, the speed in the first regime is negligible compared to the speed in the second regime, while in zone B, the speed in the first regime is not negligible compared to the speed in the second regime. Schematic height-versus-time diagrams in these two zones are shown in inset in Fig. 4.21(a).
- Another experimental observation is that in the first regime, there is a volume under which the speed of the droplet is zero, "zero" being defined as moving by less than a few pixels on the recorded video during the whole duration of the first regime (*e.g.* 11 μL in the experiments presented in Fig. 4.21(a), although first regime speeds values remain negligible compared to second regime speeds until 20 μL) whereas in the second regime, the speed of the smallest deposited droplets is not exactly zero: there seems to be no threshold volume below which a droplet does not move in the second regime.

- In the case of a 50% water - 50% glycerol mixture (Fig. 4.21(b)), only one regime is visible in our experiments for volumes larger than 25 μL . Corresponding points are classified as first regime measurements: for points just below 25 μL , we observe that the first regime is long and the second one begins close to the end of our sample. However, the possibility of the second regime to occur at a distance larger than the sample is excluded by performing experiments with larger samples that also show one single regime above 25 μL . The same behavior is also observed (for higher volumes) for higher glycerol-water mixing ratios. This last experimental result is not yet understood, but an hypothesis could be that a droplet moving too fast does not have time to get covered by uncrosslinked chains.

4.5.2. Discussion of the results obtained for the first regime

We compare the speeds measured in the first regime to existing results in the literature by plotting the results using the dimensionless $Ca = \mu U / \gamma$ and $Bo = \rho_l V^{2/3} g / \gamma$ numbers (where μ is the liquid viscosity, U the droplet speed, γ the liquid-air surface tension, ρ_l the liquid density, V the droplet volume, and $g = 9.81 \text{ m}\cdot\text{s}^{-2}$), as explained in chapter 1. Fig. 4.22(a) shows the speeds of droplets of various water-glycerol mixing ratios: the speed is negligible below a threshold value for the volume of the droplet, and the relationship between Ca and Bo is almost linear above this threshold. These results are similar to those obtained in [36] for silicone oil drops sliding down a glass plate coated with fluoropolymers. We also perform experiments with the same liquids on toluene-treated PDMS samples, and plot the results in Fig. 4.22(b). The speed is zero below a threshold value for the volume of the droplet, and the relationship between Ca and Bo is almost linear above this threshold, as for the results obtained in the first regime on an untreated PDMS sample.

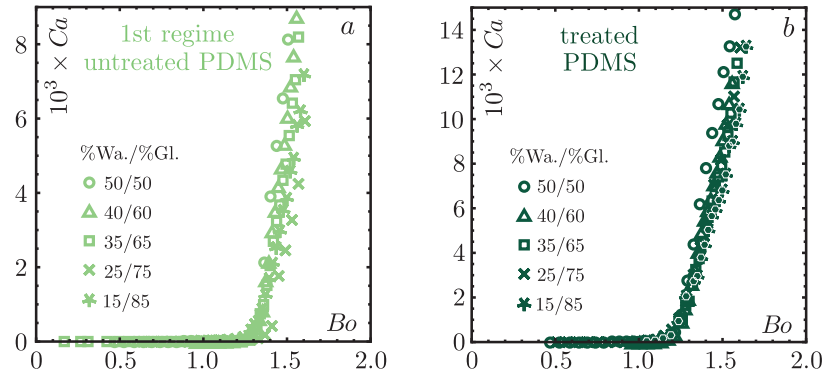


Figure 4.22 – Capillary number Ca as a function of Bond number Bo , for different water-glycerol mixtures. (a) Results for the speed in the first regime on untreated PDMS. (b) Results for the single speed observed on treated PDMS.

We therefore have a collapse of the data in terms of Ca and Bo numbers for different water-glycerol mixtures both in the first regime on untreated PDMS and in the single regime on toluene-treated PDMS. For clarity sake, we choose to focus on one single water-glycerol mixing ratio to do the comparison between the first regime on untreated PDMS and the single regime on toluene-treated PDMS. Results are shown in Fig. 4.23(a) for 35% water and 65% glycerol mixture droplets. The shape of the two curves obtained

on treated PDMS and on untreated PDMS (first regime) is the same, except for the threshold volume value V_t below which the droplet speed is negligible (Fig. 4.23(a)). A collapse of the two curves is obtained by plotting $V - V_t$, as shown in Fig. 4.23(b). The small difference in the threshold volumes V_t between the two curves can be explained by differences in advancing and receding angles on the two different samples. The values measured for advancing and receding contact angles are compatible with this hypothesis, but the uncertainties on our measurements of the contact angle hysteresis are too large to use these values to rescale our data.

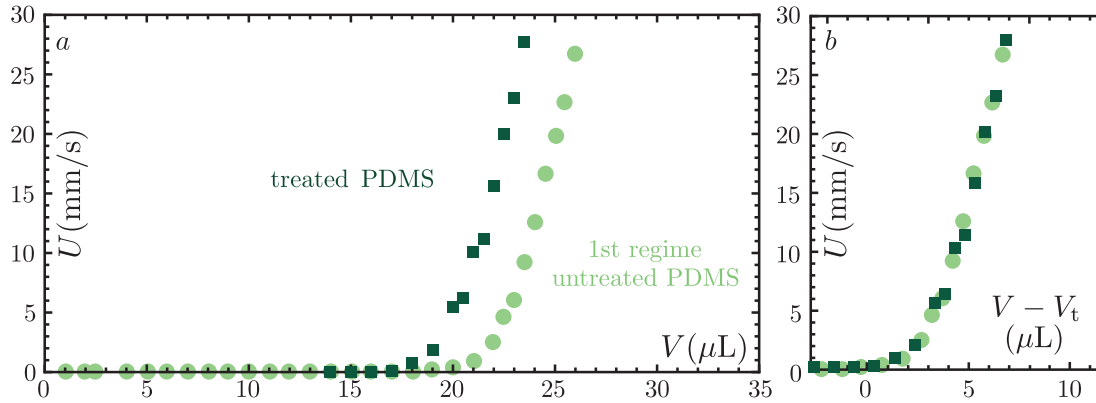


Figure 4.23 – (a) 65% glycerol - 35% water droplet speeds on treated PDMS (dark green squares) as a function of its volume, compared to the results for the first speed on untreated PDMS (light green circles). (b) Speeds as a function of the difference between the droplet volume V and the threshold volume V_t , on treated PDMS (dark green squares) and on untreated PDMS (light green circles)

We conclude that a droplet in the first regime on untreated PDMS behaves exactly as a droplet on toluene-treated PDMS. This means that the influence of the uncrosslinked chains on the dynamics in the first regime is negligible. We make a parallel with the surface tension evolution as a water bath is progressively covered with oil chains: below a given surface concentration, the surface tension of the liquid bath does not vary. In our case, we infer that below a given surface concentration (before the speed transition), the dynamics of the droplet is not affected by the oil chains.

4.5.3. Discussion of the results obtained for the second regime

The dynamics observed in the second regime presents some similarities with droplet dynamics observed in the case of Slippery Lubricant Infused Porous Surfaces (SLIPS). We summarize below the recent interest for SLIPS and discuss the results obtained in the second regime in our experiments.

a) Droplet dynamics on Slippery Lubricant Infused Porous Surfaces (SLIPS)

The manufacturing of smart slippery surfaces is a cutting-edge research field since Johanna Aizenberg's group pioneering work [167], published in 2011. Texturing a substrate with micro- or nano-pillars is a well known technique to manufacture superhydrophobic surfaces. However, filling the gaps enclosed in this micro- or nano-texture with oil makes

the surface even more water-repellent. A substrate that involves a porous medium infiltrated with oil to create a non-wetting surface is called a Slippery Lubricant Infused Porous Surface (Fig. 4.24(a)).

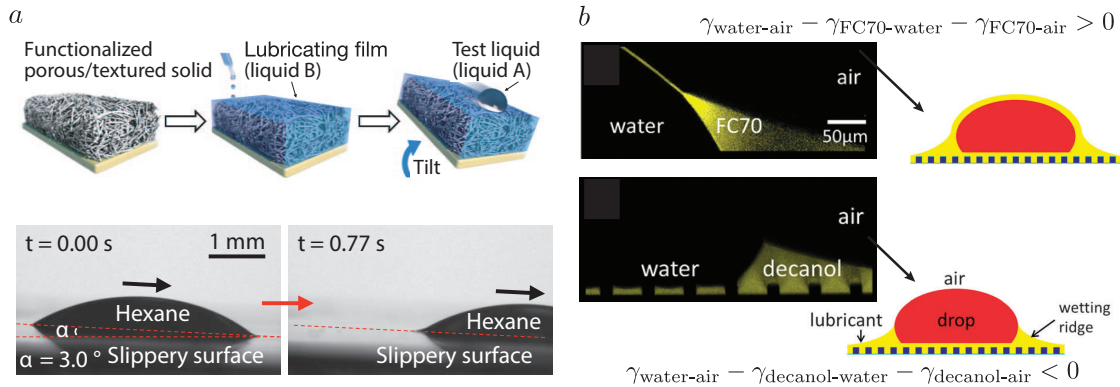


Figure 4.24 – (a) Top: Slippery Lubricant Infused Porous Surface schematic. Bottom: Non-wetting properties of such a surface. Reproduced from [167]. (b) Confocal microscopy visualization of a water drop on a slippery lubricant infused surface: depending on the spreading parameter of the oil on water, the oil completely covers the droplet (top) or forms only wetting ridges (bottom). Adapted from [168].

Several questions linked to our study are addressed in the literature about SLIPS: a first question is whether a droplet deposited on a SLIPS is covered by an oil film. Confocal microscopy experiments [168] result in a direct visualization of wetting ridges and thin films around droplets depending on the oil/drop system chosen (more precisely, depending on the value of the spreading parameter of the oil on the droplet liquid, Fig. 4.24(b)). This experimental observation confirms that when the spreading parameter of oil on water is positive, an oil film covers the whole droplet. It also shows that, in addition to this film, a wetting ridge of dimensions larger than the film thickness develops at the triple line. A confocal microscopy observation of our (PDMS oil)/(water drop) system with appropriate fluorescent dyes could confirm the existence of an oil film and the exact geometry of the wetting ridge, and is part of the perspectives of this work.

Another important question is the mobility of a droplet on such a Lubricant Infused Surface. In [169], a water droplet is deposited on a lubricant-impregnated surface where an oil film is present between the droplet and the posts. The droplet speed is shown to be set by the competition between the weight of the droplet and the viscous dissipation inside the oil wetting ridge (Fig. 4.25), and the authors argue that this result would be valid either for cloaked or uncloaked droplets, since inertial and gravitational forces in the cloaking films are very small.

b) Analysis of the speeds in the second regime

The droplet dynamics on untreated PDMS in the second regime involves two main differences with the dynamics in the first regime: there seems to be no threshold volume below which a droplet does not move, and the dissipation processes seem to occur both in the droplet and in the oil cover (the oil cover being defined as the thin film around the droplet and the wetting ridge at the interface with the elastomer surface).

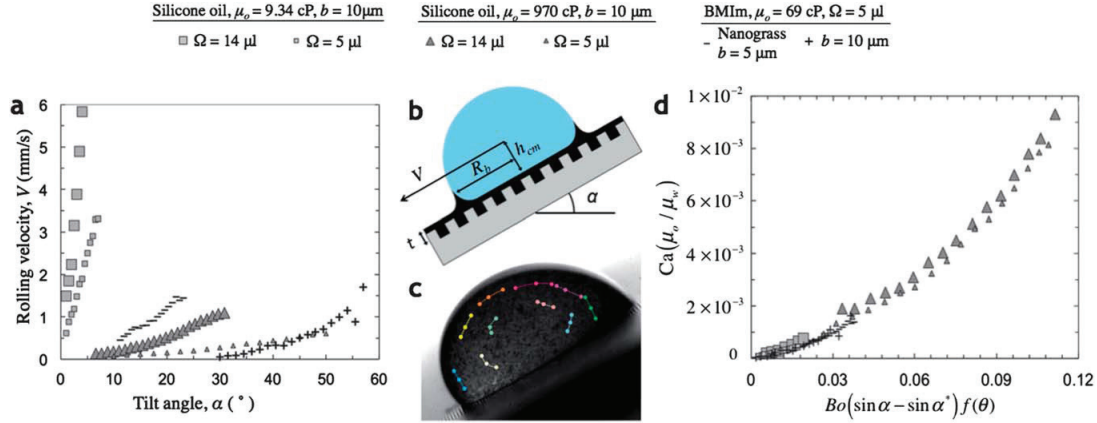


Figure 4.25 – (a) Measured velocities of water droplets on lubricant-impregnated surfaces as a function of substrate tilt angle for various lubricant viscosities μ_o , post spaces b , and droplet sizes Ω . (b) Schematic of a water droplet moving on a lubricant-impregnated surface. (c) Particle tracking inside the droplet reveals that it rolls rather than slides on the surface. (d) Collapse of the curves shown in (a) onto a master curve, by using a model where the major dissipation source is viscous dissipation in the oil wetting ridge: Ca number, calculated for the water droplet and multiplied by the ratio between oil and water viscosities, is plotted as function of Bo number multiplied by $(\sin \alpha - \sin \alpha^*)$, where α is the tilt angle and α^* the threshold tilt angle, and by $f(\theta) = \Omega^{1/3}/R_b$, with R_b defined on (b). Reproduced from [169].

Indeed, the asymptotes of the curves in the first and second regimes in Fig. 4.26 are almost parallel for a viscous fluid (Fig. 4.26(a)) while for a less viscous liquid, the slope of the red curve is smaller than the slope of the green one (Fig. 4.26(b)). This means that some dissipation occurs in the oil cover, and is visible in the case of a non-viscous droplet, and hidden by the huge dissipation rate in the droplet in the case of a viscous droplet.

In the literature, the dynamics of a water droplet on a lubricant-impregnated surface has been shown to depend on the oil viscosity. Smith et al [169] evaluate the contribution of each viscous dissipation term (viscous dissipations in the droplet, in the thin oil film below the droplet, and in the oil ridge) and conclude that taking into account only the dissipation rate inside the wetting ridge, which dominates over the two other terms, is sufficient to explain their experimental data. However, a rescaling using the model proposed by Smith et al does not lead to a collapse of the data in our experiments: in the case of a viscous droplet, the dissipation inside the droplet is not smaller than the dissipation in the wetting oil ridge.

We propose here a simple model involving two dissipation terms: viscous dissipation in the droplet and viscous dissipation in the oil wetting ridge. The viscous dissipation in the oil ridge is assumed to be equal for droplets of the same size but of various water-glycerol mixing ratios. The viscous force that brakes the droplet is then not only

$$F_\mu = A \frac{\mu U S}{h} \simeq A \mu U V^{1/3}$$

but

$$F_{\mu\text{tot}} = A \mu U V^{1/3} + B \mu_o U R_b$$

where μ_o is the PDMS oil viscosity, $R_b \simeq V^{1/3}$ is the radius of the contact zone of the

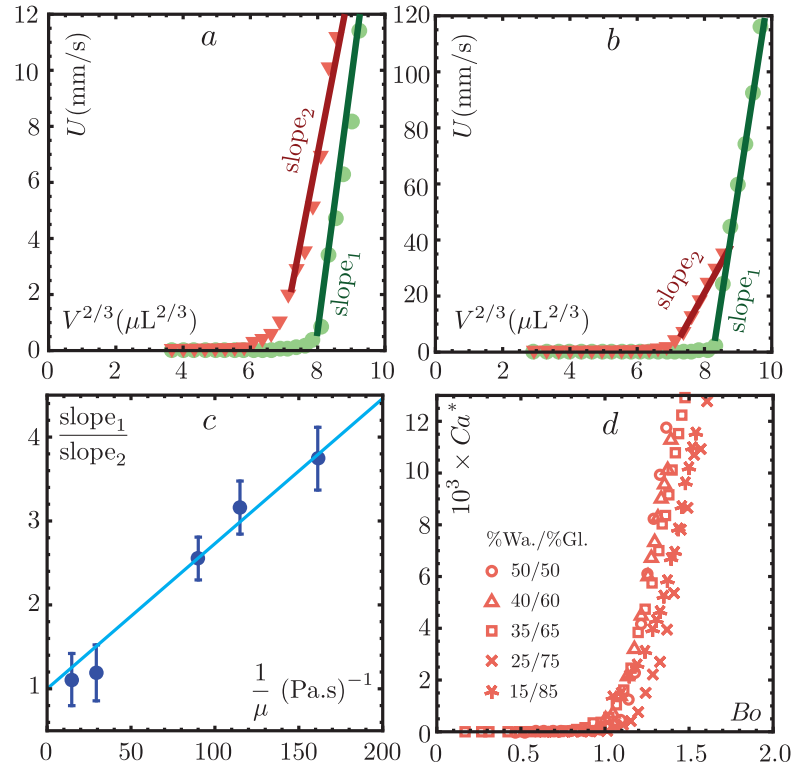


Figure 4.26 – (a) Droplet speed in the first (green circles) and second (red triangles) regimes in the case of a 75% glycerol - 25% water mixture, as a function of $V^{2/3}$, where V is the droplet volume. The linear part of the curve is fitted and the slope of the fit is denoted slope_1 for the first regime and slope_2 for the second regime. (b) Same graphic for a 50% glycerol - 50% water mixture. (c) Ratio between the slopes measured for the linear part in the first and second regimes, as a function of the inverse of the water-glycerol mixture viscosity. An affine relationship with intercept equal to unity is found, in agreement with our simple model. (d) A modified Capillary number Ca^* is used to plot the speed of the droplets in the second regime as a function of their weight, through the Bo number.

droplet on the substrate [169], and A and B are two constants linked to the geometry of the droplet and of the wetting ridge, assumed to be independent of the droplet size and water-glycerol mixing ratio to keep the model as simple as possible. Within the theoretical framework used to explain the results in the first regime, the slope of the asymptotes at large volume in Fig. 4.26(a) and (b) should be proportional to $1/(A\mu)$ in the first regime (slope_1), and to $1/(A\mu + B\mu_o)$ in the second regime (slope_2). In this case, the relationship between slope_1 , slope_2 , A , B , μ , and μ_o yields:

$$\frac{\text{slope}_1}{\text{slope}_2} = 1 + \frac{B\mu_o}{A\mu}$$

We plot in Fig. 4.26(c) the ratio between the two slopes as a function of $1/\mu$. The results are consistent with an affine relationship, with an intercept equal to unity. This curve gives us information about the ratio of energy dissipated in the droplet and in the wetting ridge: the slope of the affine fit is equal to $C = B\mu_o/A = 0.0173$. To plot all our

data on a same graph, we then choose a new version of the capillary number, defined as:

$$Ca^* = (\mu + C)U/\gamma$$

This allows all the curves to have the same slope for the linear part at high droplet volumes (Fig. 4.26(d)).

However, an experimental observation is not taken into account in this model: we do not observe a threshold volume below which a droplet does not move in the second regime, but there seems nevertheless to be a threshold volume below which the droplet speed is negligible. This phenomenon might be linked to a dependence of the contact angle hysteresis on the geometrical properties of both the droplet and the wetting ridge. A newly published study [170] performed in the case of liquid infused surfaces highlights the dependence of contact angle hysteresis of a droplet surrounded by an oil wetting ridge on the ratio between the Laplace pressures inside the droplet and inside the wetting ridge. Although a priori valid only in the case where the droplet is not cloaked by oil, these results interestingly suggest a candidate phenomenon to explain an apparent variation of the pinning force as a function of the droplet volume in our experiments.

4.6 Consequences and potential applications

4.6.1. A simple test to evaluate the presence of uncrosslinked oligomers

Silicone elastomers are used in contact with water in a wide range of applications, ranging from elastocapillarity to microfluidics. Beyond the recent interest for capillarity on soft solids, PDMS is an easy-to-use material to build microchannels as it is patternable by soft lithography, optically transparent, gas-permeable and flexible [171], and is thus a perfect candidate for rapid prototyping. It has however some drawbacks, pointed out in [117]: among them, leaching of uncrosslinked oligomers from the polymer network into microchannel media has been reported in the context of cell culture in PDMS microchannels [159]; material coming from the PDMS microchannel was even found in the cell membranes. A washing protocol is the best solution to get rid of most uncrosslinked oligomers present in elastomer samples and should be used to avoid unpredictable consequences of the presence of these uncrosslinked chains.

In this context, our experiment provides a simple test to check if an elastomer contains uncrosslinked chains, by depositing a water droplet on the sample and looking at the droplet dynamics. With an appropriate droplet size, the dynamics can simply be analyzed by eye, without video recording. A two-regime behavior observed on an elastomer is an indication that uncrosslinked oligomers are present. However, if only one regime is observed, we recommend prudence when it comes to drawing conclusions: in the case of a PDMS sample swelled with a large amount of silicone oil, only one regime is observed, as the droplet is immediately covered with silicone oil. A one-regime behavior is thus either an indication of the absence of uncrosslinked chains, or of their presence in large proportions.

4.6.2. Similarities between our elastomer samples and SLIPS substrates: a *delayed slippery surface*

a) Untreated PDMS: a slippery surface in the second regime

A PDMS elastomer sample containing a few percents of uncrosslinked oligomers becomes more slippery when a droplet has extracted uncrosslinked chains and is covered with a thin oil film: the speed in the second regime is higher than the speed in the first regime. We even showed in section 4.5 that the tiniest droplets that we deposit do not move during the first regime and have a small but non-zero speed in the second regime: there seems to be no threshold volume (in fact a minuscule threshold volume not reached in the experiments) for a droplet to slide down in the second regime. This is quite similar to what happens on SLIPS surfaces: usually the liquid-repellency of a surface is quantified by a threshold angle for a droplet to slide down an inclined plane (Fig. 4.24(a)), but thinking in terms of threshold volume is equivalent.

b) Advantages and drawbacks of PDMS plates compared to usual SLIPS

Slow cloaking dynamics In the case of a SLIPS substrate, oil is immediately available to cover the droplet, whereas for a PDMS sample, an extraction process has to occur, which makes the process of covering the droplet with oil longer. The surface is thus not immediately slippery, which can be seen as a drawback, but some applications could take advantage of this delay to allow droplets to stay on a vertical substrate for a while, before a self-cleaning step that happens naturally after a few minutes.

Limited slipperiness but easy manufacturing protocol In the second regime, our PDMS samples are not as slippery as SLIPS, but their manufacturing process do not require to create a micro- or nano-structure: the PDMS crosslinked network plays the role of the nano-texture, and uncrosslinked oligomers naturally present in silicone elastomer samples make it not necessary to infuse this PDMS network with another silicone oil. Using PDMS samples swelled with silicone oil is a strategy already used in the literature to manufacture SLIPS with an easy protocol [172]. Here, we highlight that the swelling step might be skipped, taking advantage of the uncrosslinked oligomers naturally present in the substrate.

Durability Another challenge in the SLIPS research field is to create durable SLIPS substrates, ensuring that oil does not disappear from the textures. Many recent studies towards a better durability of SLIPS substrates have been performed, focusing on resistance to shear-driven failure [173, 174], or on the number of droplets after which the surface is no longer slippery [175]. In all these studies, the durability of the SLIPS substrate is shown to mainly depend on the lengthscale of the texture. A droplet deposited on PDMS samples still exhibits two regimes after the sample was subjected to descents of several thousands droplets. However, a quantitative study of the durability of our samples goes beyond the scope of this work.

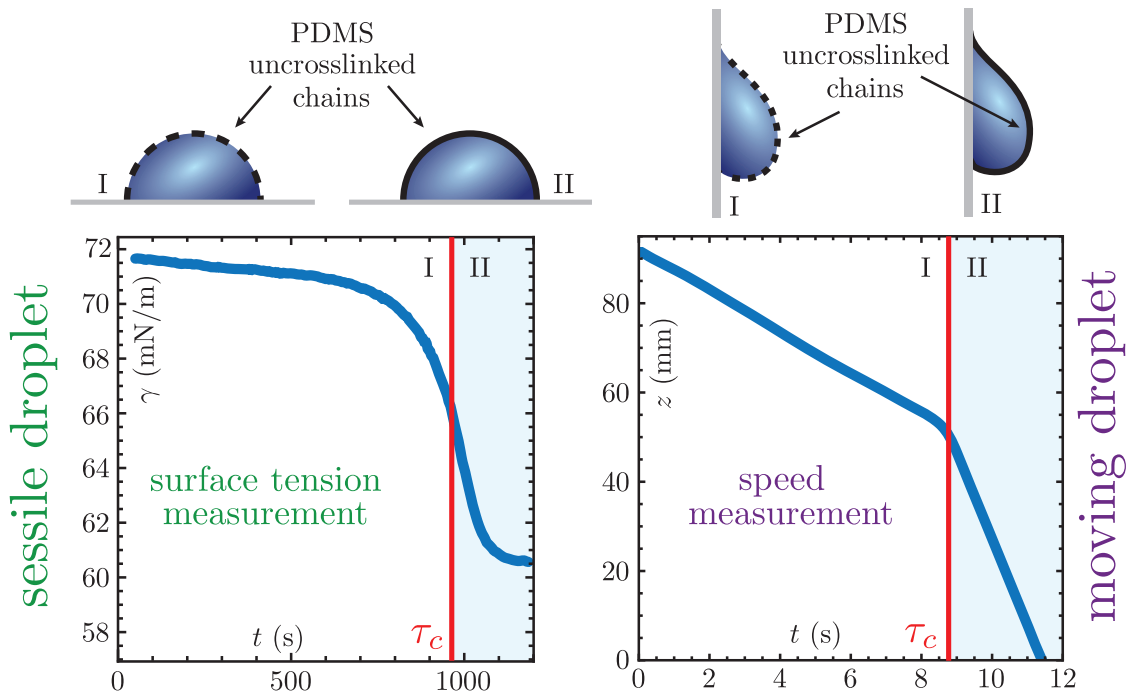
The study that has been presented in this chapter 4 is the subject of our article on the role of uncrosslinked chains in droplets dynamics on elastomers [176], published in *Soft Matter* and reproduced in the appendix of this manuscript.

Conclusion

We have shown that uncrosslinked chains found in most commercial elastomers are responsible for an unexpected droplet dynamics: an aqueous droplet deposited on a vertical silicone elastomer plate exhibits successively two very different descent regimes with two different constant speeds. We therefore investigated this phenomenon in order to understand the underlying mechanisms. One important result is that this two-regime behavior disappears if the elastomer is treated to remove the uncrosslinked chains, and reappears when re-swelling the treated elastomer with silicone oil, thus demonstrating the crucial role of uncrosslinked chains in the droplet dynamics. Our study reveals how minute amounts of contaminants have dramatic effects on the wetting dynamics, as each droplet is gradually covered by those uncrosslinked chains during its descent. The sudden change in droplets velocities coincides with a sudden change in surface tension due to the water-air interface contamination by silicone oligomers: we conjecture that before the sudden transition, the droplet is only partially covered with some patches of uncrosslinked chains, while after the transition, a thin oil film completely covers the droplet. The dynamics in the first regime is different than in the second regime: in the first regime the droplet can be modeled as a pure liquid droplet, with no impact of the uncrosslinked oil chains on its dynamics, while in the second regime, the oil cover has to be taken into account to explain the droplet dynamics. These findings emphasize the need for particular care in silicone elastomer samples preparation, as a few percent of uncrosslinked chains in the elastomer can lead to astonishing unwanted effects. This result could impact various research domains in which silicone elastomers are used in contact with water: our study also provides a simple test to evaluate the presence of unintended free oligomer chains by looking at the dynamics of water droplets on a test surface.

Chapter 5

Extraction of uncrosslinked chains at triple lines: contamination dynamics



In this chapter, more exploratory than the previous ones, we focus on the cloaking dynamics of a water-air interface by uncrosslinked chains contained in silicone elastomer samples. Surface tension measurements are first carried out at the scale of one single droplet to obtain direct results on the variation of interfacial tension of a droplet during its two-regime dynamics on a silicone elastomer with uncrosslinked chains. Measurements performed on sessile droplets then reveal that a droplet lying on a silicone elastomer horizontal plate is also subjected to a surface tension change after a time lapse. A contamination time is thus defined and investigated for both sessile and moving droplets. Additionally, we demonstrate that the extraction of uncrosslinked oligomers occurs mainly at the triple line, and highlight the possibility of extraction in various experimental setups involving air - water - silicone elastomer contact lines, such as partially immersed silicone elastomer plates or air bubbles sliding up PDMS planes immersed in a water bath.

Contents

5.1	Link between surface tension evolution and duration of the first regime	124
5.1.1.	Measurement of the surface tension of one droplet during its descent	124
5.1.2.	Cloaking of a sessile droplet, lying on a horizontal PDMS surface	128
5.2	Localization of extraction at triple lines	131
5.2.1.	Cloaking of a flat liquid bath by oligomers extracted from a partially immersed PDMS plate	131
5.2.2.	Cloaking of a bubble deposited on a PDMS plate in a water bath	135
5.3	Sessile droplets contamination dynamics	136
5.3.1.	Contamination time as a function of the droplet radius	137
5.3.2.	Influence of other parameters: preliminary experiments	139
5.4	Moving droplets contamination dynamics	140
5.4.1.	Experimental results	140
5.4.2.	Discussion	141
5.5	Tuning the elastomer and droplet properties to achieve functionality	142

5.1 Link between surface tension evolution and duration of the first regime

In this section, we further investigate the surface tension modification of a droplet before and after the speed transition observed when the droplet is moving down a vertical plate made of silicone elastomer with uncrosslinked chains. The results presented here supplement the information already obtained in chapter 4: measurements are performed at the scale of a single droplet, whereas previous experiments consisted in collecting an assembly of droplets to perform surface tension measurements.

5.1.1. Measurement of the surface tension of one droplet during its descent

A better knowledge of the surface tension evolution of a droplet during its descent would allow us to correlate the speed of a droplet to its actual surface tension at each moment of the descent. As we cannot perform surface tension measurements on a moving droplet, we investigate experimental setups that allow us to move an inclined plane back into a horizontal position to perform surface tension measurements on sessile droplets on horizontal planes.

a) Surface tension measurements of sessile droplets

As explained in chapter 2, measuring the surface tension of a sessile droplet is not possible with the classical ring tensiometer used in the previous chapter, as the probe – well adapted to perform surface tension measurements of large liquid baths – is larger than the droplet diameter. Our first strategy was to use a Femtotools FT-S100 sensor

(described in section 2.2), and measure the maximal force exerted on the sensor when withdrawing it from a droplet. The experimental setup is shown in Fig. 5.1(a) and (b): a FT-S100 sensor is attached to a SmarAct nanopositioner SLC-1730. The sensor movement along the vertical axis is controlled with a manual joystick. The force exerted on the sensor is recorded as a function of time during the whole duration of the experiment: results are presented in Fig. 5.1(c). After being washed with ethanol, the sensor tip is positioned above a sessile droplet. It is then moved down into the droplet, and withdrawn from the droplet, as illustrated in Fig. 5.1(d). The movement of the sensor in these preliminary experiments is manually controlled, which explains that it is not smooth; however, a special care is given to the withdrawal of the sensor from the liquid bath. When the sensor detaches from the droplet, a maximum force, denoted F_{\max} , is exerted on the sensor. When this force is reached, the triple line is attached on the rectangular part of the sensor, of width $300\ \mu\text{m}$ and thickness $50\ \mu\text{m}$. Assuming a zero-degree contact angle (achieved by pinning of the triple line on the sensor tip), and neglecting the Laplace pressure inside the droplet, the surface tension γ of the droplet is given by $F_{\max} = \gamma L_s$ where L_s is the perimeter of the sensor, equal to $700\ \mu\text{m}$. Results shown in Fig. 5.1(c) correspond to a $25\ \mu\text{L}$ droplet of deionized water deposited on a horizontal plate (polystyrene Petri dish).

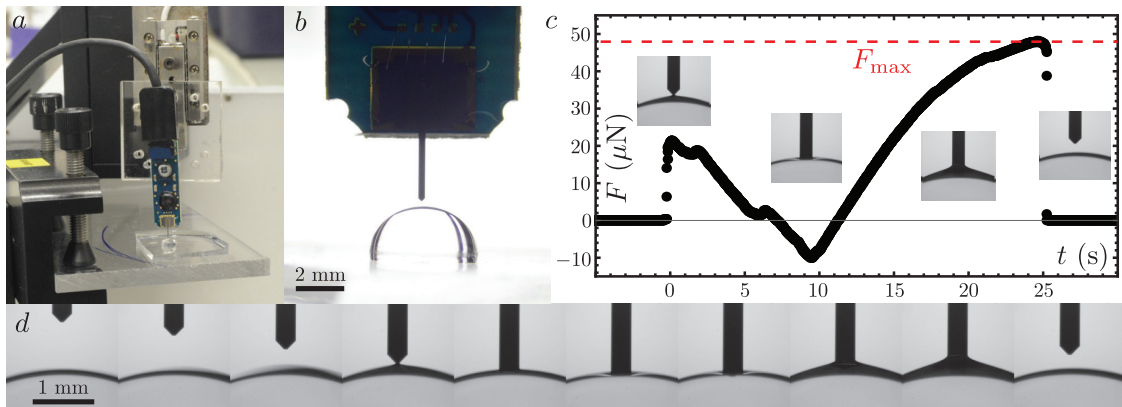


Figure 5.1 – (a) Femtotools FT-S100 sensor mounted on a SmarAct nanopositioner SLC-1730: the sensor motion is controlled in the vertical direction. (b) Zoom on the sensor tip and on the droplet: the sensor tip is positioned above the middle of the droplet. (c) Force exerted on the sensor as a function of time during the whole duration of the experiment. The sensor is moved down into the droplet and then withdrawn from the droplet. A maximum force F_{\max} is recorded when the contact line detaches from the sensor tip. The pictures only have an illustrative purpose and do not correspond to the actual droplet used for this graph. (d) Zoom on the sensor tip during the experiment: the sensor is inserted into the droplet, and withdrawn from the droplet. Due to pinning, the contact angle of the liquid on the sensor tip at the end of the withdrawal step is close to 0° .

The surface tension of the water droplet measured with this setup is found to be $68 \pm 2\ \text{mN/m}$, at 20°C . This value is a few percents lower than expected, due to several issues with this technique: the cleaning of the tip is not easy as it is extremely fragile, the sensor tip geometry is not simple, and the contact angle on the sensor is not exactly 0° . The Laplace pressure term coming from the curved interface has not been taken into account: in this setup, the resulting force exerted on the sensor due to Laplace pressure is one thousand times smaller than the surface tension force for a $25\ \mu\text{L}$ water droplet.

This setup allowed us to make preliminary observations to gain insight into two facets of the contamination dynamics:

- a moving water droplet on Dow Corning Sylgard 184 PDMS stopped in the first regime and a similar droplet stopped in the second regime seem to have different surface tension values.
- a sessile water droplet on Dow Corning Sylgard 184 PDMS is found to have a surface tension close to the one of pure water a few seconds after deposition, but the force measured on the sensor half an hour after deposition seems to correspond to a lower value of surface tension.

However, these experiments are not precise and difficult to carry out without damaging the sensor tip, reproducibility being an issue as well. Further investigations are thus performed using a Kibron EZ-Pi+ tensiometer, described in chapter 2, which allows for more precise surface tension measurements. Experiments with this apparatus were carried out at LPS Orsay (MMOI group); we are grateful to Emmanuelle Rio and Emilie Forel for their help with this device. The sensor probe of the Kibron EZ-Pi+ tensiometer is an inert metal cylinder of 500 μm diameter and allows us to perform precise measurements of the force exerted on the tip while it is automatically withdrawn from a liquid. This setup can also be used for surface tension measurements as a function of time, and cleaning issues are avoided by using a butane torch. However, when working with droplets for which the radius of the probe is not negligible compared to the radius of curvature of the droplet, a Laplace pressure corrective term needs to be included to obtain the real value of surface tension, as explained in chapter 2. All the surface tension values given in the following paragraphs are corrected to take into account Laplace pressure: droplets of given volumes have been deposited on a polystyrene Petri dish, making contact angles comparable to that on PDMS. The curvature at the top of the droplet have been recorded, as well as the value of the difference between measured and real surface tension (due to the existence of Laplace pressure), as shown in Fig. 2.16(b). This calibration is used to calculate the Laplace pressure term as a function of the volume of the droplet. When measuring the surface tension of a droplet after its descent, the non-axisymmetric shape of the droplet (due to gravity and contact-line pinning) is approximated to the axisymmetric shape of a droplet of same volume for the calculation of the Laplace pressure term. In the case of sessile droplets, the volume of the droplet that is considered is the initial volume of the droplet: evaporation is not taken into account. However, it could cause a modification of the Laplace pressure term as well as a reduction of the total water-air interface area: this point will be discussed when required.

b) Surface tension measurements as a function of the distance traveled by a droplet

We are not able to measure the surface tension of a droplet while it is moving, as mentioned in the introductory paragraph of this section. To record the surface tension of a droplet during its descent, we thus design the experiment illustrated in Fig. 5.2: a deionized water droplet of volume $V = 45 \mu\text{L}$ is deposited on a Dow Corning Sylgard 184 PDMS inclined plane, making an angle equal to 45° with the horizontal. Once the droplet has traveled a distance d on the inclined plane, the plane is moved back into a horizontal position, and the surface tension of the droplet is measured as a function of d with a

Kibron EZ-Pi+ tensiometer. A new droplet is used for each value of d , to induce minimal disruption in the system: each droplet travels a distance d , its surface tension is measured within 30 seconds after the end of the descent step, and the droplet is then thrown away. We show in the following sections that contamination timescales for sessile droplets are of the order of 1000 seconds, so the potential additional contamination during the 30 seconds of the measurement is assumed to be negligible. The tilting angle is chosen to be 45° to make the tilting step easier. The volume of the droplet is also chosen for its speed to be small enough to allow us to move the plane back to a horizontal position in a time lapse during which the distance traveled by the droplet is negligible compared to d . Surface tension measurements are shown in Fig. 5.2 as a function of the distance d traveled by the droplet: we observe a sharp transition in terms of surface tension when the droplet has traveled 8 mm.

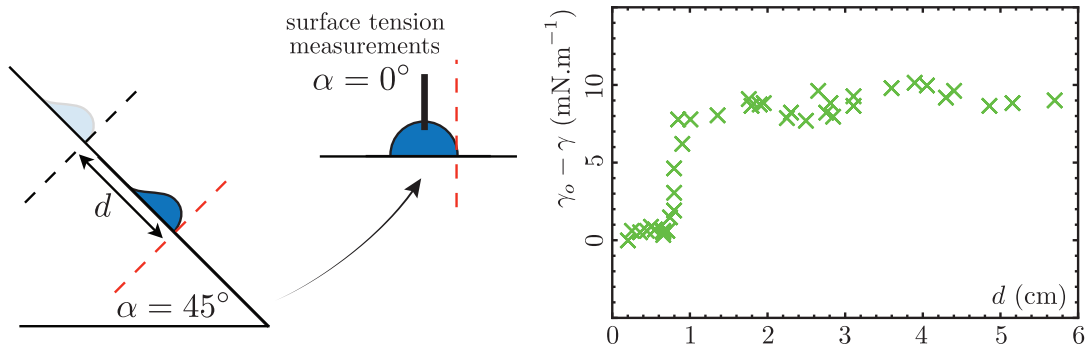


Figure 5.2 – A water droplet of volume $V = 45 \mu\text{L}$ is deposited on a 45° inclined plane made of Dow Corning Sylgard 184 PDMS. Once the droplet has traveled a distance d , the plane is moved back to a horizontal position, and the surface tension of the droplet is measured as a function of d . The graph shows the difference between the surface tension γ of a droplet that has traveled a distance d and the surface tension of pure water γ_0 , as a function of d . A sharp transition occurs when the droplet has traveled a distance equal to 8 mm, which is compared in Fig. 5.3 to the distance at which the speed transition occurs.

The comparison between the surface tension evolution and the distance-versus-time diagram for a $45 \mu\text{L}$ water droplet on a 45° PDMS tilted plane is performed in Fig. 5.3. In this figure, we turn the graph shown in Fig. 5.2 to show the distance d in ordinate, and we display this graph together with the distance-versus-time diagram. These results demonstrate that the speed transition occurs at the same time as a sudden surface tension transition from a value equal to the surface tension of pure water to another constant value, which is lower. More precisely, we show experimentally that both transitions occur at a same distance, and distance and time are linked by the distance-versus-time diagram. We can thus define the transition time (or transition distance) between the two regimes by two different ways: by looking at the speed of a droplet as a function of time, or by measuring its surface tension.

The surface tension value measured here for droplets in the second regime can be compared with the surface tension that has been measured in a Petri dish after collecting a certain amount of droplets in the previous chapter. Here, the surface tension of a water droplet is reduced by 10 mN/m at the transition between the first and the second regime.

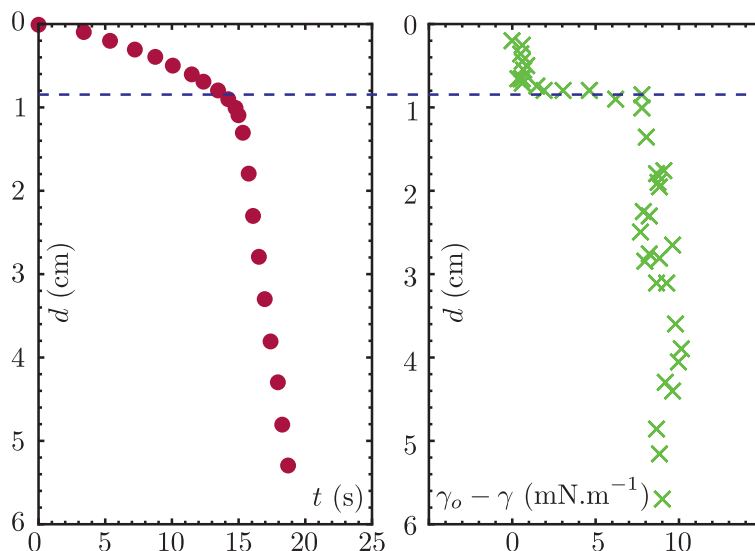


Figure 5.3 – Comparison between the distance-versus-time diagram (left) and the surface tension measurements (right) for a water droplet of volume $V = 45 \mu\text{L}$ deposited on a 45° inclined plane made of Dow Corning Sylgard 184 PDMS. The speed transition coincides with the surface tension transition: during the first regime, the droplet has a surface tension equal to the surface tension of pure water. During the second regime, it has another constant surface tension value, which is lower.

In chapter 4, after collecting 25 mL of droplets in a Petri dish, we observed a surface tension that was 19 mN/m smaller than the surface tension of pure water. One main difference between the two measurements, that could explain this result, is that when collecting hundreds of droplets, the amounts of uncrosslinked chains collected by all the droplets add up. At the scale of one droplet, the surface of the droplet might become harder to contaminate further once it is already covered by PDMS chains, resulting in a less important decrease of the surface tension for each droplet. Other factors could also cause a reduction of the surface tension measured in the collected droplets experiments: we have observed that with a toluene-washed sample, a small decrease of the surface tension occurred when collecting 25 mL of droplets in a Petri dish. This could be attributed to a small residual fraction of uncrosslinked chains, but also to a small amount of dust or surfactants collected by the droplets during the whole duration of the experiment.

Surface tension measurements on one single droplet confirm that the sudden speed change of droplets deposited on silicone elastomers with uncrosslinked chains coincides with a sudden surface tension change. Results obtained in this section highlight in particular the sharpness of the transition in terms of surface tension.

5.1.2. Cloaking of a sessile droplet, lying on a horizontal PDMS surface

As shown in the previous paragraph, surface tension is a parameter that contains the information about the transition of the droplet from one state (corresponding to the first speed regime) to another state (corresponding to the second speed regime). In preliminary experiments, we have observed that a sessile water droplet on Dow Corning Sylgard 184

PDMS was subjected to a surface tension change after a few tens of minutes. Here we investigate the surface tension evolution of a sessile droplet as a function of time, and show that a *contamination time* τ_c can be defined as the time for which a sudden surface tension decrease occurs, both for moving and for sessile droplets.

a) Temporal evolution of the surface tension

We investigate the surface tension as a function of time for a deionized water droplet of volume $V = 15 \mu\text{L}$ deposited on a horizontal Dow Corning Sylgard 184 PDMS plate. Surface tension is measured as a function of time with a Kibron EZ-Pi+ tensiometer: as preliminary experiments showed an evolution of the surface tension in a typical timescale of a few tens of minutes, the surface tension is measured every 5 seconds during 45 minutes, and results are displayed in Fig. 5.4.

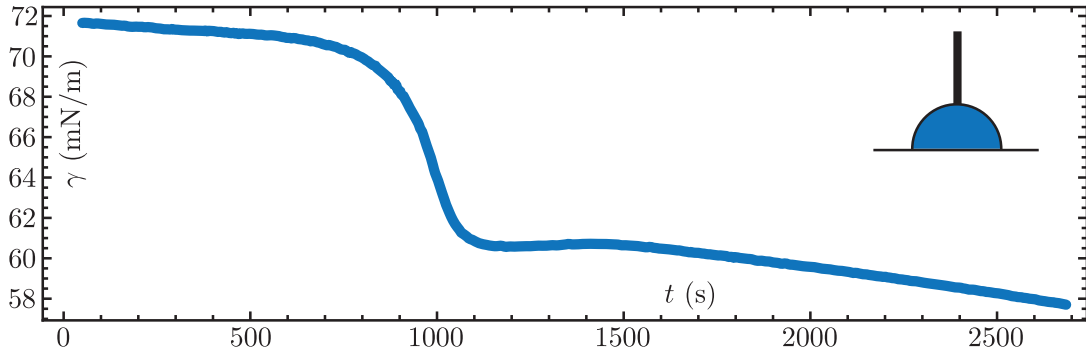


Figure 5.4 – Surface tension at the top of a water droplet of volume $V = 15 \mu\text{L}$ standing on a horizontal Dow Corning Sylgard 184 PDMS plate, recorded as a function of time with a Kibron EZ-Pi+ tensiometer. A sharp decrease of the surface tension is observed around $t = 950 \text{ s}$, corresponding to a contamination of the water-air interface by uncrosslinked PDMS chains.

We observe that the surface tension of the droplet remains close to the surface tension of pure water during a few hundreds of seconds. There is then a sharp decrease, followed by a slower decrease of the surface tension. The sharp decrease is explained by the progressive migration of uncrosslinked chains at the water-air interface, as shown in chapter 4. The slower decrease step might be explained by evaporation of the droplet. If the droplet is subjected to evaporation, the water-air interface area is reduced, and the Laplace pressure term increases if the radius of curvature of the droplet decreases. As the surface tension is estimated from the force measurement using the Laplace pressure term calculated with the droplet curvature at the beginning of the experiment, the surface tension is possibly under-estimated by a factor that increases with time. In the following paragraphs, we focus on the sharp decrease that occurs here around $t = 950$ seconds. Further analysis would be required on the long-term surface tension temporal evolution.

b) Definition of the *contamination time* τ_c

The sharp surface tension transition of a sessile droplet on PDMS can be used to define a contamination time τ_c . To do so, we calculate the average between the initial and final surface tension during this step. The time for which this average surface tension

is reached is defined as the contamination time τ_c , as illustrated in Fig. 5.5(a). The uncertainty on τ_c due to the uncertainties on the *initial* and *final* surface tensions is small compared to other sources of uncertainties. The time between the droplet deposition and the beginning of the acquisition is not precisely known (a few tens of seconds). Another issue is also observed in the experiments: unintended vibrations of the setup lead to a significantly reduced value for τ_c . A special care is given to avoid any movement around the experiment during the whole duration of the measurements. However, we need to keep in mind that some unintended movements could be the cause of the variability observed in the results.

The definition of the contamination time τ_c is also extended to moving droplets: in section 5.1, the time corresponding to the speed transition of a moving droplet has been shown to coincide exactly with the time at which surface tension changes. Measuring the time at which the speed changes is equivalent to measuring the time at which a surface tension change occurs. As speed measurements are more straightforward than surface tension measurements, the contamination time τ_c is defined in the case of moving droplets as the time for which a sudden speed change is observed, as illustrated in Fig. 5.5(b).

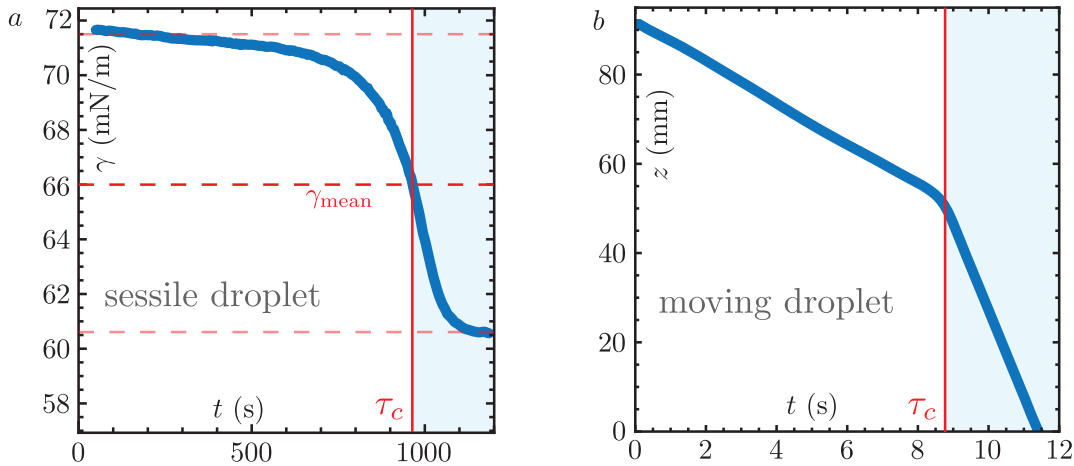


Figure 5.5 – (a) Surface tension temporal evolution of a sessile water droplet of volume $V = 15 \mu\text{L}$ standing on a Dow Corning Sylgard 184 PDMS plate. The contamination time τ_c is defined as the time for which the surface tension is equal to the mean of the initial and final values in such a temporal acquisition. (b) Height of a $22.5 \mu\text{L}$ water-glycerol mixture droplet (60% glycerol - 40% water) deposited on a vertical Dow Corning Sylgard 184 PDMS plate, as a function of time. The contamination time τ_c is defined as the time for which the speed of the droplet suddenly changes from one constant value (first regime) to a second constant value (second regime). As the speed change has been shown to coincide with a surface tension change in section 5.1, this definition is equivalent to the definition used in the case of a sessile droplet (a).

c) Spreading dynamics of uncrosslinked PDMS chains at a water-air interface

In Fig. 5.5, we notice that the timescales involved in the contamination of a water-air interface by uncrosslinked chains extracted from a PDMS plate are completely different depending on the droplet being sessile or mobile. Timescales involved in the case of

a sessile droplet are tens of minutes, while timescales involved in the case of moving droplets are seconds or tens of seconds. To further understand the cloaking dynamics of a droplet, a third timescale is investigated: the timescale needed for an uncrosslinked chain to spread and move on the water-air interface once it has been extracted from the PDMS matrix, assuming that extraction occurs at the triple line (this will be demonstrated in the following paragraph). The time required for a chain extracted at the triple line to travel for instance to the top of the droplet can be estimated by depositing a small amount of PDMS oil at the surface of a water bath with talc powder tracers and observing the spreading of the oil, visualized as an increasing diameter disk with no talc powder. Typical spreading times are much smaller than one second: the time required for a chain to move over the water-air interface is thus certainly negligible compared to the contamination time.

More precise insight can be gained from the literature: the spreading of PDMS oil on water has been investigated experimentally [161]. PDMS monolayers (v100 silicone oil) of initial radius 1 cm were shown to spread on water over six times their initial radius in less than 0.5 s. Spreading of PDMS oil at the water-air interface in a droplet geometry has been studied in the context of droplets deposited on lubricated surfaces [177, 178]. In this case, a monolayer first spreads on the droplet, followed by a nanofilm with thickness up to a few hundred nanometers. Both spreadings occur in less than a few tens of milliseconds for a millimetric water droplet deposited on a 4.8 mPa.s PDMS oil layer of thickness 8 μm , and in less than a few hundreds of milliseconds if the PDMS oil viscosity is increased to 4.8 Pa.s [177]. In all the following analysis, we thus consider that an uncrosslinked chain moves infinitely quickly on the water-air interface (compared to the contamination time) once it has reached the interface. The difference in contamination timescales between sessile and moving droplets is investigated further in sections 5.3 and 5.4.

5.2 Localization of extraction at triple lines

In chapter 4, we have conjectured that the extraction of PDMS uncrosslinked chains by a droplet deposited on a PDMS elastomer sample occurs mainly at the triple line. This hypothesis was based on a comparison between extraction of uncrosslinked chains by a water droplet and adhesion-induced phase separation observed in the case of a silica bead deposited on a soft silicone gel [160]. Here we investigate the possibility of different setups inducing extraction of uncrosslinked oligomers from a PDMS elastomer, due to the presence of a triple line between air, water, and PDMS with uncrosslinked chains.

5.2.1. Cloaking of a flat liquid bath by oligomers extracted from a partially immersed PDMS plate

We consider the following configuration: a PDMS plate is partially immersed in a water bath, exhibiting a triple line where PDMS, water, and air meet. This triple line is similar to the contact line of a water droplet on a PDMS plate: we investigate here the possibility of contamination of a water bath by uncrosslinked chains extracted from the partially immersed plate. The main advantage of this configuration compared to a sessile droplet on PDMS is that the length of the triple line, the area of the water-air interface, and the area of PDMS in contact with water can be changed independently to perform further investigations. Another important point is that evaporation plays a minor role in

this configuration, as it does not affect the area and curvature of the water-air interface.

a) Contamination time of a liquid bath

We consider a plate of Dow Corning Sylgard 184 PDMS partially immersed in a water bath, as described in the schematic in Fig. 5.6. The ratio between the perimeter of the contact line and the water-air interface area is chosen to be of the same order of magnitude as in the case of droplets deposited on PDMS plates. Surface tension of the liquid bath is measured as a function of time with a Kibron EZ-Pi+ tensiometer, and results are shown in Fig. 5.6. We observe a surface tension change after a certain amount of time, denoted τ_c and defined as for a sessile droplet on PDMS. However, we can notice that the shape of the surface tension transition is not exactly the same as in the case of a droplet. We focus on the contamination time τ_c in the following paragraphs, the exact shape of the surface tension transition going beyond the scope of this study.

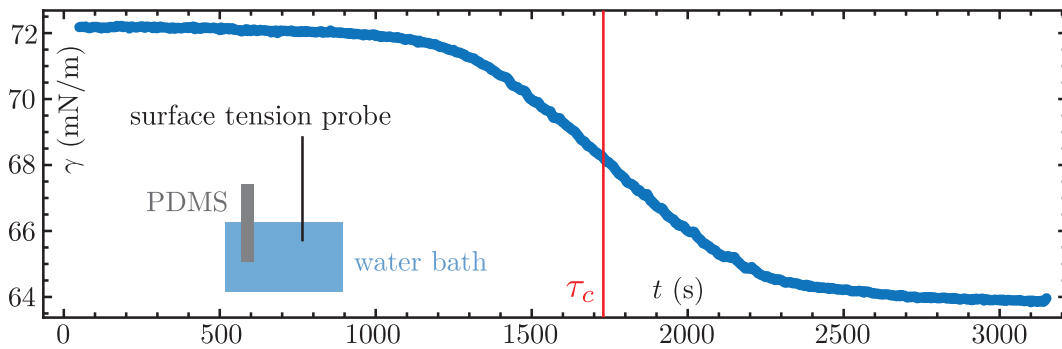


Figure 5.6 – A Dow Corning Sylgard 184 PDMS plate is partially immersed in a water bath. The total length of the PDMS-water-air contact line is 36 mm and the water bath area is 4 cm². Surface tension is recorded as a function of time with a Kibron EZ-Pi+ tensiometer, and a decrease of surface tension is observed after several tens of minutes.

b) Influence of the immersion depth of the PDMS plate

The uncrosslinked chains gradually covering the water bath are likely to be extracted at the triple line due to surface tension effects. Here we verify this hypothesis by looking at the dependence of the contamination time τ_c on the immersion depth of partially immersed PDMS plates.

We design the following setup: Dow Corning Sylgard 184 PDMS plates are partially immersed in a water bath, as shown in Fig. 5.7. The perimeter of the contact line between PDMS and water is kept constant for all experiments, but two immersion depths are investigated. The total area of PDMS in contact with water is multiplied by a factor larger than five between the two setups: if a significant amount of PDMS chains are extracted at other locations than the triple line, the contamination time should be significantly lowered when increasing the contact area between water and PDMS. For each immersion depth, four identical experiments are performed. The results displayed in Fig. 5.7 correspond to the average of the measurements for each immersion depth, error bars being representative of the statistical uncertainties. No significant difference is observed in the contamination

time τ_c between the two immersion depths, highlighting that extraction of uncrosslinked chains mainly occurs at the triple line. The length of the contact line between PDMS and water is thus certainly the parameter that needs to be varied to change the contamination time τ_c . Quantitative experiments varying the perimeter of the triple line are part of the perspectives of this study.

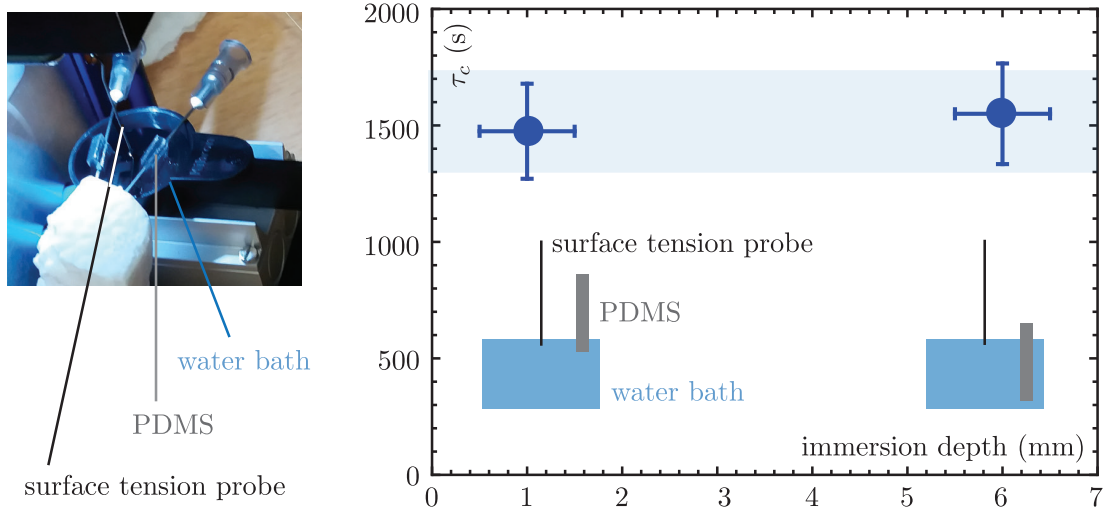


Figure 5.7 – Setup used to investigate the dependence of the contamination time τ_c on the immersion depth of PDMS plates. Dow Corning Sylgard 184 plates are partially immersed in a water bath: the immersion depth is the only parameter that is varied, the perimeter of the contact line between PDMS and water is kept constant. The area of the water bath is kept constant as well: the total length of the PDMS-water-air contact line is 36 mm and the water bath area is 4 cm². Each point on the graph is an average of four identical measurements, and the error bars correspond to statistical uncertainties. An increase of the immersion depth by a factor larger than five leads to no significant modification of the contamination time τ_c , demonstrating that extraction of PDMS uncrosslinked chains is mainly localized at the triple line. The light blue band is a guide for the eye: given our uncertainties, the contamination time in the two cases can be considered to be the same.

c) Ellipsometric preliminary experiments

A better knowledge of the thickness of oil films on our droplets could be gained from ellipsometric measurements. This technique has been described in chapter 2. However, in the case of a droplet, the curvature of the interface makes the measurements complicated: a microscope objective would be required to reduce the size of the illumination zone to a size at which the droplet is locally approximately flat. Using a water bath contaminated with a partially immersed PDMS plate instead of a water droplet deposited on a PDMS plate allows us to perform measurements with a flat interface.

Ellipsometric measurements were carried out at LPS Orsay (MMOI group) with Marion Grzelka, whose help is gratefully acknowledged. However, experiments shown here are only preliminary. The container used for the water bath is a square Petri dish of 12 cm sides, to avoid the effects of menisci on the flatness of the water-air interface. A dark background is positioned in the interior of the container to avoid unintended reflections

at the Petri dish-water interface. The material used for this dark background is carefully chosen to avoid contaminating the water-air interface with surfactants: no significant surface tension change is observed after 24 hours of immersion of the background in the water bath. We first perform a control experiment with only pure water (of surface tension 72.8 mN/m): the ellipsometric parameters Δ and Ψ , defined in chapter 2, are measured as a function of the angle of incidence (AOI). The corresponding measurements are shown in black in Fig. 5.8. We then perform the same experiment with water in which several pieces of PDMS were partially immersed overnight and withdrawn from the bath before the ellipsometric measurements. The results are displayed in red in Fig. 5.8. The surface tension is measured afterwards (to avoid any disruption in the experiment), and is found to be 69.3 mN/m. This means that the ellipsometric measurements have been performed in a setup in which the contamination was stopped just before τ_c . No significant difference is observed between the results of the control experiment (with pure water) and the results for the water bath with uncrosslinked chains, of surface tension 69.3 mN/m. A fit on these data using a model with one PDMS oil layer above a water bath leads to a value close to 1.5 nm for the oil layer thickness, both in the case of the control experiments and of the bath with uncrosslinked chains. Given the small difference of refractive index between oil and water and the small thickness of the oil layer, our measurements are not precise enough to see a difference between the bath with uncrosslinked chains and the control bath. The issue of keeping the surface of water perfectly clean in the control experiment needs also to be tackled in further work.

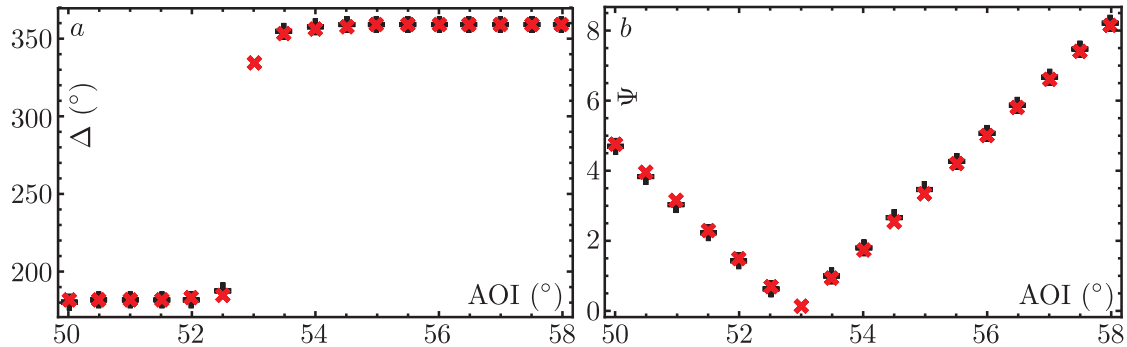


Figure 5.8 – Ellipsometric parameters Δ (a) and Ψ (b) recorded as a function of the angle of incidence (AOI) for a pure water bath in black (control experiment) and for a water bath with uncrosslinked chains in red. The surface tension of the bath with uncrosslinked chains is found to be 69.3 mN/m. No significant difference is observed between the two setups and further experiments are required with higher surface concentrations in PDMS chains.

Further experiments would include measurements of the thickness of the oil layer when stopping the contamination (by withdrawing the PDMS partially immersed from the liquid bath) at times much larger than τ_c , corresponding to a surface tension close to 64 mN/m. If a significant difference is found between the control experiment (with pure water) and the experiment with a complete layer of uncrosslinked chains, the next step would be to perform measurements stopping the contamination at different times around τ_c , to link the surface tension evolution to the thickness evolution in our experimental setup, or even to perform ellipsometric measurements as a function of time if the evolution is slow enough.

5.2.2. Cloaking of a bubble deposited on a PDMS plate in a water bath

Another example of a water-air interface in contact with PDMS is achieved by investigating setups with air bubbles in water (Fig. 5.10(a)). As migration of uncrosslinked chains has been shown to occur at the triple line in the previous paragraphs, we predict that an air bubble sliding up on an immersed PDMS plate could exhibit two sliding regimes.

We first consider the case of a bubble sliding up a vertical solid plate (with no uncrosslinked chains). The question of the final speed of such a bubble is mathematically identical to the question of the final speed of a droplet sliding down a vertical plate [42], except that dissipation mechanisms occur mainly in the surrounding liquid. Indeed, dissipation occurs mainly in the liquid in the two cases, which means in the droplet or in the surrounding medium depending on the object being a droplet or a bubble. Recent studies have been performed on bubbles sliding on fibers [179]. However, most experiments reported in the literature in the case of bubbles sliding below inclined immersed planes focus on bubbles that do not come completely in contact with the plane, with a thin liquid film between the plate and the bubble. Here the bubbles are completely in contact with the plate, making finite value contact angles. The simplest approach predicts that an air bubble should reach a final constant speed after a short transient. We verify this hypothesis experimentally by carrying out two control experiments before studying bubble dynamics on PDMS plates. An air bubble is deposited on a vertical plate immersed in water, the setup being the same as the one shown in Fig. 5.10(a) except for the vertical plate which is first chosen to be polyester. On a vertical polyester plate, an air bubble exhibits one single speed regime, as shown in Fig. 5.9(a). We then switch the polyester plate to a toluene-treated PDMS plate: one single speed regime is observed as well, as shown in Fig. 5.9(b).

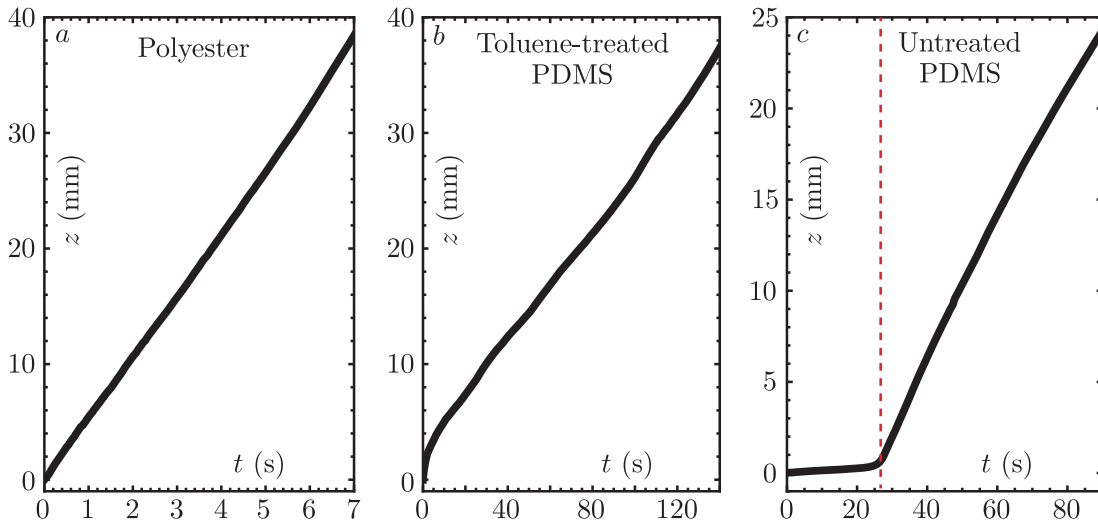


Figure 5.9 – Bubbles are deposited on various samples to qualitatively observe whether a one- or a two-regime behavior occurs. On a polyester plane (a) and on a toluene-washed PDMS plane (b), only one single speed regime is observed. On untreated Dow Corning Sylgard 184 PDMS (c), two regimes are obtained. The volume of the air bubbles is not yet controlled in the experimental setup.

On the contrary, two regimes are observed for an air bubble sliding up a Dow Corning Sylgard 184 PDMS vertical plate, as illustrated in Fig. 5.9(c) and in Fig. 5.10(b). These results with air bubbles surrounded with water are similar to the results obtained with water droplets surrounded with air, as uncrosslinked chains are extracted at the triple line and coat the water-air interface. Quantitative experiments, including a control of the volume of the deposited bubble, are part of the perspectives of this study.

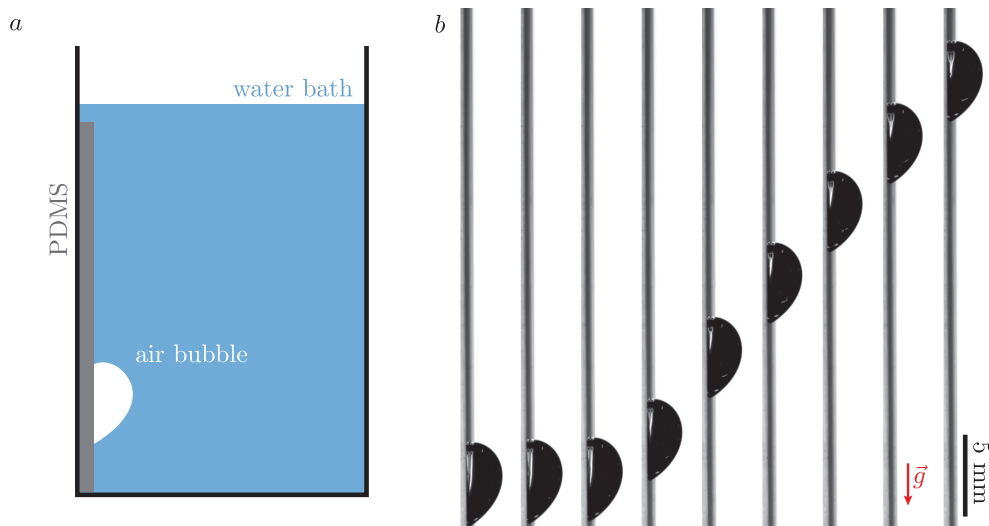


Figure 5.10 – (a) Experimental setup: an air bubble is deposited with a syringe on a Dow Corning Sylgard 184 PDMS vertical plate immersed in a water bath. (b) Results obtained with this setup: snapshots are taken every 10 seconds. We clearly identify two sliding regimes, and explain the sharp speed transition by the migration of uncrosslinked chains from the PDMS plate to the water-air interface.

We have shown that the unexpected phenomenon observed with aqueous droplets deposited on silicone elastomer plates occurs in other situations where a aqueous liquid - silicone elastomer - air triple line is present: it is the case for an air bubble on an immersed PDMS plane and for a partially immersed PDMS sample. These results highlight that being careful with uncrosslinked oligomers migration is required not only in the particular case of water droplets rolling on silicone elastomers.

5.3 Sessile droplets contamination dynamics

As explained in section 5.1.2., the covering of a sessile droplet by uncrosslinked chains occurs with a timescale that is much larger than the timescales involved when a droplet is moving. In this section, we investigate the influence of the sessile droplet size on the contamination time τ_c , and discuss other parameters, tested in the context of preliminary experiments.

5.3.1. Contamination time as a function of the droplet radius

a) Experimental results

We first investigate the contamination dynamics of a sessile droplet as a function of the droplet size. Our experimental setup is the following: a droplet of volume V is deposited on a horizontal Dow Corning Sylgard 184 PDMS plate, and its surface tension is recorded as a function of time. The contamination time τ_c is determined for each droplet volume by taking the average of one to three measurements, and the error bars are representative of statistical uncertainties. As contamination takes several tens of minutes, the number of experiments is limited due to time constraints. The contamination time τ_c is then plotted in Fig. 5.11 as a function of the base radius of the droplet R_b , calculated from the droplet volume V by assuming that the droplet is a half sphere. Results are compatible with a linear fit, shown in Fig. 5.11.

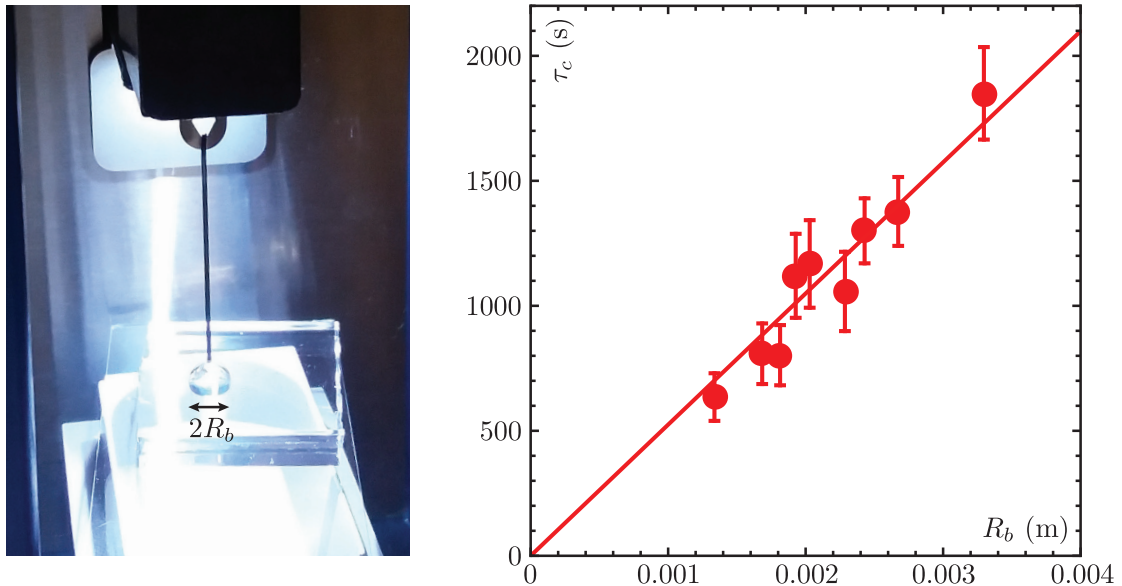


Figure 5.11 – Contamination time τ_c as a function of the base radius R_b of a water droplet deposited on a Dow Corning Sylgard 184 plate. Measurements are performed with a Kibron EZ-Pi+ tensiometer. Each point is an average of one to three measurements, the error bars being representative of statistical uncertainties. The red line is a linear fit, showing that our results are compatible with a linear relation $\tau_c \propto R_b$.

b) Discussion

In all the following analysis, we neglect evaporation, and focus on a simple first order approach. We observe that our experimental results are compatible with a linear relationship between the contamination time τ_c and the base radius R_b . The contamination time is in fact an integral quantity: $t = \tau_c$ when the surface concentration in uncrosslinked chains has reached a critical value c_1 . From our measurements, we are thus not able to precisely define a migration flow rate of uncrosslinked chains towards the water-air interface as a function of time: we can only focus on an average flow rate over the period

going from $t = 0$ to $t = \tau_c$. As surface tension decreases as a function of time, the instantaneous migration flow rate, driven by surface tension, is likely to decrease as a function of time as well.

We consider an average flow rate of uncrosslinked chains per unit length of contact line Q_ℓ (that is allowed to depend on R_b). The perimeter of the contact line is equal to $L_{cl} = 2\pi R_b$, while the area of the water-air interface that is likely to be covered by uncrosslinked chains is equal to $S_{wa} = 2\pi R_b^2$. The time needed to reach a critical surface concentration c_1 in uncrosslinked chains on the water-air interface is thus inversely proportional to $L_{cl}Q_\ell/S_{wa} = Q_\ell/R_b$. The relationship between τ_c and R_b then yields $\tau_c \propto R_b/Q_\ell$. In this context, our experimental results highlight that Q_ℓ is independent of R_b , as we observe that $\tau_c \propto R_b$.

We can wonder whether the evolution of the instantaneous flow rate as a function of time changes as a function of R_b . We focus on the shape of the surface tension curves as a function of time to gain some insight on the temporal evolution of the flow rate, for different values of R_b . We can rescale our surface tension curves by the contamination time τ_c , as shown in Fig. 5.12. This allows us to see that the relative duration of the surface tension transition is similar for all the droplet radii on this rescaled graph. The instantaneous flow rate of uncrosslinked chains at the contact line seems to be the same at times t/τ_c for different values of R_b , as the surface tension evolution has the same shape. However, the surface concentration in uncrosslinked chains is not directly known (especially in parts of the graph where the surface tension does not vary much).

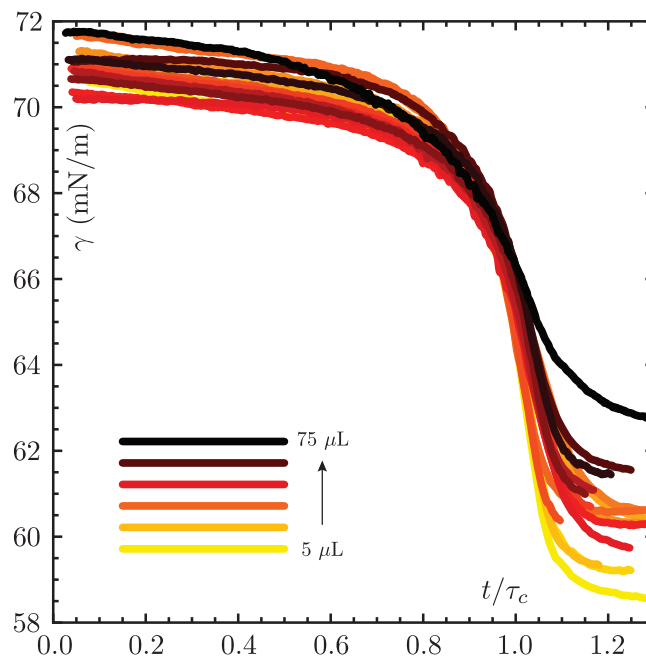


Figure 5.12 – Surface tension as a function of time rescaled by the contamination time τ_c for sessile droplets of various volumes sitting on Dow Corning Sylgard 184 PDMS. The relative duration of the transition is the same for all droplet volumes, as the curves collapse when rescaling the time by τ_c . Droplets volumes are going from $5 \mu\text{L}$ (yellow) to $75 \mu\text{L}$ (black); orange, red, and brown colors being used for intermediate droplet volumes.

Some differences can be observed between the initial and final surface tension in Fig. 5.12 for various droplet sizes. Differences in initial surface tension mainly come from the uncertainty on the Laplace pressure corrective term, while differences in final surface tension probably also result from a higher influence of evaporation in the case of small droplets.

The details of the extraction mechanisms are complex, and, especially, the understanding of the instantaneous uncrosslinked chains flow rate at the triple line goes beyond the scope of this study. Diffusion mechanisms might be at play, and the details of the extraction dynamics depend on many parameters: the chains might be located preferably at the free surface of PDMS, which would result in a two-dimensional diffusion problem, or might come from the bulk matrix, which would be a three-dimensional diffusion system. The ratio between the size of one oligomer and the distance between nodes in the crosslinked network certainly also comes into play: understanding these mechanisms is part of the perspectives of this study. However, some parameters have already been tested in the context of preliminary experiments with PDMS samples re-swelled with silicone oils of various viscosities.

5.3.2. Influence of other parameters: preliminary experiments

As demonstrated in chapter 4, uncrosslinked chains can be removed from Dow Corning Sylgard 184 PDMS samples by using a washing procedure with toluene as a swelling solvent. Washed samples can then be reswelled with silicone oil of known properties, resulting in a control of the viscosity and proportions of the uncrosslinked oligomers present in the PDMS matrix. Square pieces of PDMS of sides $\simeq 1$ cm and of thickness $\simeq 1$ mm, washed with toluene to get rid of uncrosslinked chains, are then re-swelled during one month with small amounts of silicone oil of two different viscosities. The washed PDMS pieces are weighted, and silicone oil is deposited on their surface. One month later, swelling appears to be approximately homogeneous, and the samples are weighted again, after being rinsed with deionized water. The percentage of uncrosslinked chains is calculated by taking into account the difference between the weight before and the weight after the swelling process. However, swelling is not perfectly homogeneous, and techniques to obtain swelled samples of better quality have to be developed for further investigations.

The results of our preliminary observations are shown in Table 5.1: a water droplet of volume $V = 20 \mu\text{L}$ is deposited on 3 different samples, swelled with different amounts of v50 and v100 silicone oils. The contamination time is recorded, and shown in the right column of the table.

Viscosity (mPa.s)	Proportion, in weight (%)	Contamination time τ_c (s)
100	3.1	100 ± 10
100	6.0	37 ± 10
50	1.4	110 ± 10

Table 5.1 – Toluene-washed PDMS samples are re-swelled with commercial silicone oil: the viscosity of the oil is given in the first column, while the proportion of added oil (in weight) is given in the second column. In the last column, we record the contamination time τ_c of a water droplet of volume $V = 20 \mu\text{L}$.

Two trends can be extracted from these results: when increasing the amount of uncrosslinked chains, the contamination time seems to decrease. This result was to be expected, in the light of two limit cases: on a sample with no uncrosslinked chains, the contamination time is infinite, while on a lubricant infused surface, the contamination time is negligible compared to contamination times on our PDMS samples [177].

The oil viscosity also seems to have an impact on the contamination time. We can compare the first and the last line of Table 5.1: similar contamination times are found for two different viscosities while the proportions are completely different. Further experiments are required to gain a better knowledge of the contamination time as a function of both viscosity and proportion of uncrosslinked chains. However, re-swelling washed samples involves some issues: swelling might be not homogeneous, and a larger concentration in chains might be found near the free surface of PDMS. A better control of the repartition of the oil is required. Another path to avoid these issues could be to study the influence of adding silicone oil in PDMS when the two parts of the elastomer kit are mixed.

5.4 Moving droplets contamination dynamics

The contamination time τ_c in the case of a moving droplet is much shorter than contamination times investigated in the case of sessile droplets. We here study the influence of the speed U of a droplet – in the first speed regime – on the value of τ_c .

5.4.1. Experimental results

The experimental setup is the following: water droplets of constant volumes are deposited on PDMS inclined planes, and the angle of inclination is varied in order to change the droplet speed in the first regime without affecting its volume. We choose to change the inclination angle instead of the droplet volume: this allows us to reach different speeds without varying significantly the perimeter of the contact line (which is a parameter that is likely to influence the contamination time). However, we perform experiments with three droplet volumes, to rapidly test the influence of the droplet size. The contamination time is recorded as a function of the speed of the droplet and shown in a log-log diagram in Fig 5.13. Yellow points correspond to 20 μL droplets, orange points to 40 μL droplets, and red points to 60 μL droplets. Angles of inclination are varied between 57° and 90° for 20 μL droplets, between 33° and 45° for 40 μL droplets, and between 24° and 35° for 60 μL droplets. The droplets shapes are slightly different when changing the angle of the inclined plane, but to first order, we will neglect this shape modification in the discussion.

No significant difference is observed between the curves for the different volumes. This can be explained by the limited volume variation range in our experiments: droplets of smaller volumes are immobile on a vertical plane due to pinning forces. Uncertainties, that are mainly statistical and can be estimated through the scatter of our data, do not allow us to distinguish between the three volume cases.

We observe that a power law with a negative exponent (lower than unity in absolute value, close to $-2/3$) fits well our data, except from a small deviation at small speeds. This deviation was to be expected, as the contamination time in the case of a sessile droplet is not infinite. An investigation of smaller speeds is part of the perspectives of these

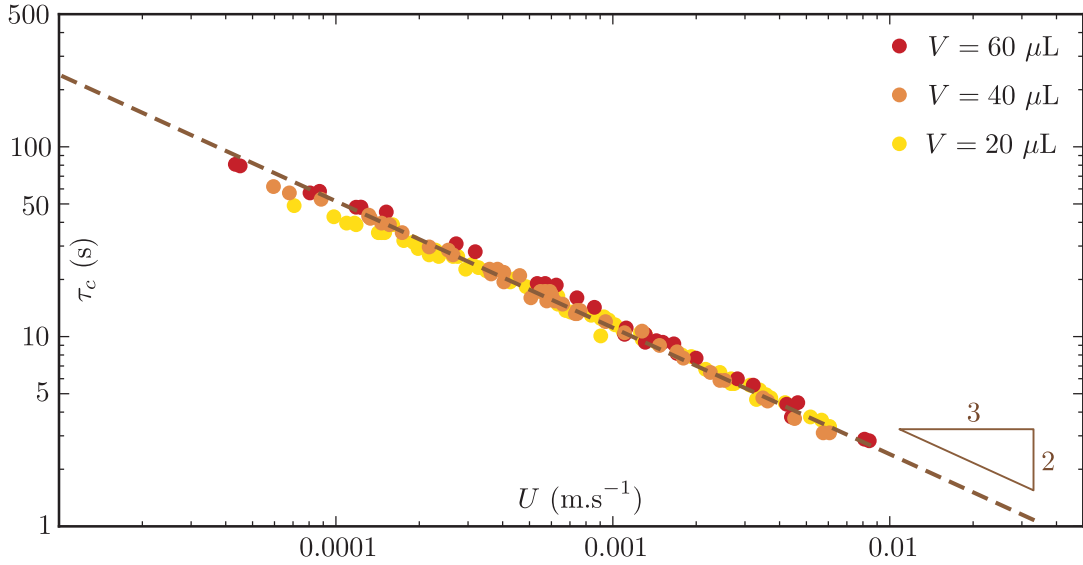


Figure 5.13 – Water droplets of volumes 20 μL (yellow), 40 μL (orange), and 60 μL (red) are deposited on Dow Corning Sylgard 184 PDMS inclined planes. The angle of inclination is varied to change the droplet speed. We record the contamination time τ_c as a function of the droplet speed in the first regime U , and show that our data are consistent with a power law fit. Performing measurements over a larger range of speeds and testing the reproducibility of these results is part of the perspectives of this work.

experiments: it requires a better spatial resolution on the videos to keep uncertainties below a reasonable level even at small speeds, as well as a better analysis of the very first instants of deposition of the droplets, during which the contact line is moving on the substrate at a higher speed than during its descent. The experimental results shown in Fig 5.13 are obtained on one single Dow Corning Sylgard 184 PDMS sample: reproducibility of the results on various samples should also be tested.

5.4.2. Discussion

The order of magnitude of the contamination timescales are different for a sessile and a moving droplet, with a strong influence of the speed of a droplet on the contamination time. Two approaches can be followed to try to understand this behavior, as the sessile and moving droplet setups present two major differences:

- the driving force pulling uncrosslinked chains towards the water-air interface, that was equal (per unit length) to the surface tension of the interface in the sessile droplet case, is now modified by the flow inside the droplet, and certainly depends on the speed of the droplet. The advancing and receding parts of the droplet might also play two different roles in the moving droplet setup.
- in the case of a moving droplet, the fresh surface explored by the droplet during the first regime is equal to the product of its speed by its contamination time, multiplied by the droplet width. In the case of a sessile droplet, no fresh surface is available.

We focus on the second point: if the number of chains collected was proportional to the area of fresh surface explored by a droplet during the first regime, the contamination time would be inversely proportional to the speed of the droplet. We observe that the negative exponent of the power law fitting our experimental results is smaller than one in absolute value: this means that the proportion of chains collected per unit area depends on the speed of the droplet. The fastest the droplet the smallest the number of chains collected per unit area. The candidates for the mechanisms underlying these phenomena are numerous, and the detailed modeling of the experimental results obtained here goes beyond the scope of this study.

5.5 Tuning the elastomer and droplet properties to achieve functionality

In this section, we highlight perspectives of the work presented in chapters 4 and 5. Beyond a better understanding of the contamination dynamics that would be achieved by performing the additional experiments mentioned in the previous sections, as well as a further modeling of the contamination times both for sessile and moving droplets, one main perspective of this work is to use the observed phenomenon to achieve functionality. Our setup has already been compared to a Slippery Lubricant Infused Porous Surface in chapter 4, showing in particular that our PDMS samples can be considered as *delayed slippery surfaces*.

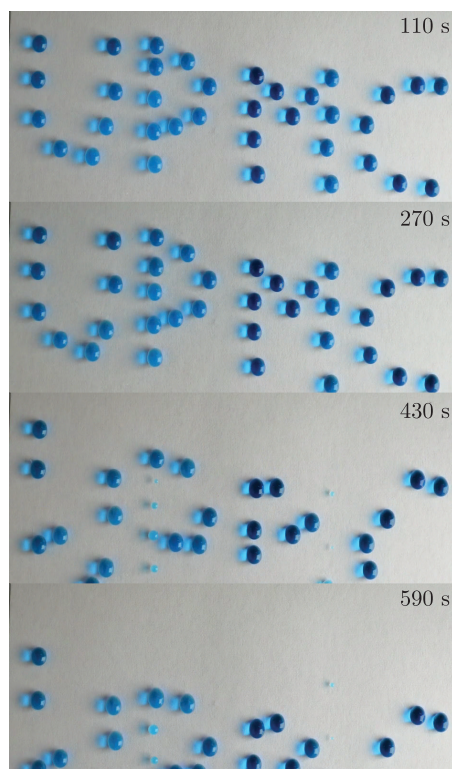


Figure 5.14 – 10 μL droplets of 60% glycerol - 40% water mixture are deposited on a vertical PDMS plate. The droplets stay in place for a while, before a natural self-cleaning step.

This idea can be investigated further to the light of the results obtained in chapter 5: the resting time of a droplet on an inclined (or even vertical) plane can be tuned by choosing the droplet size and the proportion and viscosity of uncrosslinked chains. An example of a steady configuration followed by a self-cleaning step on PDMS is shown in Fig 5.14: droplets are almost immobile during the first part of the experiment, and begin to move quasi-simultaneously after a certain time lapse (the slight difference between droplets contamination times might be mainly explained by slight differences in droplets volumes).

A PDMS plate with uncrosslinked chains thus allows droplets to stay at a constant position for a controlled amount of time before a self-cleaning step: this material could be used for optical applications such as short-lived water lenses, or chemical processes such as limited time exposure to a reactant. It also opens perspectives in terms of droplets manipulation, as it allows for moving a substrate on which a droplet stays immobile – even subjected to diverse movements and various inclinations of the setup – before being automatically released when desired, tuning the time at which the droplet begins to move by controlling both the elastomer and droplets properties.

Conclusion

In this chapter, we have presented results that supplement our study on wetting dynamics on elastomers with uncrosslinked chains, with a particular focus on the time required for uncrosslinked oligomers to contaminate a water-air interface in contact with a silicone elastomer, inducing a sharp surface tension transition. Contrary to results shown in the previous chapter, surface tension measurements have been performed at the scale of one single droplet, demonstrating a coincidence between the time at which a sudden speed transition occurs and the time at which a sudden surface tension transition occurs. The extraction of uncrosslinked chains has been shown to occur mainly at the triple line, and various configurations including water - air - silicone elastomer contact lines have been tested, showing that an air bubble sliding up a vertical PDMS plane exhibits two speed regimes, and that a PDMS plane that is partially immersed in a water bath leads to a contamination of the water surface. Temporal evolution of the surface tension of sessile droplets have also been investigated, resulting in a consistent definition of a contamination time τ_c both for sessile and moving droplets: this contamination time has been shown to vary over several orders of magnitude between sessile and moving droplets. Different parameters have been tested to gain a better knowledge on the contamination processes in both cases: the contamination time of a sessile droplet has been shown to be proportional to its base radius. In the case of a moving droplet, the influence of the droplet speed has been investigated. Although the precise modeling of these phenomena is part of the perspectives of this study, some candidate approaches have been mentioned. A complete understanding of the contamination time could result in well controlled *delayed slippery surfaces* on which droplets stay in place for a controlled amount of time before a natural self-cleaning step occurs.

Conclusion

Results presented in this thesis can be divided into two main parts, a first one focusing on capillarity-triggered snap-through instabilities (chapter 3), and a second one on extraction of uncrosslinked oligomers from silicone elastomers by water droplets (chapters 4 and 5). Here we summarize the results and give perspectives for each of these two main projects.

In order to reveal the ability of capillary forces to trigger snap-through instabilities, we first considered a dry setup, using point-force indentation on a buckled thin strip clamped horizontally at both ends. As the vertical force reaches a threshold value, the arch snaps to a downward configuration. We then replaced this usual dry load by a droplet. Drops of increasing volume are deposited or hung on the same strip: as the volume of the drop is increased, the height of the strip decreases until snapping occurs. By showing that critical snapping loads are different for sitting-drop, hanging-drop, and dry setups, we have demonstrated the importance of capillary forces in this experiment. We have shown that the combined effects of surface tension and Laplace pressure can be seen as two effective bending moments acting toward the instability or hindering it, depending on the configuration. The possibility of reverse elastocapillary snap-through, where the droplet is put under the beam, was then tested and successfully observed. It constitutes an additional evidence of the predominance of capillary forces at small enough scales. A phase diagram of equilibrium configurations and their stability has been built experimentally and theoretically, highlighting that both the volume of the droplet and its position along the buckled strip are crucial parameters. We have also shown that the elastocapillary snap-through dynamics is mainly driven by elastic forces and that fluid forces and fluid inertia only play a minor role: capillarity is driving the system toward instability but elasticity is ruling the subsequent dynamics. Eventually, upscaled setups with soap bubbles as well as condensed-vapor-induced snap-through were successfully investigated.

Perspectives of this work include implementation of this phenomenon to build smart actuators, taking advantage of the release of elastic energy that occurs when a snap-through instability is triggered. An extension of this study to the case of shells, instead of strips, would also be interesting, and allow for building elastocapillary jumping poppers.

In the following chapters, we develop our observations and investigations of an unexpected droplet dynamics on silicone elastomer plates. An aqueous droplet deposited on such an elastomer has been shown to exhibit two regimes characterized by two constant speeds. Numerous candidate hypotheses explaining the underlying phenomenon were tested. The sliding-to-rolling transition hypothesis was discarded as we have shown experimentally that droplets roll in both regimes. A possible change in the droplet

composition was then investigated, first by turning the setup upside down to use the same droplet on the same sample several times. The behavior of the droplet during the first descent is completely different from its behavior during the following descents: the first descent shows two distinct regimes, whereas the following descents only exhibit one regime, corresponding to the second regime of the first descent. Uncrosslinked chains present in the elastomers were then removed using a washing procedure with toluene as a swelling solvent. Droplets dynamics on washed samples exhibits one single regime, providing evidence of the crucial role of uncrosslinked oligomers in wetting dynamics on silicone elastomers. Additionally, a two-regime behavior can be recovered by re-swelling washed samples with commercial silicone oil.

A direct visualization of the oligomers was then performed at the surface of a liquid bath composed of thousands of droplets collected after their descent on untreated PDMS samples: our study reveals how minute amounts of contaminants can have dramatic effects on the wetting dynamics. Surface tension measurements of droplets collected in a Petri dish after their two-regime descent show that a sharp surface tension decrease coincides with the sudden speed change: each droplet is gradually covered with uncrosslinked chains during its descent, and once a critical surface concentration is reached, a sharp surface tension transition occurs. Correlating these results to insight from the literature, we infer that in the first speed regime, only patches of silicone oil are present on the droplet, the speed transition occurring only when a uniform oil layer is formed.

The speeds of droplets of various volumes and various viscosities were investigated in both the first and the second regimes. We have shown that the first regime dynamics is set by the competition between the weight of the droplet, capillary pinning forces, and viscous dissipation inside the drop, leading to a linear relationship between the Capillary and the Bond numbers above a threshold. The second regime presents some similarities with the dynamics observed in the case of water droplets on Slippery Lubricant Infused Porous Surfaces, as dissipation mechanisms occurring in the oil cover affect the droplet dynamics.

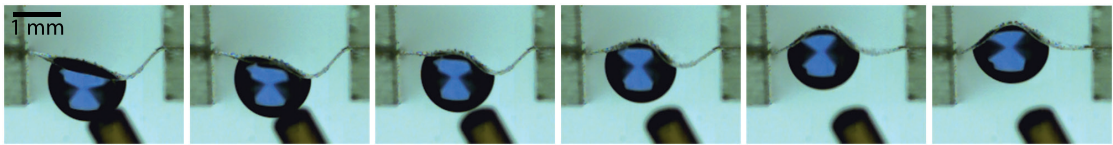
In a second part of this study, we focused on surface tension measurements at the scale of one single droplet. We first confirmed experimentally the coincidence between the speed change and the surface tension change. We have then demonstrated that a sessile droplet is also subjected to a sharp surface tension transition: the contamination timescales are however very different from the case of a moving droplet. We have shown that extraction of uncrosslinked oligomers occurs mainly at the triple line, by investigating various experimental setups where a water - air - silicone elastomer triple line is present, such as a silicone elastomer plate partially immersed in a water bath, or an air bubble sliding up a silicone elastomer plate immersed in water. We eventually investigated the contamination timescales in the case of both sessile and moving droplets.

These findings could impact various research domains such as microfluidics or elastocapillarity as they contribute to a better knowledge of the interaction between water and silicone elastomers, and provide a simple test to evaluate the presence of unintended free oligomer chains by looking at the dynamics of water droplets on a test surface. Perspectives of this work mainly include further investigation of the oil layer with ellipsometric measurements, as well as contamination time measurements in the case of samples re-swelled – in a controlled manner – with silicone oil of known properties. A better understanding of the experimental results obtained for contamination times in the sessile and moving droplet cases could also be an interesting extension of our study. Before

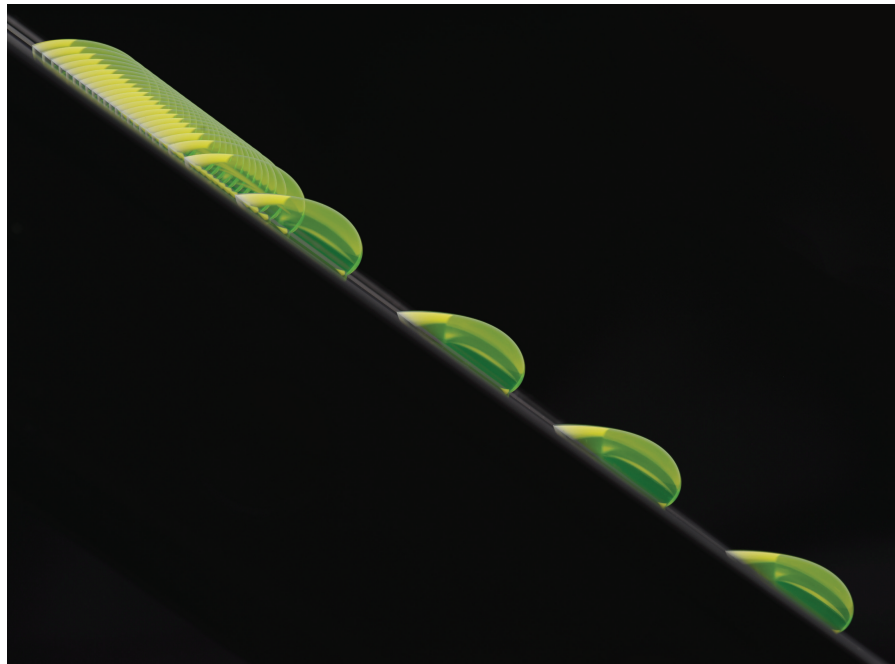
observing an unexpected droplet dynamics on silicone elastomers, the detailed study of dissipation processes in both the viscoelastic elastomer sample and the liquid droplet was part of our project. It is still an interesting perspective, as we now have clues to understand the two-regime dynamics observed on elastomers, and to remove this two-regime behavior by a washing procedure. However, we believe that this unexpected phenomenon could also be turned into interesting applications, inspired by slippery surfaces. In the case of a SLIPS substrate, the surface is immediately slippery. In the case of a silicone elastomer with uncrosslinked chains, a delay allows droplets to stay on a vertical substrate for a while, before a self-cleaning step happening naturally after a few minutes.

Appendix: published articles

A. Fargette, S. Neukirch, and A. Antkowiak, *Elastocapillary snapping: Capillarity induces snap through instabilities in small elastic beams*, Physical Review Letters, **112**, 137802 (2014). [157]



A. Hourlier-Fargette, A. Antkowiak, A. Chateauminois and S. Neukirch, *Role of uncrosslinked chains in droplets dynamics on silicone elastomers*, Soft Matter, **13**, 3484-3491 (2017), with an highlight on the inside front cover. [176]



Elastocapillary Snapping: Capillarity Induces Snap-Through Instabilities in Small Elastic Beams

Aurélie Fargette,^{1,2,3} Sébastien Neukirch,^{2,3} and Arnaud Antkowiak^{2,3}

¹*Département de Physique, École Normale Supérieure, 24 rue Lhomond, 75005 Paris, France*

²*CNRS, UMR 7190, Institut Jean Le Rond d'Alembert, F-75005 Paris, France*

³*UPMC Université Paris 06, UMR 7190, Institut Jean Le Rond d'Alembert, F-75005 Paris, France*

(Received 5 July 2013; revised manuscript received 14 November 2013; published 4 April 2014)

We report on the capillarity-induced snapping of elastic beams. We show that a millimeter-sized water drop gently deposited on a thin buckled polymer strip may trigger an elastocapillary snap-through instability. We investigate experimentally and theoretically the statics and dynamics of this phenomenon and we further demonstrate that snapping can act against gravity, or be induced by soap bubbles on centimeter-sized thin metal strips. We argue that this phenomenon is suitable to miniaturization and design a condensation-induced spin-off version of the experiment involving a hydrophilic strip placed in a steam flow.

DOI: 10.1103/PhysRevLett.112.137802

PACS numbers: 61.41.+e, 46.32.+x, 47.55.D-, 68.03.Cd

Elastic arches and spherical shells can sustain large loads but they all eventually fail through an elastic instability, called snapping or snap-through buckling; see Refs. [1,2] for early studies on the subject. This phenomenon is central to the failure of arches and vaults but has also been exploited to actuate bistable switches or valves [3] with point force [4], electrostatic [5], piezoelectric [6], or vibrational [7] loading. Snapping is also a useful mechanism in the design of responsive surfaces with applications to on-demand drug delivery, optical surface properties modification, or on-command frictional changes [8]. Nature provides examples of practical applications of snapping in prey capturing by carnivorous plants [9], fast ejection of spores [10], or underwater plant suction traps [11]. Similarly, polymersomes [12] or malaria infected blood cells [13] also exhibit snapping events (or fast shell eversion) that promote fast ejection of drug components or parasites. These examples differ in their triggering mechanisms, but they all involve a snapping instability including fast movements and curvature reversals that are a consequence of the sudden release of stored elastic energy and its transfer into kinetic energy.

Here we show how capillary forces may be used to trigger snap-through instabilities: a drop deposited on a thin buckled elastic strip induces snapping, possibly even

against gravity, as illustrated in Fig. 1 and the Supplemental Material [14]. Our experiments consist in loading buckled elastic strips with either transverse point forces or water droplets. Initially flat elastic strips of length L and width w are carefully cut out of a thin polymer film made of polydimethylsiloxane (PDMS, Sylgard 184 Elastomer base blended with its curing agent in proportion 10:1), spin-coated and cured at 60 °C for two hours. The resulting thickness h of the samples is quantified with an optical profilometer. The Young's modulus of our samples, measured using a Shimadzu testing machine, is found to be $E = 1.50 \pm 0.05$ MPa, enabling us to evaluate their bending rigidity $EI = Eh^3w/12$. Experiments are carried out with two different strips whose geometrical and mechanical properties are reported in Table I. These PDMS strips are clamped at both ends in microscope slides with cut edges. In point-force induced snapping, force-displacement data are gathered with a microforce sensor using capacitive deflection measurement [15] (Femtools FT-S270) and a nanopositioner (SmarAct SLC-1730). Capillary snapping is investigated by depositing water drops (surface tension γ) with Hamilton syringes or a syringe pump (Harvard Apparatus) with polytetrafluoroethylene (PTFE) coated needles. The elastocapillary length $L_{ec} = \sqrt{Eh^3/12\gamma}$ of

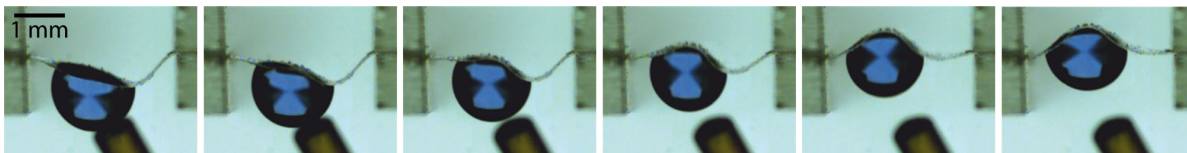


FIG. 1 (color online). Snapping against gravity. Using a PTFE coated needle, a drop is gently deposited under a downward buckled PDMS strip (case S2 in Table I). Within a few milliseconds, capillary forces induce a snap-through elastic instability of the strip which jumps to the upward buckled state. Note that in this setup surface tension overcomes both elastic forces and gravity. The liquid is tap water dyed with blue ink for visualization purposes. The time interval between each snapshot is 5 ms.

TABLE I. Length L , width w , thickness h , confinement parameter Δ , elastocapillary length L_{ec} and typical bending dynamics time T for the two experimental setups.

Setups	L (mm)	w (mm)	h (μm)	Δ/L	L_{ec}/L	T (ms)
S1	5.0	1.07	68.3	0.95	6.7	34
S2	3.5	0.98	33.7	0.90	13.6	33

the samples is reported in Table I. Video acquisition is carried out with an ultrafast Photron SA-5 camera.

In order to reveal the role of capillarity in snap-through instability, we start with considering a “dry” setup. When confined axially, an initially straight beam buckles and adopts an arched shape; the stronger the confinement the higher the arch. If one now fixes the confinement and applies a downward vertical force F at the middle point of the beam, the height Y of the arch decreases; see Fig. 2. As this vertical force reaches a threshold $F = F^*$ the arch snaps to a downward configuration [1,2,16]. This threshold value for snap-through is known to depend on the position x of the applied force and reaches a local maximum when $x/\Delta = 1/2$ [17]. In Fig. 2, a comparison is made between experiments and theory. Theoretical bifurcation curves are computed using Kirchhoff equations [18] and experiments are carried on the strip S1 (see Table I) in a setup where the arch height Y is reduced. As we controlled Y instead of the force F , configurations in the asymmetric branch are stable and snap-through really only occurs as F reaches zero. We nevertheless keep on referring to the point $F = F^*$ as the snapping threshold. It should be noted that the fixed

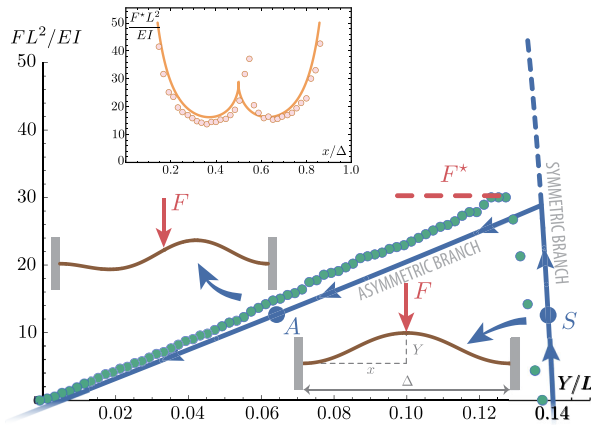


FIG. 2 (color online). Snap-through instability with point force. An elastic strip S1 is clamped at both ends with fixed $\Delta = 0.95L$ and vertical indentation at $x/\Delta = 1/2$ is performed. The bifurcation diagram (theory: blue curve, experiments: filled circles) comprises a symmetric and an asymmetric branch connecting at $F = F^*$ (experimentally measured $F^* = 55 \mu\text{N}$). Inset: Evolution of the snapping threshold F^* as a function of the indentation position x , evidencing two preferential positions where the threshold is minimal: $x/\Delta \approx 0.37$ and 0.63 .

confinement $\Delta = 0.95L$ is small enough for the precise way with which the vertical loading is applied to be disregarded [16], but large enough for extension effects to be negligible [19].

We now replace the point load with a water drop. Drops of increasing volume are deposited or hung on the same strip (case S1 in Table I). The height of the arch Y is recorded as a function of the total weight F of the drop; see Fig. 3. As the volume of the drop is increased, the height of the arch decreases until a limit is reached where snap-through occurs. We remark that much heavier drops are required to trigger the snap-through instability in the hanging-drop setup as compared to the sitting-drop setup, the dry setup being intermediate. We conclude that only considering the weight of the drop is not enough; i.e., capillary forces have a strong influence on snap-through. As known in shell indentation, the response of elastic structures to external loads strongly depends on whether the

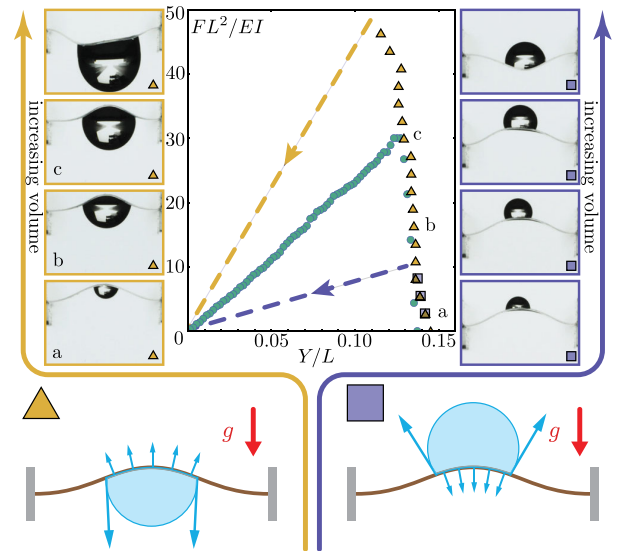


FIG. 3 (color online). Influence of capillarity on the bifurcation diagram of Fig. 2. Drops of increasing volume are hung below (orange triangles) or deposited above (purple squares) the elastic strip S1, buckled upward with $\Delta = 0.95L$. As the nondimensional drop weight FL^2/EI increases, the deflection Y/L of the strip midpoint decreases, up to a point where snapping occurs (indicated by the dashed lines on the diagram). For comparison we plot the data of Fig. 2, filled circles, performed on the same S1 strip. For both square and triangle sets, the volume increase between each measure is $0.5 \mu\ell$, corresponding to a nondimensional force increase of 2.73. The left (orange) panel shows hanging configurations with, from bottom to top, $V = F/\rho g = 0.5 \mu\ell, 3 \mu\ell, 5.5 \mu\ell, 9 \mu\ell$, with $\rho = 1000 \text{ kg/m}^3$. The right (purple) panel shows sitting configurations with, from bottom to top, $V = 0.5 \mu\ell, 1 \mu\ell, 1.5 \mu\ell, 2 \mu\ell$. Note that the present dead loading (squares and triangles) makes the asymmetric branch unstable, as opposed to the rigid loading setup of Fig. 2.

loading is performed through point forces or distributed pressure loads [20]. In our case the water drop applies distributed hydrostatic and Laplace pressures as well as localized meniscus forces; see Fig. 3. The combined action of Laplace and meniscus forces can be seen as two opposite effective bending moments, promoting the eversion of the strip [21] when the drop is located above, and hindering it when located below.

To further investigate relative strengths of capillarity, weight, and elastic forces, we study the following setup: an elastic strip (case S2 in Table I) is buckled downward and a drop is hung at a given location under the strip; see Fig. 4(c). Parameters are the total weight F of the drop and the abscissa x_M of the middle point of the wet region of the beam. Experiments show that snapping only occurs for specific values of F and x_M ; see Fig. 4(b). For small drops (i.e., small F), capillary forces exceed self-weight (a drop deposited under a rigid surface is stable if small enough) but are not powerful enough to overcome elastic forces, mainly because the lever arm of the effective bending moments discussed earlier is not large enough: the wet length is indeed a key factor in determining the behavior of elastocapillary systems [22]. Consequently the system

stays in the downward configuration. For moderate drops (with larger wet lengths) we see in Fig. 4(b) that provided the location of the drop is carefully chosen, snapping occurs, resulting in a final state where the strip is bent upward: in this case capillary forces overcome both weight and elastic forces. For large drops capillarity still defeats elasticity but self-weight is too large and the system stays in the downward configuration.

To understand the different regions of the (x_M, F) phase diagram we numerically compute equilibrium and stability of the drop-strip system in the following way. We consider a 2D setting where a liquid drop of given volume is hung under an elastic strip of length L , thickness h , and bending rigidity $Eh^3/12$. The strip is clamped at both ends which are separated by a fixed distance Δ . We use the arclength s along the strip to parametrize its position $\mathbf{r}_s(s) = (x_s(s), y_s(s))$. The unit tangent, $\mathbf{t}_s(s) = d\mathbf{r}_s/ds$, makes an angle $\theta_s(s)$ with the horizontal: $\mathbf{t}_s = (\cos \theta_s, \sin \theta_s)$. The drop lies between positions $s = s_A$ and $s = s_B$ on the strip, and the shape of the liquid-air interface, parametrized with its own arclength σ , is $\mathbf{r}_i(\sigma) = (x_i(\sigma), y_i(\sigma))$ and has total contour length ℓ ; see Fig. 4(c). The bending energy of the strip and gravity potential energy of the water are

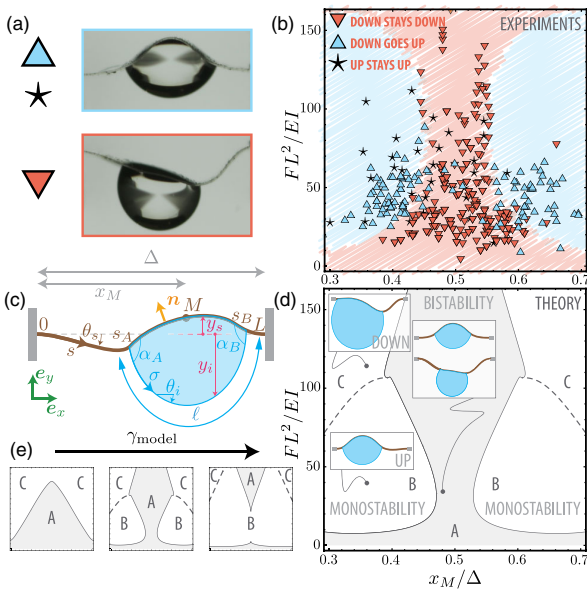


FIG. 4 (color online). Phase diagram for elastocapillary snapping: A drop is hung under a strip and the conditions for snapping to occur are investigated. (a) Possible final states of the system. (b) Experimental phase diagram plotted in the (x_M, F) plane. Triangles (respectively, \star) correspond to experiments where the drop is deposited on an initially downward (respectively, upward) buckled strip. (c) Model notations. (d) Theoretical phase diagram showing bistable A and monostable B and C regions. Note that here FL^2/EI corresponds to $12\rho AgL^2/Eh^3$. (e) Evolution of the theoretical phase diagram as the surface tension used in the model γ_{model} takes the values 0.38γ , 0.67γ , and 0.96γ (from left to right).

$$E_{\text{bend}} + E_{\text{hydro}} = \frac{Eh^3}{24} \int_0^L [\theta'_s(s)]^2 ds + \rho g \int \int_A y dA \quad (1)$$

where $\mathcal{A} = \int_0^\ell y_i(\sigma) x'_i(\sigma) d\sigma - \int_{s_A}^{s_B} y_s(s) x'_s(s) ds$ is the area between the strip and the liquid-air interface. The energy per unit area of solid-liquid (respectively, solid-air and liquid-air) interface is noted $\gamma_{\ell s}$ (respectively, γ_{sv} and γ). The total interface energy is then

$$E_{\text{surf}} = (s_B - s_A)\gamma_{\ell s} + [L - (s_B - s_A)]\gamma_{sv} + \gamma\ell. \quad (2)$$

We minimize the total potential energy $U = E_{\text{bend}} + E_{\text{hydro}} + E_{\text{surf}}$ [23] under the constraints of inextensibility $\mathbf{r}'_s(s) = \mathbf{t}_s$, constant area \mathcal{A} , and matching conditions $\mathbf{r}_s(s_A) = \mathbf{r}_i(0)$ and $\mathbf{r}_s(s_B) = \mathbf{r}_i(\ell)$. This constrained minimization problem is solved by considering the following Lagrangian functional:

$$\mathcal{L}[\mathbf{r}_s(s), \theta_s(s), s_A, s_B, \mathbf{r}_i(\sigma), \theta_i(\sigma), \ell] = U - \boldsymbol{\mu} \cdot \boldsymbol{\psi} \quad (3)$$

where the vector $\boldsymbol{\psi}$ comprises all the constraints and $\boldsymbol{\mu}$ is the vector of associated Lagrange multipliers; see Ref. [24]. Classical minimization and continuation techniques are used to track equilibrium states along branches in bifurcation diagrams. Note that in this 2D model the effective surface of the drop is not minimal because of its cylindrical shape. To counterbalance this effect we have used a reduced surface tension $\gamma_{\text{model}} = 0.67\gamma$, analogous to the surface correction coefficient introduced in Ref. [25]. In the computations, sliding of the drop is prevented by constraining the mean position $s_M = (s_A + s_B)/2$ and the



FIG. 5. Condensation-induced snapping. The experiment approximately lasts three minutes.

mean contact angle $(\alpha_A + \alpha_B)/2 = 110^\circ$. Stability of the system is assessed by computing the linearized dynamics about the equilibrium solution. Results are shown in Fig. 4(d) where the theoretical (x_M, F) phase diagram is plotted. The continuous curve, later referred to as the instability curve, corresponds to loss of the stability of an equilibrium configuration. The dashed curve corresponds to the smooth transition from downward buckled states ($y_M < 0$) to upward buckled states ($y_M > 0$). These two curves divide the (x_M, F) plane into three regions. In region A, which lies below the instability curve, downward and upward buckled configurations are both found to be stable. As the crossing of the instability curve is associated with the loss of stability of one of the configurations, in the two regions above the instability curve there is only one stable configuration: upward for region B, below the dashed curve, and downward for region C, above the dashed curve. We remark that the shape of the instability curve and hence the topology of the phase diagram is altered by changes in the value of γ_{model} , as shown in Fig. 4(e). These numerical results shed light on experimental findings: in the bistable region A, a drop deposited under a downward buckled strip leads to a downward final state unless the perturbation created during the deposition is too large and the system jumps to an upward final state, whereas in the monostable region B the final state is always an upward configuration. As a cross-check we have experimentally hung drops under upward buckled strips and found that in regions A and B the system stays in the upward configuration, thereby confirming the bistability of region A; see \star markers in Fig. 4(b).

We next show that snapping may be induced remotely. The lower side of a PDMS strip is treated with a hydrophilic coating. The strip is then buckled downward and placed in a steam flow. Water droplets nucleate on the hydrophilic side of the strip, coalesce, and eventually induce snapping; see Fig. 5. This phenomenon could be used to build moisture sensors that would snap once ambient humidity has reached a given threshold.

We finally investigate time scales involved in the dynamics of the snapping instability. The shape of the beam as it leaves the unstable equilibrium is recorded with a high-speed camera. The vertical position $y_s(s = L/2, t)$ of the midpoint of the beam is extracted from the image sequence. From the fit $y_s(L/2, t) = y_0 + y_1 e^{\mu t}$ we obtain the growth rate μ . From this growth rate μ we define a snapping time $\tau_{\text{snap}} = 1/\mu$ and plot τ_{snap} as a function of the length L of the beam. For dry snapping and in the case of

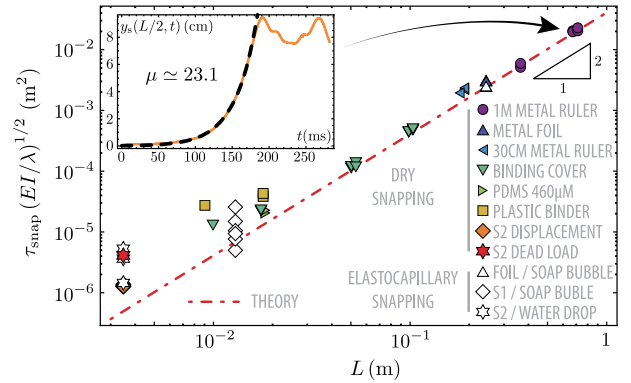


FIG. 6 (color online). Snapping dynamics. Typical time τ_{snap} for snapping in different setups. The dashed line is the theoretical prediction for dry snapping $\tau_{\text{snap}} = (L^2/24)\sqrt{\lambda/EI}$.

controlled vertical displacement the instability occurs as the force reaches zero. At this point the beam has an unstable equilibrium shape corresponding to the second buckling mode of the planar elastica. We numerically compute the growth rate to be $\mu = 24.26/T$ for $\Delta = 0.95L$ where $T = L^2\sqrt{\lambda/EI}$ is the typical time of bending dynamics (see Table I) and λ is the mass per length of the beam. As the growth rate weakly depends on the confinement Δ (e.g., $\mu = 24.42/T$ for $\Delta = 0.9L$; see also Ref. [19]) we use an approximate theoretical prediction $\tau_{\text{snap}} = T/24$ for dry snapping. Experiments performed with various materials and confinements, e.g., dry setups involving $L = 0.7$ m metal beams, show that, apart from a deviation at small lengths attributed to viscous effects in the strip, theory agrees nicely with experiments; see Fig. 6. Additional experiments with capillary S1 and S2 setups, but also setups with soap bubbles actuating $L = 0.25$ m metal foil strips (see the Supplemental Material [26]), show that the snapping time appears to be the same for dry and wet snapping.

In summary we have shown that the snap-through of a beam can be triggered by capillary forces. More precisely a drop deposited under a downward buckled beam can induce a snap-through instability that drives the system to an upward configuration. As in adhesive film separation [27] or in the pull-out of a soft object from a liquid bath [28], the elastic energy stored in the system before the instability is suddenly released in the form of kinetic energy and is mainly “lost.” We nevertheless showed in our setup that part of the energy could be used to lift the liquid drop. We have also shown that the elastocapillary dynamics is mainly driven by elastic forces and that fluid forces and fluid inertia only play a minor role: capillarity is driving the system toward instability but elasticity is ruling the subsequent dynamics. The typical scaling of surface forces makes elastocapillary snapping a good candidate for miniaturization and its use as a microactuator might be

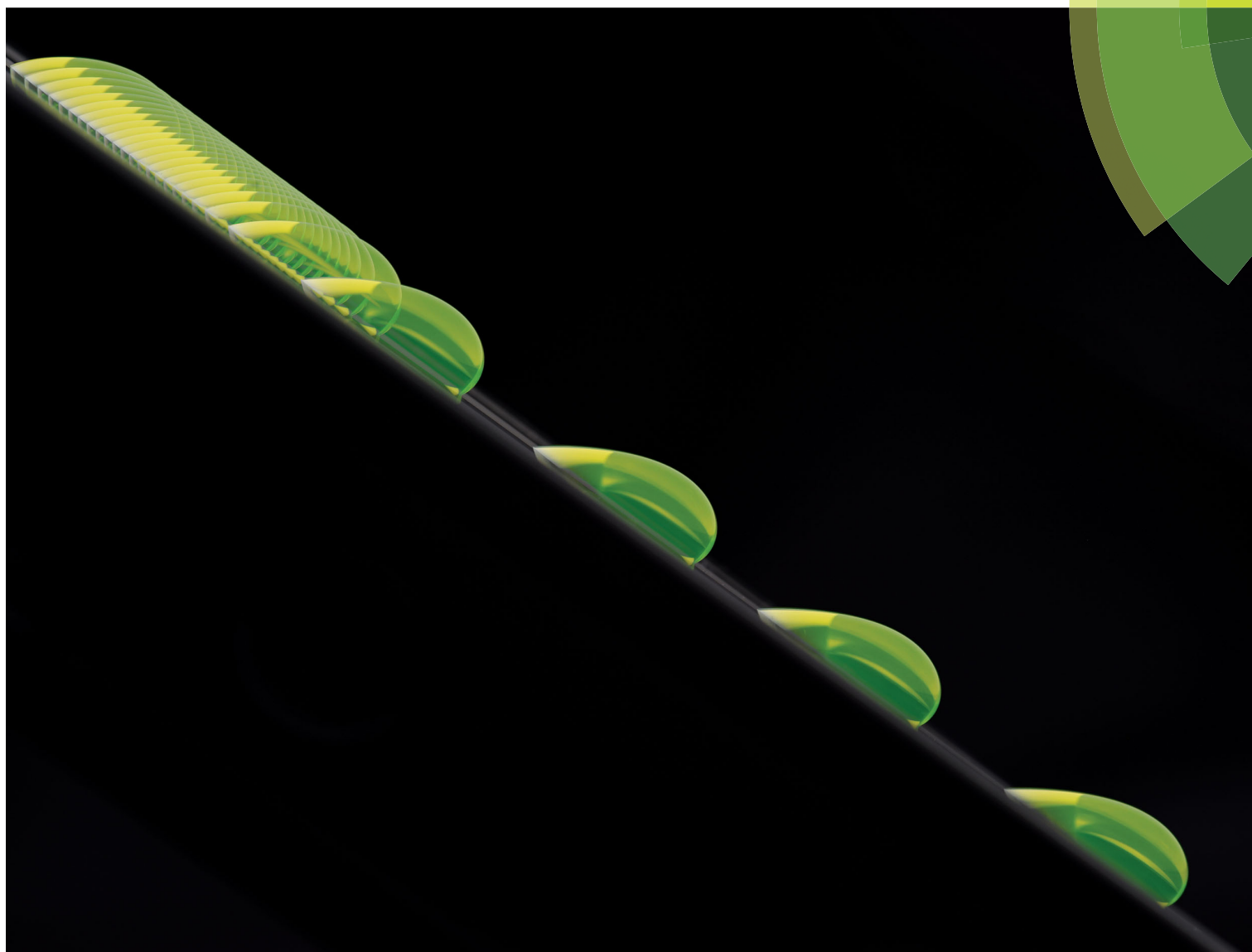
envisaged. In any case the present study is an example of a constructive use of capillarity at small scales.

The present work was supported by ANR Grant No. ANR-09-JCJC-0022-01. Financial support from “La Ville de Paris—Programme Émergence” is also gratefully acknowledged. We thank G. Debrégeas for optical profilometer measurements, F. Monti for oxygen plasma treatment of PDMS samples, and F. Brochard-Wyart for discussions.

-
- [1] S. Timoshenko, *Philos. Mag.* **43**, 1023 (1922), Series 6.
 [2] S. P. Timoshenko, *J. Appl. Mech.* **2**, 17 (1935).
 [3] W. Schomburg and C. Goll, *Sens. Actuators A* **64**, 259 (1998).
 [4] J. Qiu, J. H. Lang, and A. H. Slocum, *J. Microelectromech. Syst.* **13**, 137 (2004).
 [5] Y. Zhang, Y. Wang, Z. Li, Y. Huang, and D. Li, *J. Microelectromech. Syst.* **16**, 684 (2007).
 [6] C. Maurini, J. Pouget, and S. Vidoli, *Eur. J. Mech. A. Solids* **26**, 837 (2007).
 [7] J. Casals-Terre, A. Fargas-Marques, and A. Shkel, *J. Microelectromech. Syst.* **17**, 1082 (2008).
 [8] D. Holmes and A. Crosby, *Adv. Mater.* **19**, 3589 (2007).
 [9] Y. Forterre, J. M. Skotheim, J. Dumais, and L. Mahadevan, *Nature (London)* **433**, 421 (2005).
 [10] X. Noblin, N. O. Rojas, J. Westbrook, C. Llorens, M. Argentina, and J. Dumais, *Science* **335**, 1322 (2012).
 [11] O. Vincent, C. Weißkopf, S. Poppinga, T. Masselter, T. Speck, M. Joyeux, C. Quilliet, and P. Marmottant, *Proc. R. Soc. B* **278**, 2909 (2011).
 [12] E. Mabrouk, D. Cuvelier, F. Brochard-Wyart, P. Nassoy, and M.-H. Li, *Proc. Natl. Acad. Sci. U.S.A.* **106**, 7294 (2009).
 [13] M. Abkarian, G. Massiera, L. Berry, M. Roques, and C. Braun-Breton, *Blood* **117**, 4118 (2011).
 [14] See Supplemental Material at <http://link.aps.org/supplemental/10.1103/PhysRevLett.112.137802> for video SV1.
 [15] Y. Sun, S. Fry, D. Potasek, D. Bell, and B. Nelson, *J. Microelectromech. Syst.* **14**, 4 (2005).
 [16] J.-S. Chen and S.-Y. Hung, *Eur. J. Mech. A. Solids* **30**, 525 (2011).
 [17] J. M. T. Thompson and G. W. Hunt, *Int. J. Solids Struct.* **19**, 445 (1983).
 [18] B. Audoly and Y. Pomeau, *Elasticity and Geometry: From Hair Curls to the Nonlinear Response of Shells* (Oxford University Press, New York, 2010).
 [19] A. Pandey, D. E. Moulton, D. Vella, and D. P. Holmes, *Europhys. Lett.* **105**, 24 001 (2014).
 [20] S. P. Timoshenko and J. M. Gere, *Theory of Elastic Stability* (McGraw-Hill, New York, 1961), 2nd ed.
 [21] P. Podio-Guidugli, M. Rosati, A. Schiaffino, and V. Valente, *SIAM J. Math. Anal.* **20**, 643 (1989).
 [22] A. Antkowiak, B. Audoly, C. Josserand, S. Neukirch, and M. Rivetti, *Proc. Natl. Acad. Sci. U.S.A.* **108**, 10 400 (2011).
 [23] Note that the gravity potential energy of the strip is small compared to the other energies and is therefore not listed in the present formulation. It was nevertheless included in the computations and its effect was indeed negligible.
 [24] S. Neukirch, A. Antkowiak, and J.-J. Marigo, *Proc. R. Soc. A* **469**, 20130066 (2013).
 [25] M. Rivetti and S. Neukirch, *Proc. R. Soc. A* **468**, 1304 (2012).
 [26] See Supplemental Material at <http://link.aps.org/supplemental/10.1103/PhysRevLett.112.137802> for video SV2.
 [27] C. Gay and L. Leibler, *Phys. Today* **52**, No. 11, 48 (1999).
 [28] M. Rivetti and A. Antkowiak, *Soft Matter* **9**, 6226 (2013).

Soft Matter

rsc.li/soft-matter-journal



ISSN 1744-6848



PAPER

Aurélie Hourlier-Fargette, Sébastien Neukirch *et al.*

Role of uncrosslinked chains in droplets dynamics on silicone elastomers



Role of uncrosslinked chains in droplets dynamics on silicone elastomers†

Aurélie Hourlier-Fargette,^{id}*^{ab} Arnaud Antkowiak,^{id}^{ac} Antoine Chateauminois^d and Sébastien Neukirch*^a

Cite this: *Soft Matter*, 2017, **13**, 3484

Received 3rd March 2017,
Accepted 5th April 2017

DOI: 10.1039/c7sm00447h

rsc.li/soft-matter-journal

We report an unexpected behavior in wetting dynamics on soft silicone substrates: the dynamics of aqueous droplets deposited on vertical plates of such elastomers exhibits two successive speed regimes. This macroscopic observation is found to be closely related to microscopic phenomena occurring at the scale of the polymer network: we show that uncrosslinked chains found in most widely used commercial silicone elastomers are responsible for this surprising behavior. A direct visualization of the uncrosslinked oligomers collected by water droplets is performed, evidencing that a capillarity-induced phase separation occurs: uncrosslinked oligomers are extracted from the silicone elastomer network by the water–glycerol mixture droplet. The sharp speed change is shown to coincide with an abrupt transition in surface tension of the droplets, when a critical surface concentration in uncrosslinked oligomer chains is reached. We infer that a droplet shifts to a second regime with a faster speed when it is completely covered with a homogeneous oil film.

1 Introduction

Commonly used in industry, silicone elastomers also serve as easy-to-make substrates in various academic research domains. Very popular in elastocapillarity, for both experiments on slender bendable structures^{1,2} and on thick softer substrates,^{3–6} they are even more widely spread in microfluidics, *e.g.* for biological cultures in microfluidic channels.^{7,8} However, drawbacks in the use of these elastomers have been reported, for example absorption issues into the polymer bulk,⁹ or leaching of unreacted oligomers from the polymer network into the microchannel medium.⁸ Beyond the interest of understanding droplet dynamics on stiff inclined surfaces,^{10–15} the development of soft materials has led to a growing interest for soft-wetting dynamics. A droplet deposited on a soft substrate is able to induce a wetting ridge at the contact line,^{5,16} resulting in an additional source of dissipation when this triple line is moving.¹⁷ The recent design of Slippery Lubricant Infused Porous Surfaces also leads to novel wetting dynamics studies,¹⁸ to understand how droplets

slide or roll on a micro- or nano-textured substrate infused with oil. Soft commercial elastomers like poly(dimethylsiloxane) (PDMS) Sylgard 184 from Dow Corning are known to contain a small fraction of uncrosslinked low-molecular-weight oligomers,¹⁹ the effects of which on wetting dynamics are not completely understood. However, it has been shown recently that adhesion of a silica microbead on a soft elastomer gel leads to a phase separation which transforms the classical three-phase contact line into a four-phase contact zone, in which air, silica, liquid silicone, and silicone gel meet.²⁰

Here we show that uncrosslinked chains also play a major role in wetting dynamics in spite of their small amount within the silicone elastomers under consideration: a droplet of water–glycerol mixture deposited on a vertical silicone elastomer surface with no initial speed is shown to exhibit two different regimes characterized by two different constant speeds, as illustrated in Fig. 1 and in Video 1, ESI.† We demonstrate the crucial role of uncrosslinked oligomers in this two-regime dynamics, and highlight that the sharp transition between the two speed regimes coincides with a sharp transition in surface tension as the droplet is progressively covered by uncrosslinked chains. Experimental results in the literature²¹ show a correlation between the surface tension and the thickness of a PDMS oil layer on a water bath. We infer from our surface-tension measurements that the two regimes are linked to two different states of the droplet: in the first regime, the droplet is only partially covered with some patches of uncrosslinked oligomers, while in the second regime, the droplet is completely covered by a uniform oil layer, with probably oil wetting ridges at the

^a Sorbonne Universités, UPMC Univ Paris 06, CNRS, UMR 7190, Institut Jean Le Rond d'Alembert, F-75005 Paris, France.

E-mail: aurelie.fargette@dalembert.upmc.fr, sebastien.neukirch@upmc.fr

^b Département de Physique, École Normale Supérieure, CNRS, PSL Research University, F-75005 Paris, France

^c Surface du Verre et Interfaces, UMR 125 CNRS/Saint-Gobain, F-93303 Aubervilliers, France

^d ESPCI & CNRS, UMR 7615, Laboratoire de Sciences et Ingénierie de la Matière Molle, F-75005 Paris, France

† Electronic supplementary information (ESI) available. See DOI: 10.1039/c7sm00447h

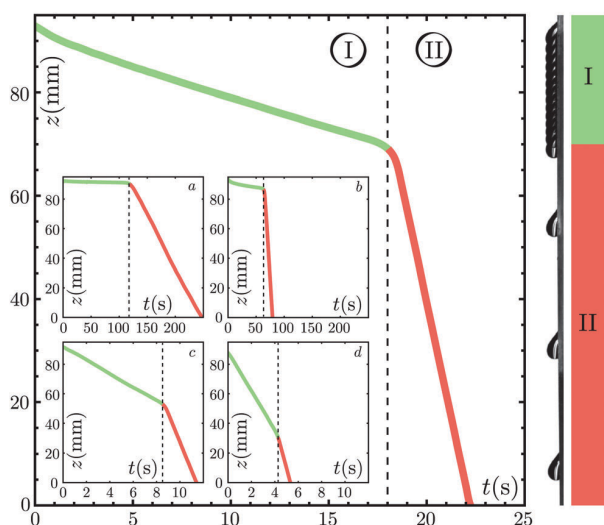


Fig. 1 A 40% water–60% glycerol mixture droplet of volume 21.5 μL is deposited with no initial speed on a vertical PDMS surface. Two regimes with two different constant speeds are identified (I and II). Right: Snapshots are taken every 1.28 s and superimposed together. Inset: Same experiment with droplets of volumes 14 μL (a), 18 μL (b), 22.5 μL (c) and 24 μL (d).

triple line. We show that the first regime dynamics is set by the competition between the weight of the droplet, capillary pinning forces, and viscous dissipation inside the drop, while the second regime presents some similarities with the dynamics observed in the case of water droplets on Slippery Lubricant Infused Porous Surfaces.¹⁸

2 Experimental methods

2.1 Silicone elastomer samples

Unless otherwise specified, elastomer samples are made of PDMS (Dow Corning Sylgard 184 Elastomer base blended with its curing agent in proportion 10:1 by weight, cured during 2 hours at 60 °C) molded in 12 cm square Petri dishes to get flat samples with a thickness of a few millimeters. The Young's modulus of our PDMS samples, measured with a Shimadzu testing machine, was found to be $E = 1.8 \pm 0.1$ MPa. In order to test the generality of the observed phenomenon, some experiments were also carried out using other commercially available silicone elastomers, such as polyvinylsiloxane (PVS, Elite Double 22 Zhermack), RTV EC13 and EC33 polyaddition silicone polymer (Esprit Composite), and PDMS Sylgard 184 cured during 24 h at 120 °C.

2.2 Droplet deposition and video acquisition techniques

Droplets of water–glycerol mixtures (deionized water and glycerol 99+% pure, Acros Organics), which properties are given in Table 1, are deposited on polymer samples with an electronic micropipette (Sartorius eLINE 5–120 μL). Surface tensions have been measured with a Krüss K6 manual tensiometer (hanging ring). Videos have been captured with a Hamamatsu Orca Flash digital CMOS camera, with frame rates going from 10 to 1000 frames per second.

Table 1 Water and glycerol mixing ratios, temperature T during the experiments, viscosity μ , density ρ and surface tension γ , measured experimentally for the different mixtures used

Glycerol (%)	Water (%)	Temperature T (°C)	Viscosity μ (mPa s)	Density ρ (kg m^{-3})	Surface tension γ (mN m^{-1})
50	50	19.3 ± 1.0	6.2 ± 0.2	1124 ± 1	69.0 ± 0.5
60	40	25.3 ± 1.0	8.7 ± 0.2	1150 ± 1	68.4 ± 0.5
65	35	27.0 ± 1.0	11.1 ± 0.2	1164 ± 1	67.9 ± 0.5
75	25	20.7 ± 1.0	34.1 ± 0.5	1192 ± 1	67.1 ± 0.5
85	15	27.5 ± 1.0	68.1 ± 1.0	1219 ± 1	66.5 ± 0.5

3 Role of uncrosslinked polymer chains

3.1 Unexpected dynamics for an aqueous droplet on a vertical elastomer plate

Fig. 1 shows the dynamics of a water–glycerol mixture droplet deposited on a vertical PDMS plate. Two distinct regimes characterized by two different constant speeds are evidenced. This two-regime behavior is observed for various droplet volumes (insets of Fig. 1) and various water–glycerol mixing ratios, from pure water to 90% glycerol mixture. The same qualitative behavior is also obtained on several commercial silicone elastomers, as shown in Fig. S1, ESI.† These observations contrast with experiments on treated glass¹⁵ during which a single constant speed is reached after a short transient.

Droplet dynamics on a vertical surface usually results from a competition between the weight of the droplet, capillary forces, and viscous dissipation inside the drop. For a droplet of volume V and density ρ on a vertical surface, the gravitational force is given by:

$$F_g = \rho V g. \quad (1)$$

The descent of the drop begins only if $F_g > F_{cl}$, F_{cl} being the contact-line pinning force:

$$F_{cl} \propto \gamma w (\cos \theta_{sr} - \cos \theta_{sa}), \quad (2)$$

where γ is the surface tension of the liquid–air interface, w the width of the droplet, θ_{sr} the static receding angle and θ_{sa} the static advancing angle. A more precise determination of the onset of motion is given in the literature.¹³ Once steady motion is reached, the value of the droplet speed is obtained by balancing the weight F_g with the sum of the contact line pinning force F_{cl} and the viscous dissipation force in the droplet F_μ . F_μ can be derived using different approaches, depending on the dissipation being located in the bulk or in the receding corner of the droplet.^{22,23} The simplest approach yields:

$$F_\mu \propto \frac{\mu U \mathcal{S}}{h}, \quad (3)$$

where U is the droplet speed, μ the viscosity of the liquid, \mathcal{S} the contact area, and h the droplet height. For low Re viscous drops (with $\text{Re} = UV^{1/3}\rho/\mu$), assuming that $w = h = \sqrt{\mathcal{S}} = V^{1/3}$ leads to a linear relationship between Ca and Bo where $\text{Ca} = \mu U/\gamma$ is the capillary number, and $\text{Bo} = \rho V^{2/3}g/\gamma$ is the Bond number (this relationship has been found to capture the dynamics of

droplets even when Re is of order one¹⁵). This description, as well as more detailed approaches taking into account the details of the viscous dissipation processes in the droplet^{11,12,23} or in the elastomer,^{3,17,24} cannot explain the two regimes in our experiments.

Different candidates can be responsible for the sudden change in the droplet speed: droplet shape bistability, modification of the droplet composition due to an interaction with the substrate, sliding to rolling transition, change in shape of the tail of the droplet and pearling transition.^{15,25,26} Volumes have been kept under the threshold for which pearling occurs. Tracking particles in the water–glycerol mixture reveals that, in both regimes, the drop is rolling rather than sliding over the surface, with no significant difference in the motion of the fluid between the two regimes (Video 2, ESI†).

Turning the setup upside down after a droplet has slid down allows us to reuse the same droplet and same sample for a second descent and to observe that the behavior of a droplet during the first descent is completely different from its behavior during the following descents. The first descent shows two distinct regimes, whereas the following descents only exhibit one regime, corresponding to the second regime of the first descent (Fig. S2, ESI†). This observation advocates for a modification of the droplet composition during its first descent.

3.2 Toluene-treated plates

When PDMS oligomers are crosslinked to form the polymer network, a few oligomer chains are not incorporated into the network.¹⁹ A PDMS sample thus contains uncrosslinked low-molecular-weight oligomers, which can be extracted from the bulk PDMS by swelling in a good solvent. Accordingly, treated PDMS samples are obtained using the following procedure: the samples are fully immersed for one week in a toluene bath which is renewed every day in order to keep the concentration in extracted PDMS oligomers low. Following this extraction, the PDMS substrate is subsequently de-swollen by progressively replacing toluene by a poor solvent of PDMS, namely ethanol. The samples are ultimately dried out in a vacuum oven. An average mass loss of 5% is measured, which corresponds to the weight fraction of the extracted uncrosslinked chains.

As illustrated in Fig. 2, a water–glycerol mixture droplet rolling down on such a treated elastomer only exhibits one speed regime. A one-regime behavior is also observed for various droplet volumes and various water–glycerol mixing ratios, from pure water to 90% glycerol mixture, deposited on vertical toluene-treated PDMS plates. These results show that the two-regime behavior observed on untreated samples is due to the presence of uncrosslinked oligomer chains. Reswelling a toluene-washed sample with a commercial PDMS v50 oil (Sigma Aldrich) enables us to recover the two-regime behavior, as shown in the inset in Fig. 2. This experiment provides an additional evidence of the crucial role played by the free oligomers of the substrate. Enhanced wetting hysteresis have already been observed in the case of PDMS grafted chains²⁷ but could not explain a two regime behavior. Here, a possible migration of the uncrosslinked chains to the water–air interface is investigated.

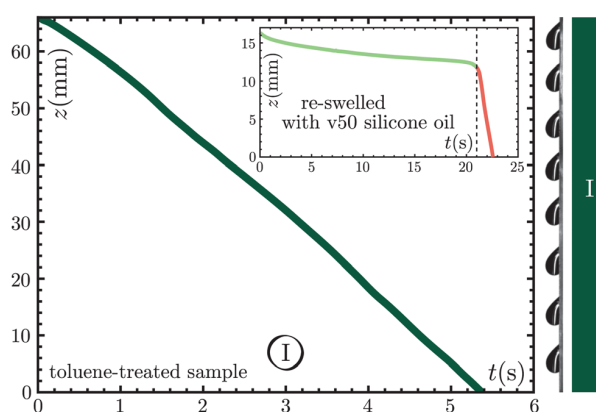


Fig. 2 A 40% water–60% glycerol mixture droplet of volume 21.5 μL is deposited with no initial speed on a vertical toluene-treated PDMS surface and a single regime is identified. Right: Snapshots are taken every 0.64 s and superimposed together. Inset: Droplet dynamics on a toluene-treated PDMS sample re-swelled with commercial v50 PDMS oil. A 50% water–50% glycerol mixture droplet of volume 18 μL is deposited with no initial speed on a vertical surface and two different regimes with two constant speeds are identified.

In the case of lubricant-infused surfaces, where a water drop rests on top of a thin layer of liquid oil, different wetting configurations are possible depending on the relative intensity of the surface tensions.^{18,28} Denoting γ_{wa} , γ_{wo} , and γ_{oa} the surface tensions of the water–air, water–oil, and oil–air interfaces respectively and introducing the wetting parameter $S = \gamma_{\text{wa}} - (\gamma_{\text{wo}} + \gamma_{\text{oa}})$, there are typically two possible situations for the wetting configuration: if $S > 0$ the oil completely covers the droplet and forms a thin film around it, whereas if $S < 0$ only a ridge of oil forms at the triple line. Interesting results about the composition of the uncrosslinked chains likely to migrate at the water–air interface are found in the literature in the context of biological cell cultures in PDMS microchannels: a mass spectroscopy analysis of water aspirated from Sylgard 184 PDMS microchannels has given evidence of the presence of free chains of various lengths, in a continuous range of fewer than 20 to more than 90 dimethylsiloxane units.⁸ As in the case of a v50 commercial silicone oil, the oil spreading parameter on water is positive, we conjecture the formation of a thin film of liquid PDMS around water–glycerol mixture droplets.

Now in the case where the substrate is a soft PDMS gel, uncrosslinked chains may phase-separate from the core of the gel and act as the thin layer of liquid oil mentioned above – such a phase separation was reported in the case of adhesion.²⁰ Here we show that a water droplet can extract uncrosslinked oligomers from the PDMS elastomer, evidencing the existence of capillarity-induced phase separation at the triple line. This hypothetical oil film on a single droplet is anyhow invisible to the naked eye, but collecting 1500 such droplets in a beaker after their two-regime descent on an untreated PDMS sample results in a direct visualization of oil at the surface of the beaker, as shown in Fig. 3c. The colored zones correspond to thicknesses of the order of light wavelengths, transparent lenses correspond to thicker oil zones, while the grey background corresponds to a

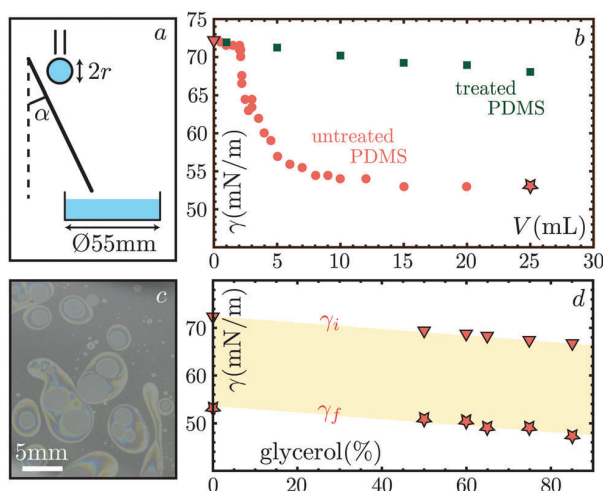


Fig. 3 (a) Experimental setup, with $\alpha = 29.2^\circ$ and $r = 2$ mm. (b) Surface tension of given volumes of water droplets collected just after reaching the second speed regime during their descent on untreated PDMS (red circles), compared to the same experiment performed on toluene-treated PDMS, with droplets collected after their descent on the 10 cm sample (dark green squares). (c) Surface of a beaker in which 1500 water droplets (of $33 \mu\text{L}$ each) were collected after reaching the second speed regime. The colored zones correspond to thicknesses of the order of light wavelengths, and transparent lenses correspond to thicker oil zones. (d) Initial and final values of the surface tension for the different liquids described in Table 1. Error bars are of the order of magnitude of the markers size.

thinner zone. The oil film is not homogeneous, in agreement with results in the literature about PDMS oil spreading at the surface of a water bath.²¹ It is thus difficult to evaluate the quantity of oil extracted by each droplet. A rough estimate, obtained by multiplying the surface of the beaker by a thickness of 500 nm (typical optical wavelength) gives the following result: the order of magnitude of the oil volume collected by each droplet is about 10^5 times smaller than the typical droplet volume. The control experiment on a toluene-treated PDMS sample leads to no visible oil at the surface of the beaker.

3.3 A silicone oligomer coating around a droplet modifies its surface tension

Surface-tension measurements of PDMS oil chains spread on a flat water–air interface performed in the literature²¹ give some insight into our current work: the surface tension of a water bath covered with PDMS oil chains is shown to be equal to pure water surface tension under a critical surface concentration in PDMS chains, and suddenly decreases above this threshold, to reach a plateau corresponding to the surface pressure of a homogeneous interface. Similar surface tension observations performed with natural oils such as olive or castor oil were already reported more than one century ago by A. Pockels,²⁹ Lord Rayleigh,³⁰ and I. Langmuir.³¹

Observing a sudden decrease of surface tension in our experiment would thus bring additional information about the presence of a thin oil film at the droplet–air interface: we focus on the surface tension of the droplets before being deposited on the substrate and

after reaching the second regime. An *in situ* measurement of the droplet–air surface tension proves to be difficult, and hanging droplet measurements have the drawback of requiring droplet collection inside a capillary tube, possibly breaking a thin oil film present on the droplets. Thus, we use the following setup: water–glycerol droplets of radius $r = 2.0$ mm are deposited with a syringe pump onto an inclined PDMS plane (Fig. 3a). Droplets are rolling down the plane and collected in a 55 mm diameter Petri dish after reaching the second regime. Surface tension of the liquid in the Petri dish is then measured as function of the collected volume for both droplets rolling down untreated Sylgard 184 PDMS and toluene-treated PDMS. For the untreated sample, Fig. 3b shows a dramatic decrease of surface tension around a collected volume of 3 mL, which corresponds to about 100 droplets. If we assume that each droplet is covered by a homogeneous thin film of oil, we calculate that the surface covered by this liquid oil in the Petri dish would be about 100 times larger than on one single droplet. A collected volume of 3 mL thus corresponds to the situation for which the thickness of the oil film on the Petri dish is of the same order as the thickness of the oil film on a droplet in the second regime. The same experiment performed with various Petri dish sizes and materials (polystyrene and glass) results in a collapse of all the data when rescaled with the Petri dish surface, as shown in Fig. S3, ESI.† We therefore conjecture that as the droplet is rolling down on PDMS, it is gradually covered with oil and eventually submitted to a change in surface tension. Building on results from Lee,²¹ we argue that the surface tension change occurs when a critical surface concentration on the droplet is reached, corresponding to the presence of a homogeneous oil film. We infer that this sharp transition in terms of surface tension is linked to a sudden change in the droplet state: before the transition, the droplet is only partially covered with some patches of uncrosslinked oligomers, while after the transition, the droplet is completely covered by an oil layer. Hence, we explain the sudden change in speed between the two regimes by the sudden transition between these two states for the droplet.

We also generalize the results obtained for water to various water–glycerol mixing ratios. The initial surface tension γ_i in the Petri dish before droplet collection, and the final surface tension γ_f measured when a 25 mL volume of droplets has been collected are both shown in Fig. 3d as a function of water–glycerol mixing ratio. We see that the difference between the initial and final surface tensions is constant, $\gamma_i - \gamma_f \approx 19 \text{ mN m}^{-1}$, showing that the surface pressure of the oil film formed at the surface of the liquid bath when collecting 25 mL of droplets remains constant as a function of the water–glycerol mixing ratio.

4 Quantitative speed measurements and discussion

4.1 Experimental observations

A quantitative measurement of the velocities in the first and second regimes on untreated PDMS is shown in Fig. 4a as a function of droplet volume, for a 35% water and 65% glycerol mixture.

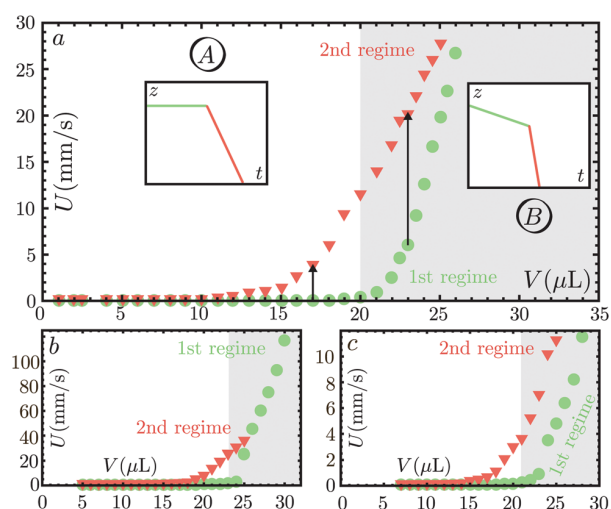


Fig. 4 (a) 65% glycerol–35% water droplet speeds on untreated PDMS as a function of its volume, in first (light green circles) and second regime (red triangles). Insets: Schematic phase diagrams in zone A (the speed in the first regime is negligible compared to the speed in the second regime) and zone B (the speed in the first regime is not negligible compared to the speed in the second regime). (b) Same experiment for a 50% glycerol–50% water mixture. (c) Same experiment for a 75% glycerol–25% water mixture. Error bars are of the order of magnitude of the markers size.

The difference between the first and second regime speed is measured by looking at a vertical line drawn on this graph (black arrows). The graph can be divided into two zones A and B. In zone A, the speed in the first regime is negligible compared to the speed in the second regime. As shown on the height *versus* time diagrams in inset of Fig. 4a, in zone A, a droplet deposited on a vertical PDMS substrate seems to be unmoving until reaching the second regime once the droplet is covered by oil. In zone B, the speed in the first regime is not negligible compared to the speed in the second regime.

Examples for different water–glycerol mixing ratios are given in Fig. 4b and c. In Fig. 4b, we show results obtained for a less viscous fluid, with a 50% glycerol–50% water mixture.[‡] In Fig. 4c, we show results obtained for a more viscous fluid, with a 75% glycerol–25% water mixture. By comparing Fig. 4a–c, we observe that the difference in behavior between the first and second regime (that can be quantified by looking at the shape of the experimental curves at large volumes) depends on the fluid viscosity. This phenomenon will be further discussed in the following sections.

Another experimental observation is that in the first regime, there is a volume under which the speed of the droplet is zero[§] (e.g. 11 μL in the experiments presented in Fig. 4a, although first

[‡] For this mixture, only one regime is observed for volumes larger than 25 μL . Corresponding points are classified as first regime measurements. The same behavior is also observed (for higher volumes) for higher glycerol/water mixing ratios. Although our understanding of this phenomenon is not complete, an hypothesis could be that a droplet moving too fast does not have time to get covered by uncrosslinked chains.

[§] “zero” being defined as moving by less than a few pixels on the recorded video during the whole duration of the first regime.

regime speeds values remain negligible compared to second regime speeds until 20 μL) whereas in the second regime, the speed of the smallest deposited droplets is not exactly zero: there seems to be no threshold volume below which a droplet does not move in the second regime.

4.2 Droplet speed in the first regime

In this discussion paragraph, we compare the dynamics in the first regime on untreated PDMS to the single regime dynamics on toluene-treated PDMS.

The speeds measured in the single regime observed on a toluene-treated PDMS sample are shown in Fig. 5a. All results of the experiments conducted with the different liquids mentioned in Table 1 collapse onto a single curve when using the dimensionless numbers Ca and Bo : below a critical Bo number, the droplet is virtually immobile as pinning forces overcome the droplet weight. Above this critical Bo number, the relationship between Ca and Bo is linear. Results obtained in the first regime on an untreated PDMS sample are shown with the same data processing, and a collapse onto a single curve is also obtained when plotting Ca as a function of Bo . This result means that in the first regime, the dynamics is set by the usual balance between gravity, capillary pinning forces, and viscous dissipation inside the droplet. Our results in the first speed regime are consistent with the first order theory derived at the beginning of Section 3.

A comparison between measurements on treated samples in the first regime and on untreated samples is performed in Fig. 6, for a 35% water and 65% glycerol mixture. For clarity sake, we choose to do the comparison on only one water glycerol mixing ratio without loss of generality. The shape of the two curves obtained on treated PDMS and on untreated PDMS is the same, except for the threshold volume value V_t below which the droplet speed is negligible (inset of Fig. 6).

The small difference in the threshold volumes V_t between the two curves can be explained by differences in advancing and receding angles on the two different samples.[¶] Hence we conclude that a droplet in the first regime on untreated PDMS behaves exactly as a droplet on a treated sample, *i.e.* as if it was not polluted by uncrosslinked oligomers. Some uncrosslinked oligomers are certainly present on the droplet but do not affect its dynamics. Especially, uncrosslinked oligomers might be present preferentially at the surface of water, forming no significant oil wetting ridges during the first regime. Oil wetting ridges are likely to both lubricate the droplet and dissipate energy, causing a different dynamics.

4.3 Droplet speed in the second regime

The droplet dynamics on untreated PDMS in the second regime involves two main differences with the dynamics in the first regime: there seems to be no threshold volume below which a droplet does not move, and the dissipation processes appear to occur both in the droplet and in the oil layer.

[¶] The values measured for advancing and receding contact angles are compatible with this hypothesis, but the uncertainties on our measurements of the contact angle hysteresis are too large to use these values to rescale our data.

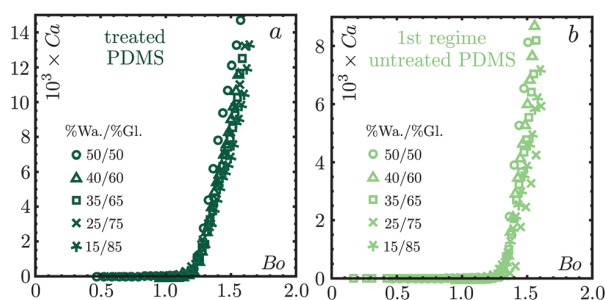


Fig. 5 Capillary number Ca as a function of Bond number Bo , for all liquids described in Table 1. (a) corresponds to results on treated PDMS and (b) to results for the speed in the first regime on untreated PDMS. Error bars are of the order of magnitude of the markers size.

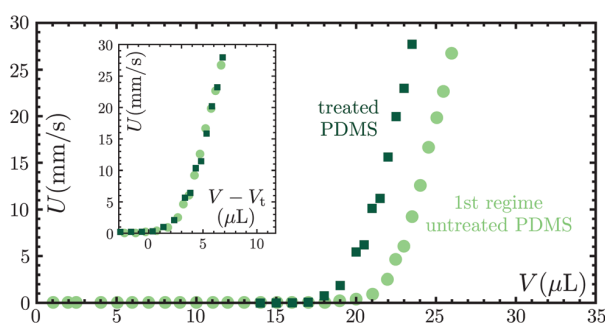


Fig. 6 65% glycerol–35% water droplet speed on treated PDMS (dark green squares) as a function of its volume, compared to the results for the first speed on untreated PDMS (light green circles). Inset: Speed as a function of the difference between the droplet volume V and the threshold volume V_t , on treated PDMS (dark green squares) and on untreated PDMS (light green circles). Error bars are of the order of magnitude of the markers size.

Indeed, the asymptotes of the curves in the first and second regimes in Fig. 7a and b are almost parallel for a viscous fluid (Fig. 7a) while for a less viscous liquid, the slope in the second regime is smaller than the slope in the first regime (Fig. 7b). This is an indication for some dissipation occurring inside the oil cover, visible in the case of a less viscous droplet, but hidden by the huge dissipation rate in the droplet in the case of a viscous droplet. The contribution of the oil cover to the dissipation could come both from the oil thin layer wrapping the droplet and from oil wetting ridges. Given the estimated thickness for the oil layer, we assume that the dissipation in the oil occurs mainly in wetting ridges.

In the literature, the dynamics of a water droplet on a Slippery Lubricant Infused Surface is shown to depend on the oil viscosity. Smith *et al.*¹⁸ evaluate the contribution of each viscous dissipation term (viscous dissipation in the droplet, viscous dissipation in the thin oil film below the droplet, viscous dissipation in the oil ridges). They conclude that taking into account only the dissipation rate inside the wetting ridge, which dominates over the two other terms, is sufficient to explain their experimental data. However, a rescaling using the model proposed by Smith *et al.* does not lead to a collapse of all the

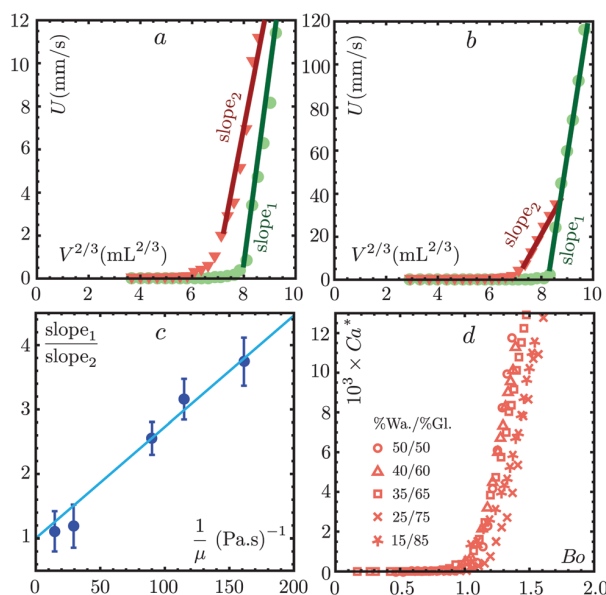


Fig. 7 (a) Droplet speed in the first (green circles) and second (red triangles) regimes in the case of a 75% glycerol–25% water mixture, as a function of $V^{2/3}$, where V is the droplet volume. The linear part of the curve is fitted and the slope of the fit is denoted slope_1 for the first regime and slope_2 for the second regime. (b) Same graphic for a 50% glycerol–50% water mixture. (c) Ratio between the slopes measured for the linear part in the first and second regimes, as a function of the inverse of the water–glycerol mixture viscosity. An affine relationship with intercept equal to unity is found, in agreement with our simple model. (d) A modified Capillary number Ca^* is used to plot the speed of the droplets in the second regime as a function of their weight, through the Bo number.

data in our experiments: in the case of a viscous droplet, the dissipation inside the droplet is not smaller than the dissipation in the oil wetting ridge.

Here we propose a simple model involving two dissipation terms: viscous dissipation in the droplet and viscous dissipation in the oil wetting ridge. The viscous dissipation in the oil ridge is assumed to be equal for droplets of the same size but of various water–glycerol mixing ratios. The viscous force that brakes the droplet is then not only

$$F_\mu = A \frac{\mu U \mathcal{L}}{h} \simeq A \mu U V^{1/3} \quad (4)$$

but

$$F_{\mu_{\text{tot}}} = A \mu U V^{1/3} + B \mu_o U R_b \quad (5)$$

where μ_o is the PDMS oil viscosity, $R_b \simeq V^{1/3}$ is the radius of the contact zone of the droplet on the substrate,¹⁸ and A and B are two constants linked to the geometry of the droplet and of the wetting ridge, assumed to be independent to the droplet size and water–glycerol mixing ratio to keep the model as simple as possible.

If using the theoretical framework described at the beginning of Section 3, the slope of the asymptotes at large volume in Fig. 7a and b should be proportional to $1/(A\mu)$ in the first regime (slope_1), and to $1/(A\mu + B\mu_o)$ in the second regime (slope_2).

In this case, the relationship between slope_1 , slope_2 , A , B , μ , and μ_0 yields:

$$\frac{\text{slope}_1}{\text{slope}_2} = 1 + \frac{B\mu_0}{A\mu} \quad (6)$$

We plot in Fig. 7c the ratio between the two slopes as a function of $1/\mu$. The results are consistent with an affine relationship, with an intercept equal to unity. This curve gives us information about the ratio of energy dissipated in the droplet and in the wetting ridge: the slope of the affine fit is equal to $C = B\mu_0/A = 0.0173$. To plot all our data on a same graph, we then choose a new version of the Ca number, defined as:

$$\text{Ca}^* = (\mu + C)U/\gamma \quad (7)$$

This allows all the curves to have the same slope for the linear part at high droplet volumes (Fig. 7d).

However, an experimental observation is not taken into account in this model: we do not observe a threshold volume below which a droplet does not move in the second regime, but there seems nevertheless to be a threshold volume below which the droplet speed is negligible. This phenomenon might be linked to a dependence of the contact angle hysteresis on the geometrical properties of both the droplet and the wetting ridge. A newly published study³² performed in the case of liquid infused surfaces highlights the dependence of contact angle hysteresis of a droplet surrounded by an oil wetting ridge on the ratio between the Laplace pressures inside the droplet and inside the wetting ridge. Although *a priori* valid only in the case where the droplet is not cloaked by oil, these results interestingly suggest a candidate phenomenon to explain an apparent variation of the pinning force as a function of the droplet volume in our experiments.

5 Conclusions

We have shown that uncrosslinked chains found in most commercial elastomers are responsible for an unexpected droplet dynamics: an aqueous droplet deposited on a vertical silicone elastomer plate exhibits successively two different regimes with two different constant speeds. This phenomenon disappears if the elastomer is treated in order to extract uncrosslinked chains from the silicone network, and reappears when re-swelling such an elastomer with a silicone oil, thus demonstrating the crucial role played by uncrosslinked chains in the droplet dynamics. Our study reveals how minute amounts of contaminants have dramatic effects on the wetting dynamics. A direct visualisation of the oligomers has been performed at the surface of a liquid bath composed of thousands of droplets collected after their descent on untreated PDMS samples. We have also shown that the sudden change observed in droplets speeds coincides with a sudden change in surface tension due to the surface contamination by silicone oligomers: we conjecture that before this surface tension change, the droplet is only partially covered with some patches of uncrosslinked chains, while after the surface tension decrease, a thin oil film completely covers the droplet.

The dynamics in the first regime is different from the dynamics in the second regime because the droplet exhibits two different states: in the first regime the droplet can be modeled by a pure liquid droplet, with no impact of the uncrosslinked oil chains on its dynamics, while in the second regime, the oil cover (including possible wetting ridges) has to be taken into account to explain the droplet dynamics. Our findings could impact various research domains such as microfluidics or elastocapillarity as it contributes to a better knowledge of the interaction between water and silicone elastomers, and provides a simple test to evaluate the presence of unintended free oligomer chains by looking at the dynamics of water droplets on a test surface.

Acknowledgements

We thank Laurent Limat, Cédric Boissière, Paul Grandgeorge, and Alexis Prevost for discussions. The present work was supported by ANR grant ANR-14-CE07-0023-01.

References

- 1 C. Py, P. Reverdy, L. Doppler, J. Bico, B. Roman and C. N. Baroud, *Phys. Rev. Lett.*, 2007, **98**, 156103.
- 2 A. Fargette, S. Neukirch and A. Antkowiak, *Phys. Rev. Lett.*, 2014, **112**, 137802.
- 3 A. Carré, J.-C. Gastel and M. E. R. Shanahan, *Nature*, 1996, **379**, 432–434.
- 4 R. W. Style, C. Hyland, R. Boltyskiy, J. S. Wettlaufer and E. R. Dufresne, *Nat. Commun.*, 2013, **4**, 2728.
- 5 S. J. Park, B. M. Weon, J. S. Lee, J. Lee, J. Kim and J. H. Je, *Nat. Commun.*, 2014, **5**, 4369.
- 6 S. Karpitschka, A. Pandey, L. A. Lubbers, J. H. Weijss, L. Botto, S. Das, B. Andreotti and J. H. Snoeijer, *Proc. Natl. Acad. Sci. U. S. A.*, 2016, **113**, 7403–7407.
- 7 E. Berthier, E. W. K. Young and D. Beebe, *Lab Chip*, 2012, **12**, 1224–1237.
- 8 K. J. Regehr, M. Domenech, J. T. Koepsel, K. C. Carver, S. J. Ellison-Zelski, W. L. Murphy, L. A. Schuler, E. T. Alarid and D. J. Beebe, *Lab Chip*, 2009, **9**, 2132–2139.
- 9 R. Mukhopadhyay, *Anal. Chem.*, 2007, **79**, 3248–3253.
- 10 C. Huh and L. Scriven, *J. Colloid Interface Sci.*, 1971, **35**, 85–101.
- 11 O. V. Voinov, *Fluid Dyn.*, 1976, **11**, 714–721.
- 12 R. G. Cox, *J. Fluid Mech.*, 1986, **168**, 169–194.
- 13 E. B. Dussan V., *J. Fluid Mech.*, 1985, **151**, 1–20.
- 14 M. E. Shanahan and A. Carré, *C. R. Acad. Sci., Ser. IV: Phys., Astrophys.*, 2000, **1**, 263–268.
- 15 N. Le Grand, A. Daerr and L. Limat, *J. Fluid Mech.*, 2005, **541**, 293–315.
- 16 L. Limat, *Eur. Phys. J. E: Soft Matter Biol. Phys.*, 2012, **35**, 1–13.
- 17 M. Shanahan and A. Carré, *Colloids Surf., A*, 2002, **206**, 115–123.
- 18 J. D. Smith, R. Dhiman, S. Anand, E. Reza-Garduno, R. E. Cohen, G. H. McKinley and K. K. Varanasi, *Soft Matter*, 2013, **9**, 1772–1780.

- 19 J. N. Lee, C. Park and G. M. Whitesides, *Anal. Chem.*, 2003, **75**, 6544–6554.
- 20 K. E. Jensen, R. Sarfati, R. W. Style, R. Boltanskiy, A. Chakrabarti, M. K. Chaudhury and E. R. Dufresne, *Proc. Natl. Acad. Sci. U. S. A.*, 2015, **112**, 14490–14494.
- 21 L. T. Lee, E. K. Mann, D. Langevin and B. Farnoux, *Langmuir*, 1991, **7**, 3076–3080.
- 22 P.-G. de Gennes, F. Brochard-Wyart and D. Quere, *Capillarity and Wetting Phenomena: Drops, Bubbles, Pearls, Waves*, Springer-Verlag, New York, 2003.
- 23 B. A. Puthenveetil, V. K. Senthilkumar and E. J. Hopfinger, *J. Fluid Mech.*, 2013, **726**, 26–61.
- 24 S. Karpitschka, S. Das, M. van Gorcum, H. Perrin, B. Andreotti and J. H. Snoeijer, *Nat. Commun.*, 2015, **6**, 7891.
- 25 T. Podgorski, J.-M. Flesselles and L. Limat, *Phys. Rev. Lett.*, 2001, **87**, 036102.
- 26 M. Ben Amar, L. J. Cummings and Y. Pomeau, *Phys. Fluids*, 2003, **15**, 2949–2960.
- 27 H. She, D. Malotky and M. K. Chaudhury, *Langmuir*, 1998, **14**, 3090–3100.
- 28 F. Schellenberger, J. Xie, N. Encinas, A. Hardy, M. Klapper, P. Papadopoulos, H.-J. Butt and D. Vollmer, *Soft Matter*, 2015, **11**, 7617–7626.
- 29 A. Pockels, *Nature*, 1892, **46**, 418–419.
- 30 L. Rayleigh, *Philosophical Magazine Series 5*, 1899, **48**, 321–337.
- 31 I. Langmuir, *J. Am. Chem. Soc.*, 1917, **39**, 1848–1906.
- 32 C. Semperebon, G. McHale and H. Kusumaatmaja, *Soft Matter*, 2017, **13**, 101–110.

Bibliography

- [1] S. Timoshenko, *History of strength of materials: With a brief account of the history of theory of elasticity and theory of structures* (Courier Corporation, 1953). 2, 3
- [2] P. M. Reis, *A perspective on the revival of structural (in) stability with novel opportunities for function: From buckliphobia to buckliphilia*, *Journal of Applied Mechanics* **82**, 111001 (2015). 4
- [3] B. Audoly and S. Neukirch, *Fragmentation of rods by cascading cracks: Why spaghetti does not break in half*, *Physical Review Letters* **95**, 095505 (2005). 4
- [4] B. Audoly and Y. Pomeau, *Elasticity and geometry: from hair curls to the non-linear response of shells* (Oxford University Press, 2010). 4
- [5] J. T. Miller, A. Lazarus, B. Audoly, and P. M. Reis, *Shapes of a suspended curly hair*, *Physical Review Letters* **112**, 068103 (2014). 4
- [6] S. Xu, Z. Yan, K.-I. Jang, W. Huang, H. Fu, J. Kim, Z. Wei, M. Flavin, J. McCracken, R. Wang, A. Badea, Y. Liu, D. Xiao, G. Zhou, J. Lee, H. U. Chung, H. Cheng, W. Ren, A. Banks, X. Li, U. Paik, R. G. Nuzzo, Y. Huang, Y. Zhang, and J. A. Rogers, *Assembly of micro/nanomaterials into complex, three-dimensional architectures by compressive buckling*, *Science* **347**, 154–159 (2015). 4, 5
- [7] J. Shim, C. Perdigou, E. R. Chen, K. Bertoldi, and P. M. Reis, *Buckling-induced encapsulation of structured elastic shells under pressure*, *Proceedings of the National Academy of Sciences* **109**, 5978–5983 (2012). 4
- [8] K. Krieger, *Buckling down*, *Nature* **488**, 146 (2012). 5
- [9] S. Timoshenko, *Theory of Elastic Stability, 2nd edition* (Tata McGraw-Hill Education, 1970). 6
- [10] G. Domokos, *Global description of elastic bars*, *Zeitschrift für angewandte Mathematik und Mechanik* **74**, T289–T291 (1994). 7
- [11] L. Landau and E. Lifshitz, *Theory of elasticity, 2nd edition* (Pergamon Press, 1970). 9, 53
- [12] S. Timoshenko, *Buckling of flat curved bars and slightly curved plates*, *Journal of Applied Mechanics* **2**, 17–20 (1935). 10
- [13] A. B. Pippard, *The elastic arch and its modes of instability*, *European Journal of Physics* **11**, 359 (1990). 10

- [14] P. Patricio, M. Adda-Bedia, and M. Ben Amar, *An elastica problem: Instabilities of an elastic arch*, *Physica D: Nonlinear Phenomena* **124**, 285–295 (1998). [10](#)
- [15] J.-S. Chen and S.-Y. Hung, *Snapping of an elastica under various loading mechanisms*, *European Journal of Mechanics - A/Solids* **30**, 525–531 (2011). [10](#), [73](#)
- [16] A. Pandey, D. E. Moulton, D. Vella, and D. P. Holmes, *Dynamics of snapping beams and jumping poppers*, *Europhysics Letters* **105**, 24001 (2014). [10](#), [11](#), [73](#)
- [17] D. P. Holmes and A. J. Crosby, *Snapping surfaces*, *Advanced Materials* **19**, 3589–3593 (2007). [10](#), [11](#)
- [18] D. Vella and L. Mahadevan, *The “Cheerios effect”*, *American Journal of Physics* **73**, 817–825 (2005). [11](#), [12](#)
- [19] X.-Y. Ji, J.-W. Wang, and X.-Q. Feng, *Role of flexibility in the water repellency of water strider legs: Theory and experiment*, *Physical Review E* **85**, 021607 (2012). [11](#), [12](#), [24](#)
- [20] J. Jurin, *An account of some experiments shown before the Royal Society; With an enquiry into the cause of the ascent and suspension of water in capillary tubes*, *Philosophical Transactions* **30**, 739–747 (1717). [12](#)
- [21] T. Young, *An Essay on the Cohesion of Fluids*, *Philosophical Transactions of the Royal Society of London* **95**, 65–87 (1805). [12](#), [16](#)
- [22] P.-S. Laplace, *Traité de mécanique céleste; Supplément au dixième livre, sur l’action capillaire*, Courcier, Paris (1806). [12](#), [13](#)
- [23] C. V. Boys, *Soap-bubbles, and the forces which mould them* (Society for Promoting Christian Knowledge; E. & J. B. Young, London, New York, 1890). [12](#), [13](#), [14](#), [15](#), [33](#)
- [24] P.-G. De Gennes, F. Brochard-Wyart, and D. Quéré, *Capillarity and wetting phenomena: Drops, bubbles, pearls, waves* (Springer-Verlag New York, 2003). [13](#), [15](#), [16](#), [19](#)
- [25] I. Langmuir, *Oil lenses on water and the nature of monomolecular expanded films*, *The Journal of Chemical Physics* **1**, 756–776 (1933). [16](#)
- [26] F. E. Neumann, *Vorlesungen über mathematische Physik: Vorlesungen über die Theorie der Capillarität*, vol. 7 (BG Teubner, 1894). [16](#)
- [27] G. Lester, *Contact angles of liquids at deformable solid surfaces*, *Journal of Colloid Science* **16**, 315–326 (1961). [16](#), [36](#)
- [28] P. G. De Gennes, *Wetting: statics and dynamics*, *Reviews of Modern Physics* **57** (1985). [17](#)
- [29] R. E. Johnson JR and R. H. Dettre, *Contact angle hysteresis*, (1964). [17](#)
- [30] C. Huh and L. Scriven, *Hydrodynamic model of steady movement of a solid/liquid/fluid contact line*, *Journal of Colloid and Interface Science* **35**, 85–101 (1971). [17](#), [18](#), [21](#)

- [31] D. Bonn, J. Eggers, J. Indekeu, J. Meunier, and E. Rolley, *Wetting and spreading*, *Reviews of Modern Physics* **81**, 739–805 (2009). 17, 18
- [32] R. L. Hoffman, *A study of the advancing interface. I. Interface shape in liquid-gas systems*, *Journal of Colloid and Interface Science* **50**, 228–241 (1975). 18, 19
- [33] T. D. Blake, *The physics of moving wetting lines*, *Journal of Colloid and Interface Science* **299**, 1–13 (2006). 18, 19
- [34] O. V. Voinov, *Hydrodynamics of wetting*, *Fluid Dynamics* **11**, 714–721 (1976). 18
- [35] R. G. Cox, *The dynamics of the spreading of liquids on a solid surface. Part 1. Viscous flow*, *Journal of Fluid Mechanics* **168**, 169–194 (1986). 19
- [36] N. Le Grand, A. Daerr, and L. Limat, *Shape and motion of drops sliding down an inclined plane*, *Journal of Fluid Mechanics* **541**, 293–315 (2005). 19, 21, 22, 23, 93, 97, 113, 115
- [37] P. Hayoun, *Partial wetting of thin liquid films in polymer tubes*, Ph.D. thesis, UPMC Paris 6 (2016). 19
- [38] G. Macdougall and C. Ockrent, *Surface energy relations in liquid/solid systems. I. The adhesion of liquids to solids and a new method of determining the surface tension of liquids*, *Proceedings of the Royal Society of London A: Mathematical, Physical and Engineering Sciences* **180**, 151–173 (1942). 19, 20
- [39] Y. I. Frenkel, *On the behavior of liquid drops on a solid surface. 1. The sliding of drops on an inclined surface*, *Journal of Experimental and Theoretical Physics (USSR)*, (arXiv preprint physics/0503051 for the English translation by V. Berejnov (2005)) **18** (1948). 19, 20
- [40] J. Bikerman, *Sliding of drops from surfaces of different roughnesses*, *Journal of Colloid Science* **5**, 349–359 (1950). 19, 21
- [41] C. Furmidge, *Studies at phase interfaces. I. The sliding of liquid drops on solid surfaces and a theory for spray retention*, *Journal of Colloid Science* **17**, 309–324 (1962). 20
- [42] E. B. Dussan V. and R. T.-P. Chow, *On the ability of drops or bubbles to stick to non-horizontal surfaces of solids*, *Journal of Fluid Mechanics* **137**, 1–29 (1983). 20, 135
- [43] E. B. Dussan V., *On the ability of drops or bubbles to stick to non-horizontal surfaces of solids. Part 2. Small drops or bubbles having contact angles of arbitrary size*, *Journal of Fluid Mechanics* **151**, 1–20 (1985). 20
- [44] G. D. Yarnold, *The motion of a mercury index in a capillary tube*, *Proceedings of the Physical Society* **50**, 540 (1938). 21
- [45] S. P. Thampi, R. Adhikari, and R. Govindarajan, *Do liquid drops roll or slide on inclined surfaces?*, *Langmuir* **29**, 3339–3346 (2013). 21

- [46] R. F. Allen and P. R. Benson, *Rolling drops on an inclined plane*, Journal of Colloid and Interface Science **50**, 250–253 (1975). [21](#)
- [47] E. B. Dussan V. and S. H. Davis, *On the motion of a fluid-fluid interface along a solid surface*, Journal of Fluid Mechanics **65**, 71–95 (1974). [21](#)
- [48] T. Podgorski, J.-M. Flesselles, and L. Limat, *Corners, cusps, and pearls in running drops*, Physical Review Letters **87**, 036102 (2001). [21](#), [23](#), [24](#), [113](#)
- [49] H.-Y. Kim, H. J. Lee, and B. H. Kang, *Sliding of liquid drops down an inclined solid surface*, Journal of Colloid and Interface Science **247**, 372–380 (2002). [21](#)
- [50] B. A. Puthenveetil, V. K. Senthilkumar, and E. J. Hopfinger, *Motion of drops on inclined surfaces in the inertial regime*, Journal of Fluid Mechanics **726**, 26–61 (2013). [21](#), [22](#), [93](#), [97](#)
- [51] L. Limat and H. A. Stone, *Three-dimensional lubrication model of a contact line corner singularity*, Europhysics Letters **65**, 365 (2004). [23](#)
- [52] S. Neukirch, B. Roman, B. de Gaudemaris, and J. Bico, *Piercing a liquid surface with an elastic rod: Buckling under capillary forces*, Journal of the Mechanics and Physics of Solids **55**, 1212–1235 (2007). [24](#), [31](#)
- [53] J. W. M. Bush and D. L. Hu, *Walking on water: Biolocotion at the interface*, Annual Review of Fluid Mechanics **38**, 339–369 (2006). [24](#), [25](#)
- [54] H. Elettro, S. Neukirch, F. Vollrath, and A. Antkowiak, *In-drop capillary spooling of spider capture thread inspires hybrid fibers with mixed solid-liquid mechanical properties*, Proceedings of the National Academy of Sciences **113**, 6143–6147 (2016). [25](#), [34](#)
- [55] J. Bico, B. Roman, L. Moulin, and A. Boudaoud, *Adhesion: Elastocapillary coalescence in wet hair*, Nature **432**, 690–690 (2004). [25](#), [33](#), [34](#)
- [56] A. K. Dickerson, X. Liu, T. Zhu, and D. L. Hu, *Fog spontaneously folds mosquito wings*, Physics of Fluids **27** (2015). [25](#), [26](#)
- [57] M. Heil, A. L. Hazel, and J. A. Smith, *The mechanics of airway closure*, Respiratory Physiology & Neurobiology **163**, 214–221 (2008). [25](#)
- [58] T. Tanaka, M. Morigami, and N. Atoda, *Mechanism of resist pattern collapse during development process*, Japanese Journal of Applied Physics **32**, 6059 (1993). [26](#)
- [59] K. K. S. Lau, J. Bico, K. B. K. Teo, M. Chhowalla, G. A. J. Amaratunga, W. I. Milne, G. H. McKinley, and K. K. Gleason, *Superhydrophobic carbon nanotube forests*, Nano Letters **3**, 1701–1705 (2003). [26](#), [27](#)
- [60] N. Chakrapani, B. Wei, A. Carrillo, P. M. Ajayan, and R. S. Kane, *Capillarity-driven assembly of two-dimensional cellular carbon nanotube foams*, Proceedings of the National Academy of Sciences **101**, 4009–4012 (2004). [26](#), [27](#)

- [61] C. H. Mastrangelo and C. H. Hsu, *Mechanical stability and adhesion of microstructures under capillary forces. I. Basic theory*, Journal of Microelectromechanical Systems **2**, 33–43 (1993). 26, 27
- [62] B. Pokroy, S. H. Kang, L. Mahadevan, and J. Aizenberg, *Self-organization of a mesoscale bristle into ordered, hierarchical helical assemblies*, Science **323**, 237–240 (2009). 26, 27, 28
- [63] M. De Volder, S. H. Tawfick, S. J. Park, D. Copic, Z. Zhao, W. Lu, and A. J. Hart, *Diverse 3D microarchitectures made by capillary forming of carbon nanotubes*, Advanced Materials **22**, 4384–4389 (2010). 26, 27, 28
- [64] D. Chandra, S. Yang, A. A. Soshinsky, and R. J. Gambogi, *Biomimetic ultrathin whitening by capillary-force-induced random clustering of hydrogel micropillar arrays*, ACS Applied Materials & Interfaces **1**, 1698–1704 (2009). 26, 27, 28
- [65] M. De Volder and A. J. Hart, *Engineering hierarchical nanostructures by elasto-capillary self-assembly*, Angewandte Chemie International Edition **52**, 2412–2425 (2013). 28
- [66] R. R. A. Syms, E. M. Yeatman, V. M. Bright, and G. M. Whitesides, *Surface tension-powered self-assembly of microstructures - the state-of-the-art*, Journal of Microelectromechanical Systems **12**, 387–417 (2003). 28, 29
- [67] R. J. Linderman, P. E. Kladitis, and V. M. Bright, *Development of the micro rotary fan*, Sensors and Actuators A: Physical **95**, 135–142 (2002). 28, 29
- [68] D. H. Gracias, V. Kavthekar, J. C. Love, K. E. Paul, and G. M. Whitesides, *Fabrication of micrometer-scale, patterned polyhedra by self-assembly*, Advanced Materials **14**, 235 (2002). 28, 29
- [69] X. Guo, H. Li, B. Yeop Ahn, E. B. Duoss, K. J. Hsia, J. A. Lewis, and R. G. Nuzzo, *Two- and three-dimensional folding of thin film single-crystalline silicon for photovoltaic power applications*, Proceedings of the National Academy of Sciences **106**, 20149–20154 (2009). 28
- [70] R. Fernandes and D. H. Gracias, *Self-folding polymeric containers for encapsulation and delivery of drugs*, Advanced Drug Delivery Reviews **64**, 1579–1589 (2012). 28
- [71] C. Py, P. Reverdy, L. Doppler, J. Bico, B. Roman, and C. N. Baroud, *Capillary origami: Spontaneous wrapping of a droplet with an elastic sheet*, Physical Review Letters **98**, 156103 (2007). 29, 31
- [72] A. Antkowiak, B. Audoly, C. Josserand, S. Neukirch, and M. Rivetti, *Instant fabrication and selection of folded structures using drop impact*, Proceedings of the National Academy of Sciences **108**, 10400–10404 (2011). 29, 30, 34, 83
- [73] J. D. Paulsen, V. Demery, C. D. Santangelo, T. P. Russell, B. Davidovitch, and N. Menon, *Optimal wrapping of liquid droplets with ultrathin sheets*, Nature Materials **14**, 1206–1209 (2015). 29

- [74] P. M. Reis, J. Hure, S. Jung, J. W. M. Bush, and C. Clanet, *Grabbing water*, *Soft Matter* **6**, 5705–5708 (2010). [29](#)
- [75] C. Py, P. Reverdy, L. Doppler, J. Bico, B. Roman, and C. N. Baroud, *Capillarity induced folding of elastic sheets*, *The European Physical Journal Special Topics* **166**, 67–71 (2009). [30](#)
- [76] B. Roman and J. Bico, *Elasto-capillarity: deforming an elastic structure with a liquid droplet*, *Journal of Physics: Condensed Matter* **22**, 493101 (2010). [30](#), [31](#)
- [77] A. E. Cohen and L. Mahadevan, *Kinks, rings, and rackets in filamentous structures*, *Proceedings of the National Academy of Sciences* **100**, 12141–12146 (2003). [31](#)
- [78] M. A. Fortes, *Deformation of solid surfaces due to capillary forces*, *Journal of Colloid and Interface Science* **100**, 17–26 (1984). [32](#)
- [79] M. E. R. Shanahan, *Contact angle equilibrium on thin elastic solids*, *The Journal of Adhesion* **18**, 247–267 (1985). [32](#)
- [80] M. E. R. Shanahan, *Equilibrium of liquid drops on thin plates; Plate rigidity and stability considerations*, *The Journal of Adhesion* **20**, 261–274 (1987). [32](#)
- [81] R. E. Johnson JR, *Conflicts between Gibbsian thermodynamics and recent treatments of interfacial energies in solid-liquid-vapor*, *The Journal of Physical Chemistry* **63**, 1655–1658 (1959). [32](#), [36](#)
- [82] J. Métois, *Elastic straining of a thin graphite layer by a liquid droplet or a non-epitaxed Pb crystallite*, *Surface Science* **241**, 279–288 (1991). [32](#)
- [83] L. Pocivavsek, R. Dellsy, A. Kern, S. Johnson, B. Lin, K. Y. C. Lee, and E. Cerda, *Stress and fold localization in thin elastic membranes*, *Science* **320**, 912–916 (2008). [32](#), [33](#)
- [84] J. Huang, M. Juskiewicz, W. H. de Jeu, E. Cerda, T. Emrick, N. Menon, and T. P. Russell, *Capillary wrinkling of floating thin polymer films*, *Science* **317**, 650–653 (2007). [32](#), [33](#)
- [85] J. Hure, B. Roman, and J. Bico, *Wrapping an adhesive sphere with an elastic sheet*, *Physical Review Letters* **106**, 174301 (2011). [32](#), [33](#)
- [86] M. Rivetti and A. Antkowiak, *Elasto-capillary meniscus: pulling out a soft strip sticking to a liquid surface*, *Soft Matter* **9**, 6226–6234 (2013). [32](#), [34](#)
- [87] M. Rivetti and S. Neukirch, *Instabilities in a drop-strip system: a simplified model*, *Proceedings of the Royal Society A: Mathematical, Physical and Engineering Science* **468**, 1304–1324 (2012). [33](#), [34](#), [80](#)
- [88] C. Duprat, S. Protière, A. Y. Beebe, and H. A. Stone, *Wetting of flexible fibre arrays*, *Nature* **482**, 510–513 (2012). [34](#), [35](#)
- [89] C. Duprat, R. Labbé, and A. Rewakowicz, *Elastocapillary mist collector*, in *APS Meeting Abstracts* (2015). [34](#)

- [90] H. Elettro, P. Grandgeorge, and S. Neukirch, *Elastocapillary coiling of an elastic rod inside a drop*, Journal of Elasticity **127**, 235–247 (2017). [34](#), [35](#)
- [91] P. Grandgeorge, A. Antkowiak, and S. Neukirch, *Auxiliary soft beam for the amplification of the elasto-capillary coiling: towards stretchable electronics*, (2017). [34](#), [35](#)
- [92] R. D. Schulman, A. Porat, K. Charlesworth, A. Fortais, T. Salez, E. Raphael, and K. Dalnoki-Veress, *Elastocapillary bending of microfibers around liquid droplets*, Soft Matter **13**, 720–724 (2017). [35](#)
- [93] R. W. Style, A. Jagota, C.-Y. Hui, and E. R. Dufresne, *Elastocapillarity: Surface tension and the mechanics of soft solids*, Annual Review of Condensed Matter Physics (2016). [36](#)
- [94] L. Limat, *Straight contact lines on a soft, incompressible solid*, The European Physical Journal E **35**, 1–13 (2012). [36](#)
- [95] M. E. R. Shanahan, *The influence of solid micro-deformation on contact angle equilibrium*, Journal of Physics D: Applied Physics **20**, 945 (1987). [36](#)
- [96] S. J. Park, B. M. Weon, J. S. Lee, J. Lee, J. Kim, and J. H. Je, *Visualization of asymmetric wetting ridges on soft solids with X-ray microscopy*, Nature Communications **5** (2014). [36](#), [38](#), [39](#)
- [97] A. Rusanov, *Theory of wetting of elastically deformed bodies. 1. Deformation with a finite contact-angle*, Colloid Journal of the USSR **37**, 614–622 (1975). [36](#)
- [98] M. E. R. Shanahan and P.-G. De Gennes, *L'arête produite par un coin liquide près de la ligne triple de contact solide/liquide/fluide*, Comptes rendus de l'Académie des Sciences. Série 2, Mécanique, Physique, Chimie, Sciences de l'Univers, Sciences de la Terre **302**, 517–521 (1986). [36](#)
- [99] D. Long, A. Ajdari, and L. Leibler, *Static and dynamic wetting properties of thin rubber films*, Langmuir **12**, 5221–5230 (1996). [36](#)
- [100] S. Mora, T. Phou, J.-M. Fromental, L. M. Pismen, and Y. Pomeau, *Capillarity driven instability of a soft solid*, Physical Review Letters **105**, 214301 (2010). [37](#)
- [101] B. Andreotti, O. Baumchen, F. Boulogne, K. E. Daniels, E. R. Dufresne, H. Perrin, T. Salez, J. H. Snoeijer, and R. W. Style, *Solid capillarity: when and how does surface tension deform soft solids?*, Soft Matter **12**, 2993–2996 (2016). [37](#)
- [102] R. Shuttleworth, *The surface tension of solids*, Proceedings of the Physical Society. Section A **63**, 444 (1950). [37](#)
- [103] Q. Xu, K. E. Jensen, R. Boltyskiy, R. Sarfati, R. W. Style, and E. R. Dufresne, *Direct measurement of strain-dependent solid surface stress*, preprint arXiv:1702.00684 (2017). [37](#)
- [104] C. Extrand and Y. Kumagai, *Contact angles and hysteresis on soft surfaces*, Journal of Colloid and Interface Science **184**, 191–200 (1996). [37](#)

- [105] J. Andrade, S. Ma, R. King, and D. Gregonis, *Contact angles at the solid-water interface*, Journal of Colloid and Interface Science **72**, 488–494 (1979). [37](#)
- [106] A. Carré, J.-C. Gastel, and M. E. R. Shanahan, *Viscoelastic effects in the spreading of liquids*, Nature **379**, 432–434 (1996). [37](#), [38](#)
- [107] R. Pericet-Camara, G. K. Auernhammer, K. Koynov, S. Lorenzoni, R. Raiteri, and E. Bonaccorso, *Solid-supported thin elastomer films deformed by microdrops*, Soft Matter **5**, 3611–3617 (2009). [38](#)
- [108] E. R. Jerison, Y. Xu, L. A. Wilen, and E. R. Dufresne, *Deformation of an elastic substrate by a three-phase contact line*, Physical Review Letters **106**, 186103 (2011). [38](#), [108](#)
- [109] M. Zhao, M. Roché, J. Dervaux, L. Royon, T. Narita, F. Lequeux, and L. Limat, *Thickness effect in the statics and dynamics of wetting on soft materials*, in APS Meeting Abstracts (2016). [38](#)
- [110] M. E. R. Shanahan and A. Carré, *Spreading and dynamics of liquid drops involving nanometric deformations on soft substrates*, Colloids and Surfaces A: Physicochemical and Engineering Aspects **206**, 115–123 (2002). [38](#), [39](#), [89](#)
- [111] T. Kajiya, A. Daerr, T. Narita, L. Royon, F. Lequeux, and L. Limat, *Advancing liquid contact line on visco-elastic gel substrates: Stick-slip vs continuous motions*, Soft Matter **9**, 454–461 (2013). [38](#), [39](#)
- [112] T. Kajiya, P. Brunet, L. Royon, A. Daerr, M. Receveur, and L. Limat, *A liquid contact line receding on a soft gel surface: dip-coating geometry investigation*, Soft Matter **10**, 8888–8895 (2014). [38](#)
- [113] S. Karpitschka, S. Das, M. Van Gorcum, H. Perrin, B. Andreotti, and J. Snoeijer, *Droplets move over viscoelastic substrates by surfing a ridge*, Nature Communications **6** (2015). [38](#), [39](#)
- [114] R. W. Style, Y. Che, S. J. Park, B. M. Weon, J. H. Je, C. Hyland, G. K. German, M. P. Power, L. A. Wilen, J. S. Wettlaufer, and E. R. Dufresne, *Patterning droplets with durotaxis*, Proceedings of the National Academy of Sciences **110**, 12541–12544 (2013). [38](#)
- [115] C. J. Howland, A. Antkowiak, J. R. Castrejón-Pita, S. D. Howison, J. M. Oliver, R. W. Style, and A. A. Castrejón-Pita, *It's harder to splash on soft solids*, Physical Review Letters **117**, 184502 (2016). [39](#)
- [116] S. Karpitschka, A. Pandey, L. A. Lubbers, J. H. Weijs, L. Botto, S. Das, B. Andreotti, and J. H. Snoeijer, *Liquid drops attract or repel by the inverted Cheerios effect*, Proceedings of the National Academy of Sciences **113**, 7403–7407 (2016). [39](#)
- [117] E. Berthier, E. W. K. Young, and D. Beebe, *Engineers are from PDMS-land, Biologists are from Polystyrenia*, Lab on a Chip **12**, 1224–1237 (2012). [43](#), [120](#)

- [118] G. C. Lisensky, D. J. Campbell, K. J. Beckman, C. E. Calderon, P. W. Doolan, R. M. Ottosen, and A. B. Ellis, *Replication and compression of surface structures with polydimethylsiloxane elastomer*, *Journal of Chemical Education* **76**, 537 (1999). [43](#)
- [119] I. D. Johnston, D. K. McCluskey, C. K. L. Tan, and M. C. Tracey, *Mechanical characterization of bulk Sylgard 184 for microfluidics and microengineering*, *Journal of Micromechanics and Microengineering* **24**, 035017 (2014). [44](#)
- [120] T. Su, J. Liu, D. Terwagne, P. M. Reis, and K. Bertoldi, *Buckling of an elastic rod embedded on an elastomeric matrix: planar vs. non-planar configurations*, *Soft Matter* **10**, 6294–6302 (2014). [45](#)
- [121] L. E. Scriven, *Physics and applications of DIP coating and spin coating*, *MRS Proceedings* **121** (1988). [46](#)
- [122] P. H. Walker and J. G. Thompson, *Some physical properties of paints*, *Proceedings of the American Society for Testing Materials* **22**, 100 (1922). [46](#)
- [123] A. G. Emslie, F. T. Bonner, and L. G. Peck, *Flow of a viscous liquid on a rotating disk*, *Journal of Applied Physics* **29**, 858–862 (1958). [46](#), [47](#)
- [124] D. E. Bornside, C. W. Macosko, and L. E. Scriven, *Spin coating: One dimensional model*, *Journal of Applied Physics* **66**, 5185–5193 (1989). [48](#)
- [125] M. Liu, J. Sun, Y. Sun, C. Bock, and Q. Chen, *Thickness-dependent mechanical properties of polydimethylsiloxane membranes*, *Journal of Micromechanics and Microengineering* **19**, 035028 (2009). [53](#), [54](#), [55](#)
- [126] Y. Sun, S. N. Fry, D. P. Potasek, D. J. Bell, and B. J. Nelson, *Characterizing fruit fly flight behavior using a microforce sensor with a new comb-drive configuration*, *Journal of Microelectromechanical Systems* **14**, 4–11 (2005). [55](#)
- [127] D. P. Holmes, M. Roché, T. Sinha, and H. A. Stone, *Bending and twisting of soft materials by non-homogenous swelling*, *Soft Matter* **7**, 5188–5193 (2011). [57](#)
- [128] J. N. Lee, C. Park, and G. M. Whitesides, *Solvent compatibility of poly(dimethylsiloxane)-based microfluidic devices*, *Analytical Chemistry* **75**, 6544–6554 (2003). [57](#), [103](#)
- [129] T. Tate, *XXX. On the magnitude of a drop of liquid formed under different circumstances*, *Philosophical Magazine Series 4* **27**, 176–180 (1864). [61](#)
- [130] W. D. Harkins and F. E. Brown, *The determination of surface tension (free surface energy), and the weight of falling drops: The surface tension of water and benzene by the capillary height method*, *Journal of the American Chemical Society* **41**, 499–524 (1919). [62](#)
- [131] O. E. Yildirim, Q. Xu, and O. A. Basaran, *Analysis of the drop weight method*, *Physics of Fluids* **17**, 062107 (2005). [62](#)
- [132] J. Frank S. Crawford, *Berkeley physics course, Volume 3: Waves* (Mc Graw-Hill, 1968). [63](#)

- [133] R. Azzam and N. Bashara, *Ellipsometry and polarized light* (North Holland, 1999). 64
- [134] L. Hines, K. Petersen, G. Z. Lum, and M. Sitti, *Soft actuators for small-scale robotics*, *Advanced Materials* (2016). 68
- [135] N. Hu and R. Burgueno, *Buckling-induced smart applications: recent advances and trends*, *Smart Materials and Structures* **24**, 063001 (2015). 68
- [136] R. Baughman, *Conducting polymer artificial muscles*, *Synthetic Metals* **78**, 339–353 (1996). 68
- [137] M. Pineirua, J. Bico, and B. Roman, *Capillary origami controlled by an electric field*, *Soft Matter* **6**, 4491–4496 (2010). 68
- [138] S. Taccola, F. Greco, E. Sinibaldi, A. Mondini, B. Mazzolai, and V. Mattoli, *Toward a new generation of electrically controllable hygromorphic soft actuators*, *Advanced Materials* **27**, 1668–1675 (2015). 68, 69
- [139] S. Boisseau, G. Despesse, S. Monfray, O. Puscasu, and T. Skotnicki, *Semi-flexible bimetal-based thermal energy harvesters*, *Smart Materials and Structures* **22**, 025021 (2013). 68
- [140] H. Lee, C. Xia, and N. X. Fang, *First jump of microgel; actuation speed enhancement by elastic instability*, *Soft Matter* **6**, 4342–4345 (2010). 68
- [141] M. R. Shankar, M. L. Smith, V. P. Tondiglia, K. M. Lee, M. E. McConney, D. H. Wang, L.-S. Tan, and T. J. White, *Contactless, photoinitiated snap-through in azobenzene-functionalized polymers*, *Proceedings of the National Academy of Sciences* **110**, 18792–18797 (2013). 69
- [142] S. Iamsaard, S. J. Asshoff, B. Matt, T. Kudernac, J. J. Cornelissen, S. P. Fletcher, and N. Katsonis, *Conversion of light into macroscopic helical motion*, *Nature Chemistry* **6**, 229–235 (2014). 69
- [143] Y. Zhu and J. W. Zu, *Enhanced buckled-beam piezoelectric energy harvesting using midpoint magnetic force*, *Applied Physics Letters* **103**, 041905 (2013). 69
- [144] J. Kim, S. E. Chung, S.-E. Choi, H. Lee, J. Kim, and S. Kwon, *Programming magnetic anisotropy in polymeric microactuators*, *Nature Materials* **10**, 747–752 (2011). 69
- [145] M. J. Harrington, K. Razghandi, F. Ditsch, L. Guiducci, M. Rueggeberg, J. W. C. Dunlop, P. Fratzl, C. Neinhuis, and I. Burgert, *Origami-like unfolding of hydro-actuated ice plant seed capsules*, *Nature Communications* **2**, 337 (2011). 70
- [146] P. Marmottant, A. Ponomarenko, and D. Bienaimé, *The walk and jump of Equisetum spores*, *Proceedings of the Royal Society of London B: Biological Sciences* **280** (2013). 70
- [147] Y. Forterre, P. Marmottant, C. Quilliet, and X. Noblin, *Physics of rapid movements in plants*, *Europhysics News* **47**, 27–30 (2016). 70

- [148] X. Noblin, N. O. Rojas, J. Westbrook, C. Llorens, M. Argentina, and J. Dumais, *The fern sporangium: A unique catapult*, *Science* **335**, 1322–1322 (2012). 70
- [149] Y. Forterre, J. M. Skotheim, J. Dumais, and L. Mahadevan, *How the Venus flytrap snaps*, *Nature* **433**, 421–425 (2005). 71
- [150] O. Vincent, C. Weisskopf, S. Poppinga, T. Masselter, T. Speck, M. Joyeux, C. Quiliet, and P. Marmottant, *Ultra-fast underwater suction traps*, *Proceedings of the Royal Society B: Biological Sciences* **278**, 2909–2914 (2011). 71
- [151] M. Abkarian, G. Massiera, L. Berry, M. Roques, and C. Braun-Breton, *A novel mechanism for egress of malarial parasites from red blood cells*, *Blood* **117**, 4118–4124 (2011). 71
- [152] J. Thompson and G. Hunt, *On the buckling and imperfection-sensitivity of arches with and without prestress*, *International Journal of Solids and Structures* **19**, 445–459 (1983). 74
- [153] C. Cohen, B. Darbois Texier, E. Reyssat, J. H. Snoeijer, D. Quéré, and C. Clanet, *On the shape of giant soap bubbles*, *Proceedings of the National Academy of Sciences* **114**, 2515–2519 (2017). 79
- [154] J. M. Kolinski, P. Aussillous, and L. Mahadevan, *Shape and motion of a ruck in a rug*, *Physical Review Letters* **103**, 174302 (2009). 89
- [155] D. Vella, A. Boudaoud, and M. Adda-Bedia, *Statics and inertial dynamics of a ruck in a rug*, *Physical Review Letters* **103**, 174301 (2009). 89
- [156] N. J. Balmforth, R. V. Craster, and I. J. Hewitt, *The speed of an inclined ruck*, *Proceedings of the Royal Society of London A: Mathematical, Physical and Engineering Sciences* **471** (2014). 89
- [157] A. Fargette, S. Neukirch, and A. Antkowiak, *Elastocapillary snapping: capillarity induces snap-through instabilities in small elastic beams*, *Physical Review Letters* **112**, 137802 (2014). 90, 149
- [158] P. Silberzan, S. Perutz, E. J. Kramer, and M. K. Chaudhury, *Study of the self-adhesion hysteresis of a siloxane elastomer using the JKR method*, *Langmuir* **10**, 2466–2470 (1994). 103
- [159] K. J. Regehr, M. Domenech, J. T. Koepsel, K. C. Carver, S. J. Ellison-Zelski, W. L. Murphy, L. A. Schuler, E. T. Alarid, and D. J. Beebe, *Biological implications of polydimethylsiloxane-based microfluidic cell culture*, *Lab on a Chip* **9**, 2132–2139 (2009). 107, 120
- [160] K. E. Jensen, R. Sarfati, R. W. Style, R. Boltyanskiy, A. Chakrabarti, M. K. Chaudhury, and E. R. Dufresne, *Wetting and phase separation in soft adhesion*, *Proceedings of the National Academy of Sciences* **112**, 14490–14494 (2015). 107, 108, 131
- [161] V. Bergeron and D. Langevin, *Monolayer spreading of polydimethylsiloxane oil on surfactant solutions*, *Physical Review Letters* **76**, 3152–3155 (1996). 109, 131

- [162] L. T. Lee, E. K. Mann, D. Langevin, and B. Farnoux, *Neutron reflectivity and ellipsometry studies of a polymer molecular layer spread on the water surface*, *Langmuir* **7**, 3076–3080 (1991). 109, 111
- [163] A. Pockels, *On the relative contamination of the water-surface by equal quantities of different substances*, *Nature* **46**, 418–419 (1892). 109
- [164] L. Rayleigh, *XXXVI. Investigations in Capillarity: The size of drops. The liberation of gas from supersaturated solutions. Colliding jets. The tension of contaminated water-surfaces*, *Philosophical Magazine Series 5* **48**, 321–337 (1899). 109
- [165] I. Langmuir, *The constitution and fundamental properties of solids and liquids. II. Liquids*, *Journal of the American Chemical Society* **39**, 1848–1906 (1917). 109
- [166] R. G. Horn and J. N. Israelachvili, *Molecular organization and viscosity of a thin film of molten polymer between two surfaces as probed by force measurements*, *Macromolecules* **21**, 2836–2841 (1988). 110
- [167] T.-S. Wong, S. H. Kang, S. K. Y. Tang, E. J. Smythe, B. D. Hatton, A. Grinthal, and J. Aizenberg, *Bioinspired self-repairing slippery surfaces with pressure-stable omniphobicity*, *Nature* **477**, 443–447 (2011). 116, 117
- [168] F. Schellenberger, J. Xie, N. Encinas, A. Hardy, M. Klapper, P. Papadopoulos, H.-J. Butt, and D. Vollmer, *Direct observation of drops on slippery lubricant-infused surfaces*, *Soft Matter* **11**, 7617–7626 (2015). 117
- [169] J. D. Smith, R. Dhiman, S. Anand, E. Reza-Garduno, R. E. Cohen, G. H. McKinley, and K. K. Varanasi, *Droplet mobility on lubricant-impregnated surfaces*, *Soft Matter* **9**, 1772–1780 (2013). 117, 118, 119
- [170] C. Semperebon, G. McHale, and H. Kusumaatmaja, *Apparent contact angle and contact angle hysteresis on liquid infused surfaces*, *Soft Matter* **13**, 101–110 (2017). 120
- [171] R. Mukhopadhyay, *When PDMS isn't the best*, *Analytical Chemistry* **79**, 3248–3253 (2007). 120
- [172] C. Howell, T. L. Vu, J. J. Lin, S. Kolle, N. Juthani, E. Watson, J. C. Weaver, J. Alvarenga, and J. Aizenberg, *Self-replenishing vascularized fouling-release surfaces*, *ACS Applied Materials & Interfaces* **6**, 13299–13307 (2014). 121
- [173] J. S. Wexler, I. Jacobi, and H. A. Stone, *Shear-driven failure of liquid-infused surfaces*, *Physical Review Letters* **114**, 168301 (2015). 121
- [174] C. Howell, T. L. Vu, C. P. Johnson, X. Hou, O. Ahanotu, J. Alvarenga, D. C. Leslie, O. Uzun, A. Waterhouse, P. Kim, M. Super, M. Aizenberg, D. E. Ingber, and J. Aizenberg, *Stability of surface-immobilized lubricant interfaces under flow*, *Chemistry of Materials* **27**, 1792–1800 (2015). 121
- [175] R. Pant, S. K. Ujjain, A. K. Nagarajan, and K. Khare, *Enhanced slippery behavior and stability of lubricating fluid infused nanostructured surfaces*, *European Physical Journal Applied Physics* **75**, 11301 (2016). 121

- [176] A. Hourlier-Fargette, A. Antkowiak, A. Chateauminois, and S. Neukirch, *Role of uncrosslinked chains in droplets dynamics on silicone elastomers*, *Soft Matter* **13**, 3484–3491 (2017). 121, 149
- [177] A. Carlson, P. Kim, G. Amberg, and H. A. Stone, *Short and long time drop dynamics on lubricated substrates*, *Europhysics Letters* **104**, 34008 (2013). 131, 140
- [178] S. Anand, K. Rykaczewski, S. B. Subramanyam, D. Beysens, and K. K. Varanasi, *How droplets nucleate and grow on liquids and liquid impregnated surfaces*, *Soft Matter* **11**, 69–80 (2015). 131
- [179] H. de Maleprade, *Functional textures : aerophilicity, propulsion and specific friction*, Ph.D. thesis, Université Paris-Saclay (2016). 135

Nomenclature

Generalities

g	Gravitational acceleration
t	Time
s	Curvilinear abscissa
$(\dot{})$	Derivation with respect to time
$()'$	Derivation with respect to s
θ	Angle between the unit tangent and the horizontal axis (otherwise specified)

Elastomers properties

ρ_e	Density of an elastomer
E	Young's modulus of an elastomer
L, w, h	Length, width and thickness of an elastomer sample (otherwise specified)
$A = hw$	Cross-section of an elastomer sample
$I = h^3w/12$	Second moment of area of the cross-section of an elastomer sample
T	Elastic characteristic timescale
Δ	Confinement parameter (otherwise specified)

Liquids and droplets properties

ρ_l	Liquid density
γ	Liquid-air surface tension
μ	Liquid viscosity (otherwise specified)
S	Spreading parameter (otherwise specified)

θ_{sr}	Static receding angle
θ_{sa}	Static advancing angle
R	Droplet radius
R_b	Droplet base radius
V	Droplet volume
U	Droplet speed

Characteristic lengthscales

L_{ec}	Elastocapillary length
L_{eg}	Elastogravitational length
L_{gc}	Gravitocapillary length

Dimensionless numbers

Bo	Bond number
Ca	Capillary number
Re	Reynolds number

Specific notations

α	Inclined plane angle
τ_c	Contamination time by uncrosslinked chains

Index

- 2D modeling of drop-strip systems, 34, 81
- Bending vs stretching, 5
- Bond number, 22, 61, 115
- Buckling
 - clamped-clamped beam, 6, 72
 - generalities, 4
- Capillary number, 19, 22, 115
- Contact angle hysteresis, 17, 116
- Contamination time τ_c , 130, 132, 136–141
- Dissipation processes, 38, 89
- Drawdown bar, 48
- Droplet deposition, 62, 63
- Droplet dynamics on inclined planes, 21
- Dynamic contact angles, 18
- Elastocapillarity, 24
- Ellipsometry, 63, 64, 133, 134
- Laplace pressure, 13, 61, 126
- Length
 - L_{ec} elastocapillary length, 30
 - L_{eg} elastogravitational length, 8
 - L_{gc} gravitocapillary length, 15
- Microforce sensors, 55, 73, 125
- Minimal surfaces, 14
- Optical profilometry, 50
- Pearling, 24, 113
- Phase diagram of a drop-strip system, 83
- Phase separation, 107
- Plate, 94
- Polydimethylsiloxane (PDMS), 43
- Reynolds number, 22
- Ridge on a soft substrate, 36
- Rolling vs sliding, 20, 98
- Slender structures, 4
- SLIPS (lubricant infused surfaces), 116–118, 120, 121
- Smart actuators, 68–71
- Snap-through or snapping
 - definition, 10
 - dynamics (dry), 85–87
 - dynamics (elastocapillary), 88
 - natural phenomena, 71
 - point-force indentation, 73
 - with a droplet, 76–78
 - with condensed water vapor, 78
 - with soap bubbles, 79
- Spin-coating, 47
- Spreading parameter, 16, 106, 117
- Strip, 94
- Surface tension
 - definition, 12
 - measurements, 58–62, 108, 110–113, 124–133, 137–139
- Swelling
 - generalities, 57
 - re-swelled elastomers, 105, 139
- Two-regime dynamics, 95
- Uncrosslinked chains
 - definition, 103
 - influence on droplet dynamics, 104
 - washing procedure, 104
- Vibrations of a beam, 8, 53
- Viscosity measurements, 58
- Young’s modulus
 - definition, 3
 - measurements, 52–54
- Young-Dupré’s law, 16

Dynamique de mouillage sur matière molle : du claquage élastocapillaire au dévalement de gouttes sur élastomères

Résumé : Dans cette thèse à l'interface entre élasticité et capillarité, nous présentons tout d'abord une instabilité élastique, le claquage, revisitée dans un contexte élastocapillaire. En déposant une goutte d'eau sous une lamelle flambée en position basse, nous parvenons à déclencher une instabilité de claquage à contresens de la gravité. Cette démonstration de la prédominance des effets capillaires à petite échelle s'accompagne d'une étude des positions d'équilibre et de la stabilité de systèmes goutte-lamelle. Nous démontrons l'influence importante de la taille et de la position de la goutte le long de la lamelle, puis étendons notre étude au cas de bulles ou de gouttes condensées à partir de vapeur d'eau. Enfin, nous nous intéressons à l'aspect dynamique de l'instabilité, qui est dictée principalement par l'élasticité, y compris dans le cas élastocapillaire.

Nous mettons ensuite en évidence un phénomène surprenant : la dynamique de descente d'une goutte d'eau sur un élastomère silicone présente deux régimes successifs, caractérisés par deux vitesses différentes. Nous montrons que les chaînes libres non réticulées présentes dans l'élastomère sont à l'origine de cette dynamique inattendue. La goutte est progressivement recouverte par des chaînes de silicone, et sa vitesse change brutalement lorsqu'une concentration surfacique critique est atteinte, ce qui se traduit par une transition brutale de tension de surface. Nous nous intéressons aux vitesses de gouttes dans les deux régimes ainsi qu'aux échelles de temps mises en jeu lors de l'extraction de chaînes non réticulées, et montrons que l'extraction de ces chaînes se produit au niveau de la ligne triple.

Mots clés : élastocapillarité, instabilités élastiques, flambage, claquage, structures élancées, élastomères silicone, gouttes, interfaces, tension de surface, dynamique de mouillage

Soft interfaces: from elastocapillary snap-through to droplet dynamics on elastomers

Abstract : This thesis focuses on interactions between liquids and elastic solids. We first revisit the snap-through instability from an elastocapillary point of view, showing that capillary forces are able to counterbalance gravity by inducing snap-through with a droplet deposited below a downward buckled elastic strip clamped at both ends. Equilibrium, stability, and dynamics of drop-strip systems are investigated, demonstrating the influence of droplet size and droplet position along the buckled strip, and showing that capillarity is driving the system toward instability but elasticity is ruling the subsequent dynamics. Spin-off versions of the experiment are also designed, including a humidity-controlled mechanical switch and upscaled experiments using soap bubbles.

We then focus on interactions between silicone elastomers and aqueous droplets to understand the mechanisms underlying an unexpected two-regime droplet dynamics observed on vertical silicone elastomer plates. After demonstrating that this two-regime dynamics is due to the presence of uncrosslinked oligomers in the elastomer, we show that the speed transition coincides with a surface tension transition. A quantitative study of the droplet speeds in the two regimes is performed, and the timescale needed for uncrosslinked oligomers to cover the water-air interface is investigated both for sessile and moving droplets. We eventually show that uncrosslinked chains are extracted from the elastomer at the water - air - silicone elastomer triple line, and demonstrate that extraction occurs in various setups such as partially immersed silicone elastomer plates or air bubbles sliding up PDMS planes immersed in a water bath.

Keywords : elastocapillarity, elastic instabilities, buckling, snap-through, slender structures, silicone elastomers, droplets, interfaces, surface tension, wetting dynamics

